

Dynamics and control of Atomic Force Microscopy

Keyvani Janbahan, Sasan

DOI

[10.4233/uuid:a79de52b-66ee-4d1b-91cc-3c53b7832e7e](https://doi.org/10.4233/uuid:a79de52b-66ee-4d1b-91cc-3c53b7832e7e)

Publication date

2019

Document Version

Final published version

Citation (APA)

Keyvani Janbahan, S. (2019). *Dynamics and control of Atomic Force Microscopy*. [Dissertation (TU Delft), Delft University of Technology]. <https://doi.org/10.4233/uuid:a79de52b-66ee-4d1b-91cc-3c53b7832e7e>

Important note

To cite this publication, please use the final published version (if applicable).
Please check the document version above.

Copyright

Other than for strictly personal use, it is not permitted to download, forward or distribute the text or part of it, without the consent of the author(s) and/or copyright holder(s), unless the work is under an open content license such as Creative Commons.

Takedown policy

Please contact us and provide details if you believe this document breaches copyrights.
We will remove access to the work immediately and investigate your claim.

**DYNAMICS AND CONTROL OF TAPPING MODE
ATOMIC FORCE MICROSCOPY**

DYNAMICS AND CONTROL OF TAPPING MODE ATOMIC FORCE MICROSCOPY

Proefschrift

ter verkrijging van de graad van doctor
aan de Technische Universiteit Delft,
op gezag van de Rector Magnificus Prof. dr. ir. T.H.J.J. van der Hagen
voorzitter van het College voor Promoties,
in het openbaar te verdedigen op vrijdag 11 October 2019

door

Aliasghar KEYVANI JANBAHAN

Master of Science in Mechanical Engineering - Applied Mechanics,
from University of Tabriz, Iran
geboren te Tabriz, Iran.

Dit proefschrift is goedgekeurd door de

promotor: prof. dr. ir. A. van Keulen

copromotor: dr. ir. J.F.L. Goosen

Samenstelling promotiecommissie:

Rector Magnificus, voorzitter

Prof. dr. ir. A. van Keulen, Technische Universiteit Delft

Dr. ir. J. F. L. Goosen, Technische Universiteit Delft

Onafhankelijke leden:

Prof. dr. R. Garcia Instituto de Ciencia de Materiales
de Madrid, CSIC, Spanje

Prof. dr. ir. habil. R. I. Leine Universiteit van Stuttgärt, Duitsland

Prof. dr. G. Schitter Technische Universität Wien, Oostenrijk

Prof. dr. U. Staufer Technische Universiteit Delft

Prof. dr. ir. J. W. van Wingerden Technische Universiteit Delft

Prof. dr. ir. J.W. van Wingerden heeft in belangrijke mate aan de totstandkoming van het proefschrift bijgedragen.



This work was supported by the Netherlands organization for applied scientific research (Toegepast Natuurwetenschappelijk Onderzoek), TNO, Early Research Program 3D Nanomanufacturing.

Keywords: Atomic Force Microscopy(AFM); nanomechanical tip-sample interactions; micro-cantilevers; transient behaviour of resonators; regularized Kalman filters; chaos in AFM;

ISBN 978-94-6384-068-2

Copyright © 2019 by A. Keyvani Janbahan

e-mail: aa.keyvani@gmail.com

An electronic version of this dissertation is available at

<http://repository.tudelft.nl/>.

*to Najibeh, Aliakbar,
and memory of Alireza.*

PREFACE

This thesis is the outcome of four years of research on "Dynamics and Control of Atomic Force Microscopy" which was supported by Early Research Program (ERP) on 3D Nanomanufacturing of the Dutch National Organization for Applied Scientific Research TNO (Nederlandse Organisatie voor Toegepast Natuurwetenschappelijk Onderzoek). The thesis contains nine chapters and four appendices. Since the chapters two till eight are prepared to be published in scientific journals individually, there are some repetitions in the beginning of the introduction of these chapters. Moreover, the order of the chapters does not follow a chronological pattern. Therefore, sometimes upcoming chapters are cited in a previous ones. In this regard, I apologize for any inconvenience reading the introductions or non-chronological cross-referencing.

*Aliasghar Keyvani Janbahan
Delft, June 2017*

CONTENTS

Preface	vii
Summary	xiii
Samenvatting	xvii
1 Introduction	1
1.1 Background to atomic force microscopy	1
1.1.1 A short history of AFM	1
1.1.2 Working principle of AFM	2
1.1.3 AFM Operation modes	4
1.1.4 TIP-sample interaction forces	5
1.2 Challenges in AFM and scope of this thesis	6
1.2.1 Challenges in surface topography measurement.	7
1.2.2 Scope of this thesis.	9
1.3 Contributions of this thesis	10
1.3.1 Understanding the tip-sample interactions in TM-AFM	10
1.3.2 Dynamics and control of cantilever in TM-AFM	11
1.3.3 Multi-harmonic AFM	12
References	13
2 Tip-Sample Interactions in High-Speed Tapping Mode Atomic Force Microscopy	19
2.1 Introduction	19
2.2 Tip-sample interactions in tapping mode AFM	21
2.2.1 One DOF Assumption	23
2.2.2 Sudden Changes in Topography	23
2.3 Energy Analysis	25
2.4 Conclusion	28
References	28
3 The Origin of Amplitude Reduction in Tapping Mode Atomic Force Microscopy	31
3.1 Introduction	31
3.2 Theory and discussions	33
3.3 Conclusions.	38
References	38

4	Modulated Model of Tapping Mode AFM for Transient Conditions	41
4.1	introduction	41
4.2	Mathematical Modeling.	44
4.3	Numerical and experimental results	48
4.3.1	Linear steady-state response	48
4.3.2	Nonlinear steady-state response	48
4.3.3	Transient response in the time domain	50
4.3.4	Nonlinear transient response in the frequency domain	52
4.4	Practical implications of transient behavior of cantilevers	56
4.4.1	Nonlinear closed-loop behavior of the TM-AFM.	56
4.4.2	Chaotic Behavior.	59
4.5	Conclusions.	59
	References	60
5	Chaos: The Speed Limiting Phenomenon in Dynamic Atomic Force Microscopy	63
5.1	Introduction	63
5.2	experimental observations	66
5.3	Mathematical modelling	67
5.4	closed-loop response of AFM	70
5.5	Chaos	71
5.6	conclusions	76
	References	77
6	Control of Tapping Mode Atomic Force Microscopy with Estimated Average Forces	81
6.1	Introduction	81
6.2	Real-time estimation of the TSI force	85
6.3	Control problem	88
6.4	Conclusions.	91
	References	92
7	Minimizing Tip-Sample Forces and Enhancing Sensitivity in Atomic Force Microscopy with Dynamically Compliant Cantilevers	95
7.1	Introduction	96
7.2	Tuning the dynamics of cantilevers	99
7.3	Tip-sample interactions for tuned cantilevers.	100
7.4	Experimental results and discussion	102
7.4.1	Imaging performance	102
7.4.2	Force Measurement	106
7.4.3	Apparent height image of DNA.	107
7.5	conclusion	108
	References	109

8	Real-Time Estimation of the Tip-Sample Interactions in Tapping Mode Atomic Force Microscopy with a Regularized Kalman Filter	113
8.1	Introduction	114
8.2	regularized Kalman filter	118
8.2.1	Transforming the input estimation to state estimation.	119
8.2.2	Regularization	120
8.2.3	Step-by-step implementation	123
8.3	results and discussion.	124
8.3.1	Case study 1: Force sensing setup	124
8.3.2	Arbitrary force-distance relationship.	126
8.3.3	Case study 2: Dynamically tuned cantilevers.	128
8.4	conclusions	129
	References	130
9	Conclusions, Discussion and Recommendations	133
9.1	Conclusions.	133
9.1.1	Understanding the tip-sample interactions	133
9.1.2	Dynamics and control of the AFM cantilever based on a modulated transient model	135
9.1.3	Multi-harmonic probes and methods	136
9.2	Recommendations	137
9.2.1	Force-controlled parallel AFM	137
9.2.2	Cantilevers with mode-multiplicity	137
9.2.3	Smart AFMs	137
A	Multi-Modal analysis of cantilever for Impulse Input	139
	References	141
B	Simultaneous AFM Nano-Patterning and Imaging	143
B.1	Introduction	143
B.2	Method and experimental demonstration	144
	References	147
C	Periodic average of Tip-Sample Interaction force	149
	References	151
D	Calculation of the nonlinear frequency response curve using demodulated formulation	153
	List of Publications	155
	Acknowledgements	159

SUMMARY

The technique of Atomic Force Microscopy (AFM) is one of the major inventions of the twentieth century which substantially contributed to our understanding of the nanoscale world. In contrast to other microscopy techniques, the AFM does not operate based on the electromagnetic waves, but nano-mechanical interactions between the sample surface and a sharp probe. Therefore, its resolution is not fundamentally limited to the diffraction limit of light, but the sharpness of the probe tip which can be as small as a few atoms. The images and data obtained by AFM have had crucial importance for the scientists in the fields of biology, material science, and experimental physics. However, AFM experiments have always involved some challenges. Particularly, the limited imaging speed, and the probability of damaging the samples hinder scientists from extracting the necessary information on the samples. Besides its applications as a research tool, the AFM could potentially solve some of the challenges in semiconductor industry as a metrology and inspection tool, however, the aforementioned limitations are even more restrictive for any industrial use. Therefore, it is imperative to develop apparatus and methods which can increase the speed and reliability of AFM. In this thesis, we try to understand the physics of AFM and contribute to its development towards a potential industrial and clinical tool, from the perspective of dynamics and control of its cantilever.

The particular AFM technique that we have studied in this thesis is the Tapping Mode (TM) AFM (also known as amplitude modulation AFM) which is renowned among other modes for its stability and lower probability of damaging the samples. Studying the dynamics of TM-AFM, we realized that the tip-sample interaction (TSI) force is the heart of an AFM, and the performance of the AFM can only be improved by better understanding, quantifying, and controlling the TSI force. Despite its importance, however, quantifying the TSI force has remained an elusive practice over the period of past two decades. The TSI force can not be directly measured in experiments, and its simulations rely on highly uncertain models. Only for steady-state conditions, there exist some theoretical models that predict the TSI forces but they are not confirmed with experiments neither well understood from physical point of view.

Therefore, a major effort in this project was spent on understanding the forces in TM-AFM and more specifically in transient conditions. In Chapter 2, the TSI force is studied in transient conditions via numerical simulations and specially designed experiments. From this study, it has been found that the existing theories do not represent the reality in transient conditions. Namely, the TSI forces can be orders of magnitude higher than expected, which makes the transient studies crucial from a destructiveness point of view. Chapter 3 which is a starting point for the upcoming three chapters, is devoted to a new basic explanation for the working concept of the TM-AFM. The TM-AFM works based on the reduction of the vibration amplitude of the cantilever while it interacts with the sample surface. The reduction of the amplitude itself is typically explained by a shift

of the resonance frequency of the cantilever due to the non-linearities of TSI force. However, this does not explain some of the recent experimental and numerical observations on the frequency dependency of the TSI force. The proposed approach attributes the reduction of the amplitude to the interference between the first Fourier component of the TSI force and the excitation force. This model is in full agreement with the previous models, moreover, it is much simpler and also clearly explains the recent observations such as frequency dependency of the TSI force and inconsistent topography images of heterogeneous samples.

The model in Chapter 3 is originally devised for the steady-state conditions. However, it forms a basis for the transient analysis of the AFM cantilever in a modulated form. Chapter 4 reports a transient analysis of the AFM cantilever in a modulated form. The transient studies that are enabled with the new model could not be achieved with the existing models. The model presented in Chapter 4 has been verified with experiments and used as a basis to study some of the counter-intuitive experimental observations (in Chapter 4 and 5), and design a new controller in Chapter 6.

In Chapter 5, the model from Chapter 4 is used to study the closed-loop AFM, and the effects of the controller gains on its stability. Both the experimental and numerical studies in Chapter 5 show that imaging with controllers faster than a certain limit takes the system to chaos. Studying the bifurcation diagrams, Poincaré sections and Lyapunov exponents using the new model, it has been confirmed that the deterministic chaos phenomenon forms an upper bound for the imaging speed of TM-AFM.

The reason behind the chaos phenomenon reported in Chapter 5 was found to be a wrong-direction response of the amplitude signal in transient situations. This wrong direction initial reaction which was also reported in Chapter 4 resembles a nonlinear version of the non-minimum-phase (NMP) problem in control theory. It was concluded that to break the bandwidth barrier of the closed loop AFM, one has to use both the amplitude and the phase signals in the control loop. A configuration that uses both the amplitude and phase signal in the control loop is presented in Chapter 6. The controller presented in Chapter 6 is just an integral action applied to a new error signal which is an “approximate delayed equivalent” of the TSI force and is obtained using a Dual Kalman filter. The TM-AFM architecture with the new controller does not suffer from the wrong direction initial response, but a delay which is less problematic than the original NMP problem. In Chapter 6 it has been shown that a substantial improvement in the imaging speed of AFM is possible.

In Chapter 6 we used an “approximate delayed equivalent” of the TSI force, because estimating the accurate real-time TSI force is impossible, yet, even such a rough approximation can increase the total bandwidth of AFM by an order of magnitude. In Chapters 7 and 8 we try to improve the force estimation by *i*) improving the dynamic response of the cantilever (Chapter 7), and *ii*) developing an optimal signal processing algorithm (Chapter 8).

One fundamental limitation for the TSI force estimation is that the output of the probe is an extremely narrow-band signal. In Chapter 7, we present a new cantilever design (dynamically tuned cantilever) which has a wider output bandwidth. Moreover, numerical and experimental results show that the cantilever presented in Chapter 7 applies much less TSI force on the sample surface in comparison to conventional cantilevers,

consequently reducing the probability of damaging the surface. The third advantage of the cantilever presented in Chapter 7 is that it exhibits a significantly higher sensitivity to the material properties of the sample which is useful in mapping the material properties of the sample. Similar cantilevers to the one presented in Chapter 7 have been reported in literature and are typically used for material properties mapping or detection of different active sites on the biological samples.

The second challenge in estimating the TSI force is the signal processing itself. Estimating the forces in dynamic systems is an input estimation problem which does not have a generic solution in control theory. In Chapter 8 we develop a new type of Kalman filter which makes it possible to estimate the effective force in a large class of dynamic systems; namely, any discrete-time linear time invariant system which goes through a semi-periodic process. Using the Kalman filter presented in Chapter 8 together with any of the wide-band cantilevers, one can estimate the TSI force with a remarkable robustness and accuracy. If used in control loop, such a force estimation can substantially increase the speed of the AFM, while reducing the chance of damaging the samples.

SAMENVATTING

Een van de belangrijkste uitvindingen van de twintigste eeuw die in hoge mate heeft bijgedragen aan ons begrip van de wereld op nanoschaal is die van de atoomkrachtmicroscopie of Atom Force Microscopy (AFM). In tegenstelling tot andere microscopietechnieken, werkt de AFM niet op basis van elektromagnetische golven, maar op basis van nanomechanische interacties tussen het sample oppervlak en een zeer scherpe naald. Daarom wordt de resolutie niet beperkt door de diffractielimiet van het licht, maar door de scherpte van de tip van de naald die soms maar uit een paar atomen bestaat. De AFM-plaatjes en AFM-data zijn van cruciaal belang voor wetenschappers op het gebied van de biologie, materiaalwetenschappen en experimentele natuurkunde. AFM-experimenten stellen ons echter voor een aantal uitdagingen. Door de beperkte beeldsnelheid en de kans op beschadiging van de samples, kunnen wetenschappers niet de benodigde informatie uit de samples halen. De AFM kan, behalve bij onderzoek, ook worden ingezet bij de oplossing van enkele uitdagingen in de halfgeleidersindustrie, hoewel de zojuist genoemde beperkingen misschien nog wel meer gelden bij industriële toepassingen. Daarom is het noodzakelijk om apparaten en methoden te ontwikkelen die de snelheid en betrouwbaarheid van de AFM kunnen verhogen. In dit proefschrift proberen we de AFM vanuit het perspectief van de dynamica en regeltechniek te bestuderen en bij te dragen aan de ontwikkeling ervan naar een potentieel industrieel en/of klinisch instrument.

De AFM-techniek waar we ons in dit proefschrift op hebben toegelegd is de Tapping Mode (TM) AFM (ook bekend als de amplitude modulatie AFM) die vermaard is om zijn stabiliteit en de kleinere kans op beschadiging van de samples. Bij het bestuderen van de dynamica van de TM-AFM, realiseerden wij ons dat de Tip-Sample Interaction (TSI) kracht de kern vormt van een AFM, en de werking van een AFM kan alleen verbeterd worden door de TSI-kracht beter te begrijpen, te kwantificeren en te beheersen. Ondanks het belang ervan, is het kwantificeren van de TSI-kracht de afgelopen twintig jaar moeilijk gebleken. De TSI-kracht kan niet rechtstreeks gemeten worden in experimenten en simulaties zijn gebaseerd op zeer onzekere modellen. Alleen onder niet-transiënte omstandigheden, bestaan er wat theoretische modellen die de TSI-krachten voorspellen, maar deze worden niet bevestigd door de experimenten, en vanuit een fysiek oogpunt worden zij ook niet goed begrepen.

Daarom is er in dit project veel aandacht besteed aan de bestudering van de krachten in TM-AFM en meer specifiek aan de krachten onder transiënte omstandigheden. In Hoofdstuk 2 wordt de TSI-kracht bestudeerd onder transiënte omstandigheden met behulp van numerieke simulaties en speciaal hiervoor ontworpen experimenten. Uit deze studie kwam naar voren dat de bestaande theorieën de realiteit onder wisselende condities niet goed weergeven. De TSI-krachten kunnen namelijk vele ordes van grootte hoger zijn dan verwacht en dit maakt de bestudering van de TSI-krachten onder transiënte omstandigheden cruciaal met het oog op beschadigingen. Hoofdstuk 3 vormt de

startpunt voor de volgende drie Hoofdstukken en is gewijd aan een nieuwe toelichting op het TM-AFM concept. De werking van de TM-AFM is gebaseerd op een reducering van de vibratie amplitude van de cantilever tijdens de interactie met het sample oppervlak. Het is kenmerkend dat de reducering van de amplitude wordt verklaard door een verschuiving in de resonantie frequentie van de cantilever door de niet-lineariteiten van de TSI-kracht. Dit is echter geen verklaring voor de recente experimentele en numerieke constatering voor wat betreft de frequentie-afhankelijkheid van de TSI-kracht. De voorgestelde aanpak schrijft de reducering van de amplitude toe aan de interferentie tussen de eerste Fourier component van de TSI-kracht en de excitatiekracht. Dit model stemt volledig overeen met de voorgaande modellen. Het is zelfs veel eenvoudiger en verklaart ook duidelijk de recent geconstateerde frequentie-afhankelijkheid van de TSI-kracht en de inconsistente topografische beelden van heterogene samples.

Het model in Hoofdstuk 3 is oorspronkelijk ontworpen voor steady-state omstandigheden. Maar het vormt ook een basis voor de transiënte analyse van de AFM-cantilever in een gemoduleerde vorm. Hoofdstuk 4 geeft een transiënte analyse van de AFM-cantilever in een gemoduleerde vorm. De transiënte studies van het nieuwe model waren niet mogelijk geweest met de bestaande modellen. Het model dat gepresenteerd wordt in Hoofdstuk 4 is geverifieerd met experimenten en gebruikt als basis om enkele contra-intuïtieve experimentele waarnemingen te bestuderen (in Hoofdstuk 4 en 5). Het model in Hoofdstuk 4 was ook de basis voor ontwerpen van een nieuwe regelaar in Hoofdstuk 6 die kan de snelheid en betrouwbaarheid van AFM vergroten.

In Hoofdstuk 5 wordt het model uit Hoofdstuk 4 gebruikt om de gesloten-lus AFM te bestuderen en de effecten van de ‘controller gains’ op de stabiliteit ervan te analyseren. Zowel de experimentele als de numerieke studies in Hoofdstuk 5 tonen aan dat gebruik maken van regelaars die sneller zijn dan een bepaalde limiet brengt het systeem tot een chaotisch toestand. Het bestuderen van bifurcatiediagrammen, Poincaré secties en Lyapunov-exponenten die gebruik maken van het nieuwe model hebben bevestigd dat het deterministische chaos verschijnsel een bovengrens vormt voor de beeldvormings-snelheid van TM-AFM.

De reden achter het chaosverschijnsel en de bovengrens in snelheid van AFM die was gerapporteerd in Hoofdstuk 5 bleek een verkeerde richting reactie van het amplitudesignaal in transiënte omstandigheden te zijn. Deze initiële reactie in de verkeerde richting, waar ook al sprake van was in Hoofdstuk 4, lijkt op een niet-lineaire versie van het non-minimum-phase (NMP) probleem in de regeltechniektheorie. Het werd geconcludeerd dat om de bandbreedtebarrière van de gesloten-lus AFM door te braken, men zowel de amplitude als het fasesignaal in de regelkring moet gebruiken. In Hoofdstuk 6 wordt een configuratie gepresenteerd die zowel de amplitude als het fasesignaal in de regelkring gebruikt. De regelaar die in Hoofdstuk 6 gepresenteerd wordt is slechts een integrale actie toegepast op een nieuw foutsignaal. Dit is een “geschatte vertraagde equivalent” van de TSI-kracht, verkregen door gebruik te maken van een Dual Kalman filter. De TM-AFM architectuur heeft niet te lijden van de initiële respons in de verkeerde richting, maar van een vertraging die minder problematisch is dan het oorspronkelijke NMP-probleem. In Hoofdstuk 6 wordt aangetoond dat er een aanzienlijke verbetering mogelijk is in de beeldvormingssnelheid van de AFM.

In Hoofdstuk 6 hebben we een “geschatte vertraagde equivalent” van de TSI-kracht

gebruikt, omdat het onmogelijk is om een juiste schatting te maken van de real-time TSI-kracht. Toch kan een ruwe benadering de totale bandbreedte van een AFM met een orde van grootte verhogen. In de Hoofdstukken 7 en 8 proberen we de krachtsinschatting te verbeteren door i) de dynamische respons van de cantilever te verbeteren (Hoofdstuk 7), en ii) een optimaal signaalverwerkingsalgoritme te ontwikkelen (Hoofdstuk 8).

Een fundamentele beperking bij het inschatten van de TSI-kracht is dat de bandbreedte van het uitgangssignaal extreem smal is in vergelijking met de bandbreedte van de TSI kracht. In Hoofdstuk 7 presenteren we een nieuw ontwerp voor een cantilever (een dynamisch afgestelde cantilever) die een grotere bandbreedte heeft. Bovendien tonen de numerieke en experimentele resultaten aan dat de cantilever uit Hoofdstuk 7 veel minder TSI-kracht uitoefent op het sample-oppervlak in vergelijking met conventionele cantilevers en dat dientengevolge de kans op beschadiging van het oppervlak vermindert wordt. Het derde voordeel van de cantilever uit Hoofdstuk 7 is dat deze cantilever aanzienlijk gevoeliger is voor de materiaaleigenschappen van het sample, hetgeen nuttig is bij het zogenaamde 'mapping' van de materiaaleigenschappen van heterogeen samples. Vergelijkbare cantilevers zijn terug te vinden in de literatuur en worden gebruikt voor het mapping van materiaaleigenschappen of het detecteren van verschillende actieve plaatsen op de biologische heterogene specimens.

De tweede uitdaging bij het schatten van de TSI-kracht is de signaalverwerking zelf. Het schatten van krachten in dynamische systemen is een probleem van het inschatten van de input en hiervoor is er geen algemene oplossing in de regeltechniek literatuur. In Hoofdstuk 8 ontwikkelen we een nieuw type Kalman-filter dat het mogelijk maakt om de effectieve kracht in een grote groep van dynamische systemen te schatten, namelijk voor elk lineair tijdinvariant systeem dat een semi-periodiek proces doorloopt. Met behulp van het Kalman-filter gepresenteerd in Hoofdstuk 8 samen met een breedband cantilever (zoals degene uit Hoofdstuk 7), kan men de TSI-kracht met een opmerkelijke robuustheid en nauwkeurigheid schatten. Bij gebruik in een regelkring, kan zo'n krachtschatting de snelheid van de AFM aanzienlijk verhogen en tegelijkertijd de kans op beschadiging van de samples verminderen.

1

INTRODUCTION

Nanotechnology has created a wealth of new products that can profoundly contribute to the well-being of societies. Matter at nanoscale behaves ultimately different than at the macroscopic scale. Understanding and employing these differences for the development of new tools and products has lately been one of the major endeavors of the science and engineering communities. With no doubt, the invention of the Atomic Force Microscopy (AFM) was a major step in understanding the nano-world. Further development of AFM, not only as a research tool, but also for industrial and clinical applications can enhance nanotechnology in fulfilling the ever-increasing demands of the society.

1.1. BACKGROUND TO ATOMIC FORCE MICROSCOPY

1.1.1. A SHORT HISTORY OF AFM

THANKS to the famous formula of Dr. Ernst Karl Abbe (1840-1905), scientists already knew that resolution of the optical microscope is limited by the diffraction limit of light [1, 2]. However, the diffraction barrier could not stop them from trying to see matter with a better resolution. The dream of visualizing matter with a resolution beyond Abbe's diffraction barrier came true in the second half of the nineteenth century when techniques such as Scanning Electron Microscope (SEM) and Scanning Tunneling Microscope (STM) were invented. In 1986, "The Nobel Prize in Physics was divided; one-half awarded to Ernst Ruska (1906-1988) for his fundamental work in electron optics, and for the design of the first electron microscope, the other half jointly to Gerd Binnig and Heinrich Rohrer for their design of the Scanning Tunneling Microscope (STM)" [3].

The invention of the STM started with an experiment to test a result of the Schroedinger's equation which suggests that electrons behave like a wave at nanometer scales. According to this equation, in a metal-vacuum-metal interface, the electrons have the probability of being present in both of the metals, and as soon as the presence of the electron in one metal is checked, the probability collapses. Meaning that the electrons can pass through the vacuum gap. This wave-like behavior of electrons, which leads to the quantum tunneling effect, has a negative exponential relationship with the distance between

the metal surfaces [4]. In 1982, Binnig *et al.* experimentally tested this relationship using an externally adjustable gap which gave them reproducible results. This experiment allowed them to measure and control the distance between two conductors with nanometre resolution. Later, in 1986, the same group scientists reported that by scanning the surface of a conductive sample with another sharp metal tip (tungsten) and keeping the distance constant, they could measure a topographical image of two different samples (gold and CaIrSn_4) [5].

The STM could image conductive samples with nanometer resolution, however, for the non-conductive ones there was no solution, yet. To be able to image the topography of non-conductive samples, Binnig *et al.* introduced the concept of the AFM [6]. The AFM was an extension of the STM in which a gold leaf-spring (cantilever) with a sharp diamond tip was placed between the sample and the tungsten tip. In this way, the topography of the non-conductive sample could be measured through the deflection of the cantilever, which itself was measured by the tunneling current method.

Ever since, there has been a significant amount of research which used AFM to study the nature at nanoscale. Researchers have developed more and more precise AFMs and used them to visualize the nanostructural composition of material [7], understand the nature of physical phenomena such as friction and wear [8], and reveal the secrets of life in molecular level through monitoring the activities of biomolecules [9]. Thanks to further developments in the field of microsystems technology and measurement techniques, researchers demonstrated that they could ultimately capture the image of individual atoms on the sample surface [7]. With these results, scientists managed to visualize matter (both conductive and non-conductive) with a resolution of three orders of magnitude smaller than Abbe's diffraction limit.

The main advantage of first generation AFM over the STM was its ability to image non-conductive as well as conductive materials. Nowadays, AFMs are also suitable for the applications that go beyond topography imaging, such as, mapping the mechanical [10], or electrical [11] properties of samples, measuring the intermolecular forces in biology [12], and even manipulation of the surface of samples with nanometer accuracy [13]. Moreover, because of their simple mechanical concept, AFMs could image samples in vacuum [14], ambient conditions, or fluidic environment [15], low or high temperatures [16], which made them a universal imaging tool.

These days, the word AFM is referred to a family of nanomechanical devices that are gaining ever-increasing scientific and industrial interest in all kinds of applications, from physics to biology and from food research to space explorations [17–20]. Besides its applications in experimental research, the AFM is entering the industrial world as well [21, 22]. It is predicted that the AFM technology will play a crucial role in the semiconductor industry as an inspection, metrology, and nano-manipulation tool [23, 24]. However, there are still many challenges on the road map of the AFM towards large-scale applications, which motivate the research in this thesis.

1.1.2. WORKING PRINCIPLE OF AFM

The working concept of the AFM, as schematically shown in Fig. 1.1, lies in touching the samples using a probe that includes an atomically sharp tip and a microcantilever beam. The probe can maneuver nanometrically precise with respect to the sample. When the

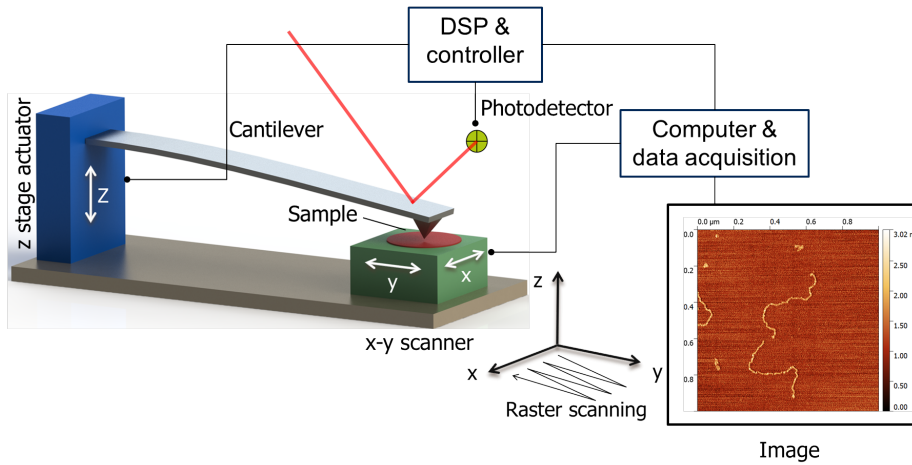


Figure 1.1: Schematic view of an AFM. The probe consist of a cantilever beam which has a sharp tip at its free end that mechanically interacts with the sample surface. The deflection of the sample is measured using a laser beam. The topographic image of the sample is captured by scanning the sample in planner directions.

cantilever is brought in a proximity of the sample surface, the atoms on the surface and the tip start to interact with each other. The so-called Tip-Sample Interaction (TSI) forces influence the mechanics of the cantilever. This effect is either the deflection of the cantilever (in static AFM) or a change in dynamic properties of the cantilever (in dynamic mode AFM). By monitoring any of these effects, one can estimate the distance between the cantilever and the sample and possibly some other characteristics of the sample. Scanning the sample surface using the x-y scanner, while keeping the effects of TSI force on the cantilever constant, a topographical image of the sample is obtained.

The AFM should at least consist of a mechanical transducer that converts the TSI force into a measurable deflection (normally a cantilever beam) a sharp tip that limits the TSI force to a small area, a deflection sensor for the cantilever/transducer, a z stage actuator, an x-y scanner, a Digital Signal Processing (DSP) unit, a controller, and a computer. Although in its original embodiment the deflection of the gold cantilever cantilever was measured by the tunneling current concept, these days, there exist many different types and materials of cantilever and their deflection is typically measured by the optical beam deflection (OBD) technique as shown in Fig. 1.1 [25]. Other popular methods for sensing the deflection of the cantilever include interferometry, capacitive, magnetic, piezoresistive and piezoelectric [26–28]. Conventionally, the x-y scanning and also actuation in z direction is done using a piezoelectric tube, but there exist also other types of actuators that will be discussed in the following sections. The x-y scanner usually moves the sample surface with respect to the probe or *vice versa* in a saw-tooth pattern which is either mounted under the sample, or is connected to the probe ¹.

¹The first one is called the sample scanning system, whereas the latter is called probe scanning system. Each one has its own advantages and disadvantages.

1.1.3. AFM OPERATION MODES

The experimental method which is used in measuring the probe-sample distance is conventionally referred to as the "operation mode". In the early stage of its invention, the AFM was operated in a static mode, in which the tip was continuously in contact with the sample surface. In this mode, which is also called the contact mode, the TSI force bends the cantilever in the vertical direction. Comparing the deflection of the cantilever with a user-defined set-point value, an error signal is generated. A feedback controller adjusts the distance between the cantilever and the surface so that the error signal is kept at zero [6]. In this manner, the topographic image of the sample represents 3D map of every point that provides the same deflection.

Soon after the invention of AFM, scientist introduced the dynamic AFM techniques where the cantilever is excited with a frequency around its resonance frequency [29, 30]. Since the cantilever is highly sensitive to the forces at its resonance frequency, it is also very susceptible to the changes of these force. Hence, any perturbation caused by the TSI force has a large effect on the amplitude and phase of the vibration of the cantilever. Measuring the motion of the cantilever, one can trace the effects of the TSI force on the cantilever.

In practice, the dynamic AFM measurements are performed through two different modulation methods. Either the resonance frequency of the cantilever is measured using a Phase Lock Loop (PLL), or the cantilever is excited with a constant frequency, and the amplitude of its motion is tracked using a Lock in Amplifier (LIA). The first method is referred to as "Frequency Modulation (FM)" AFM, and the latter is called "Amplitude Modulation (AM)" AFM. Typically, the FM-AFM is used in a vacuum environment and mainly to probe the attractive forces between the sample and the tip, hence, it is also called the non-contact AFM. Whereas the AM-AFM is employed in the ambient or liquid environments, and probes both the attractive and repulsive forces, and therefore, is called "intermittent contact" or the "Tapping Mode (TM)" AFM.

Since the cantilever is a high-quality-factor resonator (typically the quality factor is in the order of 100-10000 in air), the dynamic operation modes are substantially more sensitive than the static mode. Especially in vacuum experiments, for which the quality factor of the cantilever is the highest, any small change in the resonance frequency of the cantilever can easily be detected. Researchers used this extreme sensitivity to visualize the individual atoms on the sample surface [7, 29].

Besides the static and dynamic modes, researchers have developed the quasi-static modes [31–33]. In quasi-static modes, i.e., "peak force tapping mode" or "jumping mode", the cantilever operates in the static regime so that the deflection of the cantilever can be traced back to the TSI force. However, the tip is not always in contact with the sample. In these modes, the cantilever is brought to contact with the sample and retracted in a periodic manner. Advantageously, either a force-distance relationship can be measured during each cycle, or the frequency spectrum of the deflection signal can be analyzed [34] which enables mapping of material properties of the samples, simultaneously with the topography imaging.

Among all the different operation modes of the AFM, the TM-AFM is probably the most popular one.² This is because: 1) it applies minute forces on the surface and does

² *"This tapping mode approach has proven to be a significant blessing to biological researchers, as it has al-*

not damage the samples. 2) in contrast to the FM-AFM, it does not require a vacuum environment and is also suitable for fluidic environments. These unique properties of TM-AFM not only make it very promising for biological experiments but also for industrial applications [23] in which damaging the sample is unacceptable.

1.1.4. TIP-SAMPLE INTERACTION FORCES

To complete the explanation of the basic principle of the AFM, here we present a short description for the origin of the TSI forces from a physical point of view. More thorough explanations of the origin of TSI forces can be found in [36, 37]

When two atoms are positioned at a distance of a few nanometers from each other, they attract each other with (at least) the van der Waals force. Even if the two atoms are electrically neutral, the electron clouds of the atoms vibrate with a small amplitude due to their thermal energy. This vibration of the electron clouds with respect to the nucleus causes a temporal polarization of the atom. This temporal polarization would have a random direction for an individual atom, however, when two atoms are close to each other, an electromagnetic interaction happens. Considering all the possible random states, the total energy of the two atoms is at its lowest when the polarization vectors are aligned. Consequently, it is slightly more likely for the two atoms to have an aligned polarization vector, than opposite vectors. Therefore, the two atoms spend more time in an aligned state, in average (Fig. 1.2.A). From an electromechanical point of view, the two particles attract each other when their polarization vectors are aligned, and repel each other when their polarization vector is opposite to each other. Hence, stochastically two atoms attract each other even if they are totally uncharged. This is called the van der Waals (vdW) attraction. For a detailed derivation of the vdW forces see [38, 39]. By further decreasing the distance between the two atoms (Fig. 1.2.B), their electron clouds start to repel each other with a much stronger force, i.e., the so-called Pauli repulsion force [37].

When the tip of the AFM probe approaches the surface of a sample, the atoms at the tip of the cantilever individually interact with the atoms on the surface of the sample (Fig. 1.2.C), and a collective effect of all these atoms create the Tip-Sample Interaction (TSI) force. Since both the attractive and repulsive forces are effective only at a short distance, a rather low number of atoms on the surface participate in the generation of the TSI force. Thanks to this fact, the AFM tip only "feels" the forces from a very localized region on the sample surface. Therefore the AFM has a distinctly high lateral and vertical resolution.

Scientists have calculated the overall effect of the atomic forces and presented different models that can explain the relationship between the TSI force and the distance between the tip and the sample surface (e.g., Fig. 1.2.D). Unfortunately, these models are not universal, because of two reasons: 1) The geometry of the tip is not well defined (see for example, the difference between the Tatara model and the Hertz model [40]). 2) The TSI forces are not limited to the vdW and Pauli repulsion forces. Depending on the physical and environmental situations, other types of forces can also be present in the TSI force. For example, the tip or the sample can be electrostatically charged or polar-

lowed the characterization of samples that would otherwise be too soft or too fragile to withstand contact mode examination" describes Kuznetsov et al. in [35].

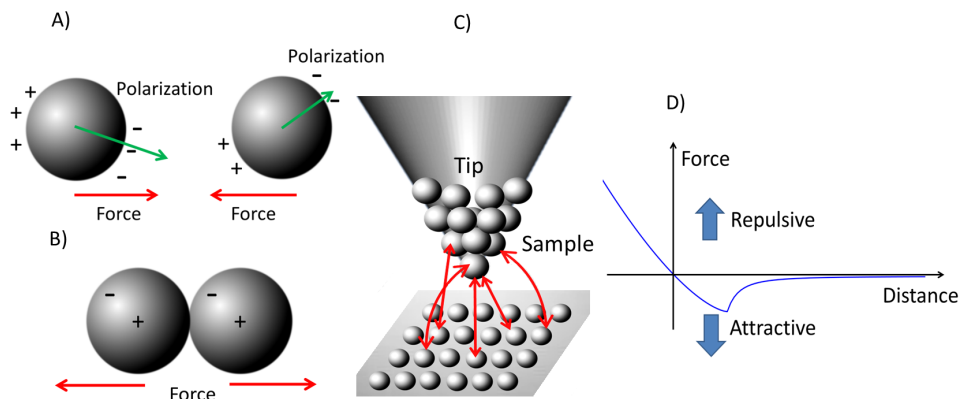


Figure 1.2: Schematic view of tip-sample interactions; A) the two atoms attract each other due to the van der Waals forces when they are closed to each other and their polarization vectors are aligned. B) the two atoms repel each other when the distance gets smaller than the atomic distance (Pauli repulsion) C) the individual atoms on the surface and the tip interact D) collectively the sum of all individual interactions generate the tip-sample interaction forces.

ized which obviously adds to the attractive forces, or there can be humidity in the environment that causes a local capillary effect [41, 42]. Needless to say that depending on the properties of the sample and the tip, many other kinds of forces such as viscoelastic forces [43], chemical bonds [44], etc. might affect the tip [36]. In this thesis, we shall only use the Derjaguin–Muller–Toporov (DMT) model [40] which is valid for a vast majority of physical experiments and is commonly adopted for theoretical studies. This model considers the attractive vdW force and a macroscopic Hertzian contact model between a perfectly flat surface and a spherical tip. We also add an extra viscoelastic term to the DMT model to account for non-conservative forces, when needed.

1.2. CHALLENGES IN AFM AND SCOPE OF THIS THESIS

Over the past 30 years, the AFM has been one of the primary tools for experimental research, especially in material science and biology. However, the end-use application of AFM as a standard tool in clinical or industrial environments is still limited. In many cases, the AFM offers the necessary functionality with the desired resolution, whereas, it suffers from the lack of speed and throughput. In some other cases, where the measurement time is not a limiting factor, the uncertainties, difficulty of the experiments, and the reliability of the results are hindering. For example, the AFM meets the metrology and inspection requirements of the semiconductor fabrication industry from a resolution point of view. However, its throughput is substantially lower than required. Moreover, it does not guarantee a completely non-destructive inspection [45]. As on other example, researchers have shown that it is possible to detect the status of viruses through their mechanical stiffness,³ though for this technique to be used in the clinical examinations,

³For example, the stiffnesses of a mature and an immature Human Immunodeficiency Virus (HIV) are significantly different and can be measured using an AFM [46].

the AFM should maintain a high level of reliability and repeatability.

In this thesis, we aim to contribute to the development of the AFM towards a high-throughput device for future clinical and industrial applications.

1

1.2.1. CHALLENGES IN SURFACE TOPOGRAPHY MEASUREMENT

As mentioned previously, the AFM has a much wider range of applications these days, however, the topographic measurement can still be considered as the primary task of the AFM, especially for the industrial use case. Hence, in this thesis, we focus on this application. The requirements for the AFM as a topography measurement tool can be split into two main parts; performing a precise and fast raster scanning, i.e. providing a lateral resolution, and measuring the local height of the sample in the z direction with high speed and resolution. The latter also determines the maximum speed allowed for the raster scanning. That is, scanning too fast without performing an accurate z measurement is meaningless. Each one of these tasks has been improved during the past three decades through design of high-performance components and development of efficient operation methods for the existing elements. Some of these challenges are discussed in the following subsections.

LATERAL RESOLUTION

The lateral resolution of the AFM is limited by the sharpness of the tip as well as the precision and bandwidth of the x-y scanner. On the one hand, researchers have been improving the sharpness of the tip using etching techniques [47] or attaching Carbon Nano-Tube (CNT) pillars to the AFM tip [48]. On the other hand, many researchers have developed different x-y scanners and scanning techniques to increase its precision and bandwidth.

The main difficulties regarding the x-y scanner can be split into two main issues; i) creep and hysteresis of the piezoelectric material, ii) mechanical resonance of the scanner. The creep and hysteresis are inherent to the piezoelectric actuators and are usually controlled by feedback techniques [49, 50], whereas the resonance problem occurs due to the saw-tooth motion pattern of the scanner and has been resolved with different approaches as follows.

In the majority of the commercial AFM systems the x-y scanning is done using a tubular piezoelectric actuator [51]. However, researchers have developed scanners with stack piezoelectric actuators which can operate with higher bandwidth without getting in resonance [52]. Also, researchers proposed alternative scanning patterns such as sinusoidal [53] or circular [54], instead of the saw-tooth pattern to eliminate the sharp changes in the direction of the motion. In a different approach, Andersson and Pao developed a compressed measurement method in which they scan only 10% of the sample area, and a computer algorithm estimates the height of the other 90% of the sample to generate the full image [55]. In this way, they could virtually increase the scanning throughput of the AFM.

VERTICAL RESOLUTION

The AFM measures the height of the samples through a strongly nonlinear contact-mechanics effect which concerns the dynamics of the cantilever, z-axis actuator, the

1

feed-back controller, and the electronic circuits. Hence, each and every component of the z-stage unit should provide a high level of accuracy and reliability. Some of the challenges regarding the vertical distance measurement can be described as follows:

1. **Parachuting effect:** In high-speed AFM if the distance between the sample surface and the cantilever suddenly increase, the cantilever can lose the contact with the surface. In these situations, the error signal saturates to its maximum, and the z-stage actuator approaches the sample with a constant speed. Consequently, the cantilever hovers above the surface without measuring the correct topography of the sample [56]. There exist methods to estimate the surface loss from the observable data, however, its prevention is not guaranteed in high-speed AFM.
2. **Resonance of the z-stage actuator:** Similar to the x-y scanner, the z-stage actuator can also experience mechanical resonances which limit the scanning speed of the AFM. To overcome this issue, researchers proposed different approaches such as, designing counterbalanced actuators with higher bandwidth [22, 57], and actively damped z-stage actuators [58]. To retain long stroke of actuation together with a high bandwidth, the use of dual z-stage actuators is suggested [59, 60]. In this approach, one of the actuators provides a long stroke with low bandwidth, and the other one provides a high bandwidth with a shorter stroke. It has also been proposed to integrate a short range actuator on the cantilever itself, which improves the bandwidth even further [61].
3. **Damage and deformation:** Considering that the contact area between the tip and the sample is subtle, even a small amount of the force applied to the contact area results in significant stresses. Consequently, it is possible to damage the sample or the tip ⁴. Especially for transient situations, (for example during the coarse approach of the cantilever towards the sample,) these forces might be too high for the sample or the tip to survive [62]. The probability of damage exists even in dynamic AFM (which is the least damaging method).

The other issue with excessive force is the deformation of the samples under the tip [63, 64]. For specimens with low elasticity, it is very plausible that different experimental conditions give different topography images. In these situations, the samples are compressed under the tip, and their height image is captured with relatively large errors. To minimize the errors in measuring the height of samples in AFM, researchers have proposed more optimized elements such as ultra-sensitive cantilevers [27], or faster electronic parts [65], as well as the different operation and control algorithms [66, 67] which ease the problem up to a certain extent.

Besides the samples, it is also possible that the tip can break or wear and lose its sharpness after a certain amount of measurements [68]. This issue might not be very critical for biological AFM, or the AFM as a research tool. However, it reduces the lifetime of the probe and hinders industrial AFM applications.

⁴A macro-scale analogous problem for imaging biological samples (e.g. DNA) with a tapping mode AFM, would be to try to measure the height of a baby elephant using the summit of the Mount Everest which is vibrating with 100 meters of amplitude.

- 4. Instability, bi-stability and chaos:** Due to the nonlinearity of the nanomechanical forces, there exists many different types of instabilities, bifurcations, and chaotic patterns that the cantilever can fall into. These nonlinearities can cause imaging artifacts such as snap-in phenomenon, in which the tip sticks to the sample, or chaotic fluctuations of the signals [69, 70]. In some studies, researchers have reported the presence of chaos in AFM as a result of attractive nonlinear van der Waals forces [71, 72], or excessive adhesion [73]. All these effects degrade the reliability of the AFM imaging. Especially for industrial and clinical applications, these effects should be completely avoided. Reducing or eliminating these instabilities demands for increasing the stiffness and/or damping of the cantilever, either physically or artificially⁵ [75]. However, adding additional damping or stiffness to the cantilever comes with the cost of reducing the sensitivity, increasing the TSI force and, consequently, increasing the probability of damage.

Needless to mention that, all these challenges are even more predominant for higher imaging speeds, which is a crucial requirement for industrial and clinical applications.

1.2.2. SCOPE OF THIS THESIS

The primary goal of this thesis is to improve the functionality of AFM considering its vertical resolution to enable its potential industrial and clinical applications. For this, we focus on tip-sample interaction forces, the dynamics of the AFM cantilever, and design of new signal processing and control techniques for tapping mode AFM.

Resolving the challenges regarding the dynamics of TM-AFM and the TSI forces can prosper the speed, reliability, and ease of use of AFM in the following manner: 1) Further reducing the TSI forces in TM-AFM can broaden its window of application for more fragile samples in biological sciences as well as more sensitive samples in industrial applications. 2) Increasing the stability of the AFM system can improve the reliability of data. 3) Having more control over the TSI forces can enable new applications such as modifications of the sample surface at the nanoscale. 4) Measuring and controlling the TSI force can also increase the speed, and guarantee non-destructive tests using the AFM.

One major challenge of the AFM is that it does not directly measure the TSI force, but the deflection of the cantilever. In static modes, the deflection of the cantilever can be translated to the TSI force by scaling with the spring constant of the cantilever. However, in dynamic modes, the TSI force is an input for the cantilever, and the input of dynamic systems are not necessarily measurable [76, 77]. To further explain this issue, the TSI force and the displacement of the cantilever in TM-AFM is schematically shown in Fig. 1.3. As it can be seen, the deflection of the cantilever (in most of the experimental conditions) is a single harmonic signal which can be represented by three parameters, i.e. the frequency, amplitude, and phase. However, the TSI force is a more complicated signal in time domain, which contains multiple harmonic components. Many of the details of the TSI force are contained in its higher harmonic components which do not propagate to the displacement signal. This makes it very challenging to measure, estimate or control the force. That is why, quantifying the TSI force has always remained

⁵Using the so-called Q-control method artificially increases the damping (and stiffness) by adding an extra excitation force which is in phase with damping (and elastic) force of the cantilever [74].

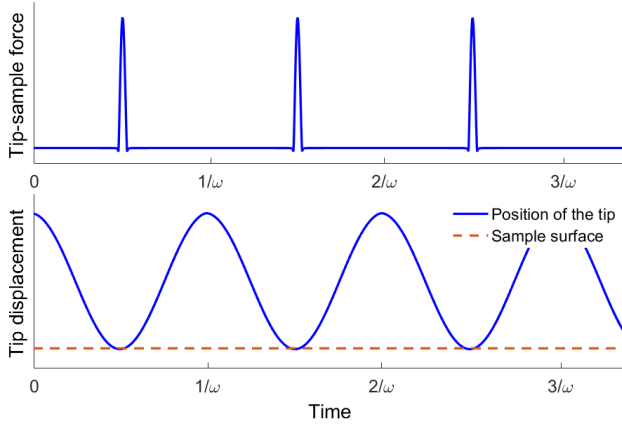


Figure 1.3: Tip-sample interaction forces and motion of the tip in tapping mode AFM.

as an important, yet elusive goal for the scientists. Considering that the height profile of the surface only affects the cantilever via the TSI force, measurement of the height is also constrained by the measurement of the TSI force. Therefore to design high speed and reliable AFMs, it is essential to have a full understanding of the TSI force.

1.3. CONTRIBUTIONS OF THIS THESIS

In the following chapters of this thesis we aim **to understand the tip-sample interaction force in tapping mode AFM and improve the performance of AFM via mechanical and control designs based on a knowledge on TSI force**. The contributions of this thesis can be divided into three sets of studies: i) Studying the TSI forces in conventional single harmonic TM-AFM, ii) Dynamics and control of the single-harmonic TM-AFM, iii) Design of cantilevers and signal processing techniques for multi-harmonic TM-AFM as an alternative solution.

1.3.1. UNDERSTANDING THE TIP-SAMPLE INTERACTIONS IN TM-AFM

One important aspect of the TSI force in tapping mode AFM is the maximum amount of repulsive force which is applied to the surface during each cycle of vibration. The so-called peak repulsive force (PRF) plays a critical role in destructiveness of the measurements, as well as lifetime of the tip. So far, many of the investigations have focused on PRF in tapping mode AFM. However, both the theoretical [78] and experimental [79] studies only considered the steady-state conditions in which the cantilever is settled to a harmonic motion pattern. To account for the transient conditions, we have analyzed a scenario in which the sample surface suddenly displaces and causes a transient motion of the cantilever. Our numerical and experimental results show that the cantilever applies orders of magnitude stronger forces on the surface during its transient motion (See Chapter 2 and [62]). Hence, the design of AFM should encounter transient conditions to prevent damage.

Other important factors which have significant effects on the TSI force are the operation parameters. The amplitude of vibration while the cantilever is far away from the sample, the set point amplitude, and the excitation frequency of the cantilever determine the TSI force up to a large extent. While the effect of the amplitude is well described in the literature [40, 78–80], the effects of the excitation frequency are often dismissed. We have numerically and experimentally shown that the excitation frequency is actually by far the most important parameter for the TSI force. Choosing a slightly wrong excitation frequency can easily cause a severe damage on the sample or the tip. While this is not favorable for imaging, it could bring a new application. We used this sensitivity of the TSI to excitation frequency for deliberately increasing and decreasing the TSI forces to devise a nano-patterning technique for semiconductor industry [24] (see also Appendix B).

We could show the effects of the excitation frequency on the TSI force using experiments and numerical simulations. However, this sensitivity could not be easily explained with the existing theories. Therefore, we have presented a new theory to understand the working mechanism of the TM-AFM, which could also explain the new observations. While the origin of amplitude reduction in AFM was previously explained based on the changes in the resonance frequency of the cantilever, our explanation attributed the amplitude reduction to an interference between the excitation force and the TSI force (see Chapter 3). This new explanation forms a basis for the control design for the TM-AFM which is explained next.

1.3.2. DYNAMICS AND CONTROL OF CANTILEVER IN TM-AFM

To design high-performance model-based controllers for the TM-AFM in the vertical direction, it is crucial to have an appropriate dynamic model of the AFM cantilever. Although the existing models can accurately explain the behavior of the AFM cantilever, these models are not suitable for control design because of two main issues: 1) nonlinearity and uncertainty of the tip-sample interaction model. 2) Presence of multiple time scales in the dynamics of the system. In TM-AFM, there is a significant gap between the time scales of the cantilever and the controller. The controller should be designed with a bandwidth in the order of bandwidth of changes in the amplitude of the motion of the cantilever, which by definition is much smaller than the resonance frequency of the cantilever. In order to derive a dynamics model of the cantilever in the time scale of the controller, we have extended the model in Chapter 3 for transient conditions (see Chapter 4). In this model, only the slowly changing amplitude and phase signals are tracked and the fast vibration of the cantilever is averaged out. The model derived in Chapter 4 has been confirmed with experiments and numerical results and could describe the dynamic evolution of the amplitude and phase due to tip-sample interaction forces. The results of this model in steady-state conditions fall back to the existing theories for the TM-AFM, while its transient solution is not achievable with the existing models.

Using the dynamics model from Chapter 4, we have studied the closed-loop dynamics of the AFM in z -direction. Based on this analysis, we found that the speed of the TM-AFM is strictly limited by chaos. In chapter 5, we have shown that in the conventional configuration of the AFM, if the controller is tuned to be faster than a certain limit, the closed loop AFM shows a chaotic behavior. Unlike the previously detected chaos and

bi-stability which could be easily concurred with simple changes in operation parameters [71, 72], the newly detected chaos is unavoidable. These results show that in the current configuration of the TM-AFM, the chaos phenomenon imposes an upper bound for the closed loop bandwidth. We concluded that the control algorithm of TM-AFM should be revised to avoid the chaotic behavior and increase the closed-loop bandwidth of the system.

The chaotic behavior of the TM-AFM that was reported in Chapter 5 is, in fact, a result of the controller which only receives the amplitude signal as the input. To improve the closed loop performance of the AFM, in Chapter 6, we present a new control algorithm which uses both the amplitude and the phase signal. In this controller, first, an approximation for the average of the TSI force is estimated from the amplitude and phase of the cantilever, then the control action is taken based on the estimated average force. Using the new controller, the amplitude and phase of the cantilever remain free to fluctuate while the height profile of the sample surface is measured from the control signals. These results show that the total closed-loop bandwidth of the system can be increased up to an order of magnitude, by adding a Kalman filter to the loop. The more accurate the estimate of the force, the better can the behavior of the closed-loop system be.

1.3.3. MULTI-HARMONIC AFM

From the results in the previous chapters, we achieve two key findings. First, the tip-sample interactions in dynamic AFM depend on many mechanical and control parameters of the system. Secondly, estimating the TSI force and using it in the control loop can considerably increase the bandwidth. However, estimating the tip-sample interactions from a single harmonic motion of the cantilever is non-complete, uncertain and has large delays. Not fully observing the TSI force, and being restricted to a single harmonic motion pattern, it is possible to damage the surface or the tip by applying an excessive mechanical load.

In Chapter 7 we aim to increase the sensitivity of the motion of the cantilever to the TSI forces by activating the second bending mode of the cantilever. Adjusting the dynamic characteristics of the cantilever through its geometric design, we show that one can reduce the TSI force, and at the same time enhance its sensitivity to the TSI force. This type of cantilevers provide a non-harmonic motion signal which contain more information on the TSI force. Yet, accurately estimating the TSI force from the enhanced output signal remain as a challenge.

In Chapter 8, we develop a new signal processing technique based on Kalman filtering for estimation of the TSI force in multi-harmonic cantilevers. As mentioned previously, the input of the dynamic physical systems is not necessarily measurable. However, a delayed and approximated value for the force input can be estimated. For the single harmonic AFM, the delay and uncertainty do not allow for any conclusion about the details of the TSI force. However, for multi-harmonic AFM, since the deflection signal contains multiple frequency components, the TSI force could be measured accurately. The results from Chapters 4 till 8 show that optimizing the cantilever and the controller at the same time can increase the imaging performance in the sense of speed, accuracy, and reliability in vertical direction. Moreover, the extra information that can be retrieved

based on the results of the Chapters 7 and 8 can be used in local detection of the material properties of the samples.

1

REFERENCES

- [1] J. S. Silfies, S. A. Schwartz, and M. W. Davidson, *The diffraction barrier in optical microscopy*, Nikon Inc., [Online]. Available: <https://www.microscopyu.com/articles/superresolution/diffractionbarrier.html>. [Accessed 28. 10. 2015] (2000).
- [2] E. Abbe, *A contribution to the theory of the microscope and the nature of microscopic vision*, in *Proceedings of the Bristol Naturalists' Society*, Vol. 1 (1874) pp. 200–261.
- [3] Nobel-Media, *The nobel prize in physics 1986*, (1999).
- [4] E. L. Wolf, *Principles of electron tunneling spectroscopy*, Vol. 152 (Oxford University Press, 2012).
- [5] G. Binnig, H. Rohrer, C. Gerber, and E. Weibel, *Surface studies by scanning tunneling microscopy*, *Physical review letters* **49**, 57 (1982).
- [6] G. Binnig, C. F. Quate, and C. Gerber, *Atomic force microscope*, *Physical review letters* **56**, 930 (1986).
- [7] F. J. Giessibl, *Afm's path to atomic resolution*, *Materials Today* **8**, 32 (2005).
- [8] J. Roa, G. Oncins, J. Díaz, X. Capdevila, F. Sanz, and M. Segarra, *Study of the friction, adhesion and mechanical properties of single crystals, ceramics and ceramic coatings by afm*, *Journal of the European Ceramic Society* **31**, 429 (2011).
- [9] T. Ando, T. Uchihashi, and N. Kodera, *High-speed afm and applications to biomolecular systems*, *Annual review of biophysics* **42**, 393 (2013).
- [10] A. Rosa-Zeiser, E. Weilandt, S. Hild, and O. Marti, *The simultaneous measurement of elastic, electrostatic and adhesive properties by scanning force microscopy: pulsed-force mode operation*, *Measurement Science and Technology* **8**, 1333 (1997).
- [11] S. Peng, Q. Zeng, X. Yang, J. Hu, X. Qiu, and J. He, *Local dielectric property detection of the interface between nanoparticle and polymer in nanocomposite dielectrics*, *Scientific Reports* **6** (2016).
- [12] O. H. Willemsen, M. M. Snel, A. Cambi, J. Greve, B. G. De Grooth, and C. G. Figdor, *Biomolecular interactions measured by atomic force microscopy*, *Biophysical Journal* **79**, 3267 (2000).
- [13] M. Ramiaczek-Krasowska, A. Szyszka, A. Stafiniak, R. Paszkiewicz, B. Paszkiewicz, and M. Tlaczala, *Application of AFM technique for creation of patterns in nanoscale*, *Opt. Appl.* **41**, 307 (2011).

- [14] F. J. Giessibl and B. M. Trafton, *Piezoresistive cantilevers utilized for scanning tunneling and scanning force microscope in ultrahigh vacuum*, [Review of scientific instruments](#) **65**, 1923 (1994).
- [15] F. Oesterhelt, M. Rief, and H. Gaub, *Single molecule force spectroscopy by afm indicates helical structure of poly (ethylene-glycol) in water*, [New Journal of Physics](#) **1**, 6 (1999).
- [16] J. Broekmaat, A. Brinkman, D. H. Blank, and G. Rijnders, *High temperature surface imaging using atomic force microscopy*, [Applied Physics Letters](#) **92**, 043102 (2008).
- [17] D. Parrat, S. Gautsch, L. Howald, D. Brändlin-Müller, N. De Rooij, and U. Staufer, *Design and evaluation of a polyimide spring system for the scanning force microscope of the phoenix mars mission 2007*, in [11th European Space Mechanisms and Tribology Symposium \(ESMATS 2005\)](#), SAMLAB-CONF-2005-028 (2005) pp. 281–287.
- [18] N. Jalili and K. Laxminarayana, *A review of atomic force microscopy imaging systems: application to molecular metrology and biological sciences*, [Mechatronics](#) **14**, 907 (2004).
- [19] H. Yang, Y. Wang, S. Lai, H. An, Y. Li, and F. Chen, *Application of atomic force microscopy as a nanotechnology tool in food science*, [Journal of food science](#) **72**, R65 (2007).
- [20] T. Akiyama, S. Gautsch, N. De Rooij, U. Staufer, P. Niedermann, L. Howald, D. Müller, A. Tonin, H.-R. Hidber, W. Pike, *et al.*, *Atomic force microscope for planetary applications*, [Sensors and Actuators A: Physical](#) **91**, 321 (2001).
- [21] H. Sadeghian, R. Herfst, J. Winters, W. Crowcombe, G. Kramer, T. van den Dool, and M. H. van Es, *Development of a detachable high speed miniature scanning probe microscope for large area substrates inspection*, [Review of Scientific Instruments](#) **86**, 113706 (2015).
- [22] R. Herfst, B. Dekker, G. Witvoet, W. Crowcombe, D. de Lange, and H. Sadeghian, *A miniaturized, high frequency mechanical scanner for high speed atomic force microscope using suspension on dynamically determined points*, [Review of Scientific Instruments](#) **86**, 113703 (2015).
- [23] H. Sadeghian, R. Herfst, B. Dekker, J. Winters, T. Bijnagte, and R. Rijnbeek, *High-throughput atomic force microscopes operating in parallel*, [arXiv preprint arXiv:1611.06582](#) (2016).
- [24] A. Keyvani, M. S. Tamer, M. H. van Es, and H. Sadeghian, *Simultaneous afm nanopatterning and imaging for photomask repair*, in [SPIE Advanced Lithography](#) (International Society for Optics and Photonics, 2016) pp. 977818–977818.
- [25] S. Alexander, L. Hellemaans, O. Marti, J. Schneir, V. Elings, P. K. Hansma, M. Longmire, and J. Gurley, *An atomic-resolution atomic-force microscope implemented using an optical lever*, [Journal of Applied Physics](#) **65**, 164 (1989).

- [26] D. Sarid, *Scanning force microscopy: with applications to electric, magnetic, and atomic forces*, Vol. 5 (Oxford University Press on Demand, 1994).
- [27] M. Li, H. X. Tang, and M. L. Roukes, *Ultra-sensitive nems-based cantilevers for sensing, scanned probe and very high-frequency applications*, *Nature nanotechnology* **2**, 114 (2007).
- [28] M. G. Ruppert, A. G. Fowler, M. Maroufi, and S. R. Moheimani, *On-chip dynamic mode atomic force microscopy: A silicon-on-insulator mems approach*, *Journal of Microelectromechanical Systems* (2016).
- [29] T. Albrecht, P. Grutter, D. Horne, and D. Rugar, *Frequency modulation detection using high- q cantilevers for enhanced force microscope sensitivity*, *Journal of Applied Physics* **69**, 668 (1991).
- [30] Y. Martin, C. C. Williams, and H. K. Wickramasinghe, *Atomic force microscope-force mapping and profiling on a sub 100-Å scale*, *Journal of Applied Physics* **61**, 4723 (1987).
- [31] J. Sotres, A. Lostao, C. Gomez-Moreno, and A. Baró, *Jumping mode afm imaging of biomolecules in the repulsive electrical double layer*, *Ultramicroscopy* **107**, 1207 (2007).
- [32] P. De Pablo, J. Colchero, J. Gomez-Herrero, and A. Baro, *Jumping mode scanning force microscopy*, *Applied Physics Letters* **73**, 3300 (1998).
- [33] T. Young, M. Monclus, T. Burnett, W. Broughton, S. Ogin, and P. Smith, *The use of the peakforcetm quantitative nanomechanical mapping afm-based method for high-resolution young's modulus measurement of polymers*, *Measurement Science and Technology* **22**, 125703 (2011).
- [34] A. Belianinov, S. V. Kalinin, and S. Jesse, *Complete information acquisition in dynamic force microscopy*, *Nature communications* **6** (2015).
- [35] Y. G. Kuznetsov, A. Malkin, R. Lucas, M. Plomp, and A. McPherson, *Imaging of viruses by atomic force microscopy*, *Journal of General Virology* **82**, 2025 (2001).
- [36] H. j. Butt, B. Cappella, and M. Kappl, *Force measurements with the atomic force microscope: Technique, interpretation and applications*, *Surface science reports* **59**, 1 (2005).
- [37] J. N. Israelachvili, *Intermolecular and surface forces* (Academic press, 2011).
- [38] E. Lifshitz, *The theory of molecular attractive forces between solids*, *Soviet physics* **2**, 73 (1956).
- [39] K. Schram, *On the macroscopic theory of retarded van der waals forces*, *Physics letters A* **43**, 282 (1973).
- [40] H. V. Guzman and R. Garcia, *Peak forces and lateral resolution in amplitude modulation force microscopy in liquid*, *Beilstein journal of nanotechnology* **4**, 852 (2013).

- [41] T. Ondarçuhu and L. Fabié, *Capillary forces in atomic force microscopy and liquid nanodispensing*, in *Surface Tension in Microsystems* (Springer, 2013) pp. 279–305.
- [42] M. Korayem, A. Kavousi, and N. Ebrahimi, *Dynamic analysis of tapping-mode afm considering capillary force interactions*, *Scientia Iranica* **18**, 121 (2011).
- [43] M. Balooch, I. Wu-Magidi, A. Balazs, A. Lundkvist, S. Marshall, G. Marshall, W. Siekhaus, and J. Kinney, *Viscoelastic properties of demineralized human dentin measured in water with atomic force microscope (afm)-based indentation*, *Journal of biomedical materials research* **40**, 539 (1998).
- [44] A. Noy, D. V. Vezenov, and C. M. Lieber, *Chemical force microscopy*, *Annual Review of Materials Science* **27**, 381 (1997).
- [45] H. Sadeghian, N. Koster, and T. van den Dool, *Introduction of a high throughput spm for defect inspection and process control*, in *SPIE Advanced Lithography* (International Society for Optics and Photonics, 2013) pp. 868127–868127.
- [46] N. Kol, Y. Shi, M. Tsvitov, D. Barlam, R. Z. Shneck, M. S. Kay, and I. Rouso, *A stiffness switch in human immunodeficiency virus*, *Biophysical journal* **92**, 1777 (2007).
- [47] M. Fotino, *Tip sharpening by normal and reverse electrochemical etching*, *Review of Scientific Instruments* **64**, 159 (1993).
- [48] N. R. Wilson and J. V. Macpherson, *Carbon nanotube tips for atomic force microscopy*, *Nature nanotechnology* **4**, 483 (2009).
- [49] R. Merry, M. Uyanik, R. van de Molengraft, R. Koops, M. van Veghel, and M. Steinbuch, *Identification, control and hysteresis compensation of a 3 dof metrological afm*, *Asian Journal of Control* **11**, 130 (2009).
- [50] S. Kuiper and G. Schitter, *Active damping of a piezoelectric tube scanner using self-sensing piezo actuation*, *Mechatronics* **20**, 656 (2010).
- [51] G. Binnig and D. P. Smith, *Single-tube three-dimensional scanner for scanning tunneling microscopy*, *Review of Scientific Instruments* **57**, 1688 (1986).
- [52] G. Schitter, K. J. Astrom, B. E. DeMartini, P. J. Thurner, K. L. Turner, and P. K. Hansma, *Design and modeling of a high-speed afm-scanner*, *IEEE Transactions on Control Systems Technology* **15**, 906 (2007).
- [53] A. Fleming, B. Kenton, and K. K. Leang, *Bridging the gap between conventional and video-speed scanning probe microscopes*, *Ultramicroscopy* **110**, 1205 (2010).
- [54] I. A. Mahmood, S. R. Moheimani, and B. Bhikkaji, *A new scanning method for fast atomic force microscopy*, *IEEE Transactions on Nanotechnology* **10**, 203 (2011).
- [55] S. B. Andersson and L. Y. Pao, *Non-raster sampling in atomic force microscopy: A compressed sensing approach*, in *American Control Conference (ACC), 2012* (IEEE, 2012) pp. 2485–2490.

- [56] T. De, P. Agarwal, D. R. Sahoo, and M. V. Salapaka, *Real-time detection of probe loss in atomic force microscopy*, [Applied physics letters](#) **89**, 133119 (2006).
- [57] Y. Yong and S. R. Mohemani, *Design of an inertially counterbalanced z-nanopositioner for high-speed atomic force microscopy*, [IEEE Transactions on Nanotechnology](#) **12**, 137 (2013).
- [58] N. Kodera, H. Yamashita, and T. Ando, *Active damping of the scanner for high-speed atomic force microscopy*, [Review of Scientific Instruments](#) **76**, 053708 (2005).
- [59] S. Kuiper and G. Schitter, *Model-based feedback controller design for dual actuated atomic force microscopy*, [Mechatronics](#) **22**, 327 (2012).
- [60] T. Sulchek, S. Minne, J. Adams, D. Fletcher, A. Atalar, C. Quate, and D. Adderton, *Dual integrated actuators for extended range high speed atomic force microscopy*, [Applied Physics Letters](#) **75**, 1637 (1999).
- [61] T. Sulchek, R. Hsieh, J. Adams, S. Minne, C. Quate, and D. Adderton, *High-speed atomic force microscopy in liquid*, [Review of Scientific Instruments](#) **71**, 2097 (2000).
- [62] A. Keyvani, H. Sadeghian, H. Goosen, and F. van Keulen, *Transient tip-sample interactions in high-speed afm imaging of 3d nano structures*, in [SPIE Advanced Lithography](#) (International Society for Optics and Photonics, 2015) pp. 94242Q–94242Q.
- [63] A. L. Weisenhorn, M. Khorsandi, S. Kasas, V. Gotzos, and H.-J. Butt, *Deformation and height anomaly of soft surfaces studied with an afm*, [Nanotechnology](#) **4**, 106 (1993).
- [64] M. Antognozzi, M. D. Szczelkun, A. N. Round, and M. J. Miles, *Comparison between shear force and tapping mode afm-high resolution imaging of dna*, [Single Molecules](#) **3**, 105 (2002).
- [65] K. Karvinen and S. Moheimani, *A high-bandwidth amplitude estimation technique for dynamic mode atomic force microscopy*, [Review of Scientific Instruments](#) **85**, 023707 (2014).
- [66] G. Schitter and A. Stemmer, *Identification and open-loop tracking control of a piezoelectric tube scanner for high-speed scanning-probe microscopy*, [IEEE Transactions on Control Systems Technology](#) **12**, 449 (2004).
- [67] G. Schitter, F. Allgöwer, and A. Stemmer, *A new control strategy for high-speed atomic force microscopy*, [Nanotechnology](#) **15**, 108 (2003).
- [68] B. Xue, Y. Yan, Z. Hu, and X. Zhao, *Study on effects of scan parameters on the image quality and tip wear in afm tapping mode*, [Scanning](#) **36**, 263 (2014).
- [69] M. C. Strus, A. Raman, C.-S. Han, and C. Nguyen, *Imaging artefacts in atomic force microscopy with carbon nanotube tips*, [Nanotechnology](#) **16**, 2482 (2005).
- [70] R. Garcia and A. San Paulo, *Attractive and repulsive tip-sample interaction regimes in tapping-mode atomic force microscopy*, [Physical Review B](#) **60**, 4961 (1999).

- [71] J. H. Cantrell and S. A. Cantrell, *Bifurcation, chaos, and scan instability in dynamic atomic force microscopy*, [Journal of Applied Physics](#) **119**, 125308 (2016).
- [72] S. Hu and A. Raman, *Chaos in atomic force microscopy*, [Physical Review Letters](#) **96**, 036107 (2006).
- [73] F. Jamitzky, M. Stark, W. Bunk, W. Heckl, and R. Stark, *Chaos in dynamic atomic force microscopy*, [Nanotechnology](#) **17**, S213 (2006).
- [74] H. Hölscher and U. D. Schwarz, *Theory of amplitude modulation atomic force microscopy with and without q -control*, [International Journal of Non-linear mechanics](#) **42**, 608 (2007).
- [75] M. Ashhab, M. Salapaka, M. Dahleh, and I. Mezić, *Melnikov-based dynamical analysis of microcantilevers in scanning probe microscopy*, [Nonlinear Dynamics](#) **20**, 197 (1999).
- [76] Q. Zou and S. Devasia, *Preview-based stable-inversion for output tracking*, in [American Control Conference, 1999. Proceedings of the 1999](#), Vol. 5 (IEEE, 1999) pp. 3544–3548.
- [77] S. Devasia, *Should model-based inverse inputs be used as feedforward under plant uncertainty?* [IEEE Transactions on Automatic Control](#) **47**, 1865 (2002).
- [78] S. Hu and A. Raman, *Analytical formulas and scaling laws for peak interaction forces in dynamic atomic force microscopy*, [Applied Physics Letters](#) **91**, 123106 (2007).
- [79] C. Su, L. Huang, and K. Kjoller, *Direct measurement of tapping force with a cantilever deflection force sensor*, [Ultramicroscopy](#) **100**, 233 (2004).
- [80] V. Vahdat and R. W. Carpick, *Practical method to limit tip-sample contact stress and prevent wear in amplitude modulation atomic force microscopy*, [ACS nano](#) **7**, 9836 (2013).

2

TIP-SAMPLE INTERACTIONS IN HIGH-SPEED TAPPING MODE ATOMIC FORCE MICROSCOPY

The maximum amount of repulsive force applied to the surface plays a critical role in sample damage and tip wear in Tapping Mode Atomic Force Microscopy (TM-AFM). So far, many investigations have focused on the tip-sample forces in TM-AFM in steady-state conditions. However, it is known that AFM can be more damaging in transient conditions. This chapter investigates the effects of transient motion of the cantilever on the tip-sample interactions via numerical and experimental studies. It is observed that, in high-speed scanning, where the changes in surface topography appear at time intervals shorter than the response time of the cantilever, the tip may crash into the sample and exert one or two orders of magnitude higher forces than in steady situations. An analytic expression has been presented to predict the forces in the worst case scenario which can be used for selection of scanning parameters in high speed TM-AFM.

2.1. INTRODUCTION

Atomic Force Microscopy has already been suggested as one of the promising technologies for metrology and inspection of nanostructures for future semiconductor applications [1, 2]. However, being a member of scanning probe techniques, it suffers from the lack of speed and throughput. One of the significant concerns in increasing the imaging rate with AFM is that the probability of damaging the tip or the sample increases with the scanning speed. Depending on the mechanical properties of the tip and the sample surface, excessive interaction forces can result in either tip wear and fracture [3], or deformation and damage the sample [4] (hereafter shortly referred to as damage).

The damage at the nanoscale can be attributed to different mechanisms such as

Parts of this chapter have been published in [Proc. SPIE Advanced Lithography 9424-100, \(2015\)](#).

fracture, plastic deformation or chemical processes[5]. Though, the stress level in contact region plays a crucial role in all these processes [5–7]. Hence a damage estimation method in AFM would be to compare the stresses in the contact area with the maximum allowable stress of the tip/sample material [3]. Using the maximum repulsive force in each cycle and considering a contact mechanics model, (e.g., Hertz, Tataru, Sneddon or a finite element model [8–10],) the maximum equivalent stress in the contact region can be estimated. Herewith, the nanoscale damage problem could be simplified to the calculation of the Tip-Sample Interaction (TSI) force.

The form of the TSI forces in AFM mainly depend on the operation mode. e.g., while non-contact AFM works with weak attractive forces, contact mode AFM exerts strong repulsive and lateral forces. Among different operation modes, the Tapping Mode (TM-AFM) is probably the most popular one, due to its reasonable speed, stability, and low damage. It has originally been devised to reduce the damage by avoiding constant contact and shear (as in contact mode AFM). However, even in tapping mode, there exists the risk of damage when imaging soft samples (e.g. biological samples) or in high-speed scanning.

Unfortunately, the TSI forces in tapping mode is not directly accessible from measurements [11]. Therefore, researchers have investigated the TSI forces and specially the Peak Repulsive Force (PRF), through modeling techniques. For example, Guzman *et al.* [9] numerically analyzed the PRF in an immersed AFM and studied differences between Tataru's and Hertzian models for contact and also effects of material properties, e.g., viscoelasticity and fluid damping on the peak repulsive force. Wang [12] used the Krylov-Bogolubov-Mitropolsky asymptotic method to solve for the nonlinear dynamic motion of a cantilever under the influence of tip-sample interactions. Based on Wang's approach, Hu and Raman[11] extracted an analytic solution for repulsive and attractive peak forces using the periodic averaging method. Based on these models, researchers proposed that to reduced the damage, the probe and the scanning parameters should match the sample properties[7]. The studies mentioned above provide comprehensive and practically applicable information on tip-sample interactions in steady-state conditions. However, choosing proper probes and operation parameters does not necessarily guarantee a non-destructive imaging.

In literature, it is often assumed that the cantilever is vibrating in steady-state conditions with a certain fixed amplitude while being engaged to the surface. However, it is well known that failure usually occurs while engaging to the surface or in fast scanning conditions where the system is in a transient situation. Especially in high-speed operation, abrupt changes in topography of the sample can induce a transient response of the cantilever which leads to large TSI force on the contact region. For example, in the presence of steep steps in topography, e.g. 3D structures (e.g., see Fig. 2.1), the tip hits the structure more abruptly, and the applied repulsive forces are much higher than the steady state conditions.

Based on the requirements of the semiconductor industry and demand for high-speed AFM, a thorough model is needed to investigate and control the damage in transient conditions. To address this issue, here, we study the tip-sample interaction when a sudden change in topography appears. The present paper is organized as follows: The next section presents theoretical and experimental investigation of tip-sample interac-

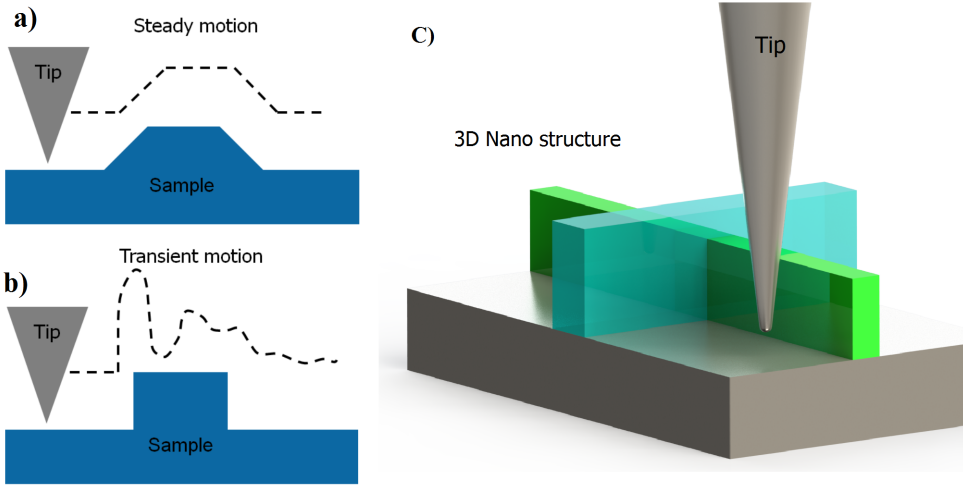


Figure 2.1: Schematic view of a tip, **a)** in steady conditions where the tip follows the topography, **b)** in transient conditions caused by a sharp step in topography, **c)** A FinFET as an example of a 3D nano structure that can cause transient conditions in AFM.

tion forces both in steady-state and transient situations. Section 2.3 presents a simple analytic expression for the PRF which is based on an apparent impedance model, and verified with numerical results. Conclusions are presented in the last section. A detailed description of the method used in Section 2.3 is presented in the A.

2.2. TIP-SAMPLE INTERACTIONS IN TAPPING MODE AFM

In TM-AFM, the cantilever is excited with a frequency (ω) closed to its fundamental resonance frequency (ω_n) using a dithering piezo actuator to reach a free air amplitude of A_i . The cantilever is brought close to the sample surface using a Z positioning actuator. Due to the tip-sample interactions, the vibration amplitude of the cantilever reduces by a factor A_r (so-called amplitude ratio) to an engaged amplitude A , i.e. $A = A_r A_i$. The role of the controller is to keep the engaged amplitude constant by adjusting the position of the cantilever or the surface. The height image of the sample is captured by recording the activity of the Z actuator, while scanning in x-y direction.

Using the linear Euler-Bernoulli beam theory, the motion of a cantilever (as a function of time t and longitudinal coordinate x) can be approximated with a lumped n-DOF coupled oscillators model as $w(x, t) \approx \sum_{i=1}^n q_i(t) \varphi_i(x)$, in which each vibration mode ($\varphi_i(x)$) has a contribution $q_i(t)$.

Considering the Derjaguin-Muller-Toporov (DMT) model[13] for the contact area, the governing equation for dynamic motion of the tip can be expressed as:

$$M\ddot{q} + C\dot{q} + Kq = \left(\frac{H_a R}{6(g_0 - w_t)^2} - \frac{4}{3} E_{eff} \sqrt{R} \delta^{3/2} \right) F_t + f_0 \sin(\omega t) F_b \quad (2.1)$$

where $w_t(t) = w(l, t)$ represents the displacement of the tip where l is the length of

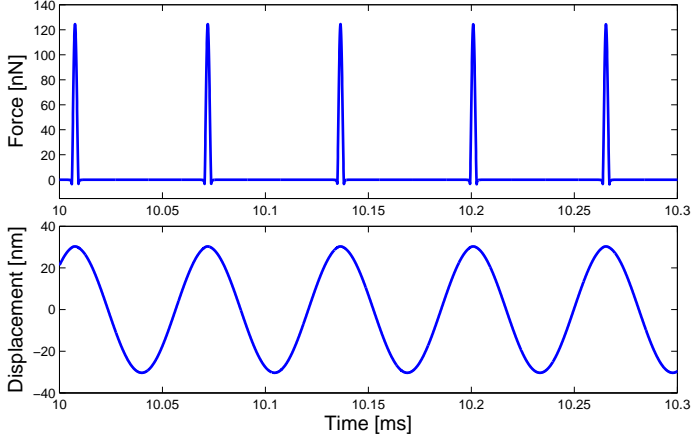


Figure 2.2: Tip-sample interaction and tip displacement for a cantilever with a spring constant of 6 N/m Q factor 50, tip radius of 10 nm , free air amplitude of 50 nm , resonance and working frequency of 100 kHz , and amplitude ratio of 90%.

the cantilever beam. Coefficients $K, C, M \in \mathbb{R}^{n \times n}$, $F_t, F_b \in \mathbb{R}^{n \times 1}$, R, H_a, f_0 are stiffness matrix, damping matrix, mass matrix, forcing vector from tip, and forcing vector from base of cantilever (dithering force), tip radius, Hamaker constant, and equivalent dithering force, respectively. The distance between undeflected position of tip and sample surface is defined as g_0 and the indentation δ is defined as $\delta = (a_0 + x_t - g_0)H(a_0 + x_t - g_0)$. The Heaviside function ($H(a_0 + x_t - g_0)$) is utilized to indicate that indentation is zero when the tip is not in contact with the sample and a_0 is the atomic separation distance. The effective stiffness of the surface, E_{eff} is given as $\frac{1}{E_{eff}} = \frac{1-\nu_t^2}{E_t} + \frac{1-\nu_s^2}{E_s}$, where E and ν are young's modulus and poisson's ratio and subscripts t and s refer to tip and sample, respectively[9].

To calculate the tip-sample interaction forces first, a 6-DOF version of Eq(2.1) was solved using a 4^{th} -order Runge-Kutta integration scheme, its convergence has been confirmed and its accuracy has been verified with previously achieved analytically results. We shall use this model for simulating the transient situations as well in the following sections. Fig. 2.2 shows the steady-state motion of the tip in time domain and accompanying tip-sample force for a cantilever which properties are given in the caption.

As it can be seen in Fig. 2.2, in steady state situations, the motion of the cantilever is harmonic. It means only the first mode of the cantilever is active, and Eq(2.1) can be truncated to a one DOF mass-spring model (as it is widely in use in the literature [9, 11, 14, 15]). However, for transient situations, because of participation of the higher modes the motion of the cantilever is more complicated than the steady state situations. In the next subsection, we experimentally demonstrate that the one DOF model does not necessarily represent the dynamics of the cantilever in transient situations.

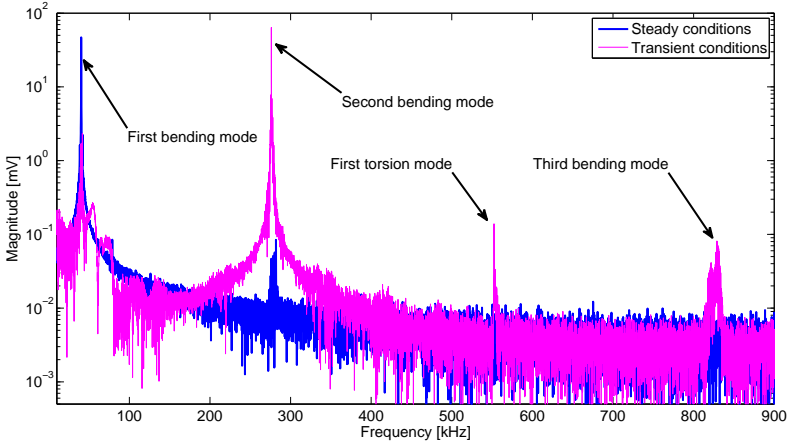


Figure 2.3: Motion spectra of the cantilever while engaged with the surface. Blue: In steady condition. Magenta curve: The cantilever engaged to a sample surface which is randomly fluctuating up and down. Free air amplitude is 1 V, amplitude ratio is 30% and the cantilever is only excited at its first resonance frequency (≈ 41 kHz).

2.2.1. ONE DOF ASSUMPTION

As mentioned previously, mainly in the literature, the AFM cantilever is approximated with a single DOF oscillator model. However, this assumption only holds for single frequency Amplitude Modulation (AM) mode imaging with normal probes in air. For example, it does not hold for some special cantilevers [16], or for multi-modal AFM [17]. Also, it is not necessarily valid while the cantilever experiences transient conditions. For example, we use a commercially available rectangular cantilever (MPP-22120 Bruker) and engage with a silicon surface in tapping mode. To keep an ongoing transient motion of cantilever, we increase the controller gains and reduce the set point amplitude. These parameters generate an instability in the control loop. Thus, the Z-stage randomly vibrates around the set-point and prevents the cantilever from reaching the steady situations. Fig. 2.3 shows the frequency spectrum of motion of the cantilever while it is in transient conditions as described above. In Fig. 2.3 the peaks on frequencies 280, 550, 840 kHz correspond to second bending mode, torsion mode and third bending mode of the cantilever, respectively. Considering that higher modes of the cantilever are also excited in transient situations, it can be concluded that one DOF oscillator assumption for the cantilever would result in large errors, i.e. the tip-sample interactions in transient situations can not be calculated via present analytic formulas or any one-DOF model.

2.2.2. SUDDEN CHANGES IN TOPOGRAPHY

There can be different stimuli to initiate a transient situation in TM-AFM. In this section, we consider a steep upward step in topography to investigate its effects on the tip-sample interactions. In high-speed scanning of 3D nanostructures, for downward steps the tip disengages and parachutes over the surface [18], while for upward steps it suddenly hits

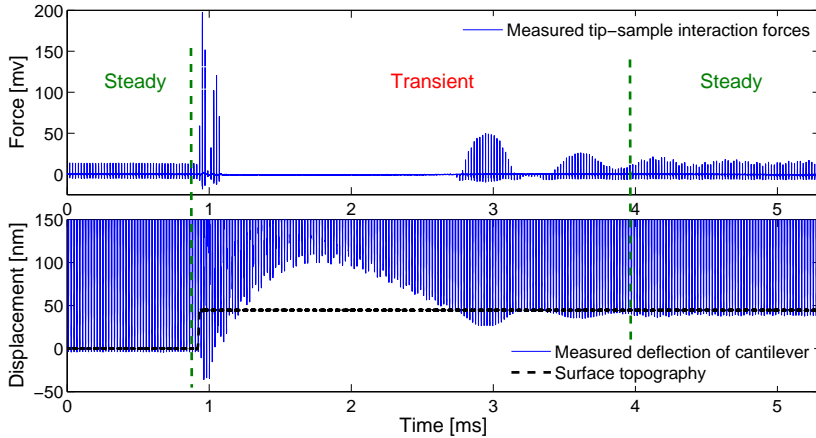


Figure 2.4: Effects of sudden change in topography on the forces and the motion of a cantilever with a resonance frequency of 49.1 kHz spring constant of 9.7 N/m , Q factor 295, free air amplitude 466 nm , and amplitude ratio 0.75%. A sudden voltage is applied to the Z piezo actuator to generate a virtual step function with an approximate height of 45 nm in topography (black dashed line).

the surface and can cause damage.

Since the forces in tapping mode cannot be (fully) reconstructed from observable signals, the applied force in a transient situation is impossible to measure while imaging on real samples. On the other hand, as it is described in Section 2.2.1 these forces can not be calculated with present analytic formulas, nor from any other one-DOF model. Thus, the forces can only be estimated via an individual experiment, or a numerical solution of the full nonlinear differential equation of the cantilever, Eq(2.1).

To experimentally investigate the effects of steep upward changes in topography, we adopt the method presented by Tamer *et al*[19, 20]. With this approach, it is possible to measure the tip-sample interactions in tapping mode AFM up to a limited bandwidth (in this case about 1 MHz). In this method, a much smaller (and higher frequency) cantilever is used as the force sensor and its deflection is measured via a separate optical beam deflection setup[21]. By applying a sudden voltage to the Z piezo actuator of the system in [20], an unexpected upward step in topography is simulated. Fig. 2.4 shows the motion of the cantilever and the tip-sample interactions filtered with a 1 MHz low pass filter. As it can be seen from Fig. 2.4, when a sudden upward step is applied to the Z-stage (time 0.8 ms), the motion of the cantilever becomes transient. In this case, the tip applies approximately 14 times higher forces on the surface, then its amplitude drops and loses the sample surface for 2 ms then it reaches the new steady state conditions with a lower amplitude.

Fig. 2.5 shows the interaction forces and tip position which is found via a numerical solution of the Eq(2.1) for the cantilever which is used in the experiments of Fig. 2.4, where the Quality factor has been reduced to 50 for better visualization of the phenomenon.

The transient situations are not only important from a damage point of view, but

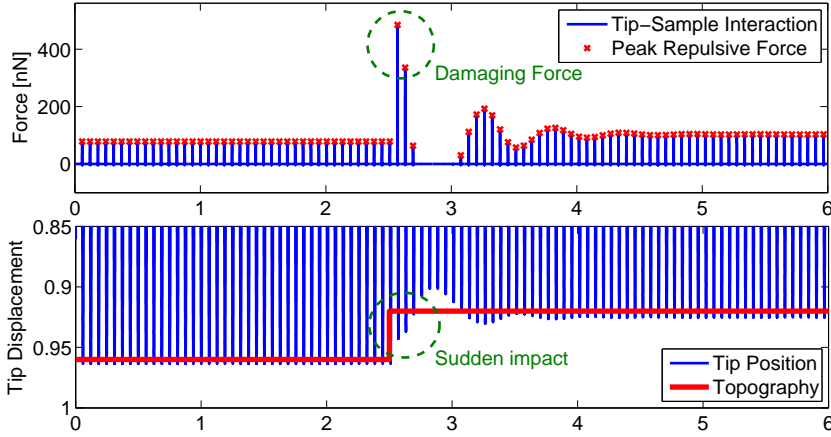


Figure 2.5: Numerical solution of the cantilever described in Fig. 2.4.

also from the control perspective. As shown in the Fig. 2.4 and 2.5, the amplitude of the cantilever does not recover uniformly after the sharp impact. The overshooting of the amplitude which occurs after encountering the steep upward step can cause instability in the closed loop system. In case the response time of the PID controller is chosen to be shorter than rise time of the amplitude (e.g., ≈ 3 ms for Fig. 2.4), it can react to the overshooting of the cantilever that generates a control signal in opposite direction (i.e., further retract when the tip is disengaged). Thus, to avoid instability, the controller has to be slower than the rise time of the cantilever. This effect limits the operation speed of the AFM. It worth to mention that we used this effect to destabilize the system deliberately to generate Fig. 2.3.

Due to the vast involvement of non-deterministic surface conditions, it is not possible to calculate the tip-sample interactions for every type of transient situations. However, even a rough approximation would be helpful to avoid (or reduce the probability of) damage in high-speed scanning. For this aim, Section 2.3 presents a closed form solution based on energy conservation law to estimate the amount of maximum force regarding size of the upward step, material properties of the sample, mechanical characteristics of the cantilever and operation parameters.

2.3. ENERGY ANALYSIS

To analytically quantify the effects of steep upward steps on the repulsive forces, we apply the energy conservation law to the time sequences right before, and at the impact time where the nano indentation reaches its maximum value.

$$PE_{cant}^1 + KE^1 + W_{vdW} = PE_{cant}^2 + KE^2 + PE_{contact} + E_{loss} \quad (2.2)$$

Eq(2.2) states that during the nanoindentation process, the difference between initial (¹) and secondary (²) potential (PE) and kinetic energy (KE) of the cantilever is enhanced

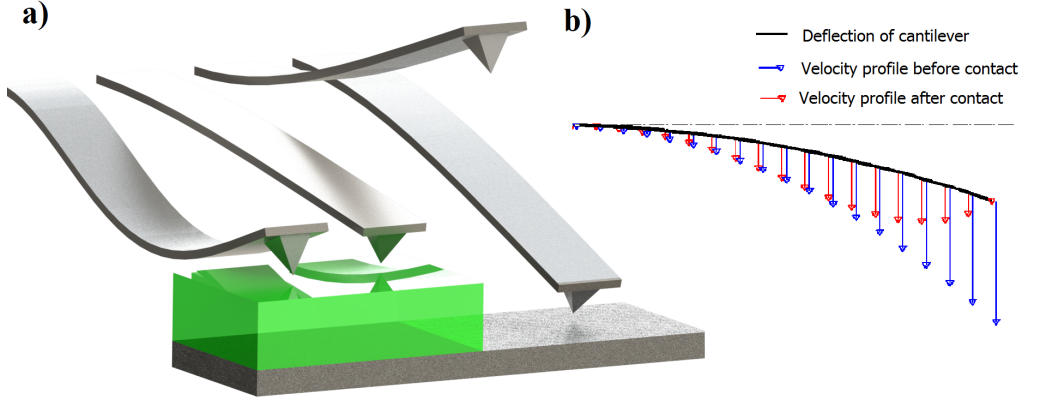


Figure 2.6: **a)** Schematic of deflection of cantilever, **b)** velocity profile along longitudinal axis of cantilever before and after the contact with steep step.

with work of vdW forces (W_{vdW}) and is transferred to an elastic energy in contact region ($PE_{contact}$). Also, some of the energy is dissipated because of the non-conservative behavior of the material during the nanoindentation process (E_{loss}).

Assuming that the nano-indentation is minuscule in comparison to the amplitude of the cantilever, it is appropriate to conclude that the changes in potential energy of the cantilever are negligible ($PE_{cant}^1 = PE_{cant}^2$). Also, since ignoring the non-conservative terms gives an overestimate of the applied force, it is reasonable to consider a conservative collision as a worst case scenario ($E_{loss} \approx 0$). Therefore, we can assume that the change in the kinetic energy, together with the work of the van der Waals forces is transformed to the strain energy in contact area ($KE^1 - KE^2 + W_{vdW} \approx PE_{contact}$).

To calculate the changes in kinetic energy, the velocity profile of the cantilever during the contact is considered. As shown in Fig. 2.6 when the tip hits the sample surface, suddenly some part of the cantilever (areas close to tip) stop moving, but the other parts (far from the tip) will not stop at the same time as the tip. The equivalent inertia of the parts of the cantilever that cease moving at the same time with the tip is called the apparent mass of the cantilever at the tip. Depending on the apparent mass of the tip, a portion of the kinetic energy of the cantilever, plus the work of vdW forces should transform to strain energy in contact. For the case of before the contact (when the cantilever is moving harmonically in steady situations), the velocity profile has the same shape as the first bending mode, yet during the indentation, it changes to a different configuration that can be considered as a combination of first few vibration modes. Fig. 2.6 describes the reasoning behind excitation of higher modes of the cantilever that was presented in Section 2.2.1.

A very relevant reference on how an elastic structure behaves due to mechanical impacts can be found in the research of Lin and Ho [22].

Considering the Hertz model, the strain energy of contact area in Eq(2.2) can be found

as:

$$PE_{contact} = \int_0^\delta \frac{4}{3} E_{eff} \sqrt{R} r^{3/2} dr = \frac{8}{15} E_{eff} \sqrt{R} \delta^{5/2}, \quad (2.3)$$

where δ is the maximum indentation, and r is a dummy variable. The work of vdW force in Eq(2.2) is:

$$W_{vdW} = \int_{a_0}^\infty \frac{H_a R}{6r^2} dr = \frac{H_a R}{6a_0}, \quad (2.4)$$

and the changes in kinetic energy of the cantilever is

$$KE^1 - KE^2 = \frac{1}{2} m_{tip} v^2. \quad (2.5)$$

where v is the velocity of the tip while it is approaching the surface and $m_{tip} = \frac{1}{4n} \rho AL$ is the apparent mass of the tip considering the n^{th} mode of vibrations. See A for more detailed description of the apparent mass. Substituting Eq(2.3) and Eq(2.5) into conservation law (Eq(2.2)), the indentation in contact area can be found as Eq(2.6):

$$\delta_{max} = 0.9745 \sqrt[2.5]{\frac{m_{tip} v^2 + \frac{HR}{3a_0}}{E_{eff} \sqrt{R}}}. \quad (2.6)$$

The maximum stress in Hertz model is calculated from the forces as[3]:

$$\sigma_{max} = \sqrt[3]{\frac{6FE_{eff}^2}{\pi^3 R^2}}. \quad (2.7)$$

Considering Eqs(2-7), the maximum stress can be found from the velocity of the tip approaching the surface. Since the motion of cantilever before the contact is harmonic, the tip speed before contact can be obtained as:

$$v = A\omega \sqrt{\frac{h}{A} \left(2 - \frac{h}{A}\right)}. \quad (2.8)$$

where h is the height of upward change in topography.

Considering Eq(2.6) and the Hertz model, the maximum repulsive force as a function of size of sudden step in topography is:

$$F(h) = 1.2827 E_{eff}^{\frac{2}{5}} R^{\frac{1}{5}} \left(Ak m_r \omega_r^2 h \left(2 - \frac{h}{A}\right) + \frac{HR}{3a_0} \right)^{\frac{3}{5}} \quad (2.9)$$

where $m_r = \frac{m_{tip}}{M_{11}}$ is the ratio between apparent mass of the tip and equivalent mass of the first mode of vibration. Consequently, the contact stress can be found by substituting Eq(2.9) in Eq(2.7) as:

$$\sigma_{max}(h) = 0.6285 E_{eff}^{\frac{4}{5}} R^{-\frac{3}{5}} \left(Ak m_r \omega_r^2 h \left(2 - \frac{h}{A}\right) + \frac{HR}{3a_0} \right)^{\frac{1}{5}} \quad (2.10)$$

Since the tip has its maximum kinetic energy while it is in the middle the stroke, the worst case scenario (maximum possible force) happens if the height of the sudden step

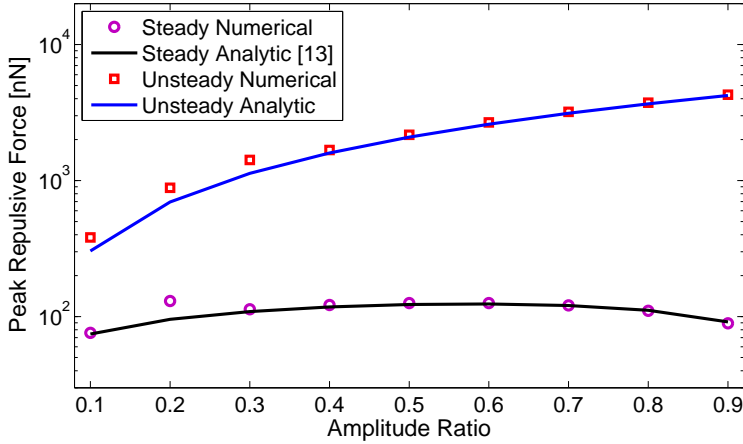


Figure 2.7: Peak repulsive forces in steady state and transient situations considering the worst case scenario where the size of step is equal to the amplitude for the cantilever described in Fig. 2.4 with free air amplitude 100 nm.

is equal to the set-point amplitude (A). To verify the analytical formula we compare the peak repulsive force in transient situations from Eq(2.9) with already validated numerical method solution of Eq(2.1). In Fig. 2.7 the blue line and the red squares are calculated considering the size of sudden changes equal to set-point amplitude, (i.e. the worst case scenario), and black line and purple circles show the steady-state situations. It should be mentioned that both the analytic formula and the numerical methods consider 4 DOF model of the cantilever.

The presented analytic formula in Eq(2.9) can be useful in selection of the scanning parameters to avoid the damage in high-speed imaging of 3D nano structures[23].

2.4. CONCLUSION

In this paper, the tip-sample interactions in tapping mode AFM were studied in transient situations. The contact forces and stresses were calculated analytically for the case of sudden upward step in topography which represents a transient situation. The analytic formula for stresses and forces was in good agreement with already verified numerical results. It has been observed that in transient situations, the cantilever cannot be considered as one DOF oscillator, and it can apply order(s) of magnitude higher repulsive forces on the surface. Also, it has been found that in transient situations, the forces also scale with the apparent mass of the tip besides the spring constant of the cantilever.

REFERENCES

- [1] H. Sadeghian, T. C. van den Dool, W. E. Crowcombe, R. W. Herfst, J. Winters, G. F. I. J. Kramer, and N. B. Koster, *Parallel, miniaturized scanning probe microscope for defect inspection and review*, *Proc. SPIE* **9050**, 90501B (2014).

- [2] H. Sadeghian, N. B. Koster, and T. C. van den Dool, *Introduction of a high throughput spm for defect inspection and process control*, *Proc. SPIE* **8681**, 868127 (2013).
- [3] M. Bloo, H. Haitjema, and W. Pril, *Deformation and wear of pyramidal, silicon-nitride afm tips scanning micrometre-size features in contact mode*, *Measurement* **25**, 203 (1999).
- [4] A. L. Weisenhorn, M. Khorsandi, S. Kasas, V. Gotzos, and H.-J. Butt, *Deformation and height anomaly of soft surfaces studied with an afm*, *Nanotechnology* **4**, 106 (1993).
- [5] T. D. Jacobs and R. W. Carpick, *Nanoscale wear as a stress-assisted chemical reaction*, *Nature nanotechnology* **8**, 108 (2013).
- [6] K.-H. Chung, Y.-H. Lee, and D.-E. Kim, *Characteristics of fracture during the approach process and wear mechanism of a silicon afm tip*, *Ultramicroscopy* **102**, 161 (2005).
- [7] V. Vahdat and R. W. Carpick, *Practical method to limit tip-sample contact stress and prevent wear in amplitude modulation atomic force microscopy*, *ACS nano* **7**, 9836 (2013).
- [8] H. Ladjal, J.-L. Hanus, A. Pillarisetti, C. Keefer, A. Ferreira, and J. P. Desai, *Atomic force microscopy-based single-cell indentation: Experimentation and finite element simulation*, *Intelligent Robots and Systems, 2009. IROS 2009. IEEE/RSJ International Conference on*, , 1326 (2009).
- [9] H. V. Guzman, A. P. Perrino, and R. Garcia, *Peak forces in high-resolution imaging of soft matter in liquid*, *ACS nano* **7**, 3198 (2013).
- [10] S. Chizhik, Z. Huang, V. Gorbunov, N. Myshkin, and V. Tsukruk, *Micromechanical properties of elastic polymeric materials as probed by scanning force microscopy*, *Langmuir* **14**, 2606 (1998).
- [11] S. Hu and A. Raman, *Analytical formulas and scaling laws for peak interaction forces in dynamic atomic force microscopy*, *Applied Physics Letters* **91**, 123106 (2007).
- [12] L. Wang, *Analytical descriptions of the tapping-mode atomic force microscopy response*, *Applied physics letters* **73**, 3781 (1998).
- [13] B. V. Derjaguin, V. M. Muller, and Y. P. Toporov, *Effect of contact deformations on the adhesion of particles*, *Journal of Colloid and interface science* **53**, 314 (1975).
- [14] J. P. Spatz, S. Sheiko, M. Moller, R. G. Winkler, P. Reineker, and O. Marti, *Forces affecting the substrate in resonant tapping force microscopy*, *Nanotechnology* **6**, 40 (1995).
- [15] S. Hu and A. Raman, *Inverting amplitude and phase to reconstruct tip-sample interaction forces in tapping mode atomic force microscopy*, *Nanotechnology* **19**, 375704 (2008).

- [16] O. Sahin, S. Magonov, C. Su, C. F. Quate, and O. Solgaard, *An atomic force microscope tip designed to measure time-varying nanomechanical forces*, *Nature nanotechnology* **2**, 507 (2007).
- [17] R. Garcia and E. T. Herruzo, *The emergence of multifrequency force microscopy*, *Nature nanotechnology* **7**, 217 (2012).
- [18] T. De, P. Agarwal, D. R. Sahoo, and M. V. Salapaka, *Real-time detection of probe loss in atomic force microscopy*, *Applied physics letters* **89**, 133119 (2006).
- [19] H. Sadeghian and M. S. Tamer, *European Patent 15181449.8*.
- [20] M. S. Tamer, H. Sadeghian, A. Keyvani, H. Goosen, and F. van Keulen, *Quantitative measurement of tip-sample interaction forces in tapping mode atomic force microscopy*, *Proceedings of the 13th International Workshop on Nanomechanical Sensing*, 199 (2016).
- [21] R. Herfst, W. Klop, M. Eschen, T. Van Den Dool, N. Koster, and H. Sadeghian, *Systematic characterization of optical beam deflection measurement system for micro and nanomechanical systems*, *Measurement* **56**, 104 (2014).
- [22] Z.-C. Lin and C.-Y. Ho, *An investigation of elastic impact problems on beams and plates*, *Journal of sound and vibration* **148**, 293 (1991).
- [23] A. Keyvani, H. Sadeghian, H. Goosen, and F. van Keulen, *Transient tip-sample interactions in high-speed afm imaging of 3d nano structures*, *Proc. SPIE* **9424**, 94242Q (2015).

3

THE ORIGIN OF AMPLITUDE REDUCTION IN TAPPING MODE ATOMIC FORCE MICROSCOPY

The origin of amplitude reduction in Tapping Mode Atomic Force Microscopy (TM-AFM) is typically attributed to the shift in resonance frequency of the cantilever due to the non-linear tip-sample interactions. However, this does not explain some of the recent numerical and experimental observations on the tip-sample interaction forces. In this paper, we present a new approach to understand the origin of amplitude reduction in TM-AFM. The proposed approach is based on interference between the tip-sample and dither force, and clearly explains the recent observations. Results obtained with the proposed formulation agree with experimental results and numerical solutions of the full nonlinear model.

3.1. INTRODUCTION

Tapping Mode Atomic Force Microscopy (TM-AFM) is a widely used microscopy technique in experimental research and industrial applications [2]. In this method, a micro-cantilever probe with a sharp tip at its end is excited with a frequency around its fundamental resonance frequency. Bringing the cantilever to a nanometric proximity of the sample surface, the tip intermittently interacts with the sample surface. Due to the intermittent interactions of the tip and the sample, the vibration amplitude of the cantilever reduces to a user-defined fraction of its value when it was far from the sample (the free air amplitude). A feedback controller keeps the reduced amplitude constant by adjusting the distance between the cantilever and the sample. While scanning sample surface, the AFM cantilever follows the topography of the sample surface, and a so-called height and phase images are captured via recording control signal and the phase of the motion of the cantilever, respectively [3].

Parts of this chapter have been published in [Applied Physics Letters](#) **112**, 163104 (2018).

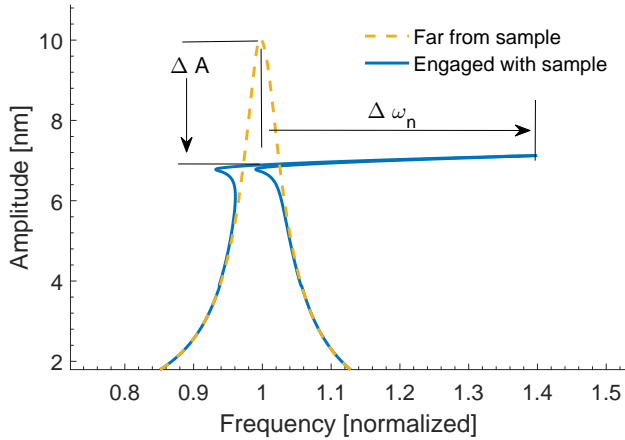


Figure 3.1: Graphical explanation of amplitude reduction based on resonance frequency shift (see e.g., [4, 5]).

The research question in this paper is: why does the amplitude reduce when the tip starts to interact with the sample? This question was a fundamental research question in the late 1990's, and was already answered then [4]. Briefly: “The amplitude reduces because the resonance frequency of the system changes.” This explanation is graphically demonstrated in Fig. 3.1, and more details can be found in [5]. While many aspects of the TM-AFM are well described with this explanation, there are still several recent observations about Tip-Sample Interaction (TSI) force which are not well understood. In this paper we present a new description for the origin of amplitude reduction in AFM that also explains the recent observations.

It must be acknowledged that, the explanation based on resonance frequency shift is mathematically precise, and is arisen from a nonlinear dynamics study of the cantilever in the presence of the Derjaguin-Muller-Toporov (DMT) force model. The DMT model describes a conservative TSI model which consists of repulsive Hertzian, and attractive van der Waals (vdW) forces. The two simplifications which has been used in the formulations of the existing theory which are: First, the dynamics of the cantilever is assumed to be a one degree of freedom (DOF) resonator model. Second, the motion of the cantilever is assumed to harmonic even in the presence of strongly non-linear TSI forces. In fact, experiments and numerical simulations show that none of these assumptions are restricting. The TSI force can be considered as a conservative force whereas the non-conservative effects can be added later. The motion of the cantiver is mainly harmonic, and hence, it is a legitimate choice to consider the cantilever as a one DOF resonator [6]. There are exceptional cases for which these assumptions are restricting (such as multi-frequency AFM, transient situations, and aqua medium measurements [7–9]). Yet, for the single harmonic TM-AFM in air, the existing theory—based on the frequency shift—is precise. However, with this theory, the relationship between the operation parameters and the TSI force is not easily explained. For example, the maximum interaction force during each cycle, i.e., the Peak Repulsive Force (PRF), is commonly considered

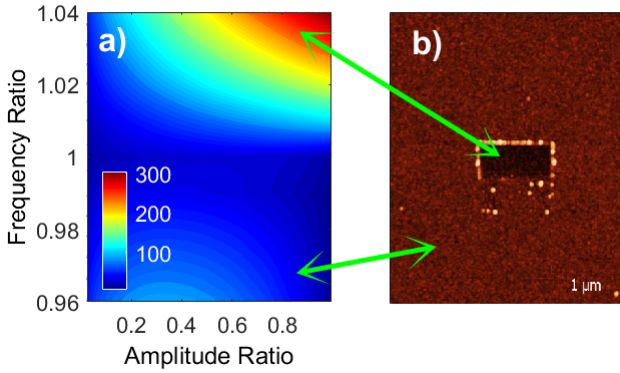


Figure 3.2: a) Peak repulsive force versus amplitude ratio and normalized excitation frequency. b) An example of nanopatterning using TM-AFM by tuning the TSI force via changing the excitation frequency [10].

to be a function of the amplitude and stiffness of the cantilever. Nonetheless, some recent observations show that the excitation frequency is much more important than the amplitude [10]. Not considering the excitation frequency, Xue *et al.* [11] reported a contradiction between their experimental results and the ones from Su *et al* [12]. One set of experiments showed an ascending relationship between the force and amplitude ratio, while the other tests show a descending relationship [11]. In fact, depending on the excitation frequency, both could be valid. If the excitation frequency is chosen slightly lower than the resonance frequency of the cantilever, the trend of the TSI force resembles the ones reported in [12], and if higher, the trend resembles reference [11].

To demonstrate the effect of excitation frequency, Fig. 3.2.a shows the PRF versus the amplitude ratio and excitation frequency which is calculated from numerical solution of the full nonlinear multi-DOF model of the cantilever. As it can be seen, the PRF has a saddle-shape trend with respect to the amplitude ratio and the excitation frequency, which shows that amplitude-force relationship can be ascending or descending. Using this trend, we have previously demonstrated a new nano-patterning technique with AFM (Fig. 3.2.b), in which, the TSI force was controlled via the excitation frequency, without changing the amplitude or the excitation power [10]. In this manner, desired patterns could be transferred to the surface, without causing any interruption in the imaging process. However, it was not possible to explain the results in Fig. 3.2 with the shift in resonance frequency. Therefore, this paper presents a different explanation for the origin of amplitude reduction in TM-AFM, which also covers the frequency dependency of the TSI force.

3.2. THEORY AND DISCUSSIONS

Consider the cantilever as a linear one DOF resonator which is excited by a dithering force and interacts with the surface through the TSI force. A normalized governing dif-

ferential equation for this cantilever can be written as:

$$\ddot{x} + \xi \dot{x} + x = f_d \Re(e^{j\omega t}) + f_{ts}(x, \dots), \quad (3.1)$$

where x, ξ, ω, f_d , and $f_{ts} \in \mathbb{R}$ represent the normalized displacement of the tip, the damping coefficient, normalized excitation frequency, the nondimensional dither force, and the tip-sample interaction force. A dot represents the time derivation, \Re is the real operator, and $j \in \mathbb{C}$ is the imaginary value $\sqrt{-1}$.

The TSI force is nonlinearly associated with the tip displacement and other physical and geometric parameters. Nonetheless, without any loss of generality, it can be considered as an unknown signal in the time domain. By keeping the TSI force unknown during the derivation of the model, we aim to present a formulation which explains the amplitude reduction in TM-AFM, independent of the interaction models. In steady state conditions, both the displacement and the TSI force are periodic in time. Hence, they both have a Fourier decomposition, with a first component at the same frequency as the excitation signal. The Fourier decomposition of the (unknown) TSI force and the displacement can be written as:

$$f_{ts}(t) = \sum_{n=0}^{\infty} \Re(F_{ts}^{(n)} e^{nj\omega t}) \quad (3.2a)$$

$$x(t) = \sum_{n=0}^{\infty} \Re(X^{(n)} e^{nj\omega t}) \quad (3.2b)$$

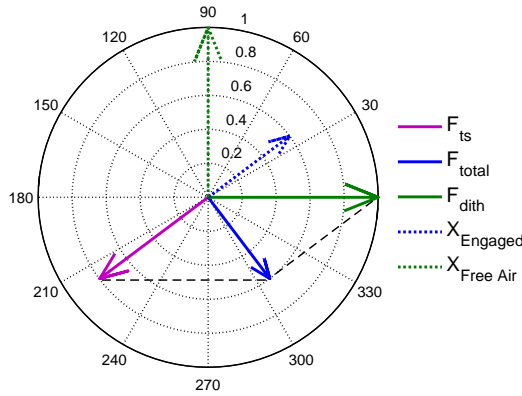
where $F_{ts}^{(n)} = |F_{ts}^{(n)}| e^{-j\varphi_{ts}^{(n)}}$, and $X^{(n)} = |X^{(n)}| e^{-j\varphi_x^{(n)}} \in \mathbb{C}$ represent the amplitude ($|F_{ts}^{(n)}|, |X^{(n)}|$) and the phase ($\varphi_{ts}^{(n)}, \varphi_x^{(n)}$) of the n^{th} ($n \in \mathbb{N}$) Fourier component of the TSI force and displacement, respectively. Note that the capital letters are used for the Fourier components of the functions. Considering Eq(3.2), the system represented by Eq(3.1) has an analytic solution for each of its frequency components as:

$$X^{(n)} = \frac{e^{-j \tan^{-1}(\frac{n\xi\omega}{1-n^2\omega^2})}}{\sqrt{(1-n^2\omega^2)^2 + n^2\xi^2\omega^2}} \Sigma F^{(n)} \quad (3.3)$$

where $\Sigma F^{(n)} \in \mathbb{C}$ represents the n^{th} Fourier component of the total force acting on the cantilever. $\Sigma F^{(1)} = f_d + F_{ts}^{(1)}$ and $\Sigma F^{(n)} = F_{ts}^{(n)}$ $n = 2, 3, \dots$.

In conventional TM-AFM configuration, only the amplitude and phase of the first harmonic motion (i.e., $X^{(1)}$) can be reliably measured and used in the control loop. Fig. 3.3 depicts a normalized version of Eq(3.3) for $n = 1$ as a phasor plot, in which, the amplitude and phase of the forces and displacements are represented, each with a vector (for $\omega = 1$). As it can be seen, when there is no TSI force, the displacement has an amplitude equal to one, and a phase delay of $\pi/2$ radian. However, in presence of the TSI force, the amplitude of total force $|\Sigma F^{(1)}|$ (solid blue) is less than the dither force per sé. This is because the TSI force (purple) is more than $\pi/2$ radian out of phase with respect to the dither force (solid green). Accordingly, the amplitude of the motion in the engaged situation (dashed blue) is lower than the free air amplitude (dashed green).

The reasoning behind the phase difference between the dither and TSI forces can be explained with the TSI model. Assuming that the contact between the tip and the sample



3

Figure 3.3: Phasor plot of the forces and displacement in TM-AFM: The explanation of amplitude reduction.

is conservative ($F_{ts} = F_{ts}(x(t))$), any of the Fourier components of the TSI force can be either 0 or π radian out of phase with the displacement x . In repulsive regime, which is the case for the majority of the experimental settings, this phase delay is π radian, whereas for attractive regime, it is 0. Rewriting Eq(3.3) with and without presence of the TSI force, one can conclude that the amplitude ratio (A_r) should be equal to force reduction ratio at the frequency of interest ($|f_d + F_{ts}^{(1)}| = A_r f_d$). Accordingly, the phase and amplitude of the first Fourier component of the force ($|F_{ts}^{(1)}|, \varphi_{ts}^{(1)}$) can be determined from the following equation:

$$f_d A_r \exp j(\varphi_{ts}^{(1)} - \theta_X^{ts} - \tan^{-1}(\frac{\xi\omega}{1-\omega^2})) = |F_{ts}^{(1)}| \exp j(\varphi_{ts}^{(1)} + f_d) \quad (3.4)$$

where $\theta_X^{ts} = 0$, or π , is the phase between the displacement and the TSI force. Eq(3.4) physically means that the first Fourier component of TSI force interferes with the dither force to generate the total harmonic force. Thus, the amplitude of the total force depends on the TSI force, dither force, and more importantly, the phase delay between them. Therefore, the origin of the amplitude reduction in TM-AFM can be explained as a destructive interference, i.e., cancellation of the dither force and the first Fourier component of TSI force. Note that the other Fourier components of the TSI force may or may not induce a motion at their frequencies, but certainly, do not contribute to the amplitude at the frequency of interest because of the orthogonality condition.

The phase difference between total force and the motion of the cantilever is dictated by the phase delay of the cantilever, i.e., $\tan^{-1}(\frac{\xi\omega}{1-\omega^2})$, and the phase between the TSI force and the motion (θ_X^{ts}) is governed by the force-distance relationship. If the contact is not conservative, the θ_X^{ts} will be slightly different than π , or zero.

The phase delay of the cantilever ($\tan^{-1}(\frac{\xi\omega}{1-\omega^2})$) also determines the sensitivity of the amplitude to the TSI force. Fig. 3.4 shows the phasor plot of the forces for two different excitation frequencies. Both frequencies have equal dither force, free air amplitude

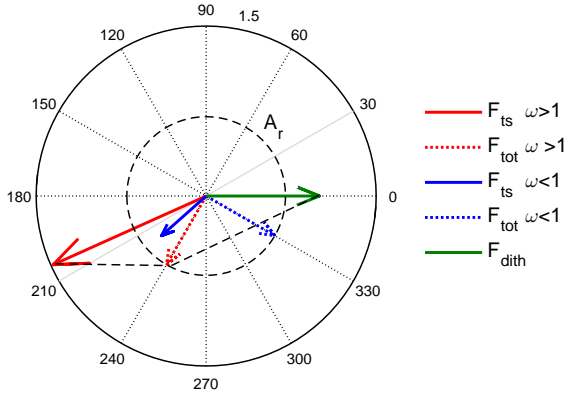


Figure 3.4: Phasor plan of the forces in TM-AFM; Explanation of frequency sensitivity of TSI force. Green: dither force, Blue: excitation frequency lower than resonance, Red: excitation frequency higher than resonance frequency.

and amplitude set-point. However, to reduce the total force (dashed arrows), the one with higher excitation frequency (red arrows) requires stronger TSI force than the one with lower excitation frequency (blue arrows). This observation explains the reasoning behind the frequency dependency of the TSI force shown in Fig. 3.2.

Fig. 3.5 shows the magnitude of the first Fourier component of the force versus the amplitude ratio and the excitation frequency, obtained from Eq(3.4). To verify the results from the new formulation, we compared the $F_{ts}^{(1)}$ calculated from Eq(3.4) with the numerical solution of the nonlinear problem (using DMT model). We found that the first Fourier component of the TSI force obtained by this method agrees with the nonlinear model up to a numerical roundoff error, regardless of the parameters of the DMT model. Fig. 3.6 compares the average of the forces achieved with the presented linear model and numerical solution of the nonlinear model for different amplitude ratios, while the excitation frequency is equal to resonance frequency ($\omega = 1$). Fig. 3.7 shows the same curve as Fig. 3.6 for different excitation frequencies while keeping the amplitude ratio constant ($A_r = 0.7$).

The presented model in Eq(3.4) does not require the parameters of the force model, and it cannot provide the PRE, however, at the frequency of interest (excitation and measurement frequency), there is no difference between this method and the full nonlinear model. Hence, It can be concluded that the DMT modulus of the sample, (i.e. elasticity, tip radius, Hamaker constant), and the distance between the cantilever and the sample surface, do not individually have any effect on the amplitude and phase of the cantilever at the frequency of interest. Consequently, they cannot be measured with conventional single frequency TM-AFM. This explains why the height image of soft samples is often not equal to their true value [13], and often depends on the operation parameters etc. The same reasoning holds for calculating the peak repulsive force or any other

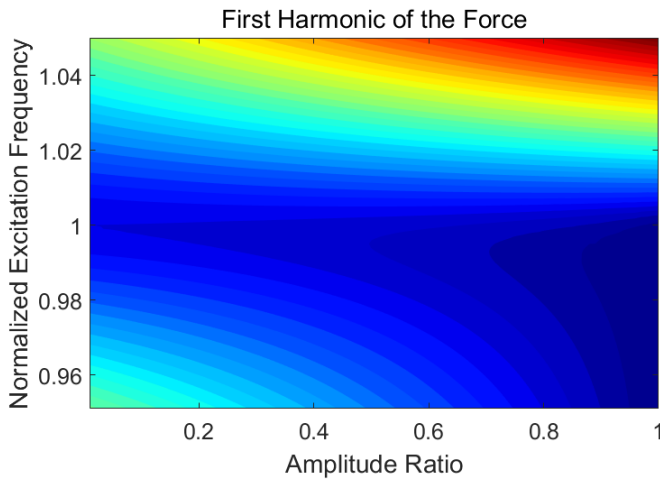


Figure 3.5: Magnitude of first Fourier component of the tip-sample interaction Force vs. amplitude ratio (horizontal) and excitation frequency (vertical); Explanation of frequency sensitivity of TSI force.

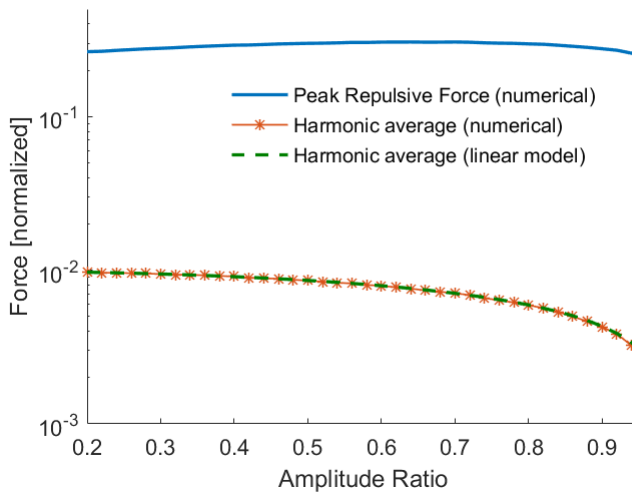


Figure 3.6: Peak Repulsive Force and first Fourier component of the force vs. amplitude ratio ($w=1$) (validation of a horizontal line in Fig. 3.5)

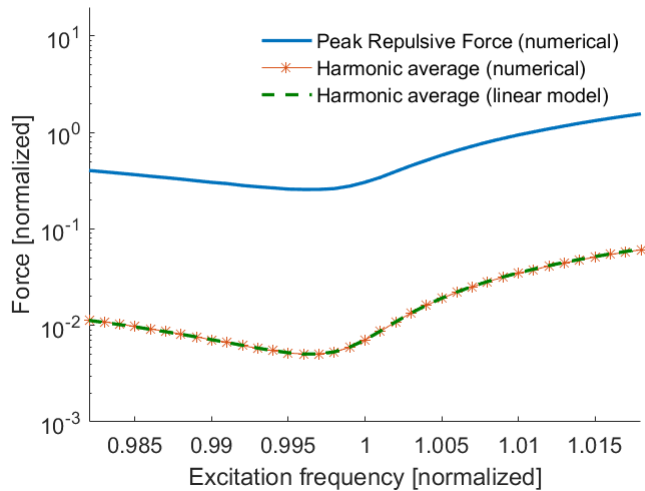


Figure 3.7: Peak Repulsive Force and first Fourier component of the force vs. amplitude ratio ($A_r = 0.7$) (validation of a vertical line in Fig. 3.5)

detail of the TSI force. Since the amplitude and phase (the only observable signals) do not depend on the details of the tip-sample interaction force, it is impossible to extract the force distance curve in TM-AFM without assuming its shape, or performing a sweep measurement.

3.3. CONCLUSIONS

Besides the shift in resonance frequency of the cantilever, the origin of amplitude reduction in TM-AFM can be attributed to an interference between the excitation force and the tip-sample interaction force. This analogy explains the relationship between the excitation frequency, amplitude ratio, and the applied force much clearly. Moreover, with this explanation, it is evident that the single harmonic TM-AFM does not measure the true height profile of the samples but a geometric locus of all the points on the sample that apply the same average force on the cantilever.

REFERENCES

- [1] A. Keyvani, H. Sadeghian, H. Goosen, and E. van Keulen, *On the origin of amplitude reduction mechanism in tapping mode atomic force microscopy*, [Applied Physics Letters](#) **112**, 163104 (2018).
- [2] H. Sadeghian, R. Herfst, J. Winters, W. Crowcombe, G. Kramer, T. van den Dool, and M. H. van Es, *Development of a detachable high speed miniature scanning probe microscope for large area substrates inspection*, [Review of Scientific Instruments](#) **86**, 113706 (2015).
- [3] N. Jalili and K. Laxminarayana, *A review of atomic force microscopy imaging systems:*

- application to molecular metrology and biological sciences*, *Mechatronics* **14**, 907 (2004).
- [4] L. Wang, *Analytical descriptions of the tapping-mode atomic force microscopy response*, *Applied physics letters* **73**, 3781 (1998).
- [5] A. San Paulo and R. Garcia, *Unifying theory of tapping-mode atomic-force microscopy*, *Physical Review B* **66**, 041406 (2002).
- [6] T. R. Rodriguez and R. Garcia, *Tip motion in amplitude modulation (tapping-mode) atomic-force microscopy: Comparison between continuous and point-mass models*, *Applied Physics Letters* **80**, 1646 (2002).
- [7] S. Basak and A. Raman, *Dynamics of tapping mode atomic force microscopy in liquids: Theory and experiments*, *Applied Physics Letters* **91**, 064107 (2007).
- [8] A. Keyvani, H. Sadeghian, H. Goosen, and F. van Keulen, *Transient tip-sample interactions in high-speed afm imaging of 3d nano structures*, in *SPIE Advanced Lithography* (International Society for Optics and Photonics, 2015) pp. 94242Q–94242Q.
- [9] R. Garcia and E. T. Herruzo, *The emergence of multifrequency force microscopy*, *Nature nanotechnology* **7**, 217 (2012).
- [10] A. Keyvani, M. S. Tamer, M. H. van Es, and H. Sadeghian, *Simultaneous afm nanopatterning and imaging for photomask repair*, in *SPIE Advanced Lithography* (International Society for Optics and Photonics, 2016) pp. 977818–977818.
- [11] B. Xue, Y. Yan, Z. Hu, and X. Zhao, *Study on effects of scan parameters on the image quality and tip wear in afm tapping mode*, *Scanning* **36**, 263 (2014).
- [12] C. Su, L. Huang, K. Kjoller, and K. Babcock, *Studies of tip wear processes in tapping modeTM atomic force microscopy*, *Ultramicroscopy* **97**, 135 (2003).
- [13] A. L. Weisenhorn, M. Khorsandi, S. Kasas, V. Gotzos, and H.-J. Butt, *Deformation and height anomaly of soft surfaces studied with an afm*, *Nanotechnology* **4**, 106 (1993).

4

MODULATED MODEL OF TAPPING MODE AFM FOR TRANSIENT CONDITIONS

Many investigations have focused on steady-state nonlinear dynamics of cantilevers in Tapping Mode Atomic Force Microscopy (TM-AFM). However, a transient dynamic model—which is essential for a model-based control design—is still missing. In this paper, we derive a mathematical model which covers both the transient and steady-state behavior. The steady-state response of the proposed model has been validated with existing theories. Its transient response, however, which is not covered with existing theories, has been successfully verified with experiments. Besides enabling model-based control design for TM-AFM, this model can explain the high-end aspects of AFM such as speed limitation, image quality, and eventual chaotic behavior.

4.1. INTRODUCTION

Atomic Force Microscopy (AFM) is a powerful tool for imaging the surface of samples with a sub-nanometer resolution which has many different applications in experimental sciences such as physics and biology[1–4]. Nowadays, AFM is also attracting more and more attention in the semiconductor industry as an inspection and metrology tool. The latter applications demand much stricter requirements regarding throughput, accuracy, reliability, and non-destructiveness [5–8]. To improve the imaging throughput and reliability of AFM, it is essential to understand its physics and optimize its mechanical parts and controllers.

A popular and promising AFM-based measurement technique, both for research and industrial applications, is the Amplitude Modulation (AM-AFM) or the Tapping Mode AFM (TM-AFM). TM-AFM is mainly popular because it applies very small forces on the

Parts of this chapter have been published in [Nonlinear Dynamics 97:1601–1617 \(2019\)](#).

sample surface and, consequently, has lower probability of damaging the sample. The nondestructiveness of TM-AFM can be so important that, e.g., researchers in the field of biology refer to it as *a blessing* [9].

The TM-AFM works as follows: A cantilever with a sharp tip attached to its free end is excited at a frequency around its fundamental resonance frequency, and brought close to the surface of the sample. At a certain distance from the sample surface, the tip starts to interact with the sample via different forces such as van der Waals (vdW) interaction, Pauli repulsion, squeezed film damping, hydro-capilarity, electrostatic forces, etc [10]. As a result of the Tip-Sample Interaction (TSI) forces, the amplitude of the motion of the cantilever reduces [11, 12]. A feedback control loop adjusts the distance between the cantilever and the sample surface using a piezoelectric (z -stage) actuator, such that the amplitude of the cantilever is kept constant at a user-defined fraction of its free air amplitude. While raster scanning the sample surface, and keeping the amplitude constant, the output signal of the controller is recorded and interpreted as the height profile of the sample.

In case the amplitude of the cantilever has a one-to-one relationship with its distance to the surface, keeping the amplitude constant would mean keeping the distance constant. Therefore, any fluctuation in the height profile of the sample is compensated with the z -stage control unit, and the height profile of the sample can be measured via the control signal. However, as schematically shown in Fig. 4.1, the relationship between the amplitude and the distance is not always one-to-one, and consequently, the height measurement is not always trivial. For example, at the far right-hand side of Fig. 4.1, where the sample is far from the cantilever, obviously there is no interaction and the amplitude is independent of the distance. If this situation happens during imaging, the error signal saturates and a so-called parachuting-type artifacts appear on the image [4, 13]. Similarly, at the far left-hand side of the curve in Fig. 4.1, where the attractive forces exceed a certain value, the tip snaps onto the surface and sticks to it; the so-called snap-in phenomena. Thus, independent of small variations of the distance, the amplitude remains zero [14]. Another situation where amplitude and height do not have a one-to-one relationship is the coexistence of the attractive and repulsive regimes [15]. At two different distances from the surface, the TSI force can reduce the amplitude of the cantilever to the same value. In one regime the average force is attractive and in the other, it is repulsive. In Fig. 4.1, if the distance between the cantilever and the sample is h_1 , the vibration amplitude could be either A_1 or A_2 . Similarly, if the measured amplitude is equal to A_2 , the distance could be either h_1 or h_2 . In this case, a certain amplitude may corresponds to two different height values and *vice versa*. Hence the controller fluctuates between the two height values which causes artifacts on the image. Researchers have studied these nonlinear effects, their consequences, and the related problems, extensively [15–17]. However, all these studies consider a steady-state condition and the transient response of the cantilever is neglected.

The nonlinearities are not the only cause for distortion of the amplitude-distance relationship, also transient behavior of the cantilever can distort this one-to-one relationship. The amplitude-distance relationship in Fig. 4.1 is only valid for steady-state situations, i.e. where the amplitude signal is settled to a constant value. For example, suppose that the system is initially settled to Point A in Fig. 4.1, then, suddenly, the sur-

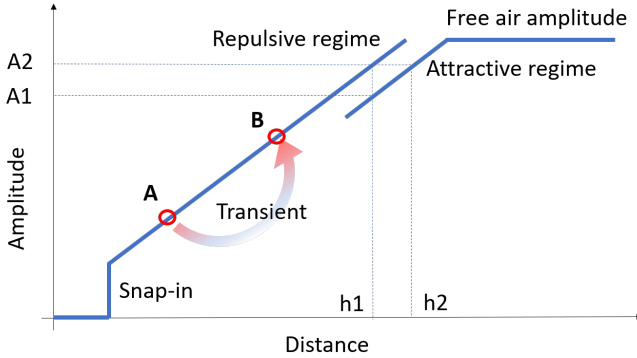


Figure 4.1: Schematic representation of relationship between amplitude and distance, depicting the reasoning for parachuting effect, coexistence of attractive-repulsive regimes, snap-in phenomenon and transient behavior.

face is retracted up to a distance corresponding to Point *B*. Obviously, the amplitude of the cantilever can not adapt suddenly. Therefore, it might follow a different trajectory than the linear steady-state one. How fast the amplitude can adjust itself to the variations in the height totally depends on its dynamic trajectory. This problem is crucial for high-speed AFM, where the changes of the distance happen in time intervals that are comparable or shorter than the cantilevers response time. Note that, the transient response of the cantilever is not taken in account in control design for AFM. Hence, such a transient behavior of the cantilever may cause a closed-loop chaotic behavior in presences of non-linear tip-sample interactions [18]. It has been previously reported that this chaotic behavior strictly limits the speed of the TM-AFM and can only be avoided by reducing the control gains and imaging speed [18].

To understand and improve the speed limit of AFM, an in depth investigation of the transient response of the cantilever is crucial. However, the transient dynamics of the cantilever, which governs the overall performance of AFM, is often ignored or purely discussed from a tip-sample interactions point of view [19]. Therefore, here we try to answer the following research question: How does the amplitude (and phase) of the motion of the cantilever evolve in transient situations? For this, we derive a set of governing differential equations based on Fourier components of the force and displacement. Different aspects of the proposed model are verified with experiments and compared with existing steady-state models. The proposed model is generic in a sense that it does not contain a certain tip-sample interaction model and enables graphical interpretations. A graphical interpretation is helpful for understanding the effects of cantilever dynamics on high-end aspects such as image quality and speed limit. Moreover, the proposed model can be a first step towards designing model-based controllers for high-speed nondestructive TM-AFM.

This paper is further organized as follows: In Section 4.2, we present a detailed derivation of the proposed mathematical model based on an averaging approach. In Section 4.3, we present analytic, numerical, and experimental results based on the proposed

model. This is divided into four different subsections. The first subsection shows that the linear steady-state response of the proposed model is exactly equal to a steady-state response of a one Degree-Of-Freedom (DOF) resonator. The second subsection compares the nonlinear steady-state response of the proposed method with the existing theories for TM-AFM. In the third subsection, we introduce the transient response in time domain and verify it with experiments. Finally, in the fourth subsection, we use a specific experiment to verify the transient response in frequency domain, and try to explain some of the existing experimental results. Section 4.4 is devoted to practical implications of the transient behavior for high-speed TM-AFM. This section consists of two subsections. The first subsection explains the effect of cantilever dynamics on image quality based on closed-loop non-linear simulation. The second subsection graphically explains the reason behind chaotic behavior of TM-AFM as a consequence of high control gains as previously reported in [18].

4.2. MATHEMATICAL MODELING

According to experiments and previously achieved numerical results, despite the strong nonlinearities of the tip-sample interactions, the motion of the cantilever in conventional TM-AFM is harmonic up to a large extent [20]. The reason behind this harmonic motion is the extreme contrast between the sensitivity of the cantilever to different forces. The cantilever is highly sensitive to the forces that correspond to its resonance frequency, and almost not responsive to any other forces. Therefore, the Fourier component of the forces which correspond to the fundamental resonance frequency of the cantilever generate a measurable displacement, while the effects of the other forces are likely to be obscured by the noise [20]. When this contrast is low (low Quality(Q)-factor [21] or Multi-Harmonic cantilevers[22, 23]) or if the TSI force is so strong that it compensates for the low sensitivity, the motion of the cantilever can contain some higher frequency components. However, for conventional TM-AFM, and in the presence of measurement noises, it is almost impossible to measure the higher frequency content of the motion.

Considering only a single harmonic motion, it is a legitimate choice to model the AFM cantilever as a one DOF mass-spring-damper system. For brevity we start with a non-dimensional form of a one DOF model of the AFM cantilever as:

$$\ddot{x} + \xi \dot{x} + x = F_d \cos(\omega t) + f_{ts}, \quad (4.1)$$

where x is the non-dimensional displacement of the tip, with over-dot representing the time derivative. $\xi = \frac{1}{Q}$ is the damping ratio, with Q being the Q-factor of the cantilever. F_d , f_{ts} and ω represent the normalized driving force, TSI force, and excitation frequency, respectively.

Although Eq(4.1) represents the dynamics of the cantilever up to a reasonably high precision, it is not very useful for control design purposes. As mentioned before, the motion of the cantilever only contains one harmonic component and the controller observes its amplitude, which by definition varies much slower than the motion of the cantilever. In practice, a Lock-In Amplifier (LIA) demodulates the motion of the cantilever into its amplitude and phase, and feeds them to the controller. The details of the LIA are outside the scope of this paper, however, it is essential to note that there does not exist any transfer-function or linear approximation for the LIA. Hence, to incorporate the

functionality of the LIA, one should either solve for the strongly nonlinear multiple-time-scale dynamics of the cantilever which is coupled with the LIA, or derive a demodulated model, directly. Obviously, the first would not be efficient for applications such as control design or long time-horizon simulations. Moreover, the TSI force (f_{ts}) in Eq(4.1) is normally a continuous, but non-differentiable function. Theoretically, such functions do not have any Taylor-series approximation, which makes it even more elusive for stability analysis in control design. To overcome these problems, we opt for deriving a demodulated model for the cantilever.

Defining $s_1 \triangleq \dot{x}$ and $s_2 \triangleq x$, Eq(4.1) reads in state-space format:

$$\begin{cases} \dot{s}_1 \\ \dot{s}_2 \end{cases} = \begin{cases} -\xi s_1 - s_2 + f_{ts} + F_d \cos(\omega t) \\ s_1 \end{cases}. \quad (4.2)$$

Since the amplitude and the phase evolve with a much slower time scale, it is useful to define a new time coordinate τ , assuming that the signals in τ domain are constant during one cycle of vibration of the cantilever. Thus, τ shall be used to describe any slowly varying function. A function $f(\tau)$ is called “slow” in contrast to a rapidly varying periodic function $g(t)$ with the periodicity of T , if it has the following property:

$$\int_0^T f(\tau)g(t)dt \approx f(\tau) \int_0^T g(t)dt \quad (4.3)$$

Note that, τ by itself does not differ from t , it is only a notation which is introduced to explicitly separate the slowly varying functions from quickly changing ones.

Assuming that each of the state variables are harmonic functions with slowly varying amplitude and phase (hereafter referred to as semi-harmonic), one can write:

$$s_i(t) \approx A_i(\tau) \cos(\omega t + \varphi_i(\tau)) = \Re[A_i(\tau) e^{j(\omega t + \varphi_i(\tau))}].$$

where $i = 1, 2$, $j = \sqrt{-1}$, and \Re indicates the real operator (\Im will be used for the Imaginary operator). Note that the static component and all the higher harmonics of the s signal is filtered by LIA, and bandwidth of the A and φ is limited to that of the LIA. By defining $X_i(\tau) \triangleq A_i(\tau) e^{j\varphi_i(\tau)} \in \mathbb{C}$, the state variables can be written as the following explicit multiplication of a slowly varying complex function and a pure harmonic function:

$$s_i(t) = \Re \left[\underbrace{X_i(\tau)}_{\text{slow}} \underbrace{e^{j\omega t}}_{\text{harmonic}} \right]. \quad (4.4)$$

Hence, the complex variable $X_i(\tau)$ represents the amplitude and phase of $s_i(t)$ corresponding to frequency ω . Using the chain rule of differentiation, and since differentiation is distributive for the \Re operator, we have:

$$\dot{s}_i = \frac{d}{dt} \Re(X_i(\tau) e^{j\omega t}) = \Re \left(\frac{dX_i}{dt} e^{j\omega t} + X_i \frac{de^{j\omega t}}{dt} \right) = \Re(\dot{X}_i e^{j\omega t} + j\omega X_i e^{j\omega t}). \quad (4.5)$$

In the same manner, the TSI force is a semi-periodic signal. Thus, it can be decomposed into its semi-harmonic components as:

$$f_{ts}(t) = \Re \left(\sum_{n=0}^{\infty} F_{ts}^{(n)}(\tau) e^{jn\omega t} \right) \quad (4.6)$$

where $F_{ts}^{(n)}(\tau) \in \mathbb{C}$ represents the amplitude and phase of the n^{th} harmonic component of the tip-sample interaction force. Note that Eq(4.6) differs from the standard complex Fourier transform only in a way that the amplitude values are not necessarily constant, but represent slowly varying functions in time domain τ .

Substituting Eq(4.4) to Eq(4.6) in Eq(4.2) yields:

$$\Re[(\dot{X}_1(\tau) + j\omega X_1(\tau) + \xi X_1(\tau) + X_2(\tau))e^{j\omega\tau} - \sum_{n=0}^{\infty} F_{ts}^{(n)}(\tau)e^{jn\omega\tau} - F_d e^{j\omega\tau}] = 0 \quad (4.7a)$$

$$\Re[(\dot{X}_2(\tau) + j\omega X_2(\tau) - X_1(\tau))e^{j\omega\tau}] = 0 \quad (4.7b)$$

Multiplying both sides of Eq(4.7) with $e^{j\omega t}$ and integrating through a vibration cycle ($\int_0^{\frac{2\pi}{\omega}} (\cdot) e^{j\omega t} dt$) one can project the equations onto the space of the first harmonic component as:

$$\underbrace{\int_0^{\frac{2\pi}{\omega}} \Re[(\dot{X}_1 + j\omega X_1 + \xi X_1(\tau) + X_2(\tau) - F_d - F_{ts}^{(1)}(\tau))e^{j\omega t}] e^{j\omega t} dt}_{\Gamma_1} - \underbrace{\int_0^{\frac{2\pi}{\omega}} \Re[F_{ts}^{(0)}(\tau)] e^{j\omega t} dt}_{\Gamma_0} - \underbrace{\int_0^{\frac{2\pi}{\omega}} \sum_{n=2}^{\infty} \Re[F_{ts}^{(n)}(\tau)] e^{jn\omega t} e^{j\omega t} dt}_{\Gamma_n} = 0 \quad (4.8a)$$

$$\int_0^{\frac{2\pi}{\omega}} \Re[(\dot{X}_2 + j\omega X_2 - X_1)e^{j\omega t}] e^{j\omega t} dt = 0 \quad (4.8b)$$

Notice that we deliberately expanded the zeroth and first harmonics of the TSI force (Γ_0 , and $F_{ts}^{(1)}$ in Γ_1) out of the \sum (sum) operator. In this way, the equations are rearranged in frequency order where Γ_0, Γ_1 , and Γ_n represent the terms with zero frequency, first harmonic, and higher harmonics, respectively.

Moreover, from the orthogonality of harmonic functions, it is easy to check that, for $\forall n \in \mathbb{N}, c \in \mathbb{C}$ we have:

1. If $n \neq 1, \Rightarrow \int_0^{2\pi} e^{j\theta} \Re[ce^{jn\theta}] d\theta = 0$.
2. If $\int_0^{2\pi} e^{j\theta} \Re[ce^{j\theta}] d\theta = 0, \Rightarrow c = 0$.

Considering the first statement of the orthogonality above, and the definition in Eq(4.3) the last term in Eq(4.8a) vanishes ($\Gamma_n = 0$). Applying the second statement of orthogonality to the remaining terms in Eq(4.8), the \Re operator drops and the following differential

equations are obtained:

$$\dot{X}_1 = -j\omega X_1 - \xi X_1 - X_2 + F_{ts}^{(1)} + F_d \quad (4.9a)$$

$$\dot{X}_2 = -j\omega X_2 + X_1 \quad (4.9b)$$

Eq(4.9) is an ordinary differential equation with complex variables and coefficients. By defining new state parameters as $\mathbf{q} \triangleq [q_1, q_2, q_3, q_4]^T = [\Re(X_1), \Im(X_1), \Re(X_2), \Im(X_2)]^T \in \mathbb{R}^4$ and separating the real and imaginary parts of Eq(4.9), the governing differential equations for the modulated system can be written in the standard real valued state-space form as:

$$\begin{Bmatrix} \dot{q}_1 \\ \dot{q}_2 \\ \dot{q}_3 \\ \dot{q}_4 \end{Bmatrix} = \underbrace{\begin{bmatrix} -\xi & \omega & -1 & 0 \\ -\omega & -\xi & 0 & -1 \\ 1 & 0 & 0 & \omega \\ 0 & 1 & -\omega & 0 \end{bmatrix}}_{\Lambda} \begin{Bmatrix} q_1 \\ q_2 \\ q_3 \\ q_4 \end{Bmatrix} + \begin{Bmatrix} F_d + \Re(F_{ts}^{(1)}) \\ \Im(F_{ts}^{(1)}) \\ 0 \\ 0 \end{Bmatrix}, \quad (4.10a)$$

$$\begin{aligned} A_2(\tau) &= \sqrt{q_3^2 + q_4^2}, \\ \varphi_2(\tau) &= \tan^{-1}\left(\frac{q_3}{q_4}\right), \end{aligned} \quad (4.10b)$$

where

$$F_{ts}^{(1)}(\tau) = \Re(F_{ts}^{(1)}) + j\Im(F_{ts}^{(1)}) = \int_0^{\frac{2\pi}{\omega}} f_{ts}(t) e^{j\omega t} dt,$$

is the slowly varying first Fourier component of the TSI force, $A_2(\tau)$ represents the amplitude of the motion, and $\varphi_2(\tau)$ is the phase.

It might be counter intuitive to observe that the second-order system in Eq(4.1) is converted to a fourth-order system in Eq(4.10). However, it is straightforward to check that Eq(4.10) is a minimal realization, meaning that, four is the minimum dimensionality of the state-space that can accurately represent the modulated system.

It is useful to summarize the physical meaning of the equations and the derivation steps. We started with a single DOF mass-spring model of the cantilever in Eq(4.1) and Eq(4.2). Then, assumed that the amplitude and phase of the cantilever change significantly slower than the motion of the cantilever in Eq(4.3) and Eq(4.4). Furthermore, by projecting the equations onto the Fourier kernel in Eq(4.8), the differential equations for amplitude and phase at the slow time scale Eq(4.10a) have been achieved. According to Eq(4.10a), the amplitude modulated cantilever is a 4th-order linear dynamic system, with a non-linear sensing (amplitude and phase). The dynamic properties of this system depend on its Q-factor and excitation frequency. The input of the modulated system only consists of the dither force and the first harmonic of the tip-sample interaction force.

The first harmonic of the force ($F_{ts}^{(1)}$) has a nonlinear relationship with the state variables (q_i) and the distance of the cantilever from the sample surface. Appendix A presents the derivation of $F_{ts}^{(1)}$ as a function of the distance and the state parameters for the well-known Derjaguin-Muller-Toporov (DMT) force model.

4.3. NUMERICAL AND EXPERIMENTAL RESULTS

In this section, the proposed formulation is used to study the dynamic behavior of AFM cantilevers. First, the steady-state response of the proposed model is verified with existing models. Next, the transient behavior of the cantilever is studied in time and frequency domains and verified with experiments.

4.3.1. LINEAR STEADY-STATE RESPONSE

The most simple test to check the proposed model is to evaluate it for linear steady-state case. For this, the steady solution of Eq(4.10) can be calculated by putting the TSI force and the left-hand side of Eq(4.10a) equal to zero ($F_{ts}^{(1)} = 0, \mathbf{q}_{ss} = O$), thus:

$$\begin{bmatrix} -\xi & \omega & -1 & 0 \\ -\omega & -\xi & 0 & -1 \\ 1 & 0 & 0 & \omega \\ 0 & 1 & -\omega & 0 \end{bmatrix} \begin{Bmatrix} q_1 \\ q_2 \\ q_3 \\ q_4 \end{Bmatrix}_{ss} = - \begin{Bmatrix} F_d \\ 0 \\ 0 \\ 0 \end{Bmatrix}. \quad (4.11)$$

The subscript $_{ss}$ stands for steady-state. This algebraic set of equations can be solved analytically as follows. The last two equations in Eq(4.11) can be solved separately as: $q_1 = -\omega q_4$ and $q_2 = \omega q_3$. Substituting this results in the first two equations of the Eq(4.11) gives:

$$\begin{bmatrix} 1 - \omega^2 & -\xi\omega \\ \xi\omega & 1 - \omega^2 \end{bmatrix} \begin{Bmatrix} q_3 \\ q_4 \end{Bmatrix}_{ss} = \begin{Bmatrix} F_d \\ 0 \end{Bmatrix}. \quad (4.12)$$

Solving the above equation analytically, the stationary state variables become:

$$q_3 = \frac{F_d(1 - \omega^2)}{(1 - \omega^2)^2 + \xi^2\omega^2},$$

$$q_4 = \frac{-F_d\xi\omega}{(1 - \omega^2)^2 + \xi^2\omega^2}.$$

Substituting the static solution for state variables into Eq(4.10b) the following well-known relations are obtained:

$$A_{ss} = \frac{F_d}{\sqrt{(1 - \omega^2)^2 + \xi^2\omega^2}}, \quad (4.13a)$$

$$\varphi_{ss} = \tan^{-1} \frac{\xi\omega}{(1 - \omega^2)}. \quad (4.13b)$$

This shows that the static response of the proposed model in linear case indeed leads to the steady-state response of a one DOF linear resonator[24].

4.3.2. NONLINEAR STEADY-STATE RESPONSE

The proposed model eliminates the fast time scale and represents the dynamics of AFM cantilever in slow time scale. Therefore, its static response corresponds to the steady-state response of the AFM cantilever, whereas its dynamic response represents the transient behavior. In this subsection, the steady response of the proposed model is compared to the existing theories presented in [12, 17, 25]. Similar to the previous subsection, by putting the left-hand side of Eq(4.10a) equal to zero, the steady-state response

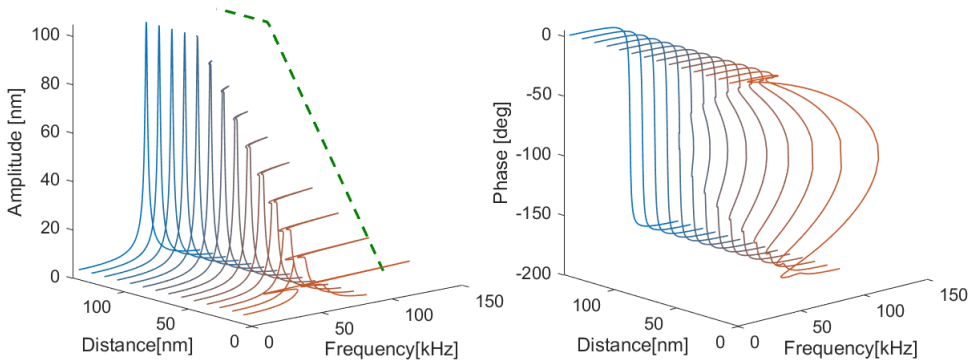


Figure 4.2: Nonlinear frequency response curves of cantilever in TM-AFM for different cantilever-sample separations; red represents the smallest and blue represent the largest distance. The green-dashed curve schematically represents the amplitude-distance relationship as shown in Fig. 4.1. Simulation parameters are the same as reference [25] and the results in this figure are in good agreement with literature, for example see reference [25].

of the AFM cantilever can be obtained. However, in contrast to the previous section, the TSI force is not equal to zero, but its relationship with state parameters has to be calculated via a so-called “force model”. For this, we used the Derjaguin-Muller-Toporov (DMT) model which consists of the attractive van der Waals (vdW), repulsive Hertz, and dissipative viscoelastic forces. For details on this model please refer to Appendix A and the references [26–28].

Using this model, the first harmonic component of the TSI force can be written as:

$$\begin{aligned} \Re(F_{ts}^{(1)}) &= \left(\beta A_2^{\frac{1}{2}} I_2\left(\frac{h}{A_2}, \frac{\sigma}{A_2}\right) - \frac{\alpha}{A_2^3} I_1\left(\frac{h}{A_2}, \frac{\sigma}{A_2}\right) \right) q_3 \\ &\quad + \gamma A_2^{-\frac{1}{2}} I_3\left(\frac{h}{A_2}, \frac{\sigma}{A_2}\right) q_1, \end{aligned} \quad (4.14a)$$

$$\begin{aligned} \Im(F_{ts}^{(1)}) &= \left(\beta A_2^{\frac{1}{2}} I_2\left(\frac{h}{A_2}, \frac{\sigma}{A_2}\right) - \frac{\alpha}{A_2^3} I_1\left(\frac{h}{A_2}, \frac{\sigma}{A_2}\right) \right) q_4 \\ &\quad + \gamma A_2^{-\frac{1}{2}} I_3\left(\frac{h}{A_2}, \frac{\sigma}{A_2}\right) q_2, \end{aligned} \quad (4.14b)$$

where, $\alpha = \frac{HR}{6kA_0^3}$, $\beta = \frac{4E_{eff}\sqrt{RA_0}}{3k}$, and $\gamma = \omega\eta\sqrt{RA_0^3}$, are the coefficients of the vdW, Hertz and viscoelastic forces, respectively. H , R , E_{eff} , h , A_0 , A_2 , and σ are Hamaker constant, tip-radius, effective stiffness of tip-sample contact, separation of the sample surface and the cantilever in its undeflected configuration, free air amplitude, actual amplitude at any time (as described in Eq(4.10b)), and the intermolecular distance, respectively. The

integral functions (I_1 , I_2 and I_3) as a function of their arguments (ζ_1, ζ_2) are defined as:

$$I_1(\zeta_1, \zeta_2) = \int_0^{2\pi} \frac{\cos(\theta) d\theta}{(\zeta_1 - \cos(\theta))_{D\zeta_2}^2}, \quad (4.15a)$$

$$I_2(\zeta_1, \zeta_2) = \int_0^{2\pi} (\cos(\theta) - \zeta_1 + \zeta_2)_{D_0}^{\frac{3}{2}} \cos(\theta) d\theta, \quad (4.15b)$$

$$I_3(\zeta_1, \zeta_2) = \int_0^{2\pi} (\cos(\theta) - \zeta_1 + \zeta_2)_{D_0}^{\frac{1}{2}} \cos(\theta) d\theta. \quad (4.15c)$$

where the discontinuity function $(a)_{D_b}$ is defined to impose the discontinuity of the forces during the contact as: $(a)_{D_b} = \begin{cases} a & \text{if } a \geq b \\ b & \text{if } a < b \end{cases}$. A detailed derivation of the force model for slow time scale and the details of DMT model is presented in Appendix A.

Typically, an arc-length continuation method is used to calculate the nonlinear frequency response of a non-linear system. However, the frequency response of the system represented by Eq(4.10) can always be transformed to a quadratic algebraic problem in terms of excitation frequency squared (ω^2), irrespective of the type of the nonlinearity. Hence, its nonlinear frequency response can also be calculated analytically as well. The details of calculating the nonlinear frequency response of the cantilever using the proposed model are presented in Appendix B.

Fig. 4.2 shows the steady-state nonlinear frequency response of the cantilever considering different cantilever-sample separations. These results were calculated with the same parameters as in [25] (spring constant 2 N/m, resonance frequency 52.4 kHz, quality factor 66.7, tip radius 20nm Hamaker constant 2.96×10^{-19} J, intermolecular distance 2.0 Å, and free air amplitude 100 nm). The nonlinear frequency responses in Fig. 4.2 are in good agreement with the results presented by Lee *et al.* [25], whereas the dashed green curve represents the amplitude-distance relationship depicted in Fig. 4.1.

These results show that the static response of the proposed model agrees with the existing models for steady-state response of the AFM cantilever. The next sections will study the transient behavior of the AFM cantilever which captures the dynamic transition between each of the lines in Fig. 4.2.

4.3.3. TRANSIENT RESPONSE IN THE TIME DOMAIN

To investigate the evolution of the amplitude and phase in the time domain, here the step response of the modulated system is studied. The assumption is that the cantilever is initially at rest (zero amplitude). Suddenly, a harmonic force with a constant amplitude and frequency is applied (i.e. dither piezo turned on). Fig. 4.3 shows the dynamic trajectory of the amplitude and phase from rest to its steady-state.

Note that the dynamic trajectory of the cantilever is a spiral of which the direction is determined by the ratio between the excitation frequency and the resonance frequency of the cantilever. If the excitation frequency is lower than the resonance frequency, the

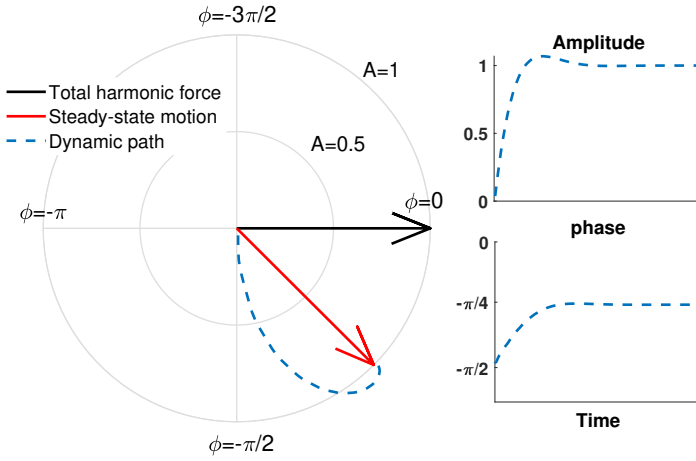


Figure 4.3: Step response of the amplitude and phase in polar and Cartesian coordinates. In the phasor plot, the distance from the center of coordinates shows the amplitude and the angle shows the phase delay. The reasoning behind overshoot of amplitude and the trajectory of phase are stem from the spiral trajectory shown in the phasor plot.

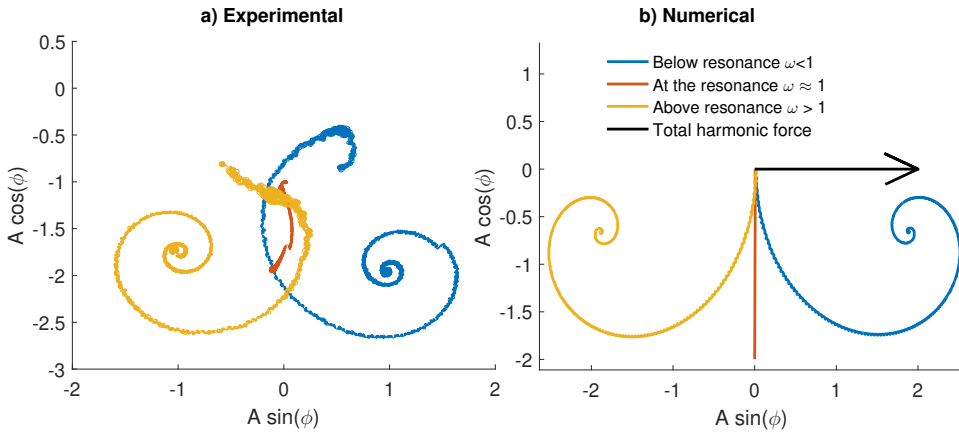


Figure 4.4: Dynamic trajectories of amplitude-phase pair with different excitation frequency. a) Experimental: A cantilever with the Q factor ≈ 300 , stiffness $\approx 1\text{Nm}^{-1}$ and fundamental resonance frequency $\approx 45\text{kHz}$ has been used in a commercial AFM system. While the cantilever was far from any sample surface, the excitation power has been suddenly increased from 3V to 6V. b) Numerical: step responses of Eq(4.10). If the excitation frequency is less than the resonance frequency of the cantilever, the dynamic trajectory is a clock-wise spiral and *vice versa*.

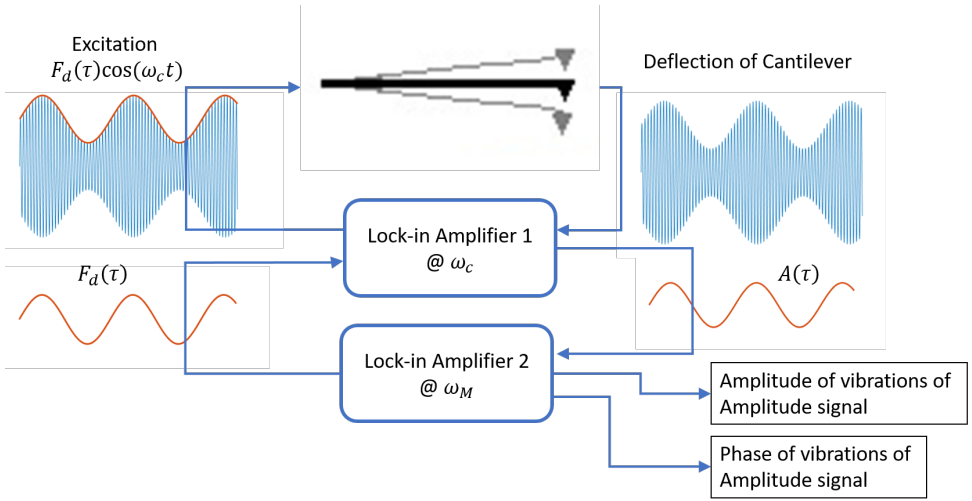


Figure 4.5: Schematic of the experimental setup for frequency domain analysis. LIA 1 modulates and demodulates the motion of the cantilever, and the LIA 2 modulates and demodulates the amplitude signals that are provided to and received from the LIA 1. The output amplitude and phase of LIA 2 represents the dynamic behavior of the modulated cantilever in frequency domain.

cantilever follows a counter-clockwise spiral, and *vice versa*. This is illustrated via numerical and experimental results in Fig. 4.4. Here, the numerical results show the step response of linear part of Eq(4.10) and experimental results are captured using a commercially available AFM and LIA , i.e. Bruker Fast-Scan and Zurich Instruments UHFLI 1.8GSa/s 600MHz. In the experiments, first the cantilever was settled to a certain amplitude and phase, then suddenly, we increase the excitation power to twice its steady value. Note that the initial point in experiments start from different phase values, with approximately identical amplitudes, because the excitation frequency was different for the three cases. Moreover, we did not start the experiment from rest condition, because the phase signal is defined based on the dither signal and can not be defined while the cantilever is at rest.

The spiral shape of the trajectory is more relevant when high speed AFM controllers are concerned. The spiral-shaped trajectory in Fig. 4.4 shows that there can be an initial response in the wrong direction, similar to the Non-Minimum-Phase (MNP) behavior in linear systems [29]. Meaning that, if for any reason one expects the amplitude to drop, it might first increase and then drop, or *vice versa*. This wrong direction of the initial response makes it very challenging for high-speed controllers. If the time constant of the controller is shorter than the settling time of the cantilever, the controller might take wrong actions based on the wrong directional response of the cantilever.

4.3.4. NONLINEAR TRANSIENT RESPONSE IN THE FREQUENCY DOMAIN

This subsection investigates the frequency domain response of the demodulated system. In order to understand the model represented by Eq(4.10) in frequency domain, it is assumed that the excitation force is modulated with another harmonic signal which has

a much lower frequency than the resonance frequency of the cantilever. Considering the linear dynamics of the modulated system, i.e. Eq(4.10a), one observes that the system has two pairs of complex conjugate poles (eigenvalues of matrix Λ in Eq(4.10)) at:

$$P_{1-4} = -\frac{\xi \pm j\sqrt{4-\xi^2 \pm 2\omega}}{2} \approx -\frac{\xi}{2} \pm j\frac{2 \pm 2\omega + \frac{\xi^2}{2} + \dots}{2} \quad (4.16)$$

Normally an AFM cantilever in ambient conditions is a highly underdamped system. Therefore one can simplify Eq(4.16) further considering that $\omega \approx 1$ and $\xi \approx 0$, and $\xi^2 \ll (1-\omega)$ ¹. In that case, one observes that the system has one pair of dominant and one pair of non-dominant poles at:

$$\begin{aligned} P_{1,2} &\approx -\frac{\xi}{2} \pm 2j \\ P_{3,4} &\approx -\frac{\xi}{2} \pm (1-\omega)j \end{aligned} \quad (4.17)$$

The non-dominant pair of poles, with complex part 2 ($P_{1,2}$), represent the up-modulation of the resonator and are not relevant for the TM-AFM problem because, besides being non-dominant, their response would be filtered by the LIA. The other two poles ($P_{3,4}$), which are dominant, actually determine the transient behavior of the AFM cantilever. Eq(4.17) suggests that the imaginary part of the dominant poles of the modulated system ($P_{3,4}$) are approximately equal to the difference between the excitation frequency and the resonance frequency of the cantilever, i.e. $|\omega_e - \omega_r|$ (or in nondimensional form $|\omega - 1|$), and their real part ($\frac{\xi}{2} = \frac{1}{2Q}$) represent the settling time of the system. In fact, the real part of the dominant poles which determine the relaxation time of the system is already known by AFM experts as it is a common knowledge that lower the Q-factor higher the speed of AFM. However, the imaginary part is not well understood.

Recently, the relationship between the real part of the poles (quality factor of the cantilever) has been experimentally confirmed by Adams *et al.* [30] They used different custom-made cantilevers with various Q-factors and showed the dependency of the settling time to the Q-factor. In their experiments, they used a piezoelectric actuator to modulate the surface height, artificially. In this way they measured the frequency response of the amplitude due to height variations. A very interesting and counter-intuitive detail in their experiments is that the magnitude of the amplitude signal could go beyond zero decibel at certain frequencies. This effect which was not explained, is an evidence of the resonance in the modulated system (see Figure 4.b in [30]). Note that the presence of a resonance can only be explained with complex conjugate poles.

To systematically investigate the resonance of the amplitude signal, we repeated the experiment presented by Adams *et al.*[30] However, with the difference that, instead of modulating the surface, we modulated the amplitude of the excitation signal. In this way the nonlinearities regarding the TSI force are out of the equation, and the pure dynamics of the cantilever is measured. For this experiment, two lock-in amplifiers were used as shown in Fig. 4.5. One of the LIAs provides the modulation/demodulation of the cantilever with the so-called carrier frequency, i.e. the excitation frequency of the dither (ω_e), whereas the second LIA modulates the amplitude of the carrier signal and extracts the amplitude and phase of the amplitude of the cantilever. In this way, effects of the

¹The In practice ξ is determined by physical conditions, while ω is partly the choice of the operator. However, if the system is not overdamped, the effects of ξ^2 are negligible, therefore, the imaginary part of the poles of the system can be considered purely dependent on the choice of excitation frequency.

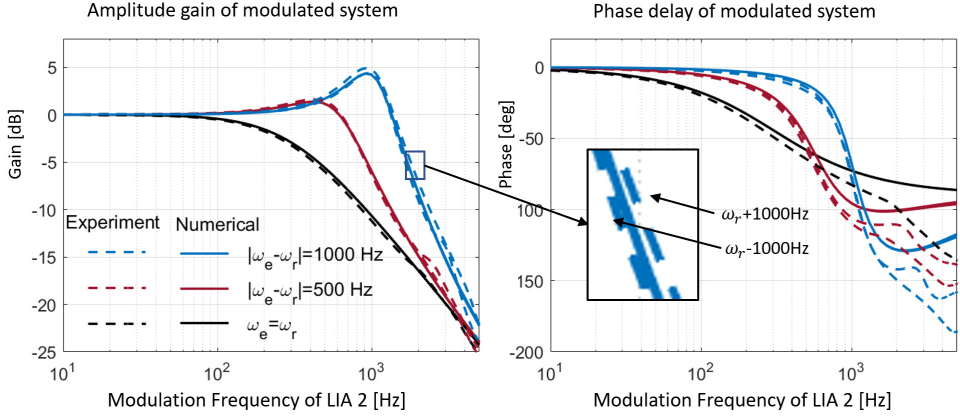


Figure 4.6: Measured (dashed lines) and calculated (solid lines) response of the amplitude of the cantilever to the fluctuations in magnitude of the total harmonic force with five different carrier frequencies. These figures show the input-output relationship of the modulated system, where the input is amplitude of the total harmonic force and the output is the amplitude of the cantilever. Magnitude and phase are directly measured via the second LIA shown in Fig. 4.5

fluctuation of harmonic force are measured depending on the frequency content of the fluctuation.

Fig. 4.6 shows both the measured and calculated frequency response of the amplitude to these fluctuations. The numerical results were achieved as follows:

The transfer function matrix for the linear part of the system (from $F(\omega_M)$ to $\mathbf{q}(\omega_M)$) is calculated as the first column of $(sI - \Lambda)^{-1}$ where s is the Laplace variable and I is a (4×4) unit matrix. Therefore, substituting a probe function as $F_d = \sin(\omega_M \tau)$, the amplitude and phase signals (A_2 and φ_2) can be calculated analytically. Then, the functionality of the second LIA can be implemented by multiplying the amplitude signal (A_2) by the probe signal and integrating as:

$$A_A = \sqrt{\left(\int_0^{2\pi} A_2 \sin(\omega_M \tau) d\tau\right)^2 + \left(\int_0^{2\pi} A_2 \cos(\omega_M \tau) d\tau\right)^2} \quad (4.18a)$$

$$\varphi_A = \tan^{-1} \frac{\int_0^{2\pi} A_2 \sin(\omega_M \tau) d\tau}{\int_0^{2\pi} A_2 \cos(\omega_M \tau) d\tau} \quad (4.18b)$$

In this way amplitude and phase (A_A, φ_A) of the amplitude signal (A_2) due to disturbance in total harmonic force (F_d) were calculated.

In Fig. 4.6, five different carrier frequencies were chosen around the resonance frequency with an interval of 500 Hz. As it can be seen, there is a good agreement between the experimental and numerical results. Both experimental and numerical results demonstrate that the peak of the amplitude occurs at a frequency equal to the difference between the carrier and the resonance frequencies ($|\omega_e - \omega_r|$), which confirms Eq(4.16).

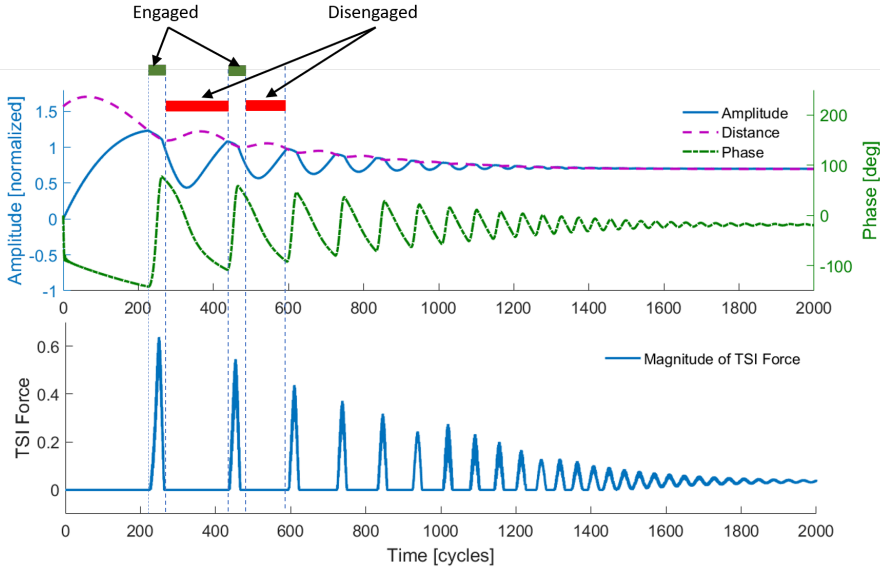


Figure 4.7: Time domain simulation results of TM-AFM while approaching the surface. In this simulation, the distance between the cantilever and the sample surface starts at 1.5 times the free air amplitude, while the cantilever is at rest. At time 0, the dither force and the PI controller are turned on. See the supplementary material for an animated version.

The experiments were done using a commercial AFM and LIAs (Bruker Fast-Scan and Zurich Instruments UHFLI 1.8GSa/s 600MHz) with a standard cantilever which has a resonance frequency of $\omega_r = 319.015\text{kHz}$ and Q-factor $Q \approx 520$. Simulations consider the same cantilever.

An other important observation from the frequency domain analysis is the slope of the decay line after resonance. The linear part of Eq(4.10) suggests that the system has one pair of dominant complex conjugate poles. Hence, the system should behave like a second-order system, and have a decay line with a slope of -40dB per decade after the resonance. However, due to the output nonlinearity (see Eq(4.10b)), the slope of the decay line can differ from -20 till -40 dB per decade, depending on the carrier frequency. This observation suggests that it would be very challenging for any system identification method to find any reliable integer-order fit for the system. This hinders the design of model-based controllers. Obviously, this problem would not appear without the output nonlinearity related to A and φ . Therefore, to design a model-based controller, one has to either design fractional order controllers[31, 32] or use the q_3 and q_4 as the control input instead of the amplitude.

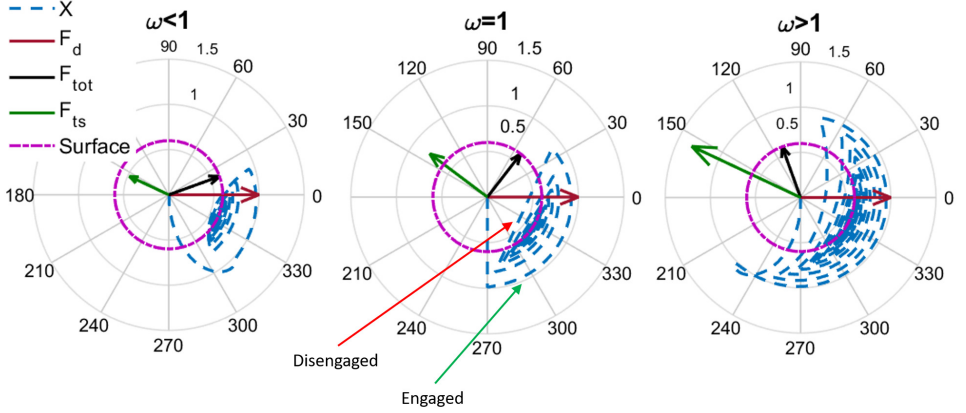


Figure 4.8: Phasor plot representation of the amplitude and phase for three different excitation frequencies. The vectors show the steady-state forces vectors. See [11] for the explanation of the steady-state situation, and supplementary material for an animated version.

4.4. PRACTICAL IMPLICATIONS OF TRANSIENT BEHAVIOR OF CANTILEVERS

In this section, the nonlinear closed-loop behavior of the system is studied. The results show the practical implications of the transient behavior of the TM-AFM on the final image quality. Also the origin for previously reported chaotic behavior of the TM-AFM [18] can be explained.

4.4.1. NONLINEAR CLOSED-LOOP BEHAVIOR OF THE TM-AFM

To investigate the nonlinear behavior of AFM in a closed-loop setting, a force model and a model for the controller are needed, besides the model of the cantilever. For the force, we use the slow time domain DMT model as presented in previous sub-sections (Eq(4.14)). A detailed derivation of the slow time model is presented in Appendix A. As the controller, an ideal Proportional-Integral (PI) controller is considered which assumes that the z -stage actuator is fast enough not to have any effect on the closed-loop dynamics of the system. In this way the distance between the cantilever and the sample (h) is defined as:

$$h(\tau) = k_p(A(\tau) - A_{set}) + k_i \int_0^\tau (A(s) - A_{set}) ds, \quad (4.19)$$

where k_p , k_i , and A_{set} are proportional gain, integral gain and set-point amplitude, respectively. Eq(4.10), Eq(4.14) and Eq(4.19) representing the cantilever (and LIA), the tip-sample interactions, and the controller are coupled with each other through shared signals A , h , and $F_{ts}^{(1)}$. Fig. 4.7 shows the simulated amplitude, phase, and the magnitude of the harmonic component of the TSI forces during an approach process.

As it can be seen from Fig. 4.7, every time that the cantilever engages the surface (i.e. the distance becomes equal to the amplitude of the cantilever) the TSI force emerges

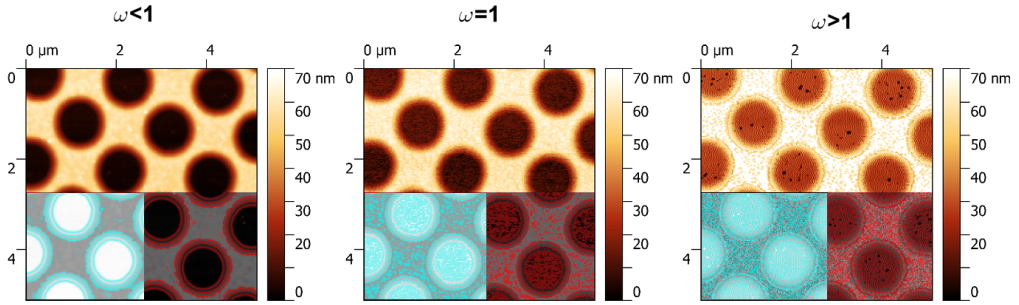


Figure 4.9: Height image of a calibration sample (UMG02B from Anfatec Instruments) with three different excitation frequencies, corresponding to Fig. 4.8. All three images are taken from the same spot on the sample, using a standard tapping mode cantilever with a resonance frequency of 72 kHz, Q factor of 200, and spring constant of 2.5 n/m. The free air amplitude, set-point amplitude, and scan rate for all three cases are 100 nm, 75 nm, and 1 Hz, respectively. The color masks are applied to exaggerate the imaging artifacts. Imaging with a lower excitation frequency adds fewer artifacts.

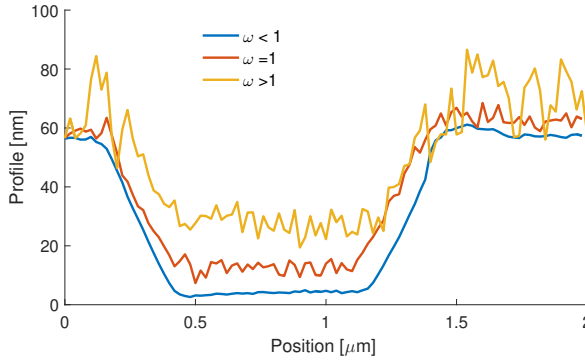


Figure 4.10: Cross-section of one of the holes in Fig. 4.9. The profiles measured with an excitation frequency less than the resonance frequency of the cantilever show a less noisy, more stable profile.

and affects the cantilever and changes its amplitude and phase. It is important to notice that during the engagement time, the TSI force causes always a considerable phase lead, while the amplitude mildly changes. However, after disengaging the surface, the amplitude value keeps reducing with a larger rate and then increases again. To further investigate the transient behavior of the amplitude and the phase, Fig. 4.8 shows the dynamic trajectory of the system in phasor plane for three different excitation frequencies. Using these graphs, we can study the following three questions: *i)* Why do the tip-sample interactions always induce a phase lead? *ii)* Why does the amplitude keep reducing and then increasing when disengaged from the surface? *iii)* Why is the image quality better when we choose an excitation frequency slightly lower than the resonance frequency of the cantilever?

Before the cantilever engages to the surface, the motion of the cantilever has a phase

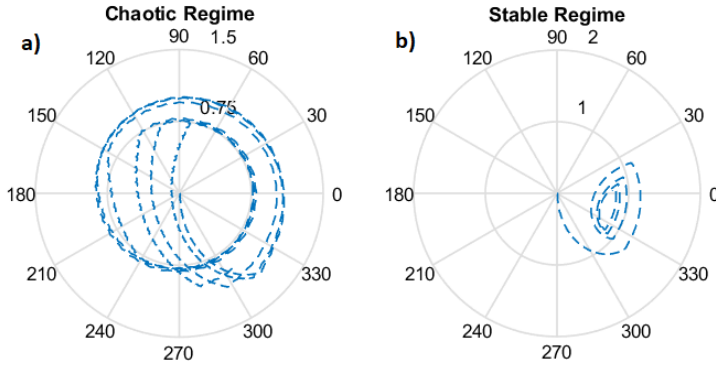


Figure 4.11: Closed-loop behavior of TM-AFM in polar coordinates. a) chaotic. b) stable. The aggressive control action causes more than 2π radians phase lead in each engage-disengage cycle and prevents the system from reaching a stable center point which generates a chaotic motion.

delay with respect to the dither force. Since the TSI force is opposite to the displacement, the direction of the total harmonic force at the first moment of the contact is upwards (a positive phase). Also because the TSI force in first engagement is much stronger than the dither force, the total harmonic force is mainly dominated by the TSI force. In this situation, the phase increases and amplitude tries to increase by indenting the tip more and more into the sample surface. Hence, the cantilever follows the circular arc in Fig. 4.8 in counter-clockwise. At the moment that the phase lead does not need to increase anymore, the cantilever loses contact with the surface and only the dither force is acting on the cantilever. After losing the connection, the cantilever follows its free trajectory which first reduces the amplitude and then increases. As explained in Fig. 4.4, the free trajectory of the motion can be either a straight line or a spiral trajectory, depending on the excitation frequency. Repeating this engaging-disengaging process for few times, the cantilever reaches its steady-state situation. The damping needed for this process is provided by all three elements: the cantilever, the non-conservative part of TSI force, and the control action.

Comparing the three different cases in Fig. 4.8, for the lower excitation frequency, the cantilever has a lower phase delay before the contact. Thus, it needs to follow a shorter trajectory on the circular arc to lose contact. On the other hand, after losing contact, it follows a counter-clockwise spiral to reach the surface again which is shorter than a clock-wise trajectory to the surface. Therefore, in total the cantilever has a shorter path to the stable steady-state situation, when it is excited with a lower frequency. That is why the images captured with a lower excitation frequency have higher image quality, which is intuitively known by experienced AFM users and is experimentally demonstrated in Fig. 4.9. For this example, a calibration sample is measured with three different excitation frequencies where all other parameters are exactly the same for all the three cases. The difference in image quality can be observed more clearly in Fig. 4.10 which illustrates the added imaging artifacts on the cross-section of one of the holes in Fig. 4.9.

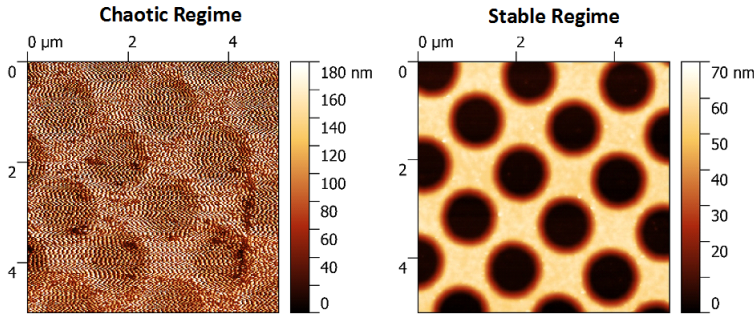


Figure 4.12: Height image of the calibration sample (UMG02B from Anfattec Instruments) with parameters corresponding to Fig. 4.11. When the cantilever is in chaotic regime (the control gains are too high), the images do not provide any useful information.

4.4.2. CHAOTIC BEHAVIOR

It has been reported that if the controller is tuned to be faster than a certain threshold, the closed-loop system shows a chaotic behavior [18]. Although the presence of chaos was confirmed by studying the Poincaré sections and Lyapunov exponents, the origin of the chaos was not explained. Fig. 4.11 shows the difference between a stable and a chaotic trajectory, and Fig. 4.12 shows the images captured with conditions corresponding to Fig. 4.11. In the scenario as explained in the previous sub-section, if the controller acts more aggressive than a certain limit, the cantilever experiences more than 2π radian phase lead before losing the surface and re-engaging. Therefore, the next attempt to re-engage does not start from a better initial point. Thus, the new initial condition is not closer to the stable point comparing the previous engaging point. Hence, the "engage/disengage" process repeats forever in a periodic or non-periodic manner, depending on the control gains. While the periodic "engage/disengage" generates a quasi-periodic regime, the non-periodic one represents the chaotic trajectory. Both these regimes have been reported in [18]. All in all, the chaotic behavior can be attributed to the wrong direction response of the amplitude signal.

4.5. CONCLUSIONS

In this paper, we presented a dynamic model for amplitude modulation (tapping mode) AFM as the first step towards a model based control design. The model graphically explains the behavior of the AFM cantilever in a slow time scale, i.e. the changes in the amplitude, phase and the control signals. The proposed model has been verified with experiments and shows that the behavior of the AFM cantilever in slow time scale is profoundly affected by the excitation frequency and Q-factor of the cantilever. According to the presented model the amplitude per sé is not the best indication of the distance, and should not be used as the error signal in the control loop. Instead, to design high-performance controllers and avoid chaos, one should consider a modulated transient model of the cantilever as a multi-input-multi-output system.

REFERENCES

- [1] N. Jalili and K. Laxminarayana, *A review of atomic force microscopy imaging systems: application to molecular metrology and biological sciences*, *Mechatronics* **14**, 907 (2004).
- [2] H. Yang, Y. Wang, S. Lai, H. An, Y. Li, and F. Chen, *Application of atomic force microscopy as a nanotechnology tool in food science*, *Journal of food science* **72**, R65 (2007).
- [3] R. Garcia and R. Perez, *Dynamic atomic force microscopy methods*, *Surface science reports* **47**, 197 (2002).
- [4] T. Ando, T. Uchihashi, N. Kodera, D. Yamamoto, A. Miyagi, M. Taniguchi, and H. Yamashita, *High-speed afm and nano-visualization of biomolecular processes*, *Pflügers Archiv-European Journal of Physiology* **456**, 211 (2008).
- [5] M.-K. Lee, M. Shin, T. Bao, C.-G. Song, D. Dawson, D.-C. Ihm, and V. Ukraintsev, *Applications of afm in semiconductor r&d and manufacturing at 45 nm technology node and beyond*, in *SPIE Advanced Lithography* (International Society for Optics and Photonics, 2009) pp. 72722R–72722R.
- [6] H. Sadeghian, R. Herfst, B. Dekker, J. Winters, T. Bijnagte, and R. Rijnbeek, *High-throughput atomic force microscopes operating in parallel*, *arXiv preprint arXiv:1611.06582* (2016).
- [7] H. Sadeghian, R. Herfst, J. Winters, W. Crowcombe, G. Kramer, T. van den Dool, and M. H. van Es, *Development of a detachable high speed miniature scanning probe microscope for large area substrates inspection*, *Review of Scientific Instruments* **86**, 113706 (2015).
- [8] R. Herfst, B. Dekker, G. Witvoet, W. Crowcombe, D. de Lange, and H. Sadeghian, *A miniaturized, high frequency mechanical scanner for high speed atomic force microscope using suspension on dynamically determined points*, *Review of Scientific Instruments* **86**, 113703 (2015).
- [9] Y. G. Kuznetsov, A. Malkin, R. Lucas, M. Plomp, and A. McPherson, *Imaging of viruses by atomic force microscopy*, *Journal of General Virology* **82**, 2025 (2001).
- [10] J. N. Israelachvili, *Intermolecular and surface forces* (Academic press, 2011).
- [11] A. Keyvani, H. Sadeghian, H. Goosen, and F. Van Keulen, *On the origin of amplitude reduction mechanism in tapping mode atomic force microscopy*, *Applied Physics Letters* **112**, 163104 (2018).
- [12] L. Wang, *Analytical descriptions of the tapping-mode atomic force microscopy response*, *Applied physics letters* **73**, 3781 (1998).
- [13] T. De, P. Agarwal, D. R. Sahoo, and M. V. Salapaka, *Real-time detection of probe loss in atomic force microscopy*, *Applied physics letters* **89**, 133119 (2006).

- [14] M. C. Strus, A. Raman, C.-S. Han, and C. Nguyen, *Imaging artefacts in atomic force microscopy with carbon nanotube tips*, [Nanotechnology](#) **16**, 2482 (2005).
- [15] R. Garcia and A. San Paulo, *Attractive and repulsive tip-sample interaction regimes in tapping-mode atomic force microscopy*, [Physical Review B](#) **60**, 4961 (1999).
- [16] A. N. Round and M. J. Miles, *Exploring the consequences of attractive and repulsive interaction regimes in tapping mode atomic force microscopy of dna*, [Nanotechnology](#) **15**, S176 (2004).
- [17] A. San Paulo and R. Garcia, *Unifying theory of tapping-mode atomic-force microscopy*, [Physical Review B](#) **66**, 041406 (2002).
- [18] A. Keyvani, F. Alijani, H. Sadeghian, K. Maturova, H. Goosen, and F. van Keulen, *Chaos: The speed limiting phenomenon in dynamic atomic force microscopy*, [Journal of Applied Physics](#) **122**, 224306 (2017).
- [19] A. Keyvani, H. Sadeghian, H. Goosen, and F. van Keulen, *Transient tip-sample interactions in high-speed afm imaging of 3d nano structures*, in *Metrology, Inspection, and Process Control for Microlithography XXIX*, Vol. 9424 (International Society for Optics and Photonics, 2015) p. 94242Q.
- [20] T. R. Rodriguez and R. Garcia, *Tip motion in amplitude modulation (tapping-mode) atomic-force microscopy: Comparison between continuous and point-mass models*, [Applied Physics Letters](#) **80**, 1646 (2002).
- [21] S. Basak and A. Raman, *Dynamics of tapping mode atomic force microscopy in liquids: Theory and experiments*, [Applied Physics Letters](#) **91**, 064107 (2007).
- [22] A. Keyvani, H. Sadeghian, M. S. Tamer, J. F. L. Goosen, and F. van Keulen, *Minimizing tip-sample forces and enhancing sensitivity in atomic force microscopy with dynamically compliant cantilevers*, [Journal of Applied Physics](#) **121**, 244505 (2017).
- [23] O. Sahin, S. Magonov, C. Su, C. F. Quate, and O. Solgaard, *An atomic force microscope tip designed to measure time-varying nanomechanical forces*, [Nature nanotechnology](#) **2**, 507 (2007).
- [24] W. Thomson, *Theory of vibration with applications* (CrC Press, 2018).
- [25] S. Lee, S. Howell, A. Raman, and R. Reifenberger, *Nonlinear dynamic perspectives on dynamic force microscopy*, [Ultramicroscopy](#) **97**, 185 (2003).
- [26] H. V. Guzman, A. P. Perrino, and R. Garcia, *Peak forces in high-resolution imaging of soft matter in liquid*, [ACS nano](#) **7**, 3198 (2013).
- [27] S. Rützel, S. I. Lee, and A. Raman, *Nonlinear dynamics of atomic-force-microscope probes driven in lennard-jones potentials*, in *Proceedings of the Royal Society of London A: Mathematical, Physical and Engineering Sciences*, Vol. 459 (The Royal Society, 2003) pp. 1925–1948.

- [28] U. D. Schwarz, *A generalized analytical model for the elastic deformation of an adhesive contact between a sphere and a flat surface*, *Journal of Colloid and Interface Science* **261**, 99 (2003).
- [29] K. Ogata and Y. Yang, *Modern control engineering*, Vol. 4 (Prentice hall India, 2002).
- [30] J. D. Adams, B. W. Erickson, J. Grossenbacher, J. Brugger, A. Nievergelt, and G. E. Fantner, *Harnessing the damping properties of materials for high-speed atomic force microscopy*, *Nature nanotechnology* (2015).
- [31] J. Sabatier, O. P. Agrawal, and J. T. Machado, *Advances in fractional calculus*, Vol. 4 (Springer, 2007).
- [32] Y. Chen, I. Petras, and D. Xue, *Fractional order control-a tutorial*, in *American Control Conference, 2009. ACC'09*. (IEEE, 2009) pp. 1397–1411.

5

CHAOS: THE SPEED LIMITING PHENOMENON IN DYNAMIC ATOMIC FORCE MICROSCOPY

This chapter investigates the closed-loop dynamics of the Tapping Mode Atomic Force Microscopy (TM-AFM) using a new mathematical model based on the averaging method in Cartesian coordinates. Experimental and numerical observations show that the emergence of chaos in conventional tapping mode AFM strictly limits the imaging speed. We show that, if the controller of AFM is tuned to be faster than a certain threshold, the closed-loop system exhibits a chaotic behavior. The presence of chaos in the closed-loop dynamics is confirmed via bifurcation diagrams, Poincaré sections and Lyapunov exponents. Unlike the previously detected chaos due to attractive forces in AFM which can be circumvented via simple changes in operation parameters, this newly identified chaos is seemingly inevitable and imposes an upper limit for the closed-loop bandwidth of the AFM.

5.1. INTRODUCTION

The Atomic Force Microscope (AFM) is a versatile instrument for topography measurement of samples with nanometer resolution. As shown in Fig. 5.1, the functioning of the AFM is based on measuring the effects of the interactions between a sample surface and a probe. The probe consists of a microcantilever beam and an atomically sharp tip. One of the most popular operation modes is the Tapping Mode AFM (TM-AFM), also known as amplitude modulation AFM. In this mode, the probe is excited around its fundamental resonance frequency such that its amplitude is set to a so called free air amplitude. The motion of the cantilever is measured (typically) using an Optical Beam Deflection (OBD) system, and its amplitude is calculated using a Lock-in Amplifier (LIA) circuit and a Digital Signal Processing unit (DSP). A set point of the amplitude is reached by bringing

Parts of this chapter have been published in [Journal of Applied Physics](#) 122, 224306 (2017).

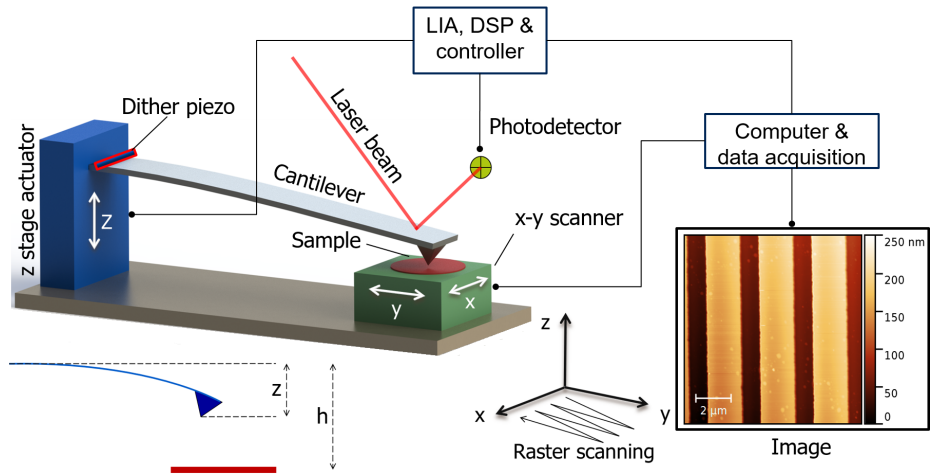


Figure 5.1: Schematic view of an AFM, showing the process of imaging the sample.

the cantilever close to the sample surface. The distance between the cantilever and the sample is adjusted using a feedback controlled piezoelectric actuator so that the amplitude of the vibration remains constant. While scanning the sample in in-plane directions (x - y , hereafter) and keeping the amplitude constant, the control signal is interpreted as the topography of the sample. Moreover, the phase delay of the cantilever provides another image which is usually interpreted as an indication of surface damping.

In general, a major issue with scanning probe microscopy techniques is their limited imaging speed, and TM-AFM is not an exception in this respect. Yet, many of the industrial applications, such as inspection and metrology in semiconductor production lines demand a high throughput. In fact, different components in the AFM architecture including cantilever, actuators, controller, and the electronic components all have a certain speed limit. Therefore, increasing the imaging speed necessitates increasing the bandwidth of every single component as well as optimization of the coupled system [1]. To enhance the speed of AFM, many researchers have studied, designed, and characterized high-bandwidth apparatus [1–7], which has led to the improvement of high speed AFMs. Thanks to the advances in precision engineering and fabrication technologies, the high speed AFMs are fast enough, for example, to capture video-rate information from biological processes [3]. However, further increase of the imaging speed, for example, to cover larger areas and capture faster processes requires substantial improvements of the bandwidth of the cantilever and stability of the closed loop system. To meet these requirements, researcher have suggested to use low-quality factor cantilevers in high-speed AFMs which has the disadvantage of increasing the TSI forces [8, 9]. In this research we aim to understand the main phenomena that are limiting a high-speed AFM from a cantilever-controller coupling point of view.

The requirements for the AFM as a topography measurement tool are twofold: 1) performing a precise and fast raster scanning in x - y direction, 2) accurate and fast measurement of the local height (h) of the sample in the Z direction. The latter also deter-

mines the maximum speed allowed for the raster scanning i.e., scanning too fast without performing an accurate Z measurement can cause crash or surface loss[10–12]. Fortunately, linear (or weakly nonlinear) parts such as actuators, sensors, filters, and the Proportional-Integral (PI) controller do have a cut-off frequency or relaxation time which determines their speed. However, for the strongly nonlinear dynamics of the cantilever interacting with the surface, determining such a limit-frequency is an elusive problem. For example, it is well-known that imaging with excessively high scanning speeds can cause imaging artifacts, parachuting effect, surface loss,[11] and damage[12]. Yet, the speed limit for which the coupled cantilever-controller combination can precisely follow the surface profile is not well-understood.

Another major concern in AFM which is not extraneous to the speed limit is its closed-loop stability. Due to the coexistence of strongly nonlinear attractive and repulsive Tip-Sample Interaction (TSI) forces, the AFM cantilever exhibits a complex behavior which includes bi-stability and chaos[13]. In this context, Garcia and San Paulo have presented a comprehensive study which demonstrates the coexistence of two stable regimes at the same time using basin of attractors and experimental results[14]. Also, researchers have reported the presence of chaos in AFM as a result of attractive nonlinear van der Waals forces [15, 16], or excessive adhesion[17]. This bistability or chaotic behavior indeed causes some artifacts and imaging problems, but it can be eliminated by minimizing the relative effects of the attractive or adhesive forces. One can use stiffer cantilevers, higher material [9] or environmental damping[8], or set a higher free air amplitude (the amplitude of the cantilever far from the sample surface) so that the elastic and repulsive part of the forces become more dominant than the attractive parts. It is also possible to increase the stiffness and damping ratio virtually using a so-called Q-control technique so that the chaotic behavior is eliminated. For example, Ashhab *et al.*[18] analyzed the dynamics of the cantilever using Melnikov's method to detect the presence of weak chaos and suggested to use a feedback loop to change the damping ratio. It should be noted that in previous studies[15–17], the presence of chaos was realized by studying solely the dynamics of the cantilever without addressing the coupled controller-cantilever dynamics. However, we will demonstrate that even if there is no chaotic behavior triggered by the cantilever per se, the controller itself can make the system chaotic, if high gains are applied to achieve fast scanning.

From a control engineering perspective, the cantilever is a part of the Z-stage control unit which ultimately performs a local distance measurement. In steady state situations, and when the repulsive forces are more dominant, the vibration amplitude of the cantilever is approximately equal to the distance between the cantilever and the surface of the sample. Thus, the approximate distance is directly measured via the amplitude signal, if the OBD is calibrated. To retain a constant distance between the cantilever and the surface, a control engineer would intuitively increase the controller gains to force the AFM head to follow the surface faster. However, in practice, this is not possible. From experimental observations, it is well-known that there exists an upper bound for the control gains of the system. For higher gains, the amplitude, phase, and the height signals vaguely fluctuate and never reach a steady state response. Consequently, it becomes impossible to capture a relevant image of the sample surface.

In this chapter, we investigate the nature of the aforementioned upper bound via

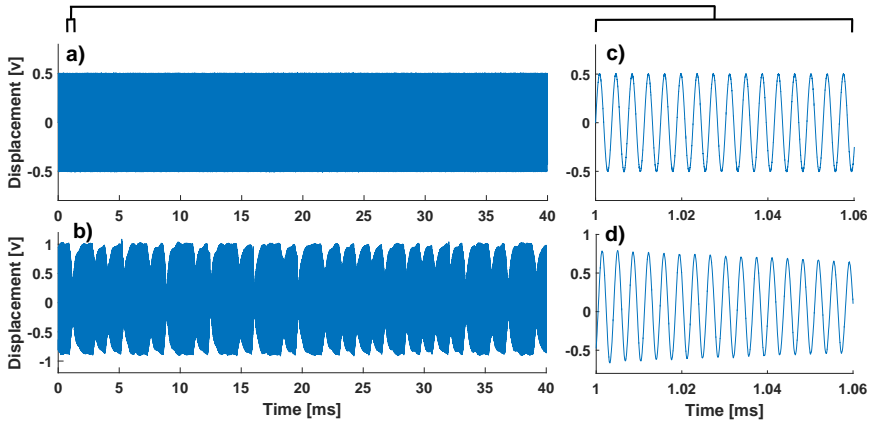


Figure 5.2: Measured motion of the cantilever while engaged with the sample surface. a) stable with low control gains, b) aperiodic with high control gains. c) and d) show a zoomed version of a) and b), respectively.

5

a new mathematical model based on an averaging method. The use of the averaging method was essential to incorporate multiple time scales of the AFM dynamics, and also to make the averaged TSI force differentiable for the stability analysis. The results show that the vague fluctuations of the amplitude that appear in the experiments are a result of deterministic chaos. The fact that high-speed (high-gain) controllers induce chaos confirms that the imaging speed of the AFM with the conventional architecture is strictly limited. The presence of chaos in the closed-loop system has been confirmed via the bifurcation diagram, Poincaré sections and Lyapunov exponents.

5.2. EXPERIMENTAL OBSERVATIONS

All the experiments in this section have been performed with a commercial Bruker FastScan AFM with a relatively low-frequency but relatively stiff cantilever (resonance frequency 60 kHz, Q factor 300 and a spring constant of 1 N/m). All other components of the AFM system are much faster than the cantilever, and consequently, their dynamics can be ignored. To avoid possible chaotic behavior due to attractive or adhesive TSI forces, their relative effects are minimized by choosing a relatively high vibration amplitude, besides having a stiff cantilever (free air amplitude of 150 nm and amplitude ratio 70 %).

To demonstrate the effect of control gains, the cantilever was approached to the surface with integral gain $k_i = 1$, and proportional gain $k_p = 5$. Moreover, the scan size was set to zero so that a single point on the sample surface is involved. In a second experiment, the integral gain was increased to 5 times its previous value, without changing the x-y position or any other setting. Fig. 5.2 compares the two cases. For the low control gain (Fig. 5.2.a and c) the probe is engaged with the surface and is vibrating harmonically. However, for the high control gain, (Fig. 5.2.b and d) the amplitude of the vibration is fluctuating in a non-periodic manner.

To show the effect of integral gain on imaging performance, Fig. 5.3 depicts the height image of a silicon dioxide on silicon grating captured with the low and high integral

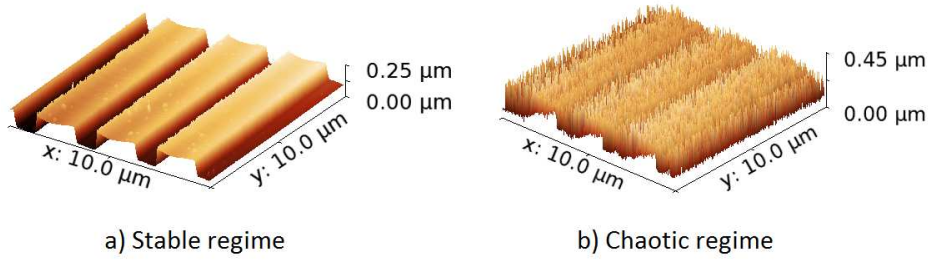


Figure 5.3: AFM imaging results of a silicon dioxide on silicon grating sample in two situations. a) stable with low control gains, b) unstable with high control gains.

gains.

It can be observed that the image obtained with the higher control gain is unstable due to the aperiodic motion seen in Fig. 5.2.b. Hence, one can conclude that increasing the measurement bandwidth in Z direction by increasing the control gains is not feasible. The nature of this aperiodic motion will be determined in the next section.

5.3. MATHEMATICAL MODELLING

In this section we try to understand the chaotic behavior of the closed-loop AFM system. Therefore, the controller and the cantilever have to be modeled as a coupled system. The coupled system, however, involves two different time scales. A fast time scale for tracking the motion of the cantilever and the tip-sample interactions, and slow time scale associated with the controller, the amplitude, and the phase signals. In TM-AFM, the cantilever vibrates with a frequency closed to its resonance frequency, and experiences the fast time scale TSI forces. However, within that time scale, no noticeable change in the state of the controller happens. That is, the controller is not affected by the instantaneous motion of the cantilever, but only by the envelope of the motion of the cantilever, which by definition is order(s) of magnitude slower than the cantilever itself. In practice, the Lock-In Amplifier (LIA), separates these two time scales by demodulating the motion signal to its amplitude and phase [19]. The details of the LIA are not within the scope of this thesis, however, it is important to note that there does not exist any transfer function or any linear approximation for the LIA. Hence, to incorporate the functionality of LIA in the closed-loop model, one should either solve the nonlinear equations in time domain, or alternatively, derive a demodulated model. The extreme nonlinearity of the LIA also makes it impossible to conduct a frequency domain stability analysis, such as those based on Nyquist or Nichols diagrams.

Although, it is theoretically possible to model the AFM system without the separation of time scales, and including all the nonlinearities and vibration modes of the cantilever [20, 21], such a model would be complex and computationally inefficient. Considering that the LIA only measures the amplitude and phase of a single harmonic component of the signal, the higher modes of the cantilever are not visible to the LIA, and consequently, do not affect the closed-loop dynamics. Alternatively, we use a single degree-of-freedom (DOF) model of the AFM cantilever and derive a demodulated model for the closed-loop

system which already incorporates the functionality of the LIA. Also, since the chaotic behavior studied in this chapter is independent of the attractive or adhesive forces, we limit the TSI force model to the Hertzian contact force. Similar multiple time scale problems have been solved with different techniques in the literature [22, 23], however, in AFM research, the slow dynamic models are limited to virial theory [24], and the periodic averaging method [25]. The periodic averaging method eliminates the short time scale from the dynamics of the system by applying a Fourier operator to the governing differential equation. However, in previously reported models [24, 25] the second-order derivatives of the amplitude and phase have been ignored which degrades the accuracy of the transient analysis.

A non-dimensional single-DOF model of the cantilever can be formulated as:

$$\ddot{z} + \xi \dot{z} + z = F_d \cos(\omega t) + F_{ts}, \quad (5.1a)$$

$$F_{ts} = -\beta(z-h)_{H_0}^{3/2}, \quad (5.1b)$$

where z denotes the nondimensional deflection of the cantilever and h is the nondimensional distance between the tip and the sample at the zero deflection configuration, both are normalized with respect to the free air amplitude. In Eq(5.1a) the dot denotes differentiation with respect to dimensionless time which is defined by normalizing the time with respect to the inverse of the eigenfrequency of the resonator. In addition, ξ is the damping ratio, ω is the normalized excitation frequency, which is also normalized with respect to the resonance frequency of the cantilever ($\omega \approx 1$ for TM-AFM). F_d is the dimensionless force equivalent to the acoustic excitation from the dither piezoelectric actuator, and β represents the Hertzian stiffness of the contact area between the tip and the sample. The subscript H_0 represents a Heaviside function used to model the discontinuity due to indentation.

Eq(5.1) can be cast into the state space representation as follows:

$$\begin{cases} \dot{q}_1 \\ \dot{q}_2 \end{cases} = \begin{cases} -\xi q_1 - q_2 - \beta(q_2 - h)_{H_0}^{3/2} + F_d \cos(\omega t) \\ q_1 \end{cases}, \quad (5.2)$$

where $q_1 = \dot{z}$ and $q_2 = z$. To separate the short and long time scales and incorporate the functionality of the LIA, we assume that the state variables in Eq(5.2) are amplitude modulated harmonic signals as:

$$q_1 = \Re(\bar{q}_1 e^{j\omega t}) = \Re((x_1 + jx_2)e^{j\omega t}), \quad (5.3a)$$

$$q_2 = \Re(\bar{q}_2 e^{j\omega t}) = \Re((x_3 + jx_4)e^{j\omega t}), \quad (5.3b)$$

in which the \bar{q}_i ($i = 1, 2$) represents the amplitude and phase of q_i in polar coordinates and x_k ($k = 1, \dots, 4$) are the Cartesian representations of \bar{q}_i , \Re is the real operator and $j^2 = -1$.

Substituting Eq(5.3) in (5.2), taking the derivatives and rearranging for \bar{q} yields:

$$\begin{cases} \dot{\bar{q}}_1 \\ \dot{\bar{q}}_2 \end{cases} e^{j\omega t} = \begin{cases} -j\omega \bar{q}_1 e^{j\omega t} - \xi \bar{q}_1 e^{j\omega t} - \bar{q}_2 e^{j\omega t} - \beta(\bar{q}_2 e^{j\omega t} - h)_{H_0}^{3/2} + F_d \cos(\omega t) \\ -j\omega \bar{q}_2 e^{j\omega t} + \bar{q}_1 e^{j\omega t} \end{cases}. \quad (5.4)$$

Applying the periodic averaging method to Eq(5.4), which is, multiplying by $e^{-j\omega t}$ and integrating over a period ($\langle \dots \rangle = \int_{t_0}^{t_0 + \frac{2\pi}{\omega}} \dots e^{-j\omega t} dt$), gives the demodulated governing differential equations for the cantilever as:

$$\begin{cases} \bar{\dot{q}}_1 \\ \bar{\dot{q}}_2 \end{cases} = \begin{cases} -j\omega \bar{q}_1 - \xi \bar{q}_1 - \bar{q}_2 + \langle F_{ts} \rangle + F_d \\ -j\omega \bar{q}_2 + \bar{q}_1 \end{cases}, \quad (5.5)$$

in which the $\langle F_{ts} \rangle = -\int_{t_0}^{t_0 + \frac{2\pi}{\omega}} \beta(\bar{q}_2 e^{j\omega t} - h)_{H_0}^{3/2} e^{-j\omega t} dt$, is the first Fourier component of the TSI force that can be calculated as:

$$\langle F_{ts} \rangle = \beta \sqrt{AI} \left(\frac{h}{A}\right) \bar{q}_2, \quad (5.6)$$

where

$$I(\zeta) = \int_0^{2\pi} (\cos(\tau) - \zeta)_{H_0}^{3/2} \cos(\tau) d\tau. \quad (5.7)$$

$A = |\bar{q}_2| = \sqrt{x_3^2 + x_4^2}$ is the amplitude of the cantilever, and ζ and τ are dummy variables. The integral function $I(\zeta)$ can be calculated separately which eliminates the need for tracking the short time scale. In this manner, instead of the TSI force which had to be tracked in the short time scale, only the periodic average (i.e., the first Fourier component) of the TSI force is considered, that instead varies slowly in time.

In this model, it is assumed that every other component of the AFM, such as actuators and electronics are infinitely faster than the cantilever. Thus, here we only couple an ideal PI controller to the modulated model of the cantilever given by Eq(5.5). As such, an additional state variable is introduced which relates the amplitude error ($A_{set} - A$), to the height signal h , with the integral and proportional actions as follows:

$$\dot{x}_5 = k_i (A_{set} - A), \quad (5.8a)$$

$$h = x_5 + k_p (A_{set} - A), \quad (5.8b)$$

where A_{set} is the set-point amplitude. In Eq(5.8), the integrator accumulates the error in the internal state of the controller (x_5) and the output of the controller is a weighted sum of the instantaneous error (with proportional gain k_p) and the accumulated error (with the integral gain k_i). Expanding the real and imaginary parts of Eq(5.4), the closed-loop model of the AFM can be written as:

$$\begin{aligned} \dot{x}_1 &= -\xi x_1 + \omega x_2 - x_3 - \beta \sqrt{x_3^2 + x_4^2} I_1 \left(\frac{k_p (A_{set} - \sqrt{x_3^2 + x_4^2}) + x_5}{\sqrt{x_3^2 + x_4^2}} \right) x_3 + f_d \\ \dot{x}_2 &= -x_1 \omega - \xi x_2 - x_4 - \beta \sqrt{x_3^2 + x_4^2} I_1 \left(\frac{k_p (A_{set} - \sqrt{x_3^2 + x_4^2}) + x_5}{\sqrt{x_3^2 + x_4^2}} \right) x_4 \\ \dot{x}_3 &= x_1 + \omega x_4 \\ \dot{x}_4 &= x_2 - \omega x_3 \\ \dot{x}_5 &= k_i (A_{set} - \sqrt{x_3^2 + x_4^2}). \end{aligned} \quad (5.9)$$

Eq(5.9) shows a dynamic relationship between amplitude, phase and height signals in frames of the Cartesian coordinates, which evolve with the slow time scale. In the next section, we shall use this model to simulate different TM-AFM scenarios and detect the nonperiodic behavior observed experimentally in Section 5.2.

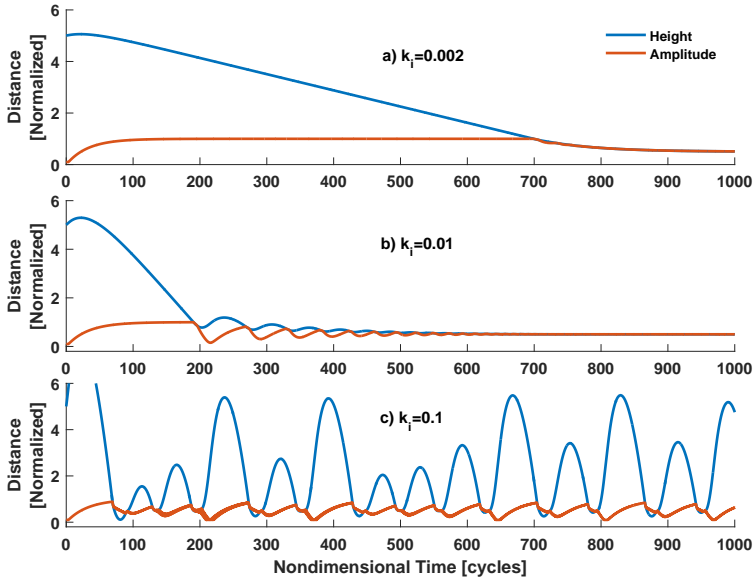


Figure 5.4: Simulated approach process with three different integral gains.

5.4. CLOSED-LOOP RESPONSE OF AFM

Many parameters ranging from deflection sensitivity of the cantilever to linearity and static gain of voltage amplifiers play a role in the total performance of the system. However, it is outside the scope of this thesis to quantitatively determine the maximum stable PI gains. Thus, we limit ourselves to a qualitative demonstration of the chaos in the coupled system, and ignore the dynamics of actuators and also dismiss the static gains and sensitivities of the system.

Fig. 5.4 shows the amplitude and height signals during an approach scenario for three different integral gain settings. In this scenario the dither piezo actuator and the controller turn on at time zero. For all three cases, the proportional gain is set to $k_p = 0.01$, the initial distance between the probe and the sample is 5 times the free air amplitude and the set-point amplitude is 0.5 times the free air amplitude. All numerical results refer to a cantilever with quality factor 100, is excited at its resonance frequency ($\omega = 1$), and the non-dimensional Hertzian modulus of the tip-sample contact is taken as $\beta = 2000$. These parameters roughly correspond to the realistic imaging conditions.

For all three cases, initially, the amplitude is less than the set-point, and the height signal increases to above 5 units. Then, as soon as the amplitude reaches its set point value, the controller starts to reduce the height. The height reduction continues until the amplitude has decreased to its set-point. In Fig. 5.4.b, the integral gain has been increased to $k_i = 0.01$. In this case, the cantilever reaches the surface faster than in Fig. 5.4.a, thus surface loss effects such as the parachuting effect [11] has been reduced. However, the amplitude and height signals fluctuate for a longer time. Fig. 5.4.c shows

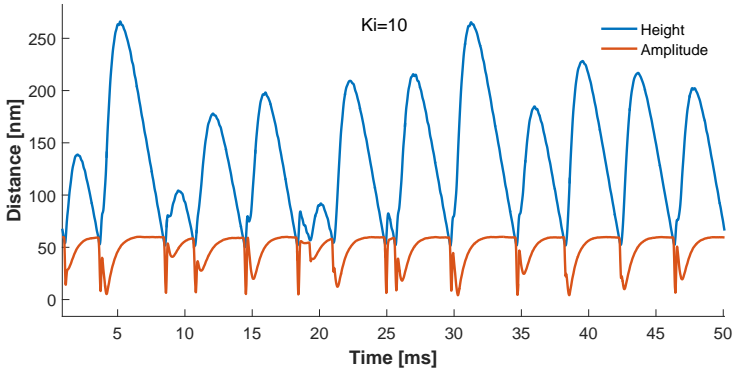


Figure 5.5: Measured amplitude and phase of the TM-AFM with high control gain ($K_i=10$)

the same scenario with an even higher controller gain ($k_i = 0.1$). Fig. 5.5 shows an experimental counterpart of Fig. 5.4.c, measured using a commercially available AFM (Bruker FastScan) and a standard tapping mode cantilever (MPP 22120). The spring constant, resonance frequency and the Quality factor of the cantilever were measured using the thermal calibration technique as 0.65 n/m , 49.01 kHz , and 180, respectively. The excitation frequency was chosen such that the free air amplitude is 5% less than the maximum amplitude, (default for AFM). The free air amplitude was set to 80 nm and the setpoint amplitude was set to 50 nm . An AFM training sample (Fused Silica) was used as the substrate, and the scanning range was set to zero to avoid any sample related deterioration as much as possible. As it can be seen, both the numerical and experimental results suggest that for high control gains, the amplitude and height signals drop and increases in a nonpredictable manner which potentially could be due to chaos.

5.5. CHAOS

In this section, the nonlinear dynamics of the system described by Eq(5.9) will be examined to confirm that the unusual response observed experimentally is indeed deterministic chaos. In order to identify the peculiar characteristics of chaos, first a bifurcation diagram of the system is obtained to study the effect of the integral gain on the behavior of the system. Next, the response of the system in the phase space will be studied which shows the attractors of the system corresponding to the different regions of the bifurcation diagram. As another indication of chaos, the non-periodicity of the response is studied using frequency spectrum and Poincaré sections. Finally, the sensitivity to initial conditions is demonstrated via time histories and Lyapunov exponents.

As mentioned earlier, many parameters can affect the response of the system, yet, here we restrict ourselves to the effects of the integral gain of the controller because of its direct relation to the bandwidth of the closed-loop system. Fig. 5.6 shows the bifurcations of the amplitude in the engaged configuration when the integral gain is increased. For small integral gains, there exists only one amplitude value (equal to the set-point amplitude) to which the system will eventually settle. Increasing the integral gain fur-

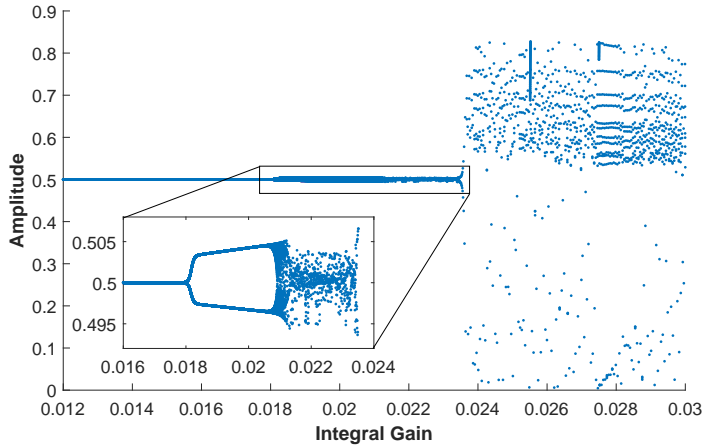


Figure 5.6: Bifurcation diagram of the TM-AFM, the steady state amplitude versus the integral gain

ther, there is a region ($k_i = 0.018 - 0.02$) where two values for the amplitude coexist. This part of the bifurcation diagram implies a periodic fluctuation of the amplitude between the two values. In practice this area is still moderately tolerable for imaging applications. This is because the two amplitudes are close to one another, thus the fluctuation between the two does not induce a considerable error signal for the controller. However, increasing the integral gain further, clouds of points are seen in the bifurcation diagram ($k_i > 0.024$) representing a chaotic motion.

To experimentally determine the upper limit of the integral gain, and verify the presence of bifurcation and chaos presented in Fig. 5.6, we repeated the same experiment as used for Fig. 5.5, but with control gains ranging between 1 and 25. For all of the experiments the proportional gain was 1. To plot the bifurcation diagram in Fig. 5.7, the amplitude values were measured on a hypersurface in state space on which the phase value is equal to its steady-state value (where $k_i = 1$). As it can be seen, for intermediate integral gains ($k_i = 2.5 - 6.5$), two values for the amplitude signal coexist, whereas, for higher control gains, a cluster of randomly distributed points were measured which indicates $k_i = 6.5$ as the upper limit of the control gain. Note that this limit is measured for the specific cantilever and experimental conditions, and does not provide a universal value by any means. Since different physical parameters of the system affect its stability (not only the integral gain), a more thorough investigation should be conducted to identify the chaotic and non-chaotic set of parameters.

Here, it should be noted that the theoretical results in Section 5.4 are achieved with a completely deterministic model, even though the cluster of points in Fig. 5.6 indicate a random-like response. In order to show the deterministic nature of the irregular fluctuations in Fig. 5.4.c, and Fig. 5.6 the geometry of the attractors of the system has to be studied in the phase space. Fig. 5.8 shows the projection of the attractors onto the x_3, x_4, x_5 space for three different integral gains within each of the sections of Fig. 5.6. As it can be seen in Fig. 5.8.a, when the integral gain is small (e.g., $k_i = 0.015$) the steady-state re-

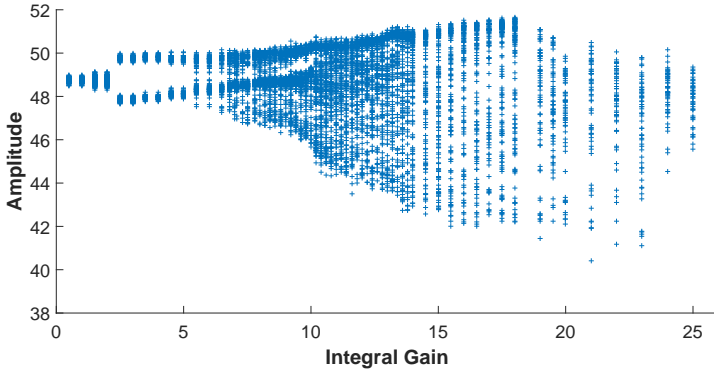


Figure 5.7: Experimental bifurcation diagram of the TM-AFM, the amplitude versus integral gain.

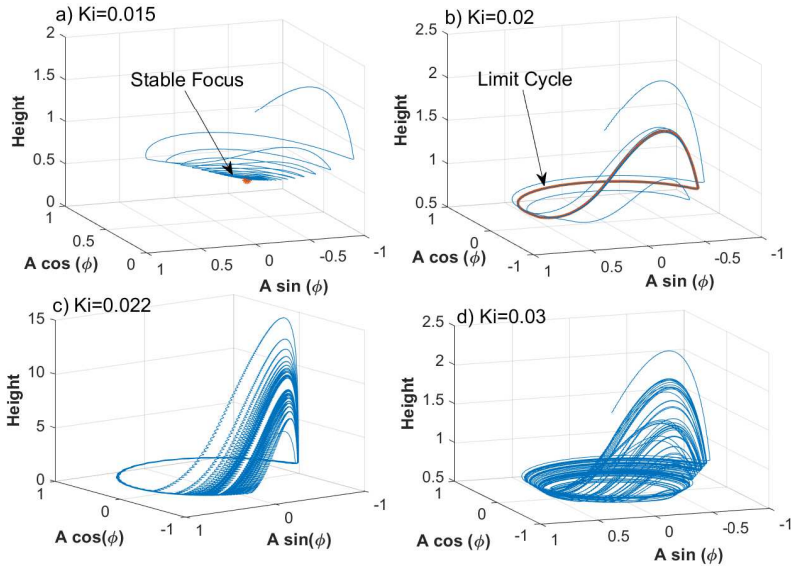


Figure 5.8: A projection of the attractors of the TM-AFM on amplitude, phase and height space. a) stable focus, b) stable limit cycle, c) and d) strange attractor. All the values are normalized with respect to the free air amplitude.

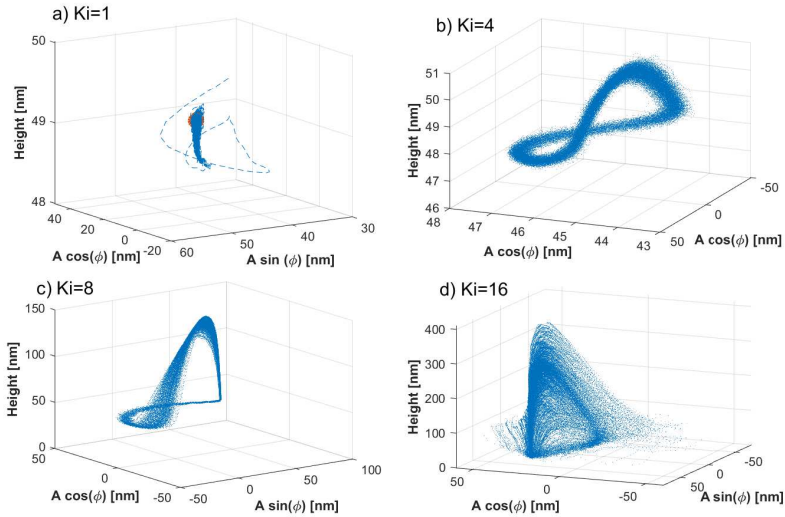


Figure 5.9: Measured projection of the attractors of the TM-AFM on amplitude, phase and height space. a) stable focus, b) stable limit cycle, c) and d) strange attractors.

sponse of the system approaches a stable focus (the orange point in Fig. 5.8.a) which has the amplitude equal to the set-point amplitude and corresponding phase and height. For the second case ($k_i = 0.02$), as the effects of the initial conditions vanish, the states of the system gradually approach a limit cycle, shown in orange in Fig. 5.8.b, and remain on that closed-loop. However, for a slightly higher value of the integral gain ($k_i = 0.022$), the limit cycle is non-existent, and the system never repeats itself. This non-existence of a steady-state response in Fig. 5.8.c and d is associated with the strange attractor, which is an indication of chaos. Fig. 5.9 shows the experimental counterpart of Fig. 5.8, in which similar behavior for all the four regimes is visible.

To further investigate the behavior of the system in the chaotic regime, we present a Poincaré section of the state space considering two different Poincaré surfaces. Fig. 5.10.a shows the Poincaré section of the system on a constant-height surface and it shows the amplitude and the phase with which the cantilever leaves the surface every time that it disengages. Fig. 5.10.b shows the amplitude and height while the phase reaches its expected value for the steady state case. The cluster of individual points in Fig. 5.10.a and b denote the complexity of the strange attractors.

The complexity of the chaotic motion in frequency domain translates to a wide spectrum of frequency components that resemble the frequency spectrum of noise. Fig. 5.11 shows the Discrete Fourier Transform (DFT) of all five state variables of the system. As it can be seen, the attractor of the system contains a wide band of frequency components. The absence of clearly distinct peaks in the DFT (Fig. 5.11) indicates that the signal is not periodic.

Perhaps the most important characteristic of a chaotic system is its sensitivity to initial conditions. The long-term response of a chaotic system is extremely sensitive to the

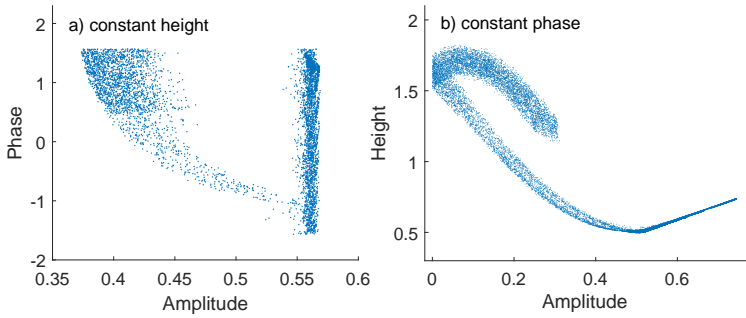


Figure 5.10: Poincaré sections of the closed-loop TM-AFM on the hyper-surfaces perpendicular to a) constant height, b) constant phase

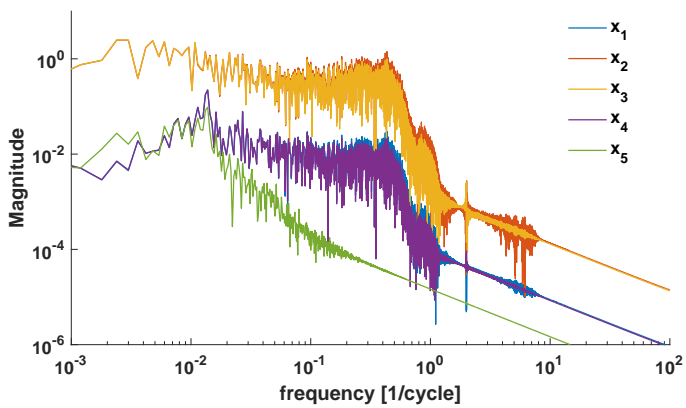


Figure 5.11: Fourier transform of the states of closed-loop AFM in chaotic situations.

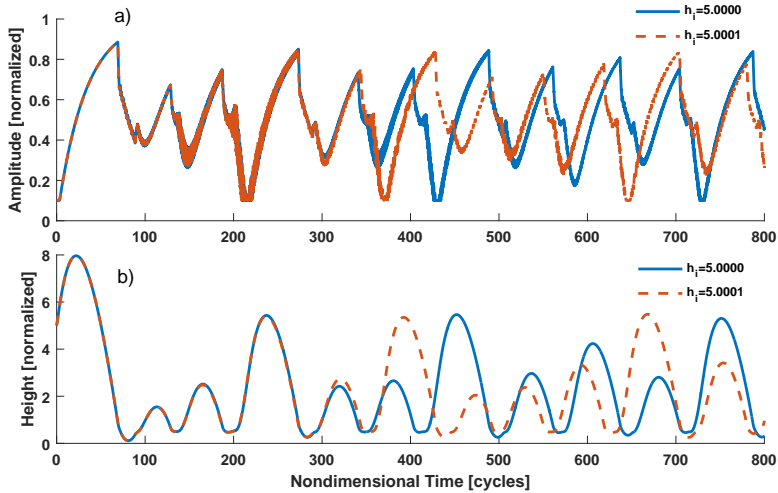


Figure 5.12: Simulated approach process with high controller gains for two different but similar initial conditions. a) amplitude, b) height.

changes in initial conditions, meaning that two trajectories with very similar initial conditions might end up in very different final configurations [26]. One simple test of initial condition dependency for TM-AFM is shown in Fig. 5.12. The same approach curve in Fig. 5.4.c is simulated with two different but close initial heights ($h(0) = 5.0000$ and $h(0) = 5.0001$). As it can be seen in Fig. 5.12, the two trajectories are almost identical at the beginning. However, after about 300 vibration cycles they start to deviate from each other.

A very important and solid indicator of sensitivity to initial conditions in dynamics systems is the Lyapunov exponents of the attractor of the system [27, 28]. Lyapunov exponents of dynamic systems show the average rate of exponential divergence of any two trajectories along their attractors. To determine the Lyapunov exponents for the closed-loop TM-AFM system, we adopt the method of QR decomposition presented by Geist *et al.* [29] Fig. 5.13 demonstrates these Lyapunov exponents for two different cases of low and high integral gains. As it can be seen in Fig. 5.13.a, for the case of low control gains, all the Lyapunov exponents of the system converge to a negative value which refers to the asymptotically stable attractor (the set-point). However, for the case with high control gains (Fig. 5.13.b), the largest Lyapunov exponent is positive, which shows that any small deviation from the attractor will exponentially grow in the state-space. The summation and all the other Lyapunov exponents (except the highest one) are negative which show that the system does not experience hyper-chaos, or a global instability.

5.6. CONCLUSIONS

Experimental results with tapping mode AFM show that it is not possible to image with control gains higher than a certain amount. Such a limit in the control gains restricts

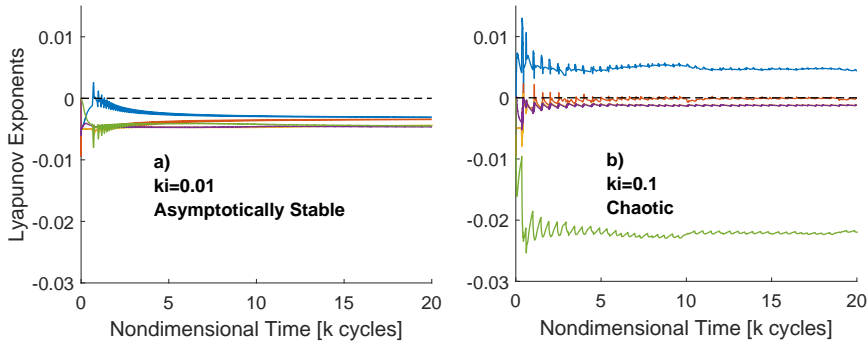


Figure 5.13: Lyapunov exponents of the closed-loop TM-AFM in case (each color shows one Lyapunov exponent). a) the control gains are low and the system is stable, b) The control gains are high and the system is chaotic.

the imaging speed of the AFM. To investigate the origin of this limit, a new nonlinear dynamics model for AFM was presented using an averaging method in Cartesian coordinates. The model incorporates the coupled dynamics of the cantilever and the controller and demonstrates that tapping mode AFM will exhibit a chaotic behavior with high controller gains. The corresponding attractors, Poincaré sections and Lyapunov exponents formally confirmed the presence of chaos in TM-AFM. Unlike the previously presented routes to chaos in AFM, the presented route of chaos does not depend on the attractive or adhesive tip-sample forces and limits the speed of TM-AFM, even when the controller and the actuators are selected ideally in terms of bandwidth. This phenomenon should be taken into account in the design of high-speed AFM and to avoid it, either the cantilever dynamics or the architecture of the closed-loop system should be modified.

REFERENCES

- [1] H. Sadeghian, R. Herfst, J. Winters, W. Crowcombe, G. Kramer, T. van den Dool, and M. H. van Es, *Development of a detachable high speed miniature scanning probe microscope for large area substrates inspection*, [Review of Scientific Instruments](#) **86**, 113706 (2015).
- [2] A. Fleming, B. Kenton, and K. K. Leang, *Bridging the gap between conventional and video-speed scanning probe microscopes*, [Ultramicroscopy](#) **110**, 1205 (2010).
- [3] T. Ando, T. Uchihashi, and T. Fukuma, *High-speed atomic force microscopy for nano-visualization of dynamic biomolecular processes*, [Progress in Surface Science](#) **83**, 337 (2008).
- [4] Y. Wang, X. Hu, L. Xu, and X. Hu, *Improving the scanning speed of atomic force microscopy at the scanning range of several tens of micrometers*, [Ultramicroscopy](#) **124**, 102 (2013).

- [5] G. Schitter, *Improving the speed of afm by mechatronic design and modern control method, geschwindigkeitsverbesserung beim afm mittels mechatronischem design und modernen regelmethode*, *Technisches Messen Plattform für Methoden, Systeme und Anwendungen der Messtechnik* **76**, 266 (2009).
- [6] H. Sadeghian, R. Herfst, B. Dekker, J. Winters, T. Bijlagte, and R. Rijnbeek, *High-throughput atomic force microscopes operating in parallel*, *Review of Scientific Instruments* **88**, 033703 (2017).
- [7] R. Herfst, B. Dekker, G. Witvoet, W. Crowcombe, D. de Lange, and H. Sadeghian, *A miniaturized, high frequency mechanical scanner for high speed atomic force microscope using suspension on dynamically determined points*, *Review of Scientific Instruments* **86**, 113703 (2015).
- [8] M. H. van Es and H. Sadeghian, *Euv blank defect and particle inspection with high-throughput immersion afm with 1nm 3d resolution*, in *SPIE Advanced Lithography* (International Society for Optics and Photonics, 2016) p. 97782Z.
- [9] J. D. Adams, B. W. Erickson, J. Grossenbacher, J. Brugger, A. Nievergelt, and G. E. Fantner, *Harnessing the damping properties of materials for high-speed atomic force microscopy*, *Nature nanotechnology* **11**, 147 (2016).
- [10] H. Sadeghian, T. C. van den Dool, Y. Uziel, and R. B. Or, *High-speed afm for 1x node metrology and inspection: Does it damage the features?* in *SPIE Advanced Lithography* (International Society for Optics and Photonics, 2015) p. 94240Q.
- [11] T. De, P. Agarwal, D. R. Sahoo, and M. V. Salapaka, *Real-time detection of probe loss in atomic force microscopy*, *Applied physics letters* **89**, 133119 (2006).
- [12] A. Keyvani, H. Sadeghian, H. Goosen, and F. van Keulen, *Transient tip-sample interactions in high-speed afm imaging of 3d nano structures*, in *SPIE Advanced Lithography* (International Society for Optics and Photonics, 2015) p. 94242Q.
- [13] R. W. Stark, *Bistability, higher harmonics, and chaos in afm*, *Materials Today* **13**, 24 (2010).
- [14] R. Garcia and A. San Paulo, *Dynamics of a vibrating tip near or in intermittent contact with a surface*, *Physical Review B* **61**, R13381 (2000).
- [15] J. H. Cantrell and S. A. Cantrell, *Bifurcation, chaos, and scan instability in dynamic atomic force microscopy*, *Journal of Applied Physics* **119**, 125308 (2016).
- [16] S. Hu and A. Raman, *Chaos in atomic force microscopy*, *Physical Review Letters* **96**, 036107 (2006).
- [17] F. Jamitzky, M. Stark, W. Bunk, W. Heckl, and R. Stark, *Chaos in dynamic atomic force microscopy*, *Nanotechnology* **17**, S213 (2006).
- [18] M. Ashhab, M. Salapaka, M. Dahleh, and I. Mezić, *Melnikov-based dynamical analysis of microcantilevers in scanning probe microscopy*, *Nonlinear Dynamics* **20**, 197 (1999).

- [19] A. V. Oppenheim, A. S. Willsky, and S. H. Nawab, *Signals and Systems (second edition)* (Prentice-Hall, Inc., Upper Saddle River, NJ, USA, 1996).
- [20] R. W. Stark, G. Schitter, M. Stark, R. Guckenberger, and A. Stemmer, *State-space model of freely vibrating and surface-coupled cantilever dynamics in atomic force microscopy*, *Physical Review B* **69**, 085412 (2004).
- [21] H.-J. Butt, B. Cappella, and M. Kappell, *Force measurements with the atomic force microscope: Technique, interpretation and applications*, *Surface science reports* **59**, 1 (2005).
- [22] C. Kuehn, *Multiple time scale dynamics*, Vol. 191 (Springer, 2015).
- [23] J. A. Sanders, F. Verhulst, and J. Murdock, *Averaging Methods in Nonlinear Dynamical Systems* (Springer-Verlag New York, 2007).
- [24] A. San Paulo and R. García, *Tip-surface forces, amplitude, and energy dissipation in amplitude-modulation (tapping mode) force microscopy*, *Physical Review B* **64**, 193411 (2001).
- [25] S. Hu, *Nonlinear dynamics and force spectroscopy in dynamic atomic force microscopy* (PhD thesis, Purdue University, 2007).
- [26] E. N. Lorenz, *Deterministic nonperiodic flow*, *Journal of the atmospheric sciences* **20**, 130 (1963).
- [27] F. C. Moon, *Chaotic and Fractal Dynamics: Introduction for Applied Scientists and Engineers* (John Wiley & Sons, 2008).
- [28] S. H. Strogatz, *Nonlinear dynamics and chaos: with applications to physics, biology, chemistry, and engineering* (Westview press, 2014).
- [29] K. Geist, U. Parlitz, and W. Lauterborn, *Comparison of different methods for computing lyapunov exponents*, *Progress of Theoretical Physics* **83**, 875 (1990).

6

CONTROL OF TAPPING MODE ATOMIC FORCE MICROSCOPY WITH ESTIMATED AVERAGE FORCES

It has been shown that the operation speed of Tapping Mode Atomic Force Microscopy (TM-AFM) in current architectures is limited by chaotic behavior. In this chapter, we demonstrate numerically that this limitation may be overcome by adding a linear observer to the AFM control loop. For this, we use a Dual Kalman filter to estimate the periodic average of the Tip-Sample Interaction (TSI) force and keep the average force constant instead of the amplitude signal. As compared to conventional TM-AFM, which uses only the amplitude signal to control the distance between the cantilever and the sample, the proposed architecture uses both the amplitude and phase and also their dynamic trajectories. Consequently, the controller relies on a more correct and robust estimate of the sample topography at any time. Simulation results show that using the proposed filter in the control loop suppresses the emergence of chaos and increases the effective operating speed of AFM by order(s) of magnitude. The performance of the Kalman filter has been verified with experiments, however, the real-time closed loop implementation of the controller should be done in a future research.

6.1. INTRODUCTION

In Tapping Mode Atomic Force Microscopy (TM-AFM), a cantilever with a sharp tip oscillates above a sample surface such that the tip intermittently interacts with the surface of the sample. The motion of the cantilever, which is affected by the Tip-Sample Interaction (TSI) force is measured typically using an optical beam deflection setup and its amplitude is determined using a Lock-In Amplifier (LIA). The amplitude signal is provided to a feedback controller as a measure of distance so that it can be kept at a constant level. Adjusting the position of the cantilever (or the surface in sample-scanning systems), the controller attempts to keep the amplitude constant. A height profile of the

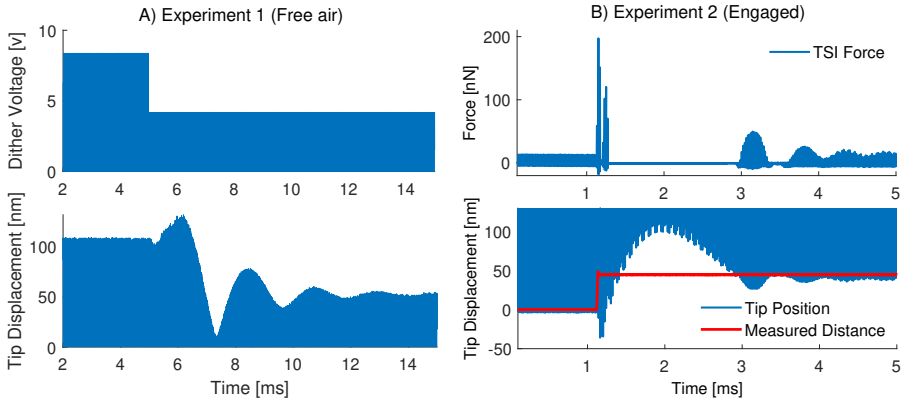


Figure 6.1: Non-minimum-phase behavior of AFM cantilever. A) Dither voltage and displacement of a (Bruker MPP-22100) cantilever far from the sample, i.e. free air condition. B) Measured TSI force, Cantilever-sample distance and the motion of the cantilever (Bruker MPP-33220) while engaged to the surface of a nano-mechanical force sensor. In both experiments, the amplitude of the motion of the cantilever shows a wrong direction initial response which is associated with Non-minimum-phase systems. Resonance frequency and the quality factor of the cantilevers in Experiment 1 and 2 are 44,4 kHz, 49.1 kHz, 400, and 295, respectively.

sample is measured through the control signal while the cantilever is scanned over the sample surface [1].

A major problem of AFM is its low speed and imaging throughput, particularly for industrial applications which demand high imaging speed and throughput[2]. The low imaging speed of AFM can be attributed to many of the components, such as the lateral scanner, z-stage actuator, cantilever, controller, as well as the electronic components. To enhance the speed of AFM, many researchers have studied, designed, and characterized high-bandwidth apparatus [3–7]. Advances in precision engineering and fabrication technologies have led to actuators and electronics that are fast enough not to limit the imaging speed[8], however, the cantilever itself, and its coupling with the controller have remained as the speed limiting elements. There exist ultra high frequency cantilevers [9] which can ease this problem up to a certain extent. However, the coupling of the cantilever and the controller is still a major challenge. It has been shown previously that closed-loop TM-AFM (the cantilever coupled with controller) exhibits a chaotic behavior above a certain bandwidth[10].

As the cantilever-controller coupling is the main limiting factor in increasing the scanning speed, this chapter is focused on design of a new controller.

In conventional TM-AFM, the motion of the cantilever does not contain enough information to calculate the TSI force, or the cantilever-sample distance. Hence, the amplitude signal is seemingly the only indication of the distance that can be used in the control loop. If the AFM operates in the repulsive regime, and the cantilever has reached its steady state, then the amplitude of the motion is almost equal to the distance. In fact, the error between the amplitude signal and the distance is negligible and a comparison between the two is used as a method for calibrating the deflection sensitivity of the cantilever. Hence, the difference between the amplitude signal and its set-point

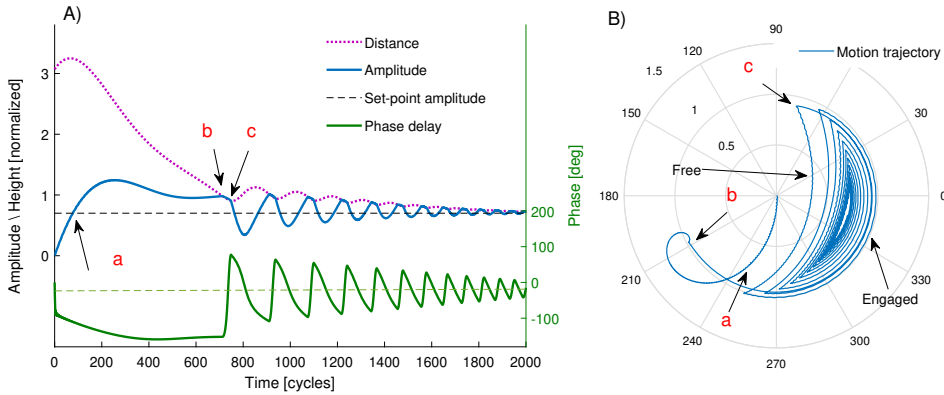


Figure 6.2: Simulated sample approach in TM-AFM. A) Time history of amplitude, distance and phase signal. B) Phase space representation of the amplitude and the phase. Points a, b and c show the first intersection of the amplitude signal with its setpoint, the first tip-sample contact, and the first disengagement, respectively. The wrong direction action of the controller, which stems from the amplitude drop shown in A, can be explained with the phase behavior in B.

value provides a good error signal for the controller. Although, this works well for low-speed TM-AFM, for high-speed AFM, where the transient behavior can not be ignored, the amplitude signal does not have a one-to-one relationship with the distance between the cantilever and the sample [11].

In fact, there is a dynamic relationship between the distance and the amplitude signal which, unfortunately, is Non-Minimum Phase (NMP). That is, the cantilever shows a wrong direction initial response for fast disturbances. For example, if the distance suddenly increases, the amplitude might first reduce and then increase instead of directly starting to increase, and *vice versa*.

To demonstrate the NMP behavior of the AFM cantilever, we performed two experiments. In the first experiment, the AFM cantilever is vibrating far from the sample, when suddenly we reduce the excitation force to half of its initial value. In the second experiment, the cantilever is engaged with the sample surface and is vibrating in a steady-state condition, where we suddenly bring the sample closer to the cantilever. The sample surface in the second experiment is a nanomechanical force sensor, which allows us to measure the TSI forces at the same time. More detailed explanation of the experimental setup for the second experiment can be found in [12, 13]. Fig. 6.1.A) and Fig. 6.1.B) show the results of the first and second experiments, respectively. In both cases, the amplitude of the motion of the cantilever shows a wrong-direction initial response which is associated with NMP systems in control theory.

This NMP behavior of the cantilever in the presence of the strong nonlinearity of the TSI force causes chaos in the closed-loop system, if the control gains are above a certain limit [10]. Such a limit on the control gains restricts the imaging speed of the AFM.

To explain the chaos caused by the NMP behavior, we present a simulation of the transient behavior of the closed-loop TM-AFM during the sample approach. Consider

that the cantilever is positioned three units of distance above the sample, and is not vibrating. At time zero, we start to excite the cantilever with an excitation force which would give a free amplitude of one unit of distance. At the same time, we turn on the PI controller which manipulates the distance to keep the measured amplitude equal to a desired set-point amplitude (taken as 0.7 units). Fig. 6.2.A shows the distance, amplitude, and phase delay of the cantilever in this simulation where the excitation frequency is 1.01 times the fundamental resonance frequency of the cantilever. Fig. 6.2.B shows the same curve in polar coordinates (phasor space). First, when the amplitude of the cantilever is below the set-point amplitude, the PI controller increases the distance between the cantilever and the surface. As soon as the amplitude signal becomes larger than the set-point amplitude (Point a in Fig. 6.2), the PI controller starts to decrease the distance. At a certain moment (Point b in Fig. 6.2) the distance becomes equal to the amplitude, and the cantilever engages the surface, i.e. taps on the surface in each cycle of vibration. During the short engaging period (from Point b to c in Fig. 6.2), the phase of the cantilever experiences a large change due to the TSI force, whereas, the change in the amplitude signal is minute. The circular arc in Fig. 6.2.B shows this process in phasor space. After disengaging the surface (Point c in Fig. 6.2), the cantilever follows its free path which includes first a reduction and then an increase in the amplitude (similar to NMP systems). The consequence of the reduction and increase of the amplitude after Point c in Fig. 6.2 is that the controller first increases and then decreases the distance. Considering that the final value for distance should be equal to the set-point amplitude, the controller is taking action in the wrong direction during the first half of the process. The magnitude of this wrong direction action is directly proportional to the control gains. Reducing the control gains reduces the speed of the AFM, and increasing the control gains increases the amount of the wrong action of the controller. In case the control gains are tuned to be higher than a certain threshold, this wrong-direction action is so large that the distance exceeds the initial distance, and the engage-disengage process does not converge to a stable focus point, but instead, leads the system to a chaotic trajectory [10]. From Fig. 6.2 it is evident that the phase signal also provides genuine information on the engage-disengage process, however, the controller is not using it. From Fig. 6.2 one can conclude that the amplitude signal alone does not provide the best error signal to the controller.

This chapter studies theoretically and numerically the possibility of breaking the speed limit of AFM by suppressing the emergence of chaos even when accompanied with high band-width controllers. To suppress chaotic behavior, we suggest defining a measure of error which is not NMP and can be calculated from the amplitude and the phase signals, so that the controller can keep the cantilever engaged. Ideally, one would try to keep the maximum TSI force constant, which would also guarantee a nondestructive imaging. However, it is impossible to measure or estimate the peak force [14]. In fact, it has been shown that only the First Fourier Component (hereafter, FFC) of the TSI force has a significant effect on the motion of the cantilever, and hence, can be reliably estimated [14]. Therefore, it would be a logical choice to construct an error signal from the FFC of the TSI force. An approximation of the FFC of the TSI force can be estimated in real time from amplitude and phase signals using a dual Kalman filter. In a similar approach, De *et al.* detected the contact loss in real time [15]. Here we first present a

method for real-time calculation of the FFC of the TSI force and then we shall use it in closed-loop AFM control.

6.2. REAL-TIME ESTIMATION OF THE TSI FORCE

To estimate the FFC of the TSI force in real time, we use the modulated dynamic model of the AFM cantilever which is presented in [11, 14]. In this model, the relationship between the FFC of TSI force and the transient response of the amplitude and the phase signal can be represented with the following non-dimensional state-space formulation:

$$\dot{\mathbf{q}} = A\mathbf{q} + B_1 f_d + B_2 \mathbf{f}_{ts}, \quad (6.1)$$

The capital letters are used for matrices, bold small letters for vectors, and normal small letters for scalars. In Eq(6.1),

$$A = \begin{bmatrix} -\xi & \omega & -1 & 0 \\ -\omega & -\xi & 0 & -1 \\ 1 & 0 & 0 & \omega \\ 0 & 1 & -\omega & 0 \end{bmatrix}, B_1 = \begin{bmatrix} 1 \\ 0 \\ 0 \\ 0 \end{bmatrix}, B_2 = \begin{bmatrix} 1 & 0 \\ 0 & 1 \\ 0 & 0 \\ 0 & 0 \end{bmatrix},$$

represent the process (A) and input (B_1, B_2) matrices of the system. $\mathbf{q} = [q_1, q_2, q_3, q_4]^T \in \mathbb{R}^{4 \times 1}$ represents a dynamic state vector of the demodulated system, $\xi, \omega, f_d \in \mathbb{R}$ are the damping ratio of the cantilever, normalized excitation frequency and the normalized driving force, respectively. $\mathbf{f}_{ts} = [\Re(f_{ts}^{(1)}), \Im(f_{ts}^{(1)})]^T \in \mathbb{R}^{2 \times 1}$ contains the real and imaginary parts of the FFC of the TSI force. The real part refers to the in-phase component with the driving force and the imaginary part is 90 degrees out-of-phase. A lock-in amplifier (digitally) calculates the amplitude (a) and the phase (φ) of the motion of the cantilever as

$$a = \sqrt{q_3^2 + q_4^2}, \quad (6.2a)$$

$$\varphi = \tan^{-1}\left(\frac{q_3}{q_4}\right), \quad (6.2b)$$

respectively. $q_3 = a \cos(\varphi)$ and $q_4 = a \sin(\varphi)$ are called the “in-phase (or x)” and “quadrature (y)” components in commercial LIAs. Eq(6.1) can be derived by taking a Fourier transform of equation of the motion of the cantilever.

Obviously, the TSI force, and hence also its FFC have a nonlinear relationship with the state variables, the cantilever-surface distance, and the mechanical properties of the tip and the sample. However, we ignore this relationship and treat the FFC of the TSI force as an unknown input and try to estimate it using a dual Kalman filter. For a more detailed explanation of dual Kalman filtering see for example [16, 17]. Since there is no information on the dynamics of the TSI force available, we only assume that the FFC of the TSI force changes very slowly in comparison to the motion of the cantilever, i.e., the TSI force follows a zero-dynamics rule. With this assumption one can augment the state variables and the FFC of TSI force in the following set of equations:

$$\begin{Bmatrix} \dot{\mathbf{q}} \\ \mathbf{f}_{ts} \end{Bmatrix} = \begin{bmatrix} A & B_2 \\ O_{2 \times 4} & O_{2 \times 2} \end{bmatrix} \begin{Bmatrix} \mathbf{q} \\ \mathbf{f}_{ts} \end{Bmatrix} + \begin{bmatrix} 1 \\ O_{5 \times 1} \end{bmatrix} f_d \quad (6.3)$$

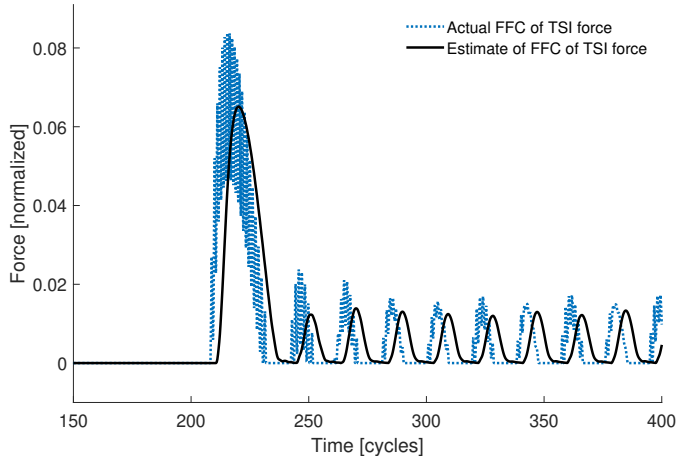


Figure 6.3: Simulated and estimated values for the first Fourier component of TSI force. The estimated force has lower bandwidth and can only be estimated with some delay that stem from zero-dynamics assumption.

Considering that the in-phase and quadrature signals (q_3 and q_4) are available in the experiments, it is easy to check that Eq(6.3) is fully observable (but not controllable). Hence, a Kalman filter (or a linear observer) can estimate the augmented state variables, i.e the state variables of the cantilever and the FFC of the TSI force).

Fig. 6.3 shows the simulated and estimated absolute value of FFC of TSI force. The FFC of the TSI force is observed with some delay and phase distortion, which is inherent to the difficulty of the input-estimation problem and stems from the zero-dynamics assumption in Eq(6.3). Note that due to causality, the exact and real-time estimation of the input of a physical system is impossible [18, 19]. Consequently, the observed TSI force is never going to be exact, nor fully real-time. However, if the observer is properly designed, the expected value of the error vanishes with time, and the covariance of the error depends on the measurement noise, sampling frequency and resolution of the digital signal processing unit.

In order to experimentally verify the performance of the proposed dual Kalman filter, we use the force measurement technique presented in [12, 13, 20]. In this method, a very high bandwidth force sensor is placed under the AFM cantilever instead of the sample surface. In the experiments, in one hand, we measured the TSI force using the high bandwidth sensor and calculated its FFC. On the other hand, ran the proposed Kalman filter on the amplitude and phase signals from the AFM head itself. Fig. 6.4 compares the FFC of the TSI force measured by the force sensor with the output of the dual Kalman filter.

As it can be seen from Fig. 6.4 and Fig. 6.3, the proposed dual Kalman filter can provide an estimate of the FFC of the TSI force with a small delay and inaccuracy. It is not within the scope of the present chapter to try to minimize these errors; here we only focus on using this estimated force in the control loop to prevent chaotic behavior, increase imaging speed, and, if possible, minimize the TSI force. In the following section,

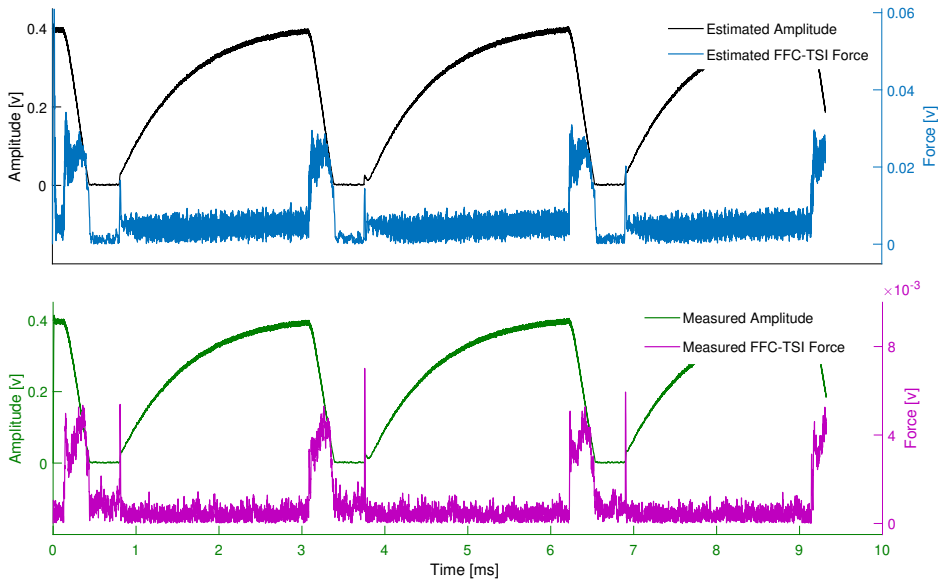
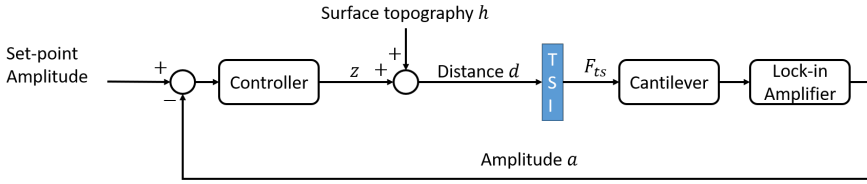


Figure 6.4: Comparison of estimated and measured first Fourier component of TSI force. The cantilever sample distance was deliberately reduced and increased to induce variations in the amplitude signal. The dual Kalman filter estimates the force which is qualitatively comparable with the measured force. Note that the force is not calibrated.

A) The control block-diagram of conventional Tapping Mode AFM:



B) Block-diagram of the proposed control algorithm:

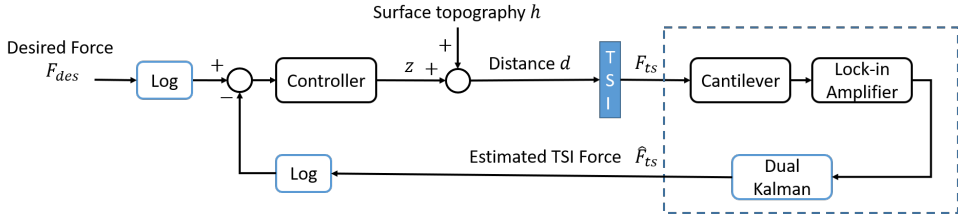


Figure 6.5: Block-diagram of the A) conventional Tapping Mode AFM, B) the proposed control algorithm. The blue dashed box can be approximated as a delay element. A logarithm function is used as a rough approximation of force-distance relationship.

we will study how the estimate FFC of the TSI force can help improving the stability of TM-AFM.

6.3. CONTROL PROBLEM

Besides the severe non-linearity of the tip-sample interaction models, a significant limitation of model-based control of TM-AFM is the high uncertainty of such relationships. In practice, our knowledge on the relationship between the TSI force and the tip-sample distance is highly uncertain; any contamination, humidity, electrostatic charge, unknown material properties of sample, as well as geometric factors such as irregular tip shape and surface roughness may affect the relationship between the TSI force and the distance. To be robust to the uncertainties, we suggest to design the simplest controller which requires minimum knowledge on the behavior of the model. Hence, we propose the control structure presented in Fig. 6.5.B. The uncertain TSI force which is depicted as the blue rectangle in the control block diagram hinders model-based control. However, considering that an approximate and delayed estimate of the TSI force is available through the proposed Kalman filter, we can consider the subsystem shown in the dashed rectangle as a delay ($\hat{\mathbf{f}}_{ts} \approx e^{-\tau s} \mathbf{f}_{ts}$, where $\hat{\mathbf{f}}_{ts}$ is the estimate of the FFC of the TSI force, τ is the delay in the Kalman filter, and s is the Laplace variable). Then, we can assume that the magnitude of the TSI force has an exponential relationship with the distance between the cantilever and the sample ($|\mathbf{f}_{ts}| \approx k e^d$, k and d being an uncertain scaling factor and non-dimensional cantilever-sample distance, respectively). Finally, an ap-

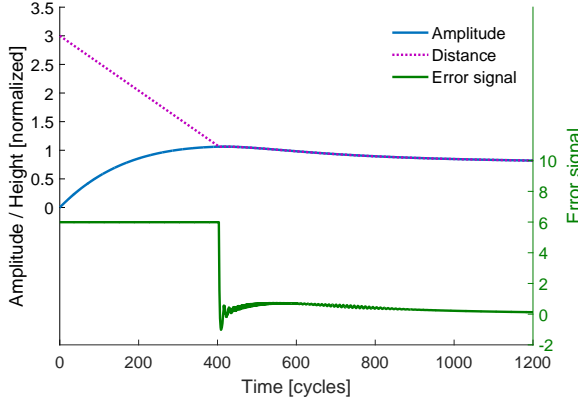


Figure 6.6: Simulated time history of amplitude, distance and the error signal in an approach process with the proposed control algorithm.

proximate model of the subsystem in Fig. 6.5.B can be written as:

$$|\hat{\mathbf{f}}_{ts}| \approx ke^{-\tau s} e^d. \quad (6.4)$$

It is maybe possible to design an optimal controller for the model in Eq(6.4) (e.g., using Cohen-Coon method), however, considering that the model is nonlinear and uncertain, and for the sake of simplicity, we propose to use a single integral action which is small enough not to have higher bandwidth than the delay.

$$z = \frac{k_i}{s} (\log(f_{des}) - \log(|\hat{\mathbf{f}}_{ts}| + \epsilon)), \quad (6.5)$$

where k_i and f_{des} are the integral gain and the desired force, and ϵ is an arbitrary very small value which has been introduced to overcome the singularity of the logarithm function while the force is zero. Higher values of ϵ reduces the speed of the approach while the lower values makes the system more sensitive to noise. Therefore, it is recommended to choose ϵ slightly bigger than the noise of the estimated force to eliminate the effects of the noise in the force estimation in the closed-loop AFM. Fig. 6.6 shows a simulation of the approach process using the proposed algorithm, and the same settings as in Fig. 6.2. Initially, when the cantilever and the surface are not interacting, the error signal is a constant value $(\log(f_{des}) - \log(\epsilon))$. As soon as the distance between the cantilever and the surface becomes equal to the amplitude of the cantilever, i.e. the cantilever engages the surface, the error signal suddenly drops. The controller attempts to keep the logarithm of the TSI force constant, without any consideration about the amplitude or the phase. Hence, the cantilever remains engaged to the sample surface and the distance between the cantilever and the surface is equal to the amplitude at any time.

To compare the imaging performance of the proposed control algorithm with conventional TM-AFM, we consider a chirp signal as the surface topography in the simulations. Fig. 6.7 shows the reference surface topography, amplitude of the cantilever, the

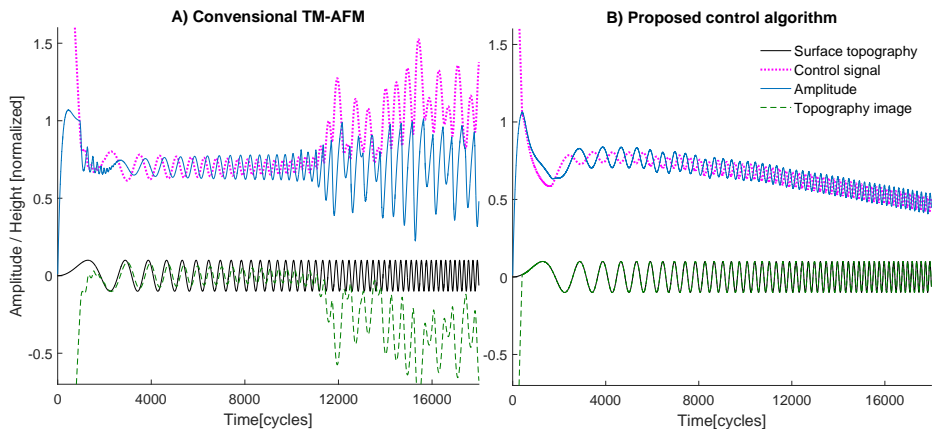


Figure 6.7: Simulation of imaging with AFM in A) conventional tapping mode configuration, B) with the proposed estimated force control. To check the maximum frequency content of the surface that the AFM can follow, the solid black line represents the surface topography, and the green dashed signal shows the image that the AFM would capture from the surface.

output of the controller, and the TM-AFM image of the surface using standard controller (Fig. 6.7.A) and the proposed control architecture (Fig. 6.7.B). With this, we aim to determine the maximum frequency content of the surface (latest time in chirp) that the AFM can still image without crashing or losing the surface. As it can be seen, the standard TM-AFM shows a chaotic behavior when the frequency content of the surface exceeds a certain amount, which is not the case for the proposed algorithm.

The conventional TM-AFM interprets the output of the control as the surface topography, which is either calculated from the applied voltage on the z-stage actuator, or measured with an additional height sensor attached to the actuator. This interpretation is only correct if the cantilever is engaged with the surface and the amplitude is constant. Hence, as it can be seen, the surface image deviates significantly from the reference surface topography, if the frequency content of the surface topography exceeds a certain limit.

However, in the proposed method, keeping the cantilever engaged to the surface, with the cost of not having a constant amplitude is the objective of the controller. In this way, the distance is measured as the summation of the amplitude signal and the control action. Hence, to measure the surface profile, it is not needed for the amplitude to remain constant and the controller is also not attempting to fix the amplitude. Consequently, the proposed method surpasses the speed limit of conventional TM-AFM. The speed of the proposed method is not limited with the relaxation time of the cantilever, instead, it is limited by the delay in estimating the FFC of the TSI force.

From a control engineering perspective, both the delay and the NMP elements impose fundamental limitations on the maximum achievable bandwidth. For AFM cantilevers, only measuring the amplitude shows a NMP behavior, however, if using a Kalman filter to combine the amplitude and phase information, one can eliminate the NMP behavior and replace it with the estimation delay. Since the estimation delay can be much

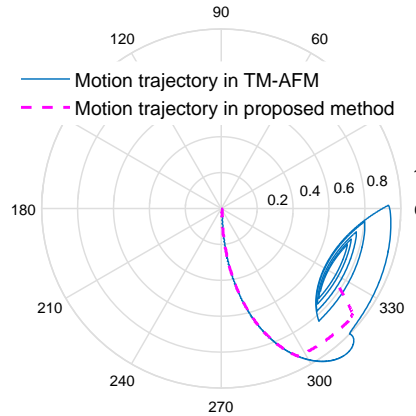


Figure 6.8: Phasor plot of the proposed method (magenta) compared to the conventional TM-AFM (blue). Use of the phase information in Kalman filter directs the system towards the stable point and prevents the fluctuations in phasor space.

smaller, (depending on the accuracy of the model and noise levels) the use of a Kalman filter can increase the maximum achievable bandwidth.

A phase space demonstration of working principle of the proposed control architecture is shown in Fig. 6.8. As compared to Fig. 6.2.B (standard TM-AFM), the proposed controller is not blind to the fluctuations of phase signal. Therefore, the controller can suppress these fluctuations leading the system to the stable focus point via a shorter path and, consequently, with a much higher bandwidth. Note that, both the standard TM-AFM and the proposed method have been simulated with the same cantilever and the same excitation frequency ($\zeta = 0.01, \omega = 0.995$).

Using the estimated FFC of the TSI as the error signal also affects the actual TSI force applied to the surface. Fig. 6.9 shows the the FFC of the TSI force in the proposed method, compared to the TM-AFM. The main observation in this graph is that the TSI force with the proposed controller experience a shorter transient condition in comparison to the TM-AFM, and the cantilever does not bounce back from the surface. It is known that AFM is more damaging in the transient conditions [21]. The proposed method could minimize the sample damage and increase the lifetime of the tip.

6.4. CONCLUSIONS

In this chapter, a new control algorithm for tapping mode AFM has been proposed that can improve the imaging speed and stability. The new TM-AFM controller attempts to keep the first Fourier component of the tip-sample interaction force constant. It has been shown experimentally and numerically that the first Fourier component of the tip-sample interaction force can be reliably estimated using a dual Kalman filter. The simulation results show that using the new error signal can suppress the fluctuations of

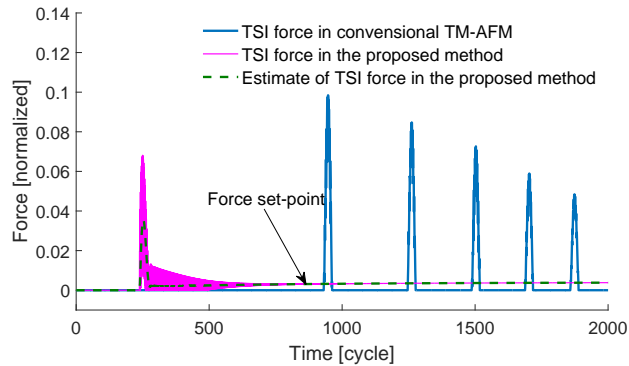


Figure 6.9: First Fourier component of the tip-sample interaction force in the proposed method, compared to the conventional TM-AFM. The dashed green line shows the controllers perception from the TSI force.

the phase signal and prevent the AFM from showing chaotic behavior even in very high imaging speeds. Further, this technique should be implemented in a real-time system to improve the imaging speed of AFM.

REFERENCES

- [1] N. Jalili and K. Laxminarayana, *A review of atomic force microscopy imaging systems: application to molecular metrology and biological sciences*, *Mechatronics* **14**, 907 (2004).
- [2] H. Sadeghian, R. Herfst, J. Winters, W. Crowcombe, G. Kramer, T. van den Dool, and M. H. van Es, *Development of a detachable high speed miniature scanning probe microscope for large area substrates inspection*, *Review of Scientific Instruments* **86**, 113706 (2015).
- [3] A. Fleming, B. Kenton, and K. K. Leang, *Bridging the gap between conventional and video-speed scanning probe microscopes*, *Ultramicroscopy* **110**, 1205 (2010).
- [4] T. Ando, T. Uchihashi, and T. Fukuma, *High-speed atomic force microscopy for nano-visualization of dynamic biomolecular processes*, *Progress in Surface Science* **83**, 337 (2008).
- [5] Y. Wang, X. Hu, L. Xu, and X. Hu, *Improving the scanning speed of atomic force microscopy at the scanning range of several tens of micrometers*, *Ultramicroscopy* **124**, 102 (2013).
- [6] G. Schitter, *Improving the speed of afm by mechatronic design and modern control methodsgeschwindigkeitsverbesserung beim afm mittels mechatronischem design und modernen regelmethoden*, *tm-Technisches Messen Plattform für Methoden, Systeme und Anwendungen der Messtechnik* **76**, 266 (2009).

- [7] L. Picco, L. Bozec, A. Ulcinas, D. Engledew, M. Antognozzi, M. Horton, and M. Miles, *Breaking the speed limit with atomic force microscopy*, [Nanotechnology](#) **18**, 044030 (2006).
- [8] R. Herfst, B. Dekker, G. Witvoet, W. Crowcombe, D. de Lange, and H. Sadeghian, *A miniaturized, high frequency mechanical scanner for high speed atomic force microscopy using suspension on dynamically determined points*, [Review of Scientific Instruments](#) **86**, 113703 (2015).
- [9] M. Li, H. X. Tang, and M. L. Roukes, *Ultra-sensitive nems-based cantilevers for sensing, scanned probe and very high-frequency applications*, [Nature nanotechnology](#) **2**, 114 (2007).
- [10] A. Keyvani, F. Alijani, H. Sadeghian, K. Maturova, H. Goosen, and F. van Keulen, *Chaos: The speed limiting phenomenon in dynamic atomic force microscopy*, [Journal of Applied Physics](#) **122**, 224306 (2017).
- [11] A. Keyvani, M. S. Tamer, J.-W. van Wingerden, H. Goosen, and F. van Keulen, *A comprehensive model for transient behavior of tapping mode atomic force microscope*, Submitted to the journal [Nonlinear Dynamics](#).
- [12] M. S. Tamer, H. Sadeghian, A. Keyvani, H. Goosen, and F. van Keulen, *Quantitative measurement of tip-sample interaction forces in tapping mode atomic force microscopy*, [Proceedings of the 13th International Workshop on Nanomechanical Sensing](#), 199 (2016).
- [13] A. Keyvani, H. Sadeghian, M. S. Tamer, J. F. L. Goosen, and F. van Keulen, *Minimizing tip-sample forces and enhancing sensitivity in atomic force microscopy with dynamically compliant cantilevers*, [Journal of Applied Physics](#) **121**, 244505 (2017).
- [14] A. Keyvani, H. Sadeghian, H. Goosen, and F. Van Keulen, *On the origin of amplitude reduction mechanism in tapping mode atomic force microscopy*, [Applied Physics Letters](#) **112**, 163104 (2018).
- [15] T. De, P. Agarwal, D. R. Sahoo, and M. V. Salapaka, *Real-time detection of probe loss in atomic force microscopy*, [Applied physics letters](#) **89**, 133119 (2006).
- [16] S. S. Haykin *et al.*, [Kalman filtering and neural networks](#) (Wiley Online Library, 2001).
- [17] A. Alasty and R. Shabani, *Nonlinear parametric identification of magnetic bearings*, [Mechatronics](#) **16**, 451 (2006).
- [18] S. Devasia, *Should model-based inverse inputs be used as feedforward under plant uncertainty?* [IEEE Transactions on Automatic Control](#) **47**, 1865 (2002).
- [19] S. Sundaram and C. N. Hadjicostis, *Delayed observers for linear systems with unknown inputs*, [IEEE Transactions on Automatic Control](#) **52**, 334 (2007).
- [20] H. Sadeghian and M. S. Tamer, European Patent 15181449.8.

- [21] A. Keyvani, H. Sadeghian, H. Goosen, and F. van Keulen, *Transient tip-sample interactions in high-speed afm imaging of 3d nano structures*, in *Metrology, Inspection, and Process Control for Microlithography*, Vol. 9424 (International Society for Optics and Photonics, 2015) p. 94242Q.

7

MINIMIZING TIP-SAMPLE FORCES AND ENHANCING SENSITIVITY IN ATOMIC FORCE MICROSCOPY WITH DYNAMICALLY COMPLIANT CANTILEVERS

In previous chapters, we show that in order to increase the control bandwidth of the AFM, it is useful to estimate the tip sample interaction forces. However, due to the harmonic motion of the cantilever in TM-AFM, it is seemingly impossible to estimate the tip-sample interactions from the motion of the cantilever. Not directly observing the interaction force, it is possible to damage the surface or the tip by applying an excessive mechanical load. The tip-sample interactions scale with the effective stiffness of the probe. Thus, reduction of the mechanical load is usually limited by the manufacturability of low stiffness probes. However, the one-to-one relationship between spring constant and applied force only holds when higher modes of the cantilever are not excited. In this chapter, it is shown that, by passively tuning higher modes of the cantilever, it is possible to reduce the peak repulsive force. These tuned probes can be dynamically more compliant than conventional probes with the same static spring constant. Both theoretical and experimental results show that a proper tuning of dynamic modes of cantilevers reduces the contact load and increases the sensitivity considerably. Moreover, due to the contribution of higher modes, the tuned cantilevers provide more information on the tip-sample interaction. This extra information from the higher harmonics can be used for mapping, and possibly identification of material properties of samples.

Parts of this chapter has been published in [Journal of Applied Physics 121, 244505 \(2017\)](#).

7.1. INTRODUCTION

An Atomic Force Microscope (AFM) is a versatile instrument that enables measurement and manipulation of samples at the nanoscale. Recent advances in AFM technology already carried its application beyond topography imaging, such as subsurface elasticity measurements [1], unfolding force measurements of biomolecules [2], thermal conductivity measurements [3, 4], surface chemical composition mapping [5], and mechanical properties mapping [6]. Nonetheless, topography imaging with Tapping Mode AFM (TM-AFM) can still be considered the most common application.

In TM-AFM, the cantilever is excited by a dithering signal with constant amplitude and a frequency near the fundamental resonance frequency of the cantilever. To prepare for scanning, the cantilever is brought in the vicinity of the sample surface until its amplitude decreases to a user-defined set-point amplitude. While scanning the surface, the amplitude is kept constant by adjusting the distance between the cantilever and the sample. The control signal which adjusts the distance is interpreted as the topography image. The phase delay between the motion of the cantilever and excitation signal is recorded as a measure of energy dissipation and can be related to adhesion, viscoelasticity or hysteresis in surface energy level [7, 8].

As shown in Fig. 7.1, in TM-AFM the tip hits the sample surface in every cycle, experiencing both attractive and repulsive Tip-Sample Interaction (TSI) forces. Since these forces occur only during a fraction of a cycle, they affect the motion of the cantilever in a weakly nonlinear manner. Consequently, the motion of the cantilever remains harmonic.

Although some theoretical studies suggest that the motion of the cantilever should include effects of higher modes, [9, 10] experiments show that effects of higher modes are negligible and most likely below the noise level [11]. Only in specific conditions, such as for extremely low Q factors (in the order of 1), the effects of higher modes could be experimentally detected. Even for low-Q measurements, the presence or detectability of the second harmonic is not guaranteed [6]. Thus, depending on the sample properties, noise level, operation parameters, etc., the higher harmonics may or may not be detected. Nonetheless, for the tapping mode AFM in air, the motion of the cantilever can be considered as purely harmonic as the higher harmonics are undetectable. Since a considerable amount of information on the TSI forces is modulated via the higher Fourier components, and the cantilever only vibrates with a single frequency, most of the information on the TSI force is lost in the noise.

The reason for a harmonic motion of the cantilever is well explained in the frequency domain [12]. Because of the large quality factor of the cantilever, its frequency response function (FRF) has orders of magnitude lower gain at frequencies other than the resonance frequency. Thus, similar to a sharp band pass filter, the cantilever only passes the frequency content of the TSI force which corresponds to its resonance frequency and attenuates the higher frequency content. Consequently, the output, i.e. the cantilever's motion, can only have one dominant frequency component, and higher harmonics are likely to be obscured by the noise.

Since the motion of the cantilever remains harmonic, the TSI force affects the cantilever as a weak nonlinearity and the amplitude and phase of the cantilever motion only evolve with the periodic average of the TSI force [13–16]. Therefore, only the informa-

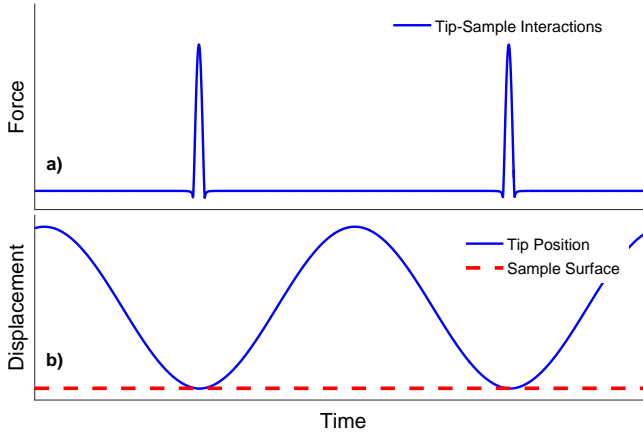


Figure 7.1: a) Tip-sample interactions, b) Dynamic motion of cantilever while touching the sample surface in TM-AFM (schematic).

tion on the periodic average of the tip-sample interaction can be extracted. On the other hand, damage does not occur due to the average of the TSI force but due to the maximum repulsive force, referred to as Peak Repulsive Force (PRF) [17]. Since it is not possible to directly measure the PRF or extract it from the periodic average of the TSI force, it is not possible to directly control it. Consequently, there is always a probability of damage in TM-AFM. In industrial applications of AFM such as metrology [18–20], it is important to avoid any damage to the sample.

To reduce the damage probability, it is wise to use the most compliant cantilever available and choose proper operation parameters, i.e. amplitude and frequency set points [17]. However, reduction of the TSI force via these methods is limited because of other practical issues, such as fabrication limits or high noise in compliant cantilevers. To capture more information on the TSI force, the motion of a cantilever should contain multiple frequency components. For this reason either the input (dither signal) or the system (cantilever and environment) have to be altered. Both options have already been explored. The first method is to introduce an auxiliary excitation signal with a different frequency which is called the “multi-modal” operation mode [21]. The second method is based on adjusting the system using multi-harmonic cantilevers [22] or operating in a fluid environment [6]. Next, some researchers utilized the sub-harmonic (static) motion to map binding sites of biological samples, known as Topography and RECOgnition (TREC) mode [23]. It must be mentioned that the TREC mode is not a general imaging technique, but rather a particular method to detect chemical binding sites of biological samples and without the presence of the binding forces, the sub-harmonic motion of the cantilever is negligible or below the noise level.

As mentioned, the Multi-modal AFM [21, 24] introduces an auxiliary excitation signal to excite one or more higher modes of the cantilever simultaneously. Multiple lock-in amplifiers are utilized to measure the amplitude and phase of the different modes (typically first and second bending mode). Consequently, two images per mode are avail-

able, i.e., amplitude and phase. The images gathered with the multimode AFM technique demonstrate that some information is modulated on higher modes which could not be extracted with standard tapping mode AFM [21]. However, the external excitation of higher modes introduces both super and sub-harmonic frequency contents. The extra energy in the second mode reciprocally increases and decreases the nanoindentation in different cycles. Thus, even a subtle amplitude of the second mode can cause a fluctuating TSI force on the sample surface which might be damaging.

The second option to acquire more information is to change the system. This can be done either by decreasing the Q factor [11] (via operating in liquid) or by increasing the response of the higher modes of the cantilever by introducing additional resonating parts to the cantilever, so-called harmonic cantilevers or force sensing cantilevers [22, 25, 26]. Since the TSI force contains peaks at integer multiples of the excitation frequency [9], the secondary resonator, can capture some of the higher frequency content of the TSI force. For example, Sahin *et al.* introduced a cantilever that has a cutout in its neck to tailor the ratio between the first and third mode [25]. They demonstrated that when the resonance frequency of the third mode is exactly 16 times the first resonance frequency, more information on the sample elasticity is modulated in the third mode. Sahin *et al.* utilized the first torsional mode of the cantilever to measure the interaction force [22]. Sarioglu *et al.* patterned comb-like trenches on the cantilever to realize the second resonator and acquire more information using an interferometer [26]. For the same purpose Li *et al.* suggested to attach a lumped mass particle to the cantilever [27] to adjust its dynamic properties. Felts and King introduced gaps inside the cantilever and showed that the ratio between the first and second resonance could be changed considerably [28]. Xia *et al.* utilized a level set optimization method to optimize the cantilever for bi-harmonic methods. [29] Lately, Loganathan and Bristow designed a bi-harmonic probe for which the second resonance frequency is two times the fundamental one. Their design consists of two cantilevers, one inside the other, and presents considerably higher force sensitivity in comparison to normal cantilevers [30].

The approaches as mentioned above, indeed gather more information on the sample. However, these designs are geometrically complex which limits their feasibility regarding fabrication of smaller cantilevers. It is well-known that in order to decrease the tip-sample forces, increase the force sensitivity, and increase the imaging speed, it is necessary to scale down the dimensions of cantilevers as much as possible [31] which requires a simple design. Moreover, it is not entirely understood how the multi-harmonic cantilevers affect the TSI force. For example, some of them might increase and others might reduce the PRF.

In this paper, we aim to reduce the TSI force with a easily scalable minimalistic change in the geometry of the cantilever. For this purpose, we propose to tune the second vibration mode of the cantilever with respect to its first mode. As a result, the second mode of the cantilever gets excited by one of the super-harmonic components of the TSI force and provides more information on the mechanical properties of the sample. Also, by choosing an even number (6) as the frequency ratio, the first and the second modes of the cantilever get self-synchronized which considerably reduces the PRF, and consequently, the probability of damaging the surface or the tip.

This paper is organized as follows: Section 7.2 presents the design of dynamically

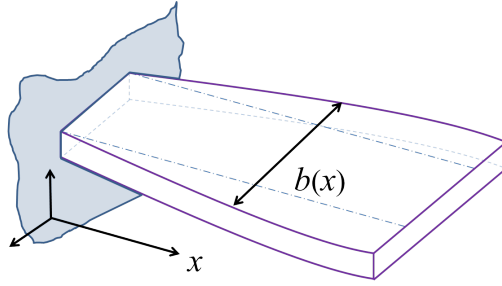


Figure 7.2: Schematic view of the cantilever with variable width.

tuned cantilevers, Section 7.3 describes the TSI force and the working principle of the proposed probe. Section 7.4 demonstrates the performance of the cantilever via experimental results. The conclusions are presented in the last section.

7.2. TUNING THE DYNAMICS OF CANTILEVERS

As mentioned in the Introduction, the TSI force in the time domain contains periodic impulse-like functions. In the frequency domain, such a periodic impulse-like function includes a large number of super-harmonic components with integer multiples of the excitation frequency. As long as none of these components coincides with any resonance frequencies of the cantilever, their effect is usually undetectable and the motion of the cantilever is nearly harmonic. In this section we propose to change the geometry of the cantilever such that its second bending mode coincides with the 6th super-harmonic component of the force. Consequently, the second bending mode will also be excited by the TSI force.

For prismatic cantilevers —provided that the Euler-Bernoulli beam theory holds— the resonance frequency of the second bending mode is approximately 6.267 times the first resonance frequency. Considering that the ratio between the first and second resonance frequencies of a prismatic cantilever is close to 6, a relatively small adjustment in shape can change this ratio to exactly 6. To tune the cantilever, we propose a trapezoidal geometry for which the width is a linear function of the axial coordinate.

Considering a homogeneous isotropic material, and the Euler-Bernoulli beam theory, the free vibration of the cantilever can be described with the following non-dimensional eigenvalue problem:

$$\left[\frac{\partial^2}{\partial x^2} \left(b(x) \frac{\partial^2}{\partial x^2} \right) - b(x) \lambda_i^2 \right] \phi_i(x) = 0, \quad (7.1)$$

where x , λ_i , and $\phi_i(x)$ represent the non-dimensional axial coordinate, i^{th} eigen frequency, and i^{th} bending mode, respectively. The width of the cantilever ($b(x)$) is normalized with respect to the width at the clamping. A linear variation of the width $b(x) = 1 + \alpha x$ is chosen, in which α is a design parameter. The eigenvalue problem Eq(7.1) has been solved using the well-known Galerkin method. Fig. 7.3 shows the frequency ratio as a function of the design parameter α , along with the corresponding mode shapes. As can be seen in Fig. 7.3, if $\alpha = -0.18$, i.e. the cantilever is slightly trapezoidal, the frequency of

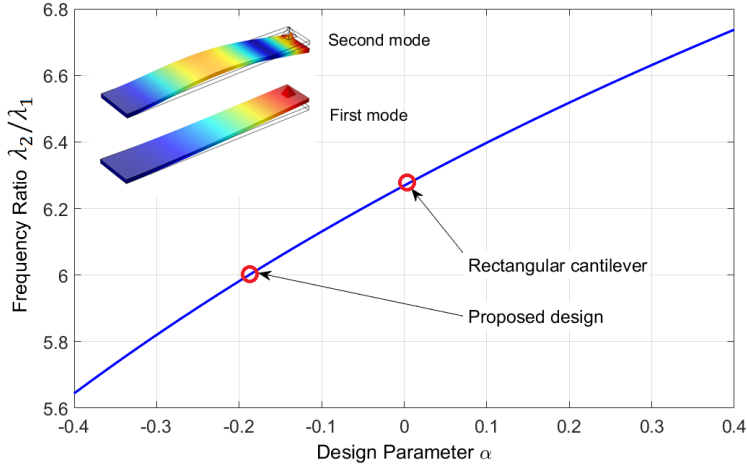


Figure 7.3: Frequency ratio of first two modes of the cantilever versus the design parameter α (i.e., the ratio of obliqueness of the cantilever).

the second mode is 6 times the frequency of the first mode. It must be mentioned that in Eq(7.1), the torsional modes, in-plane modes, bending modes in lateral direction and effects of tip mass are completely ignored. Although, the torsional modes are not excited and in-plane modes have much higher frequency, a 3D finite element method was used to validate the method and correct for the tip mass by fine-tuning the design parameter.

7.3. TIP-SAMPLE INTERACTIONS FOR TUNED CANTILEVERS

In this section, we shall discuss the dynamic behavior of the tuned cantilever in comparison with a standard cantilever. Fig. 7.4.a and 4.c show the TSI force and tip motion in the frequency domain, calculated from a full nonlinear simulation. The point frequency response functions (FRF) for the cantilever's tip (Red) are also included to demonstrate the effects of dynamic tuning. Fig. 7.4.b and 4.d show the SEM images of the corresponding cantilevers.

Since the frequency of the forced vibration only depends on the excitation frequency (and not on the eigenfrequencies of the cantilever), irrespective of the tuning, the motion of the cantilever can contain only the frequencies that are exact integer multiples of the excitation frequency (so-called harmonic and super-harmonic components). In theory, any cantilever is vibrating with all the integer multiples of the excitation frequency. But, if the vibration modes are not tuned, the amplitude of super-harmonic components are negligibly small. The proposed tuning shifts the second bending mode of the cantilever (second peak of FRF) to the frequency of the 6th Fourier component of the TSI force, thereby increasing the amplitude of the 6th super-harmonic motion.

To demonstrate only the effect of shape, Fig. 7.5 compares the simulated TSI force for rectangular and trapezoidal cantilevers while both cantilevers have the same spring constant(5 Nm⁻¹), same first resonance frequency (100 kHz) and same quality factor(100).

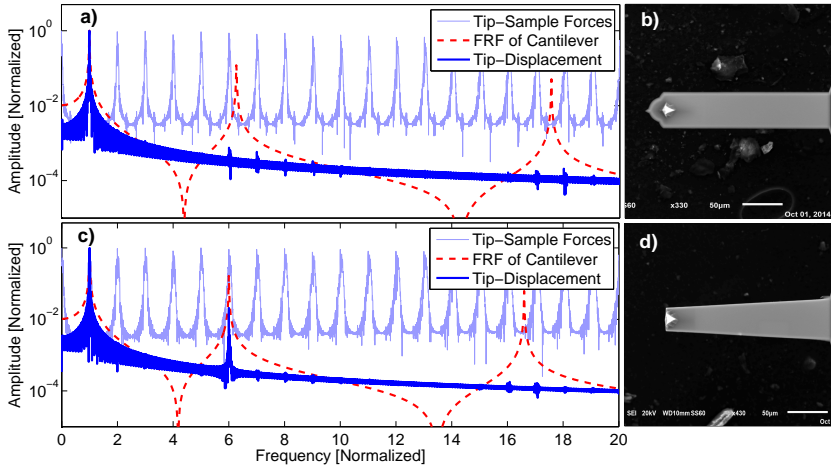


Figure 7.4: a) Simulated tip-sample interaction, FRF of the cantilever, and motion of the tip in the frequency domain for rectangular cantilever, b) SEM image of the commercially available MPP-22120 cantilever used in simulations and experiments, c) simulated tip-sample interaction, FRF of the cantilever, and motion of the tip in the frequency domain for the tuned cantilever, d) SEM image of the custom made tuned cantilever.

The motion of the proposed cantilever is not harmonic, but a superposition of two harmonic components, as shown in Fig. 7.5. The phase of the motion of the first and the second modes are synchronized in a way that the speed of the tip is reduced right before touching the sample surface. Hence, the proposed cantilever indents the sample less and consequently, applies a lower TSI force.

The reduction in approach velocity and TSI force is caused by self-synchronization of the two modes of the cantilevers. The frequency ratio of the cantilevers motion is an exact integer number, therefore the motion of the cantilever remains periodic. In other words, since the second mode is purely excited with the TSI force, its phase with respect to the first mode in steady state conditions does not change from one cycle to another. This phase synchronization happens such that the contribution of the second mode reduces the indentation.

Notice that the effects of long-range nonlinear forces such as electrostatic attraction and squeeze film effects can influence the resonance frequencies and degrade the performance of the cantilever. However, these effects are negligible in comparison to the TSI force. Thus, to avoid unnecessary complications, it is reasonable to ignore them while tuning the cantilever for TM-AFM in air or vacuum.

To quantify the force reduction for tuned cantilevers, we calculate the peak repulsive forces using a multi-harmonic extension of the periodic averaging method. Since the mathematical details of the periodic averaging method are not in the scope of this paper, we only present the final results. More information on the periodic averaging method for AFM cantilevers is available in [15]. Fig. 7.6 shows the peak repulsive forces versus the amplitude set-point for a test case with dynamic characteristics as indicated in the caption. As can be seen, the peak repulsive force for the tuned cantilever is on average

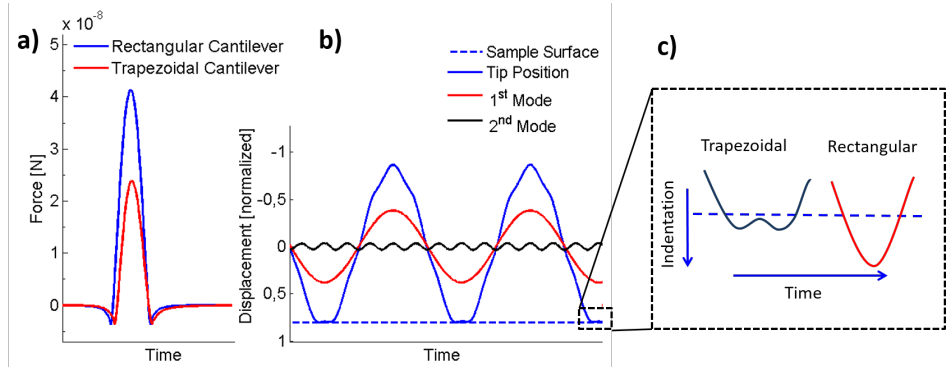


Figure 7.5: a) Tip-sample interactions in single period for rectangular and trapezoidal cantilevers. b) Tip-motion and mode participation of first and second modes for tuned cantilevers. c) Schematic explanation for reduction of indentation with tuned cantilevers. The second mode of the cantilever retracts the tip during the indentation. In the simulation, the free air amplitude was 50 nm, and the amplitude set-point was 40 nm (amplitude ratio 80%).

70% less than for a conventional cantilever.

7.4. EXPERIMENTAL RESULTS AND DISCUSSION

To fabricate and test a tuned cantilever as a proof of concept, a commercially available probe (Veeco MPP-22120, Fig. 7.4b) was patterned with a Gallium Focused Ion Beam (Ga-FIB) to the desired shape (Fig. 7.4d). The dynamic properties of the cantilever were measured before and after the patterning using the thermal calibration method[33] and are presented in Table 7.1. Here we shall first present the imaging performance of the proposed cantilever and verify the feasibility of extracting information from higher harmonics. Secondly, we demonstrate the reduction in the TSI force via a force measurement experiment, and an apparent height test.

Table 7.1: Dynamic properties of the cantilever before and after patterning

	$k[N/m]$	$\omega_1[kHz]$	$\omega_2[kHz]$	Q_1	Q_2	$\frac{\omega_2}{\omega_1}$
Before patterning	1.19	40.86	281.77	136	278	6.89
After patterning	0.87	50.50	307.28	142	274	6.08

7.4.1. IMAGING PERFORMANCE

To evaluate the imaging performance of the proposed cantilever, Fig. 7.7 shows the AFM images of a commercially available two-phase polymer sample (PS-LDPE, Bruker). The images are captured with the two cantilevers under the same imaging conditions and set-points using a Bruker Dimension Fastscan AFM. For both cantilevers the peak amplitude was set to ≈ 240 nm, the excitation frequency and the free air amplitude was chosen to be 7% below the resonance, the set point amplitude was ≈ 150 nm, and the scanning speed for both cases was $38.8 \mu m/s$. For a fair comparison, the image processing is lim-

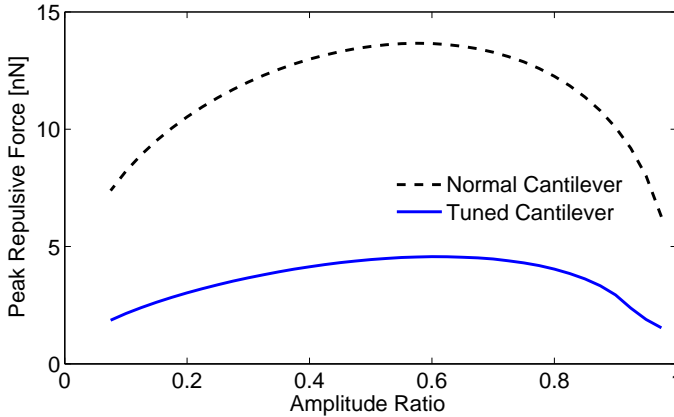


Figure 7.6: Calculated peak repulsive force versus amplitude ratio for a free air amplitude of 50 nm and tip radius 10 nm, spring constant 1 N/m and quality factor $Q_1=100$ and $Q_2=150$, considering Derjaguin-Muller-Toporov [32] modulus of silicon tip and silicon sample.

ited to a first order offset elimination in the height images, and zero-shifting the color bar relative to the minimum of the data (i.e., the color bars all start at zero). As shown in Fig. 7.7 the phase image with the tuned cantilever has considerably higher contrast while there is hardly any difference between the amplitude images. Since the stiffness of the two probes is in the same order, the extreme increase in phase sensitivity can only be explained by the dynamically increased force sensitivity. The ratio between viscoelasticity and elasticity of the sample surface affects the phase of the TSI. Since the tuned cantilever is dynamically more sensitive to the TSI force, it responds more aggressively to changes in the phase of the force as well. Consequently, the phase image captured with the dynamically tuned cantilever has more contrast in comparison to the one obtained with the standard cantilever.

As mentioned in Section 7.3, the second mode is purely excited by the TSI force. Since different frequency components contain different information on the TSI force, the motion of the second mode provides additional information on the sample which is not available from the first mode. This additional information can be extracted using an auxiliary lock-in amplifier. Fig. 7.8 shows the images gathered from the second bending mode of the cantilever. Clearly, for the tuned cantilever, the amplitude and phase of the second mode also provide information on the mechanical properties of the sample. Yet, a general mathematical calculation is needed to estimate the material properties from amplitude and phase signals. In this context, Raman *et al.*, have shown that an approximate stiffness measurement is possible using the harmonic balancing method[6]. The extra information provided by the second mode of the cantilever can also be useful in determining a more accurate height of sub-manometer structures[34]. In our experiments, we only excite the first mode of the cantilever to allow for the self-synchronization to reduce the force. However, it is also possible to use the proposed cantilever in a bi-modal AFM configuration, while preserving the periodicity of the motion. It is known that the periodicity simplifies the theoretical analysis and improves the accuracy of quantitative

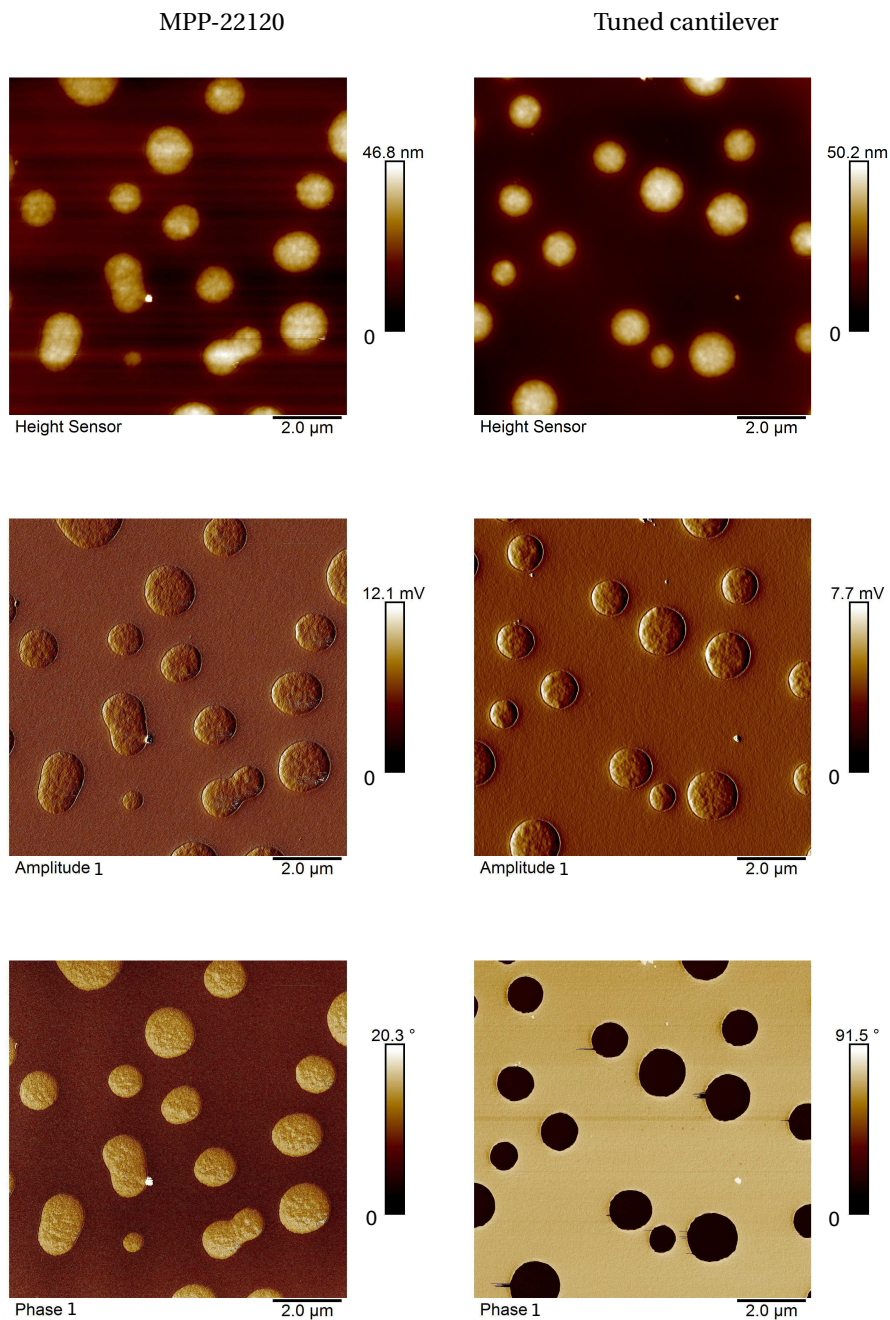


Figure 7.7: Topography (measured via height sensors), amplitude error, and phase images of a PS-LDPE sample gathered with the MPP22120 cantilever and the tuned cantilever.

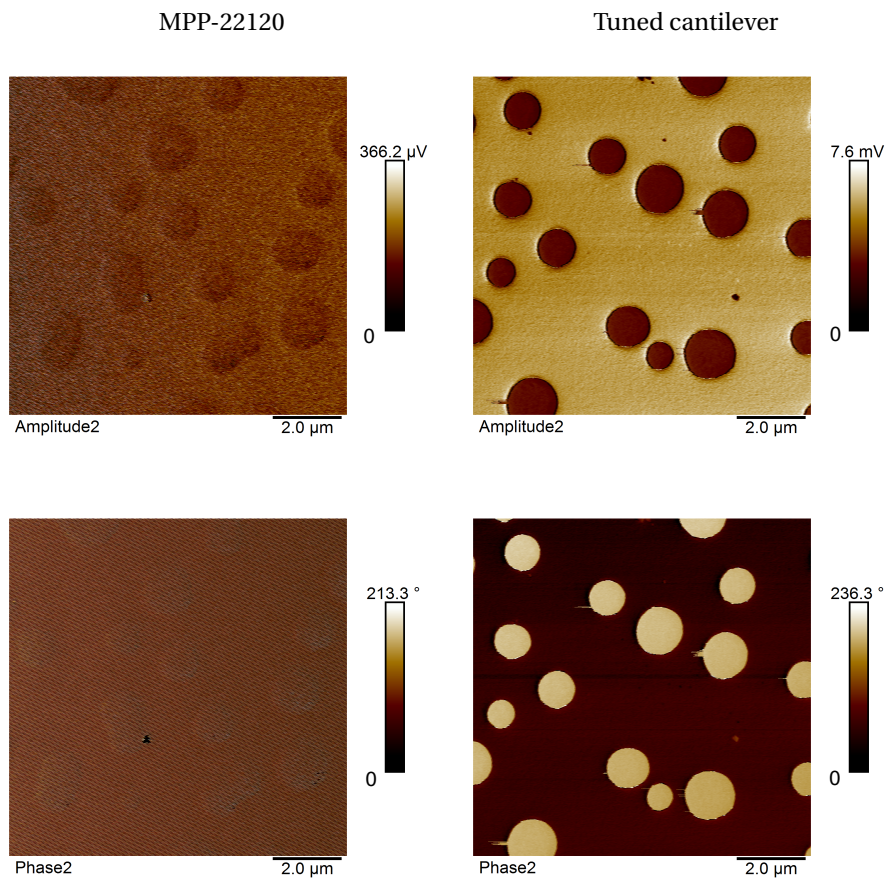


Figure 7.8: AFM images of PS-LDPE sample gathered with the MPP22120 cantilever and the tuned cantilever captured from the second mode of vibration using an auxiliary lock-in amplifier.

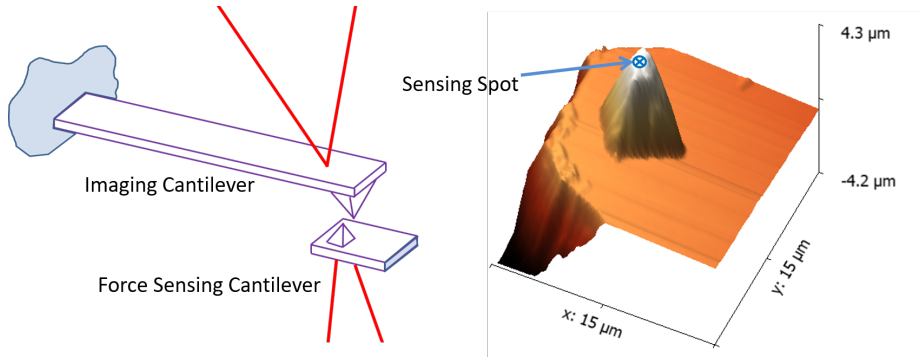


Figure 7.9: Schematic of the force sensing technique, and the image of the tip of the sensing cantilever which is captured with the imaging cantilever.

measurements.[35]

7.4.2. FORCE MEASUREMENT

To verify the reduction of the forces with tuned cantilevers, we perform the experiment as suggested by Tamer *et al.* [36, 37] in which, a force sensor is placed under the cantilever instead of the sample surface, as shown in Fig. 7.9. The force sensor itself is also a micro-cantilever with its own optical readout system. The force sensing cantilever has a much higher resonance frequency in comparison to the imaging cantilever (1.29 MHz and 50 kHz, respectively). Hence, the first few frequency components of the TSI force fall into the static regime of the sensing cantilever and can be measured. We aim to compare those frequency components in the motion of the sensing cantilever, if the two different cantilevers tap on the sensor. To make a correct comparison, we ensured that the sensitivity of the force sensor is the same in both experiments by first, tapping exactly on the same specific spot on the sensing cantilever (the sensing spot in Fig. 7.9), and secondly, measuring the thermal noise of the force sensor before and after experiment and check for any possible drift in the optical sensitivity.

For all of the experiments in this section, we chose a peak amplitude of 80 nm. The excitation frequency is chosen such that the free air amplitude is 4 percent less than the peak amplitude (76.8 nm). Fig. 7.10 shows the deflection of the imaging cantilever (in this case the tuned cantilever), in frequency and time domain, while the imaging cantilever is tapping on the sensing spot (with amplitude ratio of 60%). The inherent noise of the force sensing cantilever is measured while the two cantilevers are disengaged.

As can be seen, the deflection of the tuned cantilever contains the first and sixth harmonic of the excitation frequency, together with some other small peaks at the integer multiples of the excitation frequency. The signal from the force sensing cantilever contains first few (23 in this case) of the super-harmonic contents of the TSI force. Since the deflection of the force sensing cantilever exhibits its own noise and there exist a large amount of phase distortion between different frequency contents of the motion, the TSI force itself can not be resolved in the time domain. Therefore, to compare the forces applied with a tuned and a conventional cantilever, we only measure the peaks in the

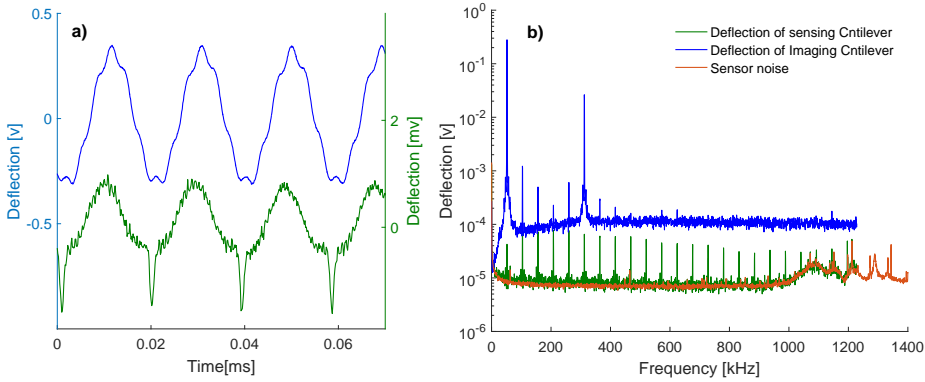


Figure 7.10: Measured signal of the optical sensor from the imaging and the sensing cantilevers, a) in time domain, b) in frequency domain.

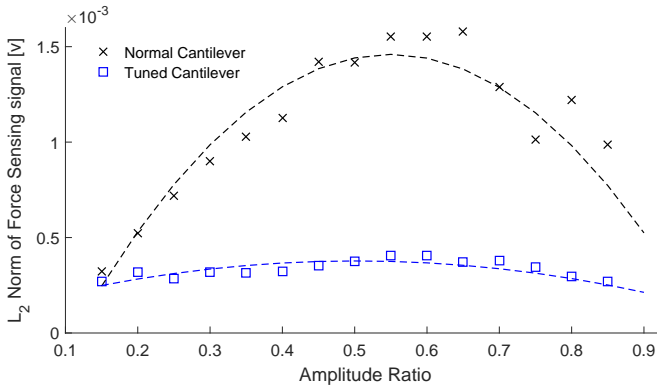


Figure 7.11: L_2 norm of the force sensor signal, as a measure of the TSI force, measured from the cantilevers in Table 7.1. Dashed lines show a quadratic data fit.

frequency domain of the sensing cantilever, and calculate their L_2 norm. The L_2 norm of a signal is the same in both time and frequency domains and represents a measure of power transmitted with the signal. Fig. 7.11 shows the results of this experiment with the two cantilevers mentioned in Table 7.1 at different amplitude set points. As can be seen, the power transmitted to the force sensing cantilever is much lower when a tuned cantilever is used. Although no calibrated TSI forces could be measured in real-time, the results in Fig. 7.11 consistently with the results in Fig. 7.6, confirm the reduction of the TSI forces with tuned cantilevers.

7.4.3. APPARENT HEIGHT IMAGE OF DNA

As mentioned previously, the forces in TM-AFM are not directly accessible from experiments. However, the apparent height of soft nanoscale samples can give an estimate of

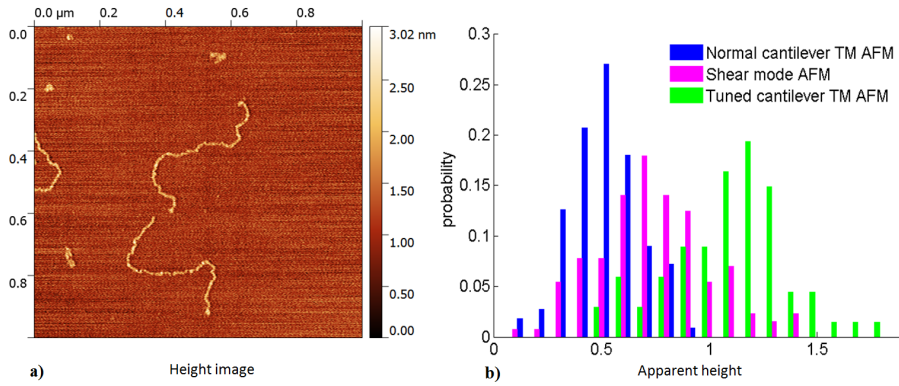


Figure 7.12: a) Height image of DNA on a mica surface captured with a tuned cantilever in tapping mode in air. Free air amplitude and working amplitude were $\approx 30 \text{ nm}$ and $\approx 25 \text{ nm}$, respectively, b) Height histogram of the DNA on a mica sample, a comparison of TM AFM with normal cantilevers, shear mode AFM and TM AFM with tuned cantilever.

the average repulsive forces. In tapping mode AFM, the repulsive forces compress the samples. Consequently, the apparent height of samples is commonly lower than their real values. Antognozzi *et al.*[38] presented a height histogram of a double-stranded DNA which was captured with TM-AFM and compared it with shear-mode AFM. Since the shear-mode AFM reduces the repulsive forces, a higher average height was observed in comparison to TM-AFM (1 nm for shear AFM and 0.6 nm for TM-AFM[39]). We use the same method to compare the average of TSI force for dynamically tuned and standard cantilevers. Fig. 7.12 a) shows the height image of a double-stranded DNA imaged in TM-AFM using a tuned probe in air. Fig. 7.12 a) compares the height histogram measured with the tuned cantilever with those measured by Antognozzi *et al.*[38] in shear mode AFM and TM AFM. As shown in Fig. 7.12, using the tuned cantilevers in TM-AFM, even a higher average height could be observed (1.2 nm) which is closer to its actual value (theoretical value 2.2 nm and X-ray measurement 2.0nm [40]). Consistently, the increased average apparent height, suggests that the tuning of the second mode reduces the repulsive forces.

7.5. CONCLUSION

In this paper, a minor adjustment of the AFM cantilever geometry has been suggested to tune its vibration modes. Such a cantilever utilizes its second mode to enhance imaging performance by capturing the 6th super-harmonic force component. Theoretical and experimental results demonstrate that it benefits from reduced tip-sample interaction forces and increased sensitivity in tapping mode AFM. At the same time, the proposed cantilever provides additional information modulated via the second bending mode which can be used to extract mechanical properties of the samples. The tapered cantilever is an easily scaled design which enables more sensitive imaging with higher contrast in material properties mapping while applying lower TSI forces, and thus, re-

ducing tip damage or sample distortion.

ACKNOWLEDGEMENT

I would like to thank Ir. Hozanna Miro from Kavli nanolab Delft, for her help in fabricating the cantilever.

REFERENCES

- [1] K. Yamanaka, H. Ogiso, and O. Kolosov, *Ultrasonic force microscopy for nanometer resolution subsurface imaging*, [Applied Physics Letters](#) **64**, 178 (1994).
- [2] K. C. Neuman and A. Nagy, *Single-molecule force spectroscopy: optical tweezers, magnetic tweezers and atomic force microscopy*, [Nature methods](#) **5**, 491 (2008).
- [3] R. Grover, B. McCarthy, D. Sarid, and I. Guven, *Mapping thermal conductivity using bimetallic atomic force microscopy probes*, [Applied physics letters](#) **88**, 233501 (2006).
- [4] J.-H. Lee and Y. Gianchandani, *High-resolution scanning thermal probe with servo-controlled interface circuit for microcalorimetry and other applications*, [Review of scientific instruments](#) **75**, 1222 (2004).
- [5] A. Noy, D. V. Vezenov, and C. M. Lieber, *Chemical force microscopy*, [Annual Review of Materials Science](#) **27**, 381 (1997).
- [6] A. Raman, S. Trigueros, A. Cartagena, A. Stevenson, M. Susilo, E. Nauman, and S. A. Contera, *Mapping nanomechanical properties of live cells using multi-harmonic atomic force microscopy*, [Nature nanotechnology](#) **6**, 809 (2011).
- [7] J. Tamayo and R. Garcia, *Relationship between phase shift and energy dissipation in tapping-mode scanning force microscopy*, [Applied Physics Letters](#) **73**, 2926 (1998).
- [8] J. Cleveland, B. Anczykowski, A. Schmid, and V. Elings, *Energy dissipation in tapping-mode atomic force microscopy*, [Applied Physics Letters](#) **72**, 2613 (1998).
- [9] R. W. Stark, G. Schitter, M. Stark, R. Guckenberger, and A. Stemmer, *State-space model of freely vibrating and surface-coupled cantilever dynamics in atomic force microscopy*, [Physical Review B](#) **69**, 085412 (2004).
- [10] K. Gadelrab, S. Santos, J. Font, and M. Chiesa, *Single cycle and transient force measurements in dynamic atomic force microscopy*, [Nanoscale](#) **5**, 10776 (2013).
- [11] S. Basak and A. Raman, *Dynamics of tapping mode atomic force microscopy in liquids: Theory and experiments*, [Applied Physics Letters](#) **91**, 064107 (2007).
- [12] T. R. Rodriguez and R. Garcia, *Tip motion in amplitude modulation (tapping-mode) atomic-force microscopy: Comparison between continuous and point-mass models*, [Applied Physics Letters](#) **80**, 1646 (2002).

- [13] J. E. Sader, T. Uchihashi, M. J. Higgins, A. Farrell, Y. Nakayama, and S. P. Jarvis, *Quantitative force measurements using frequency modulation atomic force microscopy—theoretical foundations*, *Nanotechnology* **16**, S94 (2005).
- [14] S. Hu and A. Raman, *Inverting amplitude and phase to reconstruct tip–sample interaction forces in tapping mode atomic force microscopy*, *Nanotechnology* **19**, 375704 (2008).
- [15] S. Hu and A. Raman, *Analytical formulas and scaling laws for peak interaction forces in dynamic atomic force microscopy*, *Applied Physics Letters* **91**, 123106 (2007).
- [16] L. Wang, *Analytical descriptions of the tapping-mode atomic force microscopy response*, *Applied physics letters* **73**, 3781 (1998).
- [17] V. Vahdat and R. W. Carpick, *Practical method to limit tip–sample contact stress and prevent wear in amplitude modulation atomic force microscopy*, *ACS nano* **7**, 9836 (2013).
- [18] H. Sadeghian, R. Herfst, B. Dekker, J. Winters, T. Bijmagne, and R. Rijnbeek, *High-throughput atomic force microscopes operating in parallel*, *arXiv preprint arXiv:1611.06582* (2016).
- [19] H. Sadeghian, R. Herfst, J. Winters, W. Crowcombe, G. Kramer, T. van den Dool, and M. H. van Es, *Development of a detachable high speed miniature scanning probe microscope for large area substrates inspection*, *Review of Scientific Instruments* **86**, 113706 (2015).
- [20] R. Herfst, B. Dekker, G. Witvoet, W. Crowcombe, D. de Lange, and H. Sadeghian, *A miniaturized, high frequency mechanical scanner for high speed atomic force microscope using suspension on dynamically determined points*, *Review of Scientific Instruments* **86**, 113703 (2015).
- [21] R. Garcia and E. T. Herruzo, *The emergence of multifrequency force microscopy*, *Nature nanotechnology* **7**, 217 (2012).
- [22] O. Sahin, S. Magonov, C. Su, C. F. Quate, and O. Solgaard, *An atomic force microscope tip designed to measure time-varying nanomechanical forces*, *Nature nanotechnology* **2**, 507 (2007).
- [23] J. Preiner, A. Ebner, L. Chtcheglova, R. Zhu, and P. Hinterdorfer, *Simultaneous topography and recognition imaging: physical aspects and optimal imaging conditions*, *Nanotechnology* **20**, 215103 (2009).
- [24] J. R. Lozano and R. Garcia, *Theory of multifrequency atomic force microscopy*, *Physical Review Letters* **100**, 076102 (2008).
- [25] O. Sahin, G. Yaralioglu, R. Grow, S. Zappe, A. Atalar, C. Quate, and O. Solgaard, *High-resolution imaging of elastic properties using harmonic cantilevers*, *Sensors and Actuators A: Physical* **114**, 183 (2004).

- [26] A. F. Sarioglu, M. Liu, and O. Solgaard, *High-resolution nanomechanical mapping using interferometric-force-sensing afm probes*, [Journal of Microelectromechanical Systems](#) **20**, 654 (2011).
- [27] H. Li, Y. Chen, and L. Dai, *Concentrated-mass cantilever enhances multiple harmonics in tapping-mode atomic force microscopy*, [Applied Physics Letters](#) **92**, 151903 (2008).
- [28] J. R. Felts and W. P. King, *Mechanical design for tailoring the resonance harmonics of an atomic force microscope cantilever during tip–surface contact*, [Journal of Micromechanics and Microengineering](#) **19**, 115008 (2009).
- [29] Q. Xia, T. Zhou, M. Y. Wang, and T. Shi, *Shape and topology optimization for tailoring the ratio between two flexural eigenfrequencies of atomic force microscopy cantilever probe*, [Frontiers of Mechanical Engineering](#) **9**, 50 (2014).
- [30] M. Loganathan and D. A. Bristow, *Bi-harmonic cantilever design for improved measurement sensitivity in tapping-mode atomic force microscopy*, [Review of Scientific Instruments](#) **85**, 043703 (2014).
- [31] M. Li, H. X. Tang, and M. L. Roukes, *Ultra-sensitive nems-based cantilevers for sensing, scanned probe and very high-frequency applications*, [Nature nanotechnology](#) **2**, 114 (2007).
- [32] H.-J. Butt, B. Cappella, and M. Kappell, *Force measurements with the atomic force microscope: Technique, interpretation and applications*, [Surface science reports](#) **59**, 1 (2005).
- [33] N. Burnham, X. Chen, C. Hodges, G. Matei, E. Thoreson, C. Roberts, M. Davies, and S. Tendler, *Comparison of calibration methods for atomic-force microscopy cantilevers*, [Nanotechnology](#) **14**, 1 (2002).
- [34] C.-Y. Lai, S. Santos, and M. Chiesa, *Reconstruction of height of sub-nanometer steps with bimodal atomic force microscopy*, [Nanotechnology](#) **27**, 075701 (2016).
- [35] C.-Y. Lai, V. Barcons, S. Santos, and M. Chiesa, *Periodicity in bimodal atomic force microscopy*, [Journal of Applied Physics](#) **118**, 044905 (2015).
- [36] H. Sadeghian and M. S. Tamer, European Patent 15181449.8 .
- [37] M. S. Tamer, H. Sadeghian, A. Keyvani, H. Goosen, and F. van Keulen, *Quantitative measurement of tip-sample interaction forces in tapping mode atomic force microscopy*, [Proceedings of the 13th International Workshop on Nanomechanical Sensing](#), 199 (2016).
- [38] M. Antognozzi, M. D. Szczelkun, A. N. Round, and M. J. Miles, *Comparison between shear force and tapping mode afm-high resolution imaging of dna*, [Single Molecules](#) **3**, 105 (2002).

- [39] C.-W. Yang, S. Hwang, Y. F. Chen, C. S. Chang, and D. P. Tsai, *Imaging of soft matter with tapping-mode atomic force microscopy and non-contact-mode atomic force microscopy*, [Nanotechnology](#) **18**, 084009 (2007).
- [40] H. G. Hansma, D. Laney, M. Bezanilla, R. L. Sinsheimer, and P. K. Hansma, *Applications for atomic force microscopy of dna*, [Biophysical journal](#) **68**, 1672 (1995).

8

REAL-TIME ESTIMATION OF THE TIP-SAMPLE INTERACTIONS IN TAPPING MODE ATOMIC FORCE MICROSCOPY WITH A REGULARIZED KALMAN FILTER

The real-time and accurate measurement of tip-sample interaction forces in Tapping Mode Atomic Force Microscopy (TM-AFM) is impossible. This obstruction fundamentally stems from the causality of the physical systems. Since i) the input of the dynamic systems propagate to the output with some delay, and ii), multiple inputs can generate the same output, there exist no measurement or estimation technique that can accurately estimate the force input of the systems in real-time. However, an approximate and delayed estimation can still be possible. This paper presents a general-purpose algorithm which aims to estimate a delayed approximation of the force input of TM-AFM with minimum delay and error. For this reason, first, the input estimation problem is converted to an ill-posed state observation problem. Then, a Tikhonov-like regularization technique is applied to eliminate the ill-conditioning and estimate the force input using a linear Kalman filter. The proposed input observer is remarkably robust, real-time in the order of the sampling frequency, and applicable for any Linear Time Invariant (LTI) system with a (semi-) periodic process. Simulation and experimental results show that using the proposed algorithm with a wide-band AFM probe; one can determine the TSI forces with only a few percent error and a delay in the order of sampling time. Unlike the existing force estimation techniques for AFM, this algorithm does not require any prior knowledge of the force-distance relationship which can be very beneficial in the closed-loop control of AFM.

8.1. INTRODUCTION

One of the most popular Atomic Force Microscopy (AFM) techniques is the Tapping Mode AFM (TM-AFM). In TM-AFM, a cantilever with a sharp tip attached to its free end is excited at a frequency near its fundamental resonance frequency to reach a specified free air amplitude. Then, using a piezoelectric actuator, it is brought into proximity of the sample surface. Due to the intermittent interactions of the tip and sample surface, the vibration amplitude reduces which provides an indication of the distance between the sample surface and the zero deflection configuration of the cantilever (hereafter referred to as overall distance). Scanning the sample surface while adjusting the overall distance to keep the amplitude constant, a topographic profile of the sample is recorded. At the same time, the phase of the motion of the cantilever is recorded which can provide information on the non-conservative interactions of the tip and sample [1].

During each interaction cycle, a combination of attractive, repulsive, and dissipative forces affect the tip. However, since these loads occur only during a short fraction of the vibration cycle, the cantilever only responds to a periodic average, i.e., the first Fourier component of the force, which is also referred to as the virial and dissipation pair [1, 2].¹ Since infinitely many different forces can have the same periodic average, one can conclude that full estimation of the TSI forces from TM-AFM signals is almost impossible [3]. The above argument in frequency domain reads as: the Tip-Sample Interaction (TSI) force has many frequency components, but only one of them corresponds to the fundamental resonance frequency of the cantilever. The other frequency components of the force, however, appear at frequencies for which the cantilever is relatively insensitive, and therefore, weakly appear in the output signal. Hence, the motion of the cantilever remains harmonic up to a large extent while the higher frequency content of the motion are entirely inconsiderable and indistinguishable from noise [4]. In a sense, the cantilever filters out all the information that is modulated by the higher frequency components of the TSI force and, thus, makes it extremely elusive to measure the TSI force.

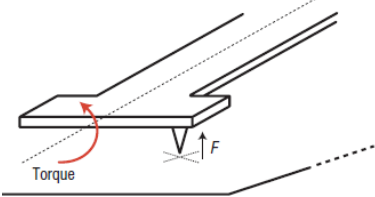
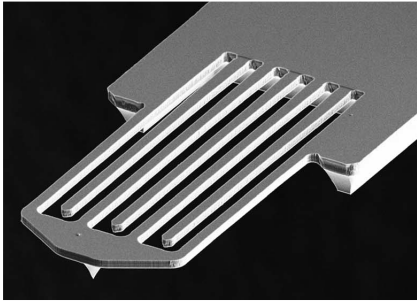
To recover the TSI force in dynamic AFM, researchers have developed different methods that can be classified roughly into three sets of approaches. The first is to assume a force-distance relationship and fit the average TSI force calculated from the experiments to its counterpart from the considered model. For example, Hu and Raman [5] estimated the peak repulsive and attractive forces in AFM by assuming the Derjaguin-Muller-Toporov (DMT) force model. The second approach which is also known as force spectroscopy applies a sweeping of a parameter, such as the overall distance or vibration amplitude, and records the displacement signal as a function of that parameter. As a result, one can calculate the force-distance curve, but not in real-time [6–8]. In this context, a very useful interpretation is presented by Sader *et al.* [9]. The third set of techniques assume that the TSI force is a periodic impulse function (similar to the first approach) and estimate the amplitude of this functions using linear observers [10–12]. With this method, one can estimate an equivalent TSI force in real-time. However, the error between the real force and its estimate remains ambiguous because the TSI force is not a periodic impulse function. In general, standard cantilevers provide only a nar-

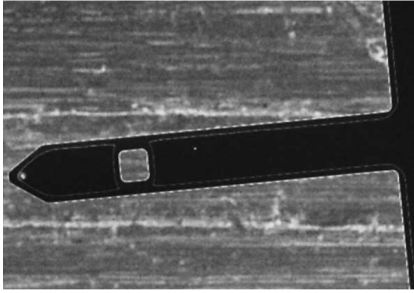
¹Virial and dissipation refer to the period average of the conservative and non-conservative forces, respectively.

rowband output signal, and tip-sample interactions are extensively wideband. Consequently, it is not possible to extract the full information on the TSI force in real-time with a single frequency AFM.

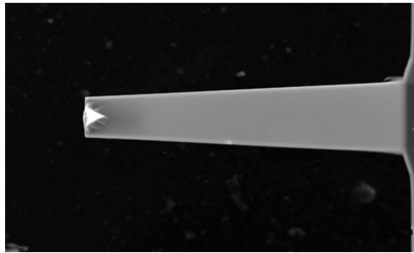
To overcome the problem of the narrowband output of the cantilever, researchers have introduced new types of probes and different experiments which provide sub- and superharmonic frequency components (hereafter referred to as wideband probes) [13–15]. The wideband probes have different embodiments and provide different output signals. However, they share a common dynamic peculiarity. That is, they have one or more additional resonator(s) which are sensitive to other frequency components of the tip-sample interaction. For example, Sahin *et al.* [14] activated the torsion mode of the cantilever as the auxiliary resonator by relocating the tip (known as Torsional Harmonic probe or HMX). Sarioglu *et al.* [15] etched a smaller cantilever near the tip of the cantilever, Shaik *et al.* [16] etched a small structure near the tip as an extra acceleration sensor, Tamer *et al.* [17] used a secondary cantilever instead of the sample, and Keyvani *et al.* [3] tuned the second bending mode of the cantilever to capture the 6th superharmonic of the forces. Table 8.1 shows a list of some of the wide band probes in the literature.

Table 8.1: An overview of some of the wideband AFM probes

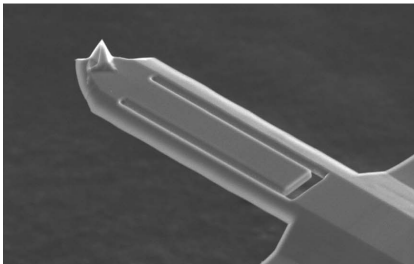
Figure (SEM image or schematic)	Name and characteristic information
	<p>Torsionally harmonic probes [14]. The torsion mode of the cantilever is excited due to the first 17 frequency components of the TSI force.</p>
	<p>Interferometric force sensing probes [15]. The high frequency content of the TSI force are captured via the small structure at the end of the cantilever and transmitted to the detector via interference pattern.</p>



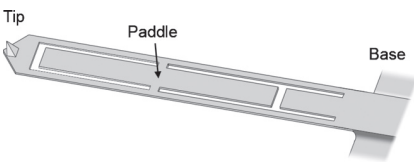
A harmonic cantilever [18]. The third bending mode of the cantilever is tuned to capture the 16th frequency component of the TSI force.



Dynamically tuned cantilevers [3]. The second bending mode of the cantilever is tuned to capture the 6th frequency content of the TSI force.



Bi-harmonic probes [13]. The second mode of the cantilever captures the second frequency component of the TSI force.



Cantilever with internal paddles [19]. The paddles introduced in the cantilever form the additional resonator(s) needed for wideband probe.

The wideband characteristics of the aforementioned probes in TM-AFM can also be replicated using normal probes, but in sub-resonance modes. The concept of wideband AFM is to be able to sense more than one frequency component of the TSI force at the output of the cantilever. This can be achieved either by introducing auxiliary resonators (as in wideband probes), or actuating the single resonator below its resonance frequency. The sub-resonance modes with conventional probes, namely the jumping mode, pulsed force mode, or the peak force tapping mode [20, 21] can be considered as the same dynamics concept as the tapping mode with wideband probes because their

output is also wideband. In these modes, the cantilever probe is slowly brought into contact with the sample surface and retracted periodically. Since the periodicity of the cycle is much lower than the resonance frequency of the cantilever, a considerable number of frequency components of the forces pass from the static band of the cantilever and provide a non-harmonic deflection signal. In these modes, if the actuation signal is significantly slower than the resonance frequency of the cantilever, it is possible to consider the cantilever as a spring and calculate the forces directly from the displacement. However, if the actuation frequency exceeds a certain amount, the cantilever resonates, and the deflection signal is not proportional to the TSI force. This limitation usually restricts the imaging speed in these modes.

The deflection signals of the wideband probes (or any probe in sub-resonance mode) contain more information on the TSI force in comparison to single frequency TM-AFM. This information can be recovered either as additional contrast source or as an estimation of the TSI force. For example, Sarioglu *et al.* [15] used the amplitude and phase of the superharmonic components to generate more images providing information on the material properties of the samples. Belianinov *et al.* [22] presented a method based on post-processing the time resolved data in jumping mode AFM. They saved the deflection signal in a large matrix (4 or 8 GB file) and performed an eigenvalue analysis of the data which mimics an unlimited number of lock-in amplifiers (as many as necessary). The latter method is computationally expensive and unfeasible for real-time applications, but guarantees that all statistically relevant information is captured.

Researchers also used different filtering techniques to estimate the TSI force in real-time using wideband probes. For example, Sahin *et al.* [23] used a harmonic balancing method to determine the TSI force, however, this approach requires an averaging step to reduce the noise. Tamer *et al.* [17] used a band stop filter to remove the vibration of the sensing cantilever from the signal. The outcome of these techniques resembles the tip-sample interactions in shape. However, whether the estimated TSI force achieved by this methods is actually "the TSI force" is still a question. For example, usually contact time and adhesion force are overestimated, while the peak repulsive force is underestimated. Besides, the estimated TSI force considerably depends on the choice of the filter parameters [17]. In these techniques, a force estimate is calculated by filtering out the vague vibrations from the displacement signal and scaling it with the spring constant of the cantilever. Nonetheless, filtering out the oscillations from the deflection signal can not simplify a dynamic problem to a static one. For a vibrating cantilever, the spring constant multiplied by the filtered deflection signal is not necessarily equal to or even proportional to the TSI force.

To calculate the TSI force, one has to consider the dynamics of the cantilever and solve an input estimation problem. Besides, the estimation algorithm should guarantee an unbiased estimate of the forces. In other words, the expected error between the estimated force (\hat{f}_{ts}) and the real forces (f_{ts}), defined as $\epsilon = f_{ts} - \hat{f}_{ts}$, should exponentially decay with time, and its variance should only depend on the measurement noise and model uncertainties.

This paper presents a new type of Kalman filter as an input observer, which gives a general solution for the real-time force estimation problem in wideband AFM. The estimated force achieved by the Kalman filter is optimum, in the sense that the expected

value for the error exponentially vanishes with time and uncertainty of the assessed value is less than the uncertainty of any of the information provided to the algorithm. The estimation method presented here does not require any prior knowledge on the tip-sample interaction model, it is computationally inexpensive, easily real-time implemented, robust and captures all the statistically relevant information. Depending on the embodiment of the wideband probe and relative noise levels, the estimated force consistently approaches the actual TSI force.

The next section describes the mathematical formulation of the input observer which consist of discrete time model of the wideband probe, converting the input observation to an ill-conditioned state observation, regularization of the ill-conditioning, and step-by-step implementation of the regularized Kalman filter. The performance of the proposed filter is evaluated using two case studies in Section 8.3, followed by the Conclusions.

8.2. REGULARIZED KALMAN FILTER

Unfortunately, the input estimation problem does not have a general solution in control theory because of two main challenges. First, if the system is nonminimum phase, its inverse is unstable, [24]. Secondly and more importantly, the inverse of a causal system is noncausal [25]. In other words, because the output of the system at any time depends on its input at previous times, the estimate of the input should be calculated using the future output data. These two problems impose fundamental limitations on real-time and exact input estimation. Hence, researchers have proposed different techniques to design stable and causal approximate inverse systems [26, 27]. Naturally, all these techniques estimate the input with some error and delay [28] for which an optimum approximation is achieved based on a tradeoff between delay and error.

The non-causality in estimating the TSI force in AFM translates to the following analogy: Since the quality factor of the AFM cantilever is in the order of 100, the effects of the TSI force at a particular time, remain relevant for the output of the cantilever for hundreds of tapping cycles. Hence, to estimate the force input at any moment, one has to wait and measure the motion of the cantilever for hundreds of cycles later. Obviously, such a delay is not acceptable. However, if a wideband probe is used, one can benefit from the other measurable frequency components of the motion to minimize the delay and the uncertainty.

Here, we suggest a new method by first transforming the unknown input estimation problem to an ill-conditioned state observation problem, and subsequently, resolving the ill-conditioning by assuming that the tip-sample interaction forces are nearly, but not exactly, periodic. We begin with a state-space representation of the cantilever as a linear dynamic system. Any of the wideband probes (or the conventional cantilevers in sub-resonance AFM) can be described with an n degrees of freedom discrete-time linear model as:

$$\begin{aligned} x_{k+1} &= Ax_k + B_1 f_k^{ts} + B_2 f_k^d + \omega_k, \\ y_k &= Cx_k + D_1 f_k^{ts} + D_2 f_k^d + \nu_k. \end{aligned} \tag{8.1}$$

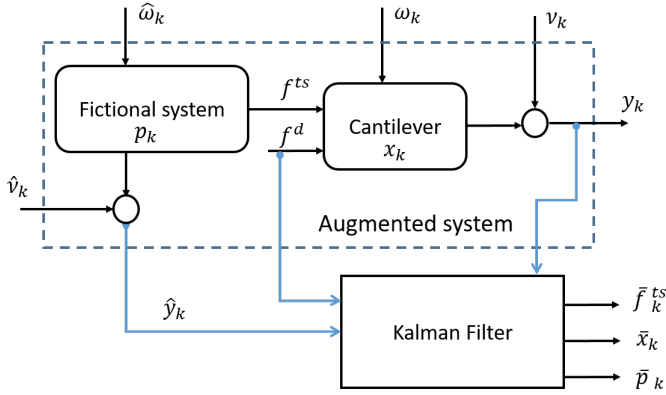


Figure 8.1: Schematic view of proposed input observer. The Kalman filter is designed based on the dynamics of the augmented system in the dashed box which does not have any unknown input. The fictional system is designed to impose the assumptions and sandwich the unknown input f^{ts} between two known system.

where $x_k \in \mathbb{R}^{n \times 1}$ represents the dynamic states of the cantilever in discrete time step k . Considering that only few vibration modes of the cantilever contribute to its dynamic motion, and each mode has two state variables, n is twice the number of vibration modes. $A \in \mathbb{R}^{n \times n}$ is the dynamic process matrix of the system, B_1 and $B_2 \in \mathbb{R}^{n \times 1}$ are the input matrices that transfer the effects of tip-sample interactions (f^{ts}) and dithering force (f^d) to the state vector, respectively. The output signals are gathered in $y_k \in \mathbb{R}^{r \times 1}$, which is a linear combination of the states with weight of $C \in \mathbb{R}^{r \times n}$. r is the number of the output channels. For example, for the HMX probes [14] $r = 2$, i.e. the vertical and torsional signals, and for dynamically tuned cantilevers [3] $r = 1$. The tip-sample interactions and dither signals are fed through to the output via weights D_1 and $D_2 \in \mathbb{R}^{r \times 1}$, respectively. The noise $\omega_k \in \mathbb{R}^{n \times 1}$ and $v_k \in \mathbb{R}^{r \times 1}$ represent the process noise (or model uncertainty) and measurement noise (or error), respectively, and are assumed to be zero-mean Gaussian processes. The measurement and process noise are assumed to be uncorrelated with respect to each other ($\mathbb{E}(\omega, v) = O$).

Note that, in Eq(8.1) only the outputs (y_k) and one of the inputs (f_k^d) can be measured. The state variables (x_k), and the unknown inputs (f_k^{ts}) are to be estimated. This will be discussed in the next subsection.

8.2.1. TRANSFORMING THE INPUT ESTIMATION TO STATE ESTIMATION

As explained above, there is no general solution for the input estimation problem in control theory. Hence, we propose to convert the input estimation problem to a standard state estimation based on the architecture shown in Fig. 8.1. The objective of having an fictional system next to the real system (cantilever) is to exploit the semi-periodicity assumption, and sandwich the unknown input between the two systems.

The fictional system in Fig. 8.1 can be written as:

$$p_{k+1} = \hat{A}p_k + \hat{\omega}_k, \quad (8.2a)$$

$$f_k^{ts} = \hat{C}p_k. \quad (8.2b)$$

$$\hat{y}_k = \hat{C}^{(2)} p_k + \hat{v}_k \quad (8.2c)$$

where Eq(8.2a) represents the dynamic process in which only the random noise input $\hat{\omega}_k$ affects the fictional state variables p . The fictional system has two outputs. The first output generates the unknown TSI force via a measurement matrix \hat{C} as in Eq(8.2b). The second output which is represented by Eq(8.2c) gives a measurable indication of the semi-periodicity assumptions. If all the system matrices are known and time-independent, the unknown input estimation problem is transformed to observation of the augmented states $([x_k^T p_k^T]^T)$ of the following Linear Time-Invariant (LTI) system, which can be done using a Kalman filter, or any linear observer.

$$\begin{pmatrix} x_{k+1} \\ p_{k+1} \end{pmatrix} = \begin{bmatrix} A & B_1 \hat{C} \\ O & \hat{A} \end{bmatrix} \begin{pmatrix} x_k \\ p_k \end{pmatrix} + \begin{bmatrix} B_2 \\ O \end{bmatrix} f_k^d + \begin{pmatrix} \omega_k \\ \hat{\omega}_k \end{pmatrix}, \quad (8.3)$$

$$y_k = [C \ D_1 \hat{C}] \begin{pmatrix} x_k \\ p_k \end{pmatrix} + D_2 f_k^d + v_k.$$

The following section presents a method to calculate a time independent set of system matrices for the fictional system, which implements the semi-periodicity assumption.

8.2.2. REGULARIZATION

Both the sub-resonance and TM-AFM are semi-periodic processes, i.e., any event that happens in each cycle is plausible, but not guaranteed, to happen again in the next cycle. On the other hand, the Fourier transform of any periodic function can only contain harmonic signals with frequencies that are integer multiples of the periodicity of the function. Therefore, a semi-periodic signal (f_k^{ts} e.g.,) can be considered as a summation of semi-harmonic signals $f_k^{ts} = \sum s_k^{(i)}$, $s^{(i)}$ being the i^{th} frequency component of the f^{ts} .

Generally, if s is a harmonic signal with frequency Ω , it should satisfy the following equation:

$$\ddot{s} + \Omega^2 s = \epsilon, \quad \epsilon = 0.$$

Yet, if the signal s deviates from being harmonic, ϵ would not vanish, instead would provide a linear measure of this deviation.

In a discrete time notation, the above equation can be written as:

$$\Omega_f^2 (s_k - 2s_{k-1} + s_{k-2}) + \Omega^2 s_k = \epsilon_k, \quad (8.4)$$

where Ω_f is the sampling frequency. Apart from finite difference truncation and a round-off error, ϵ_k provides a measure for any deviation from a harmonic signals with the frequency Ω . For multiple frequencies, Eq(8.4) can be written in matrix form as follows:

$$\begin{bmatrix} 1 & \Omega_f^2 - 2 & 1 \end{bmatrix} \begin{pmatrix} s_k \\ s_{k-1} \\ s_{k-2} \end{pmatrix} = \frac{\epsilon_k}{\Omega_f^2}. \quad (8.5)$$

Eq(8.5) shows that a signal has to be sampled at three time instances so that one can construct a linear measure of its deviation from being harmonic. Therefore, we suggest

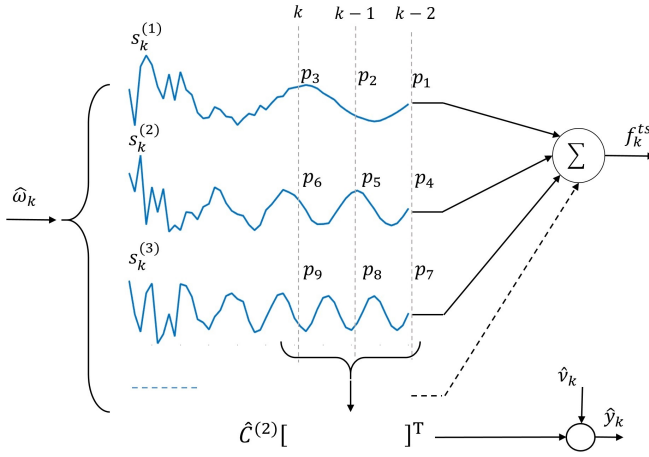


Figure 8.2: Schematic signal view of the fictional system in Fig. 8.1. The TSI force (f_k^{ts}) is a summation of N semi-harmonic signals, whereas their deviation from being harmonic is measured individually by multiplying to $\hat{C}^{(2)}$ and assembled in \hat{y}_k . Three time instances of each harmonic signal is defined as the state vector of the system.

the architecture represented by Fig. 8.2 to design the \hat{A} and \hat{C} matrices which were introduced in the previous section.

Suppose that the motion of the wideband probe consists of N frequency components that are above the noise floor. Then in the best scenario, N frequency component of the estimated TSI force can be accurate. Therefore, the TSI force has to be a summation of maximum N semi-harmonic signals. For such a configuration, the states variables for the fictional system can be defined as follows:

$$p_k = \begin{bmatrix} s_{k-2}^{(1)} & s_{k-1}^{(1)} & s_k^{(1)} & s_{k-2}^{(2)} & s_{k-1}^{(2)} & s_k^{(2)} & \cdots & s_{k-2}^{(N)} & s_{k-1}^{(N)} & s_k^{(N)} \end{bmatrix}^T, \quad (8.6)$$

where $s^{(i)}$ represents the i^{th} harmonic component of the TSI force. By defining the state variables as in Eq(8.6), the process matrix (\hat{A}) has to implement a shift register, and the first output matrix (\hat{C}) only implements the summation. In matrix notation, this reads:

$$\hat{A} = I_{N \times N} \otimes \begin{bmatrix} 1 & 0 & 0 \\ 1 & 0 & 0 \\ 0 & 1 & 0 \end{bmatrix}, \quad \hat{C} = \mathbf{1}_{1 \times N} \otimes [1 \quad 0 \quad 0], \quad (8.7)$$

where \otimes is the Kronecker product operator.

Without the fictional measurement (\hat{y}), the state observation problem of the total system is ill-conditioned, because the poles of the \hat{A} matrix are all either zero or one. In other words, the fictional system represented by Eq(8.2) is marginally stable. Physically, this means that there can be infinitely many different state values ($[x \ p]^T$) that would show exactly the same input (f^d) and output signals (y). To eliminate the ill-conditioning, the periodicity assumption in Eq(8.5) is implemented as an extra fictional output of the system. Note that the signal \hat{y} does not exist and we can not measure it.

Nonetheless, by assuming that it was measured to be always zero, we eliminate all the infinity different possibilities for state variables ($[x \ p]^T$) and retain the only the semi-periodic one:

$$\hat{y}_k = \hat{C}^{(2)} p_k + \hat{v}_k, \quad (8.8)$$

where $\hat{y}_k = 0, \forall k > 0$ and the fictional noise \hat{v}_k represents the uncertainty of the periodicity assumption. Note that Eq(8.8) does not enforce any deterministic assumption on the structure of the input (TSI force) as it contains the stochastic noise and uncertainty represented by $\hat{v} \neq 0$. Similar to the Tikhonov regularization method which compromises between the uncertainty and the error, Eq(8.8) compromises between the uncertainty and the ability to estimate the input in non-periodic conditions.

In the same way, the dynamic model of the cantilever and the measurement signals are assumed to be known, but uncertain ($\omega \neq 0, \nu \neq 0$). Considering Eq(8.5) and Eq(8.6) the $\hat{C}^{(2)}$ matrix in Eq(8.8) is defined as:

$$\hat{C}^{(2)} = \begin{bmatrix} 1, & \frac{\Omega^2}{\Omega_f^2} - 2, & 1, & & O_{1 \times 3(N-1)} \\ O_{1 \times 3}, & 1, & \frac{(2\Omega)^2}{\Omega_f^2} - 2, & 1, & O_{1 \times 3(N-2)} \\ O_{1 \times 6}, & 1, & \frac{(3\Omega)^2}{\Omega_f^2} - 2, & 1, & O_{1 \times 3(N-3)} \\ & & \ddots & & \\ O_{1 \times 3(N-1)}, & & 1, & \frac{(N\Omega)^2}{\Omega_f^2} - 2, & 1 \end{bmatrix}. \quad (8.9)$$

Finally, the problem of estimation of the tip-sample interactions in TM-AFM is converted to the standard linear state observation problem of the following augmented system:

$$\begin{pmatrix} x_{k+1} \\ p_{k+1} \end{pmatrix} = \underbrace{\begin{bmatrix} A & B_1 \hat{C} \\ O & \hat{A} \end{bmatrix}}_{\hat{A}} \begin{pmatrix} x_k \\ p_k \end{pmatrix} + \underbrace{\begin{bmatrix} B_2 \\ O \end{bmatrix}}_{\hat{B}} f_k^d + \begin{pmatrix} \omega_k \\ \hat{\omega}_k \end{pmatrix}, \quad (8.10a)$$

$$\begin{pmatrix} y_k \\ O_{N \times 1} \end{pmatrix} = \underbrace{\begin{bmatrix} C & D_1 \hat{C} \\ O & \hat{C}^{(2)} \end{bmatrix}}_{\hat{C}} \begin{pmatrix} x_k \\ p_k \end{pmatrix} + \underbrace{\begin{bmatrix} D_2 \\ O \end{bmatrix}}_{\hat{D}} f_k^d + \begin{pmatrix} v_k \\ \hat{v}_k \end{pmatrix}, \quad (8.10b)$$

$$f_k^{ts} = [O_{1 \times n} \quad \hat{C}] \begin{pmatrix} x_k \\ p_k \end{pmatrix}. \quad (8.10c)$$

It is straightforward to verify that the system in Eq(8.10) is always fully observable and well-posed. Thus, considering a known expected values for the noise covariance matrices as: $Q = \mathbb{E}\{[\omega^T \hat{\omega}^T]^T [\omega^T \hat{\omega}^T]\}$ and $R = \mathbb{E}\{[v^T \hat{v}^T]^T [v^T \hat{v}^T]\}$, a Kalman filter can be implemented to estimate its states, and consequently, the TSI force. Although the noise covariance matrices are not completely known, each part of them can be tuned to achieve an optimum performance as follows.

- The measurement noise covariance ($\mathbb{E}\{v \ v^T\}$) represents the noise in the deflection sensor, and the electronic parts.

- The process noise ($\mathbb{E}\{\omega \omega^T\}$) covers the thermal noise and any uncertainty in the dynamic model of the cantilever.
- The uncertainty in the periodicity assumption which is represented by ($\mathbb{E}\{\hat{v} \hat{v}^T\}$) can be tuned considering a trade-off between uncertainty and error in non-periodic conditions.
- The process noise of fictional part of the system ($\mathbb{E}\{\hat{\omega} \hat{\omega}^T\}$), represents the step size of the random walk search which can be tuned considering a trade-off between noise in the output and coverage speed.

Note that choosing wrong noise statistics for the Kalman filter does not lead to wrong estimations, but only can increase the noise or reduce the convergence speed. Therefore, in this paper, all the noise covariance matrices are assumed to be identity matrices scaled with a small numbers.

8.2.3. STEP-BY-STEP IMPLEMENTATION

All the calculation steps of the regularized Kalman filter for any of the wideband probes can be expressed as follows:

► **Only once:**

Step1: Either construct a model, or identify the dynamic model of the probe in state-space and transform it to a discrete-time format to find the coefficient matrices in Eq(8.3).

Step2: Based on the frequency spectrum of the measurement signal, the number of frequency components that are above the noise level N . This number determines the maximum reachable accuracy and bandwidth in TSI force estimation.

Step3: Calculate the coefficient matrices \hat{A} , \hat{C} , and ${}^2\hat{C}$ from Eq(8.7) and Eq(8.9).

Step4: Construct the augmented system model as in Eq(8.10), \bar{A} , \bar{B} , \bar{C} , \bar{D} .

Step5: Choose a set of noise covariance matrices Q and R , initial value $\bar{x}_{0|0}$ and initial covariance $\Sigma_{0|0}$.

► **In every sampling time k :**

Step1: Calculate the priory estimate as:

$$\bar{x}_{k+1|k} = \bar{A}\bar{x}_{k|k} + \bar{B}f_k^d,$$

Step2: Calculate the priory error convenience matrix as:

$$\Sigma_{k+1|k} = \bar{A}\Sigma_{k|k}\bar{A}^T + Q,$$

Step3: Calculate the Kalman gain as:

$$K_k = \Sigma_{k+1|k}\bar{C}^T (\bar{C}\Sigma_{k+1|k}\bar{C}^T + R)^{-1}$$

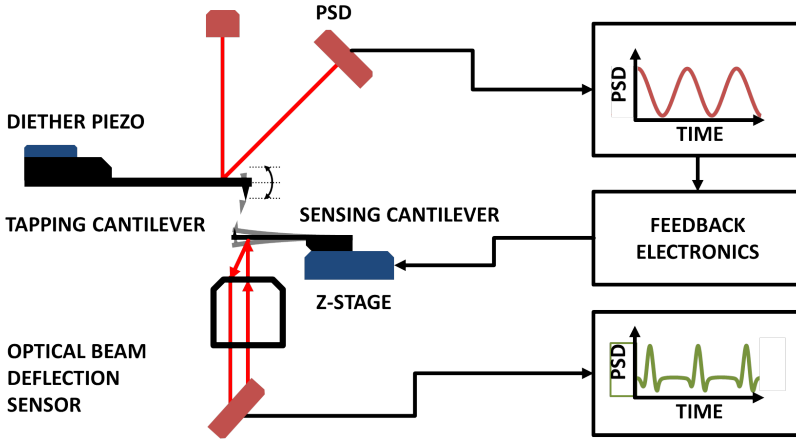


Figure 8.3: Schematic architecture of the nanomechanical force sensing setup [17]. The small cantilever simulates the sample surface at the same time as a force sensor, while the forces exerted by the large cantilever can be measured via the deflection of the small cantilever.

Step4: Calculate the posterior state estimate as:

$$\bar{x}_{k+1|k+1} = \bar{x}_{k+1|k} + K_k(\bar{y} - \bar{C}x_{k+1|k} - \bar{D}f_k^d)$$

Step5: Calculate the posterior error convenience matrix as:

$$\Sigma_{k+1|k+1} = (I - K_k\bar{C})\Sigma_{k+1|k}$$

Step6: Calculate the TSI force as:

$$\tilde{f}_k^{ts} = [O_{1 \times n} \hat{C}]x_{k+1|k+1};$$

8.3. RESULTS AND DISCUSSION

Theoretically, the estimated state variables in a linear observer approach the real state variable with exponential speed. Using a Kalman filter in observation ensures an optimum estimation speed and accuracy if the uncertainties are known. Thus, using the proposed method the estimated value of the forces (\tilde{f}_{ts}) should approach the actual tip-sample interactions in TM-AFM. To verify this statement and study the performance of the method, we apply the method to the following cases.

8.3.1. CASE STUDY 1: FORCE SENSING SETUP

To measure the TSI force in TM-AFM, Tamer *et al.* [17] presented a measurement technique that uses a small and high-frequency cantilever as a force sensor and puts it under the imaging cantilever instead of the sample surface. The schematic view of the force sensing setup is presented in Fig. 8.3.

Since the sensing cantilever has a much higher resonance frequency in comparison to the tapping cantilever, most of the frequency components of the forces are below the

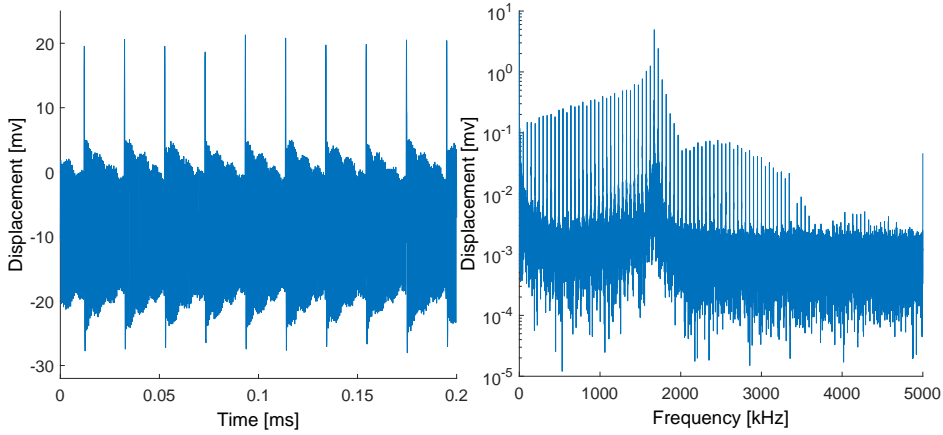


Figure 8.4: Measured deflection of sensing cantilever in force sensing setup in time and frequency domain

resonance of the sensing cantilever. Thus, the sensing cantilever can act as a wideband probe which has a non-harmonic output. This configuration mimics the sub-resonance modes for the sensing cantilever. Since the resonance frequency of the tapping cantilever is not low enough, when compared to the sensing cantilever, the sensing cantilever resonates due to the super-harmonic contents of the TSI force. With the Kalman filter proposed in the previous section, we try to estimate the TSI force from the measured deflection of the force sensing cantilever.

In this case, the resonance frequency of the sensing cantilever and tapping cantilever were measured as 1.7 MHz and 50 kHz , respectively, and the quality factor of both the cantilevers was about 250. The tapping cantilever is excited at its resonance frequency and is engaged with the sensing cantilever using a piezoelectric stage. The piezoelectric stage is controlled by a commercial AFM controller, and the motion of the sensing cantilever is measured using a separate optical beam deflection setup (Position Sensitive Detector PSD). More details about this experiment are provided in [17]. The motion of the sensing cantilever and its frequency domain representation are shown in Fig. 8.4.

As it can be seen, there are about 70 frequency components that are above the noise level, which means that the sensing cantilever can provide information on 70 frequency components of the tip-sample interactions. Applying the steps presented in Section 8.2.3, the forces are estimated and presented in Fig. 8.5.

As can be seen, the estimated values for deflection and force start from zero initial conditions and within a few sampling time reach their stationary values. To check correctness and robustness of the method, we simulate the experiment using a DMT force model [29] and add 30 dB SNR noise ($20 \log \frac{\text{Signal}}{\text{Noise}} = 30$) to the simulated deflection signal. Fig. 8.6 shows a comparison between the simulated TSI force, estimated TSI force which is achieved by applying the Kalman filter to the noisy deflection signal. The assessed value of the TSI force flawlessly follows the one from the simulations. Note that, to show the performance of the regularized Kalman filter in non-periodic situations,

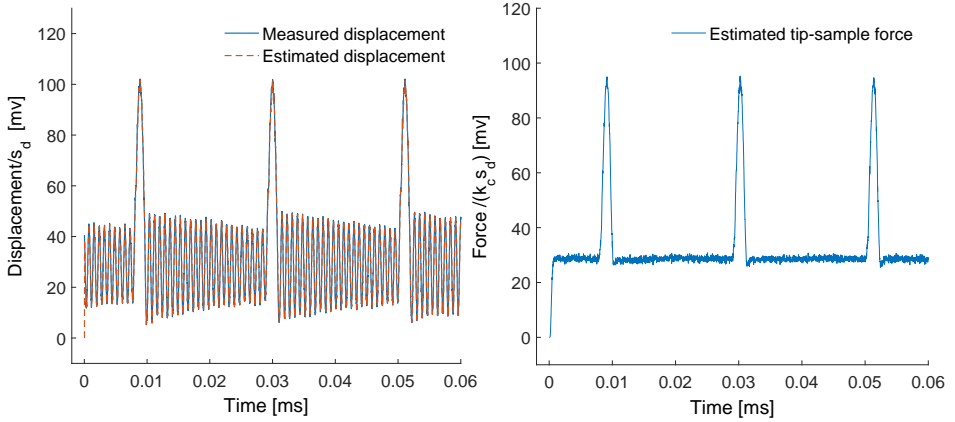


Figure 8.5: Measured deflection, estimated deflection and estimated forces from the force sensing setup. The coefficients s_d and k_c are the deflection sensitivity and spring constant of the sensing cantilever.

Fig. 8.6 intentionally presents the TSI forces in transient situations. The transient cases are more interesting than the steady state because of controller design reasons. Besides, typically the AFM can be more damaging in transient situations [30]. As it can be seen, the TSI force is not periodic in the transient situation and violates the assumption in Section 8.2.2. However, the uncertainty which is introduced in Eq(8.8) allows for its violation and estimation of the non-periodic forces.

subsectionRobustness Since a certain level of uncertainty is considered in every measurement, model, or assumption, the presented method is considerably robust to the errors in system parameters. To verify the robustness of the method, we compare the estimated forces by deliberately using wrong parameters in the first step of Section 8.2.3, as if the dynamic properties of the cantilever were measured with significant errors.

In Fig. 8.7, each curve shows a force estimate from a noisy output data, with wrong prior knowledge containing all the errors from the previous curves. As it can be seen, the performance of the Kalman filter is barely affected by the errors in the dynamic model and measurement noises.

8.3.2. ARBITRARY FORCE-DISTANCE RELATIONSHIP

The proposed filter does not consider any prior knowledge on the force models. Therefore, it can capture any arbitrary force-distance relationship. This aspect of the proposed filter can have interesting applications in the field biological AFM. For example, researchers measure the unfolding force of proteins using a chemically functionalized AFM tip [31]. Due to the frequency limitations of the cantilever, these binding and unbinding forces can only be measured up to a limited retract velocity. However, researchers have shown that the unbinding velocity has a substantial effect on the measured forces [32, 33]. We suggest that using the presented Kalman filter together with a wideband probe, the unfolding and unbinding forces can be measured more accurately, robustly and also with much higher approach-retract velocities. To simulate such a binding-

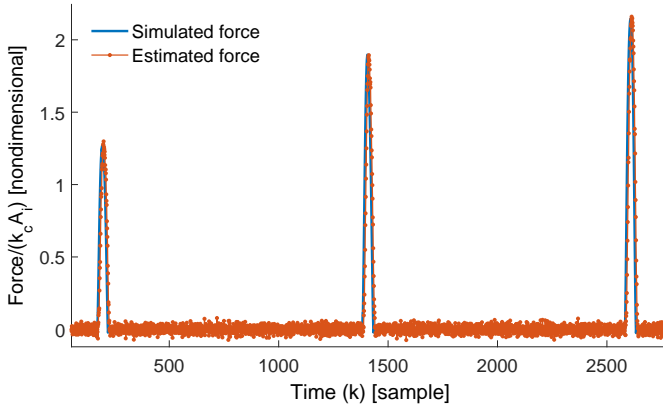


Figure 8.6: simulated and estimated tip-sample interactions from the noisy simulated deflection signal (30db SNR) in transient situation

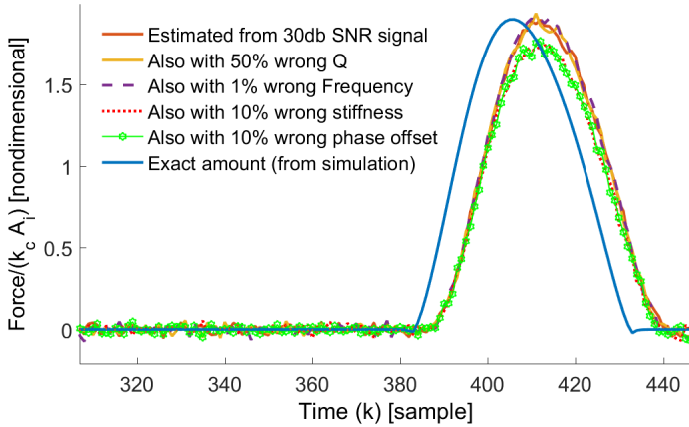


Figure 8.7: Simulated and estimated tip-sample interactions from the noisy simulated deflection signal (30db SNR) also considering wrong system dynamics. Each curve also contains all the errors from the previous curve.

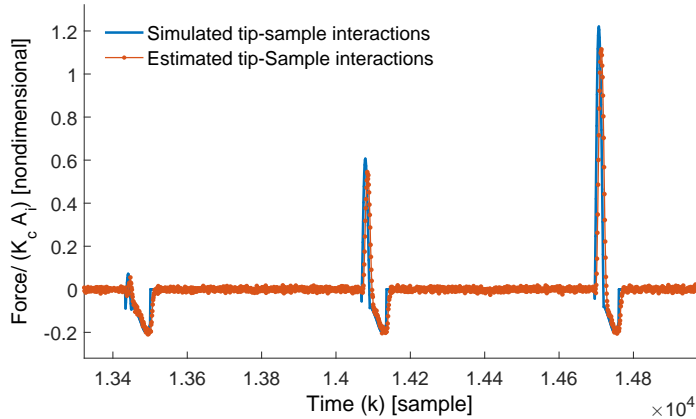


Figure 8.8: Simulated and estimated tip-sample interactions from the noisy simulated deflection signal (30db SNR) in transient situation with a binding model

unbinding experiment, we add an elastic-perfectly-plastic model to the DMT force model. In this example, the tip binds to the surface after each tap via a finite length elastic rope. This rope—which mimics the protein chain—yields in a plastic regime when the stresses exceed a certain amount.

The simulated and estimated TSI force with the above-mentioned discretionary model are presented in Fig. 8.8 (also in a transient conditions). As it can be seen, the proposed method provides an accurate estimate of the tip-sample interactions.

8.3.3. CASE STUDY 2: DYNAMICALLY TUNED CANTILEVERS

As another example of the wideband probes, here we shall present the force estimation using a dynamically tuned cantilever. As discussed in Section 8.1, using the information on the amplitude and phase of a conventional AFM probe it is possible to estimate the periodic average of the force [34]. However, the details about the TSI force are obscured by the noise. We have previously shown that [3] by passively tuning the resonance of the second bending mode of the cantilever, it is possible to pass more information on TSI force to the deflection signal. In a tuned cantilever, the 6th frequency component of the TSI force coincides with the resonance of the second bending mode of the cantilever and generates another harmonic motion with six times higher frequency. Although the cantilever itself suppresses many of the frequency components of the force, still a rough estimation of the TSI force is possible. Fig. 8.9 shows the TSI force estimation using a tuned cantilever as the wideband probe.

In Fig. 8.9, the Kalman filter tries to estimate a signal that resembles the first and sixth Fourier component of the tip-sample forces. Mathematically, the first and sixth complex periodic average of the forces defined as Eq(8.11) are equal between the real force and the estimated force. However, because the motion of the cantilever does not carry any information on the other Fourier components of the TSI force, the estimated value does

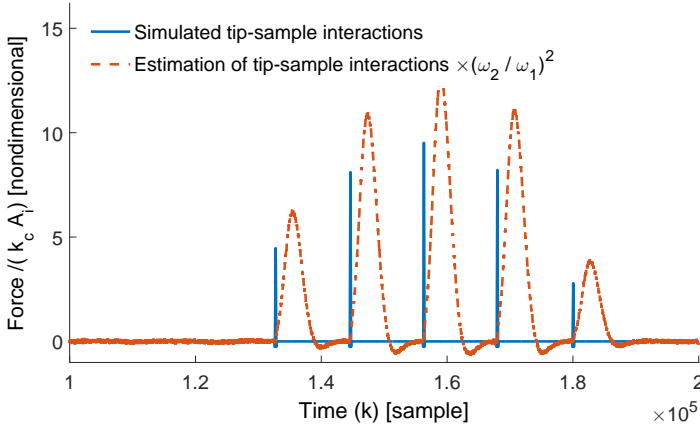


Figure 8.9: Simulated and estimated tip-sample interactions from the noisy simulated deflection signal (30dB SNR) of a dynamically tuned cantilever. It has been considered that the cantilever is not perfectly tuned and the frequency ratio between first and second mode is 6.01.

not match with the exact force.

$$P_n = \frac{\Omega}{2\pi} \int_0^{2\pi/\Omega} F_{ts}(t) e^{j(n\Omega t)} dt \quad (8.11)$$

Although the estimated force in Fig. 8.9 does not provide any useful information about the force-distance relationship, it provides a relatively good estimate of the peak repulsive force in transient situations which can be of advantage for high-speed AFM applications. One of the limiting factors in high-speed AFM is the time constant of the cantilever which is defined as the ratio between quality factor (Q) and the resonance frequency of the cantilever [35]. In practice, it means that the changes in the topography can be detected via the amplitude signal only after a Q period of oscillation. However, using the tuned cantilever and the proposed Kalman filter, the information on the second mode helps to estimate the forces in each period and reduces the time constant to $\tau = \frac{1}{\omega_g}$. Note that the quality factor of traditional cantilevers in the air is in the order of 100-1000. Thus, Controlling the estimated peak repulsive force instead of the amplitude of the first mode, one can considerably improve the speed of TM-AFM.

8.4. CONCLUSIONS

In this paper, a Tikhonov-like regularization method was applied to the Kalman filter to transform it to an input estimator for semi-periodic processes such as force estimation problem in AFM. The proposed algorithm uses all the statistically relevant information on the motion of the cantilever (output) to estimate the tip-sample interaction forces (input) in real-time, and without any prior knowledge about the force-distance relationship. The proposed input observer inherits its robustness from the Kalman filter, and its estimation latency depend on the bandwidth of the cantilever. Also the computational

load of the proposed algorithm does not differ from that of a linear Kalman filter which makes it a good potential option for model based control of AFM. The proposed filter can also be used in combination with any of the wideband probes for different purposes such as increasing the imaging speed, extracting the maximum information from the mechanical properties of the sample, or measuring the TSI forces in biological applications.

REFERENCES

- [1] R. Garcia and R. Perez, *Dynamic atomic force microscopy methods*, [Surface science reports](#) **47**, 197 (2002).
- [2] S. Hu, *Nonlinear dynamics and force spectroscopy in dynamic atomic force microscopy* (ProQuest, 2007).
- [3] A. Keyvani, H. Sadeghian, M. S. Tamer, J. F. L. Goosen, and F. van Keulen, *Minimizing tip-sample forces and enhancing sensitivity in atomic force microscopy with dynamically compliant cantilevers*, [Journal of Applied Physics](#) **121**, 244505 (2017).
- [4] T. R. Rodriguez and R. Garcia, *Tip motion in amplitude modulation (tapping-mode) atomic-force microscopy: Comparison between continuous and point-mass models*, [Applied Physics Letters](#) **80**, 1646 (2002).
- [5] S. Hu and A. Raman, *Analytical formulas and scaling laws for peak interaction forces in dynamic atomic force microscopy*, [Applied Physics Letters](#) **91**, 123106 (2007).
- [6] A. J. Katan, M. H. Van Es, and T. H. Oosterkamp, *Quantitative force versus distance measurements in amplitude modulation afm: a novel force inversion technique*, [Nanotechnology](#) **20**, 165703 (2009).
- [7] S. Hu and A. Raman, *Inverting amplitude and phase to reconstruct tip-sample interaction forces in tapping mode atomic force microscopy*, [Nanotechnology](#) **19**, 375704 (2008).
- [8] H. Holscher, W. Allers, U. Schwarz, A. Schwarz, and R. Wiesendanger, *Determination of tip-sample interaction potentials by dynamic force spectroscopy*, [Physical Review Letters](#) **83**, 4780 (1999).
- [9] J. E. Sader and S. P. Jarvis, *Interpretation of frequency modulation atomic force microscopy in terms of fractional calculus*, [Physical Review B](#) **70**, 012303 (2004).
- [10] A. Sebastian, D. R. Sahoo, and M. V. Salapaka, *An observer based sample detection scheme for atomic force microscopy*, in [Decision and Control, 2003. Proceedings. 42nd IEEE Conference on](#), Vol. 3 (IEEE, 2003) pp. 2132–2137.
- [11] D. R. Sahoo, A. Sebastian, and M. V. Salapaka, *Harnessing the transient signals in atomic force microscopy*, [International Journal of Robust and Nonlinear Control](#) **15**, 805 (2005).

- [12] K. S. Karvinen, M. G. Ruppert, K. Mahata, and S. R. Moheimani, *Direct tip-sample force estimation for high-speed dynamic mode atomic force microscopy*, [IEEE Transactions on Nanotechnology](#) **13**, 1257 (2014).
- [13] M. Loganathan and D. A. Bristow, *Bi-harmonic cantilever design for improved measurement sensitivity in tapping-mode atomic force microscopy*, [Review of Scientific Instruments](#) **85**, 043703 (2014).
- [14] O. Sahin, S. Magonov, C. Su, C. F. Quate, and O. Solgaard, *An atomic force microscope tip designed to measure time-varying nanomechanical forces*, [Nature nanotechnology](#) **2**, 507 (2007).
- [15] A. F. Sarioglu, M. Liu, and O. Solgaard, *High-resolution nanomechanical mapping using interferometric-force-sensing afm probes*, [Journal of Microelectromechanical Systems](#) **20**, 654 (2011).
- [16] N. H. Shaik, R. G. Reifenberger, and A. Raman, *Microcantilevers with embedded accelerometers for dynamic atomic force microscopy*, [Applied Physics Letters](#) **104**, 083109 (2014).
- [17] M. S. Tamer, H. Sadeghian, A. Keyvani, H. Goosen, and F. van Keulen, *Quantitative measurement of tip-sample interaction forces in tapping mode atomic force microscopy*, submitted to Journal of (2017).
- [18] O. Sahin, G. Yaralioglu, R. Grow, S. Zappe, A. Atalar, C. Quate, and O. Solgaard, *High-resolution imaging of elastic properties using harmonic cantilevers*, [Sensors and Actuators A: Physical](#) **114**, 183 (2004).
- [19] J. R. Felts and W. P. King, *Mechanical design for tailoring the resonance harmonics of an atomic force microscope cantilever during tip-surface contact*, [Journal of Micromechanics and Microengineering](#) **19**, 115008 (2009).
- [20] P. De Pablo, J. Colchero, J. Gomez-Herrero, and A. Baro, *Jumping mode scanning force microscopy*, [Applied Physics Letters](#) **73**, 3300 (1998).
- [21] A. Rosa-Zeiser, E. Weilandt, S. Hild, and O. Marti, *The simultaneous measurement of elastic, electrostatic and adhesive properties by scanning force microscopy: pulsed-force mode operation*, [Measurement Science and Technology](#) **8**, 1333 (1997).
- [22] A. Belianinov, S. V. Kalinin, and S. Jesse, *Complete information acquisition in dynamic force microscopy*, [Nature communications](#) **6** (2015).
- [23] O. Sahin, *Time-varying tip-sample force measurements and steady-state dynamics in tapping-mode atomic force microscopy*, [Physical Review B](#) **77**, 115405 (2008).
- [24] Q. Zou and S. Devasia, *Preview-based stable-inversion for output tracking*, in [American Control Conference, 1999. Proceedings of the 1999](#), Vol. 5 (IEEE, 1999) pp. 3544–3548.

- [25] S. Devasia, *Should model-based inverse inputs be used as feedforward under plant uncertainty?* [IEEE Transactions on Automatic Control](#) **47**, 1865 (2002).
- [26] G. Marro and E. Zattoni, *Exact unknown-state, unknown-input reconstruction: A geometric framework for discrete-time systems*, in *Decision and Control, 2009 held jointly with the 2009 28th Chinese Control Conference. CDC/CCC 2009. Proceedings of the 48th IEEE Conference on* (2009) pp. 6113–6118.
- [27] A. Edelmayer, J. Bokor, Z. Szabo, and F. Szigeti, *Input reconstruction by means of system inversion: A geometric approach to fault detection and isolation in nonlinear systems*, [International Journal of Applied Mathematics and Computer Science](#) **14**, 189 (2004).
- [28] S. Sundaram and C. N. Hadjicostis, *Delayed observers for linear systems with unknown inputs*, [IEEE Transactions on Automatic Control](#) **52**, 334 (2007).
- [29] B. V. Derjaguin, V. M. Muller, and Y. P. Toporov, *Effect of contact deformations on the adhesion of particles*, [Journal of Colloid and interface science](#) **53**, 314 (1975).
- [30] A. Keyvani, H. Sadeghian, H. Goosen, and F. van Keulen, *Transient tip-sample interactions in high-speed afm imaging of 3d nano structures*, in [SPIE Advanced Lithography](#) (International Society for Optics and Photonics, 2015) pp. 94242Q–94242Q.
- [31] R. Rounsevell, J. R. Forman, and J. Clarke, *Atomic force microscopy: mechanical unfolding of proteins*, [Methods](#) **34**, 100 (2004).
- [32] F. Schwesinger, R. Ros, T. Strunz, D. Anselmetti, H.-J. Güntherodt, A. Honegger, L. Jermutus, L. Tiefenauer, and A. Plückthun, *Unbinding forces of single antibody-antigen complexes correlate with their thermal dissociation rates*, [Proceedings of the National Academy of Sciences](#) **97**, 9972 (2000).
- [33] T. Strunz, K. Oroszlan, R. Schäfer, and H.-J. Güntherodt, *Dynamic force spectroscopy of single dna molecules*, [Proceedings of the National Academy of Sciences](#) **96**, 11277 (1999).
- [34] A. San Paulo and R. García, *Tip-surface forces, amplitude, and energy dissipation in amplitude-modulation (tapping mode) force microscopy*, [Physical Review B](#) **64**, 193411 (2001).
- [35] J. D. Adams, B. W. Erickson, J. Grossenbacher, J. Brugger, A. Nievergelt, and G. E. Fantner, *Harnessing the damping properties of materials for high-speed atomic force microscopy*, [Nature nanotechnology](#) (2015).

9

CONCLUSIONS, DISCUSSION AND RECOMMENDATIONS

The main motivation for the research presented in this thesis was to contribute to the development of the tapping mode atomic force microscope towards a potential industrial and clinical tool. The challenges for AFM technology in this regard include the limited imaging speed and throughput, possibility of damaging the samples, and the low reliability of the measurements. To address some of these challenges, the present thesis has been focused on the dynamics of AFM cantilevers, interaction forces between the samples and the tip, and controller design. The theoretical models presented in this thesis, in line with the numerical and experimental observations show that new mechanical designs and modern control strategies can indeed improve the performance of the AFM to beyond its current speed and performance limits.

9.1. CONCLUSIONS

This chapter summarizes the main conclusions from this thesis. They can be divided in three sub sections: i) Understanding the tip-sample interaction force (Chapters 2 and 3). ii) Dynamics and control of the AFM cantilever based on a modulated transient model (Chapters 4–6). iii) The multi-harmonic AFM cantilevers and approximation of the tip-sample forces in multi-frequency AFM (Chapters 7 and 8).

9.1.1. UNDERSTANDING THE TIP-SAMPLE INTERACTIONS

The TSI forces in TM-AFM are not measured during the experiments. That is why it is not clear in which circumstances the AFM might or might not damage the surface of the samples. In the first part of this thesis, we have conducted numerical simulations and experiments to investigate the TSI force. One important conclusion is that the TSI force can be momentarily much higher in transient situations than in the steady-state conditions. While the TSI force in steady-state situations is well described by previous models, the transient situations were not studied in literature. In Chapter 3, we have pre-

sented an explicit model for peak value of the TSI, and prevent sample and tip damage by choosing correct cantilever and operation parameters. However, just predicting the value of the TSI forces does not resolve the damage problem in high-speed AFM.

Besides the transient situations, we have found that the excitation frequency also has a large effect on the TSI forces. In the literature on AFM, the TSI forces are discussed mainly as a function of the amplitude and stiffness of the cantilever. However, the excitation frequency is actually by far the most important parameter that affects the tip-sample forces. Two different excitation frequencies for the same cantilever can apply orders of magnitude different TSI force on the sample, even if the free air amplitude and the set-point amplitudes are both the same. Based on these observations we propose that for topography imaging applications, the excitation frequency should be slightly less than the resonance frequency of the cantilever to minimize the probability of damaging the sample or the tip.

Appendix B reports on use of the sensitivity to frequency as a mechanism of controlling the TSI force. We have demonstrated a technique with which we could substantially change the TSI forces by changing the excitation frequency without changing the amplitude or dither power. In this manner, we could selectively damage the surface and by switching between the high and low force for each pixel, we could transfer any desired pattern to the sample surface.

Although the frequency dependency of the TSI force is evident from numerical and experimental observations, it is difficult to explain with the existing theories on the working mechanism of the TM-AFM. To explain the frequency sensitivity of the force, we proposed a new perspective to the working principle of the AFM, in Chapter 3. According to the existing theories, when the vibrating cantilever is brought close to sample surface, the TSI force changes the resonance frequency of the cantilever, and since we do not change the excitation frequency accordingly, the amplitude reduces. We proposed a new model which is based on linear analysis of the cantilever. According to the new model, a destructive interference between the dither force and the first Fourier component of TSI force is the reason behind the reduction of the amplitude in TM-AFM. In other words, when the cantilever is brought close to the surface of the sample, the TSI force partially cancels out the dither force, hence, the amplitude reduces. With this explanation, the phase of the cantilever determines the sensitivity of the amplitude to the TSI force, and the phase itself depends on the excitation frequency. With this model, the relationship between the amplitude, frequency and the TSI force can be clearly explained. Moreover, with this explanation, it was shown that the single harmonic TM-AFM does not measure the true height profile of the samples, but only a geometric locus of all the points on the sample that provide the same average TSI force. The main consequence of this is the inconsistency of the topography measurements, especially in the biological AFM measurements. For example, the height of a DNA stand on the mica surface is sometimes measured as 0.6 nm and some times as 1.5 nm, while its theoretical value is 2.2 nm. The new model presented in Chapter 3 clearly explains this discrepancy and attributes it to the heterogeneous composition of the sample.

9.1.2. DYNAMICS AND CONTROL OF THE AFM CANTILEVER BASED ON A MODULATED TRANSIENT MODEL

In TM-AFM, there is a large difference between the time scale of the controller and the time scale of the cantilever. The cantilever vibrates with its resonance frequency and experiences the TSI forces in a fast time scale. However, within that time scale, no considerable change in the states of the controller happens. That is, the controller is not affected by the motion of the cantilever, but only by the amplitude of the motion of the cantilever. The latter changes by definition order(s) of magnitude slower than the motion itself. In practice, a Lock-In Amplifier (LIA) circuit separates these two time scales by demodulating the motion signal into its amplitude and phase. Therefore, if the transient behavior of the closed-loop TM-AFM is considered, one either has to solve the fully nonlinear governing differential equations in the fast time scale, or incorporate the functionality of the LIA in the equations and derive a new dynamic model at the time scale of the controller. The latter is obviously more efficient in the sense of the computation time. In Chapter 4 we have derived the demodulated model of the AFM which describes the overall behavior of the AFM cantilever in the slow time scale.

The steady-state response of the new model as presented in Chapter 4, fully agrees with the previously existing theories on TM-AFM, and its transient response has been verified using experiments. According to this model, in transient situations, the amplitude-phase pair moves on a spiral path in the state space. This spiral path causes a wrong-direction initial response of the amplitude signal, which is very similar to Non-Minimum-Phase (NMP) behavior in linear systems. Considering the NMP-like behavior of the cantilever, one can conclude that controlling the TM-AFM by using the amplitude as the error signal is not necessarily the best control strategy. In Chapter 5, we show that the NMP behavior of the cantilever leads to a deterministic chaotic behavior when it is coupled with a high speed PI controller. In fact, the presence of chaos in closed-loop AFM limits the speed of operation in its conventional configuration. If the controller is tuned to be faster than a certain limit, it responds to the wrong-direction changes of the amplitude signal and eventually causes chaos. The presence of chaos in TM-AFM was confirmed by calculating the Lyapunov exponents, bifurcation diagrams, and Poincaré sections. It should be noted that similar chaotic behavior of AFM was previously reported in the literature, however, those were all due to attractive or excessive adhesive TSI force and could be circumvented via simple changes in operation parameters. However, the new cause of chaos presented in Chapter 5 is inevitable and imposes an upper limit for the closed loop bandwidth of the AFM in its current architecture.

Considering the conclusions from Chapter 4 and 5, we proposed a new control algorithm in Chapter 6, in which the control action does not depend on the amplitude signal, but a recursive linear combination of the amplitude and phase signal which approximates the TSI force. For this, we have used a dual Kalman observer that assumes a zero-dynamic for the TSI force— which means that the time derivative of the force is negligible— and tries to approximate the average of the TSI force. In this way, the Kalman filter eliminates the NMP behavior and postpones the chaos for much higher speeds. The simulation results in Chapter 6 show that to the cost of increasing the complexity of the system, the imaging speed could be improved up to few orders of magnitude depending on the noise levels.

9.1.3. MULTI-HARMONIC PROBES AND METHODS

The most important conclusion from Chapters 4 to 6 is that even a rough approximation of the TSI force would work better than the amplitude signal for control purposes. However, with normal AFM cantilevers it is impossible to fully measure the TSI forces in real-time. This is partly a fundamental problem stemming from the causality of the physical systems, and partly because of the narrow-band output of the cantilever. The problem of causality can not be resolved, however, the bandwidth of the output signal can be increased. In fact, due to the causality of the physical systems it is impossible to measure or estimate the exact input (force) in real-time, and the AFM cantilever is not an exception. However, depending on the output bandwidth, a delayed and approximate value of the input can be estimated using advanced filters. Such a filter itself should be deterministic and physically realizable, which means that its output (in this case, the estimate of the TSI force) can never have a higher bandwidth than its input (in this case, the measured deflection of the cantilever). Therefore, the first step in attempting to find the TSI forces should be increasing the output bandwidth of the cantilever.

In Chapter 7, we have proposed a change in the geometry of the cantilever, which makes the ratio between the frequency of the first two bending modes of the cantilever an integer number (6). In this manner, the second bending mode of the cantilever also gets excited with the 6th super-harmonic content of the TSI force. This design has two advantages over the conventional AFM cantilevers. First, because of its kinematic behavior, it applies less repulsive force on the sample. Experimental results show that the TSI forces could be reduced with a factor eight for the same stiffness of the probe and the same experimental conditions. Second, the output signal has a larger band-width, *i.e.*, it contains more information on the TSI force. The latter can be used either in detecting the material properties of the sample (as an additional imaging contrast source), or in combination with an input observer to estimate the TSI forces with less delay and better accuracy. In Chapter 7 we have used the additional information for material properties mapping, and in Chapter 8, for estimation of the TSI force.

In Chapter 8, we present a new type of input observer to estimate the TSI force from wide-band AFM cantilevers with minimum delay and maximum accuracy. The input estimation problem has been transformed to an ill-conditioned state observation problem, and the ill-conditioning was circumvented using a technique that is similar to Tikhonov regularization. Depending on the dynamics of the AFM cantilever (bandwidth of its output) and the noise levels, an optimum and almost real-time estimation of the TSI force could be achieved, which can be used in real-time control as described in Chapter 6.

Although the TM-AFM constitutes the main use-case for all chapters in this thesis, the outcome of Chapters 4 and 8 is more general purpose and can be used in other fields of science and engineering. The dynamic model presented in Chapter 4 describes the transient behavior of an amplitude modulated one-DOF resonator, which can be useful in modeling and control design for similar systems. Also, Chapter 8 presents an input estimation method which can be applied to any linear time invariant system with a semi-periodic process.

9.2. RECOMMENDATIONS

While this thesis studies and tries to develop solutions for a number of challenges, the AFM technology is still too immature to be considered as an effective industrial or clinical tool. There are several challenges that have to be solved which suggest many opportunities for further research and development. Here, I mention a few of them which I believe should have high priorities.

9.2.1. FORCE-CONTROLLED PARALLEL AFM

One of the methods proposed to increase the throughput of the AFM is using parallel AFM heads, and/or parallel cantilevers in a single AFM head. Although development of parallel heads and manipulating them with robotic arms seems promising, use of parallel cantilevers in a single head is crucial and still missing. According to the previous experiments and models, connecting more than one AFM cantilever in a single chip suffers from many issues regarding dynamic design and control. An important follow-up of the Chapters 4 and 6 would be to derive the modulated model for parallel AFM cantilevers and design controllers based on the estimated TSI force. Control of parallel AFM cantilevers is normally hindered by a so-called cross-talk phenomenon, in which the motion of neighboring cantilevers affect each others phase and amplitude. When the distance controller only receives the amplitude signal of each cantilever, and the TSI force on one cantilever affects an other one as well, it is impossible to run a TM-AFM experiment. However, if a Kalman filter would be used to estimate the force of each cantilever and adjust the height accordingly, many of these problems would be solved. In case of any successful result, using parallel cantilevers can enable measurement of large areas in a reasonable time frame.

9.2.2. CANTILEVERS WITH MODE-MULTIPLICITY

In Chapter 7 we have shown the potential of utilizing multiple modes of the AFM cantilever to increase its sensitivity and flow of information from the sample to the output signals. One interesting followup would be to investigate the effects of having mode multiplicity in AFM cantilevers. Since the presence of mode multiplicity would increase the sensitivity of the cantilever to any perturbations, one can expect that the AFM cantilever can reach even higher sensitivity and bandwidth. Also, it is highly recommended to develop methods to optimize the dynamics of the AFM cantilevers using shape or topology optimization techniques. It is expected that with these techniques one can design robust and high performance cantilevers. Such cantilevers can enable many applications other than height measurements.

9.2.3. SMART AFMS

Many of the clinical or industrial microscopes consist of a combination of two or more different microscopy techniques. For example, some companies produce AFMs combined with SEM or optical microscope. In general, acquiring more information on the samples, and optimally combining the information will enhance our knowledge about the samples. One fundamental approach in the case of AFM would be to combine a mechanical (or even a multi-physical) model of the sample with an AFM. The results of the

Chapter 8 show that it is possible to measure the TSI force in (almost) real-time together with its uncertainty. Combining such a system with a finite element model of the sample and updating the geometry and mechanical properties of the model with the AFM measurements can substantially change the way that micro-nano imaging is done. Using artificial intelligence techniques in processing the AFM data and combining it with the mechanical model of the sample can provide quantitative and reproducible results. This can also be applicable to the measurement of thermal, electrical or even chemical properties of samples.

A

MULTI-MODAL ANALYSIS OF CANTILEVER FOR IMPULSE INPUT

When the cantilever suddenly hits the sample surface, some part of the kinetic energy of the cantilever transfers to the potential energy in the contact area. The equivalent inertia which would provide the same amount of energy for the same attack velocity is called the apparent mass of the tip. To find the apparent mass of the tip, one can model the cantilever as a serial multi-DOF system with the same point mechanical impedance on the tip. If the point mechanical impedance of the tip is equal to that of the first mass element of the multi-DOF model shown in Fig. A.1, the tip of the cantilever, and its multi-DOF ladder model behaves the same way in transient situations. However, the other generalized coordinates do not have a one to one relationship with each other[1].

To calculate the apparent mass of the cantilever, initially, the mechanical impedance of the tip is calculated from modal governing differential equations. Then a ladder mass-spring model which has the same impedance function as the tip is synthesized. A similar technique is used in the synthesis of analog circuits for passive filtering applications, and also in mechanical impact analysis[1].

Considering the motion of the cantilever in a modal setting as: $w = \sum_{i=1}^n q_i(t)\varphi_i(x)$, similar to Eq(2.1) the dynamic motion of the beam can be described as:

$$M_{ij}\ddot{q}_j + C_{ij}\dot{q}_j + K_{ij}q_j = F_i u, \quad (\text{A.1})$$

where M, C, K, F, u and q are modal mass, damping, and stiffness matrices, forcing vector, input force, and modal coordinates, respectively. Thus, the point mechanical impedance of the tip is defined as

$$Z_p = \frac{u(s)}{sW_t(s)},$$

and the mechanical mobility is defined as

$$Y_p = \frac{sW_t(s)}{u(s)}.$$

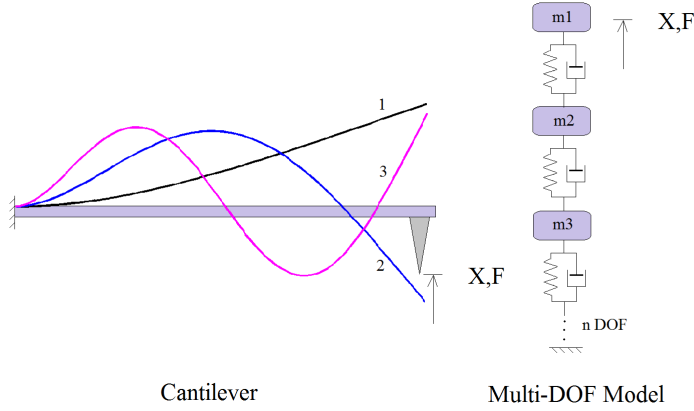


Figure A.1: Lumped model of cantilever.

where $W_t(s)$ is displacement of the tip in Laplace domain with s being the Laplace variable. By defining

$$D_{ij} = M_{ij}s^2 + C_{ij}s + K_{ij},$$

the driving point mechanical mobility is found as:

$$Y_p = s\varphi_i(l)D_{ij}^\dagger F_j. \quad (\text{A.2})$$

in which, the superscript \dagger represents the pseudo-inverse operation. To synthesize a ladder mass-spring model, the mechanical impedance in Eq.(A.2) can be written in continued fraction form that describes the mechanical impedance of the first mass element of the lumped model shown in Fig. A.1 as:

$$Y_p(s) = \frac{1}{m_1 s + \frac{1}{s/k_1 + \frac{1}{m_2 s + \frac{1}{\dots + \frac{1}{s/k_n}}}}} \quad (\text{A.3})$$

For rectangular cantilevers considering n modes of vibration the apparent mass at the free end of the cantilever is $m_{tip} = \frac{1}{4n} \rho AL$. This amount depends on the number of modes that are considered in the analysis and converges to zero considering an infinite amount of modes. However, not all of the modes of the cantilever should be considered. The number of the modes considered in these type of analysis should match the ratio between stiffness of the contact area and modal stiffness. If the modal stiffness of a certain mode is higher than the stiffness of the contact, naturally, that specific vibration mode cannot relax the contact, thus does not contribute to apparent mass. Considering a low number of modes will result in overestimation of the forces, and vice versa. To find the proper number of the modes, we argue the underlying assumption in section IV (energy

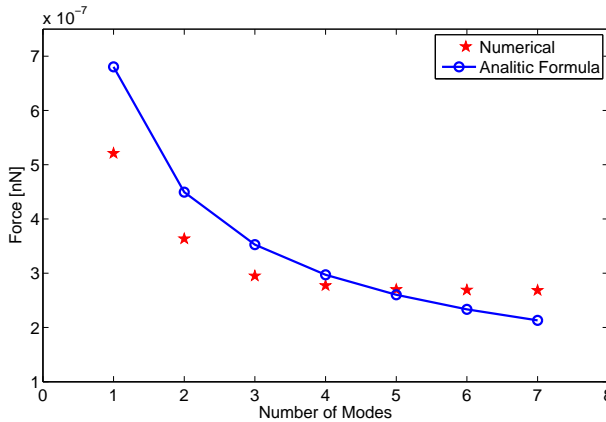


Figure A.2: Maximum repulsive force considering 2 nm sudden change in silicon surface, cantilever with spring constant of 5 N/m Q factor 50 tip radius of 10 nm free Air amplitude of 50 nm resonance and working frequency of 100 kHz.

analysis). There it was assumed that, since the indentation is small enough in comparison to the amplitude of the cantilever (i.e. the stiffness of surface is much higher than that of the cantilever), the changes in potential energy of cantilever during indentation can be neglected. However, if we consider higher modes of the cantilever, the stiffness of n^{th} mode of the cantilever (k_n) can be bigger than the stiffness of contact which violates the key assumption. The most realistic n can be chosen such that it includes the highest mode of the cantilever which is not stiffer than the equivalent stiffness of contact: $k_n < k_{\text{contact}} < k_{n+1}$. Physically the number n corresponds to the number of modes that are excited during the sudden contact (see Fig. 2.3). For example for rectangular cantilevers one can compare $k_1 = k_c, k_2 = 40.45k_c, k_3 = 317.2k_c, \dots$ with the contact stiffness $k_{\text{contact}} = 2a_0^{\frac{1}{2}} E_{\text{eff}} \sqrt{R}$ and decide about n .

Fig. A.2 shows a comparison between the numerical results and the analytic formula presented in Eq(2.9). Increasing the number of modes in the model the numerical results converges to a particular value. However, the analytic method underestimates the force when considering too much of the modes. Thus considering the contact stiffness 3-6 modes of the cantilever can be used to approximately estimate the peak repulsive forces in transient situations.

REFERENCES

- [1] Z.-C. Lin and C.-Y. Ho, *An investigation of elastic impact problems on beams and plates*, *Journal of sound and vibration* **148**, 293 (1991).

B

SIMULTANEOUS AFM NANO-PATTERNING AND IMAGING

Scanning probe based nano-machining has many applications such as fabricating nano-wires, nano-dots, single electron transistors and many other devices for physics experiments [2–4]. One of the applications that require high throughput nano-machining is repair of photomasks for optical lithography. In appendix A, we present an AFM based nano-patterning technique that can be used for fast defect repairing of high resolution photomasks and possibly other nano-patterning applications. The proposed method works based on hammering the sample with tapping mode AFM followed by wet cleaning of the residuals. On the area where a specific pattern should be written, the tip-sample interaction force is increased in a controlled manner by changing the excitation frequency of the cantilever without interrupting the imaging process. Using this method several patterns were transferred to different samples with imaging speed. While the pattern was transferred to the sample in each tracing scan line, the patterned sample was imaged in retracing scan line, hence, the outcome was immediately visible during the experiment.

B.1. INTRODUCTION

OPTICAL lithography is the main patterning technology for semiconductor industries. Thus, production, inspection and repair of high precision photomasks remain one of the challenges in high volume manufacturing. In this regards electron and focused ion beam microscopy based techniques are already in use for high precision masks repair, which each one has its own challenges and opportunities in achieving proper etching sensitivities, resolution and speed.[5–7].

Thanks to its nanoscale resolution, the atomic force microscopy (AFM) has already been suggested as one of the instruments for inspection and repair certain type of defects in 64 and 32nm node photomasks. However, there are still some challenges regarding the drift, positioning error and throughput of AFM based mask repair[8–10].

Parts of this chapter have been published in Proc. SPIE **9778**,42(1906) [1]

When the particle defect is attached to the surface with a high adhesion so that wet cleaning fails to remove it, the AFM based cleaning is applied. The Photomask repair with AFM is done with a so called nano-machining process, followed by a wet cleaning process [9]. The nano-machining process consist of multiple steps namely, locating and imaging the defect in a gentle imaging conditions, deciding about the scan direction for removal process, and high force contact mode imaging of the particle. If the adhesion of the particle is low enough then the AFM tip pushes it away from its original location, so that it can be removed in the next wet cleaning process, otherwise the force set-point is gradually increased and the contact mode imaging is performed again, while focusing the scan area to the shape of the particle. Usually these steps require multiple times scanning and scratching, with multiple operation set-points and multiple cantilevers, which result in time consumption of about two hours per each defect.

An other challenge which the AFM-based photomask repair repair is facing is the positioning error and drift. It is very important to control the location of the defect during repair process, otherwise the repair process itself introduces new defects to the mask. The contemporary AFM-based repair systems compensate the drift by forecasting its amount and direction via a so-called edge detection technique.

Here, we present a new method which replaces the scratching process with high force Tapping Mode AFM (TM-AFM) imaging which can be used simultaneously for imaging and nano-machining. For this aim, the tip-sample interactions are tuned via operation parameters of the TM-AFM so that the AFM can be quickly switched between imaging and hammering modes. Since the imaging and nano-machining are performed simultaneously, the process can probably be much faster and drift control can be done much easier. Moreover, there is no need to determine any scratching direction or use of multiple cantilevers which further reduces the time consumption.

B.2. METHOD AND EXPERIMENTAL DEMONSTRATION

In the literature, the tip-sample forces are mainly attributed to the amplitude and stiffness of the cantilever which are practically very difficult to change (if not impossible) without interrupting the image. However, As shown in Chapter 3, the excitation frequency is actually by far the most important imaging parameter that affects the tip-sample forces. Fig. B.1 shows the normalized trend of the peak repulsive force with respect to the amplitude ratio and the excitation frequency, achieved via numerical simulations and experiments.

According to Fig. B.1, the tip-sample interaction forces primarily depend on the excitation frequency, especially for when the amplitude ratio is high. Provided that the free-air and set-point amplitudes are kept constant, one can increase and decrease the forces by changing the excitation frequency without interrupting the image. The same dither voltage with two different frequency (one below and one above the resonance frequency of the cantilever) which give the same free air amplitude and amplitude ratio (the later is because of closed loop control) can apply very different peak repulsive force on the sample. If the damage threshold of a material is between these two forces then one of the situations would be damaging and the other one would be non-damaging.

In order to demonstrate the proof of concept for nano-machining, we first imaged a rectangular area on the sample with the so called writing parameters (high amplitude ra-

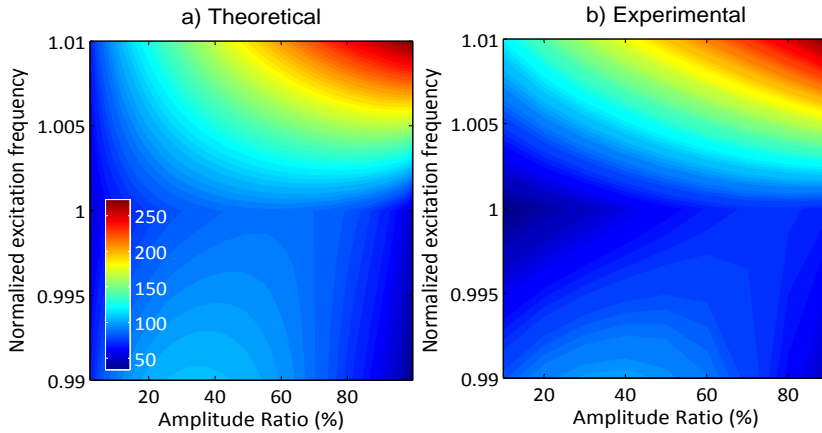


Figure B.1: Normalized peak repulsive forces versus normalized excitation frequency (vertical) and amplitude set-point (horizontal). a) theoretical, b) experimental.

tion and excitation frequency higher than the resonance of cantilever), then imaged a bigger area with its symmetric reading parameters (same free air amplitude and amplitude ratio but with lower excitation frequency). This experiment was repeated for different samples and with different free air amplitudes. The frequency offset, and free air amplitude of cantilever had to be calibrated depending on the tip and sample properties, and spring constant of cantilever to make sure that the writing configuration is damaging and reading configuration non-damaging.

Fig. B.2 shows two examples of the experiment. One square written on a thin HDMS layer coated on silicon surface and the other one is a rectangle created on the surface of silicon dioxide. Both using a single crystal diamond tip in writing configuration, and immediately imaged with the same tip in reading configuration.

In order to demonstrate a semi-automatic nano-machining, we use an external computer-programmable lock-in amplifier (Zurich instrument) and a commercial AFM system (Bruker Fastscan) with signal access module. The AFM was operated in contact mode however, deflection signal is isolated and sent to lock-in amplifier and the demodulated amplitude signal is provided back to the AFM as deflection error. In this manner, the AFM controller keeps the amplitude constant, by trying to keep the deflection error constant in contact mode. This step was necessary because it was not possible to change the operation parameters via the AFM computer itself. The two different operation parameters (same voltage, different frequency) are provided with Zurich Instruments Lock-in amplifier which was controlled with a separate computer program in Labview environment. The Labview code reads the X-Y position of the AFM head, compares it with a user provided image and decides about the excitation frequency. If the image color for accompanying pixel is black, the excitation frequency goes to writing mode and vice versa. In order to visualize the results immediately while doing the nano-machining, the afore-

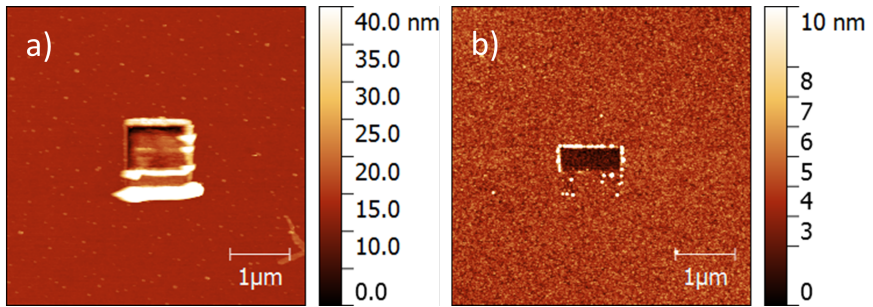


Figure B.2: Nano-machining example by changing the excitation frequency using a diamond tip. a) HDMS coated on silicon b) silicon dioxide

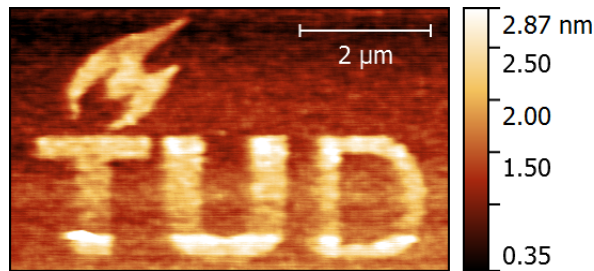


Figure B.3: The TU Delft logo patterned on silicon dioxide sample with diamond tip.

mentioned technique is only applied during the trace line, and retrace lines are only imaged with in reading mode. Fig. B.3 is an example of nano-machining method where the logo of Delft University of Technology is patterned on a silicon dioxide sample with a diamond coated cantilever.

The cantilever which was used in this example had a spring constant of $30.3N/m$ (thermally calibrated) the quality factor of 300 and fundamental resonance frequency of $199kHz$, and was excited with free air amplitude of $85nm$. The cantilever was engaged to the surface with a 90% amplitude ratio.

The Nano-machining method which was suggested here offers a the possibility of the fast and automated photomask defect repair, nonetheless there are some challenges. First, similar to other machining methods, this method should have its own window of operation in terms of materials that can be used, maximum depth that can be achieved, resolution, etc. However, these limits are not known for us yet. Secondly, a better hardware-software combination has to be developed to find the defect areas, compare the mask with the desired pattern, identify the defect type, and perform the repairing process. Last but not the least, we have only used diamond coated AFM probes in all the experiments without any consideration about the sharpness or lifetime of the tip, which also needs to be investigated.

REFERENCES

- [1] A. Keyvani, M. S. Tamer, M. H. van Es, and H. Sadeghian, *Simultaneous afm nano-patterning and imaging for photomask repair*, *Proc. SPIE* **9778**, 977818 (2016).
- [2] S. Hu, a. Hamidi, S. Altmeyer, T. Koster, B. Spangenberg, and H. Kurz, *Fabrication of silicon and metal nanowires and dots using mechanical atomic force lithography*, *J. Vac. Sci. Technol. B* **16**, 2822 (1998).
- [3] T.-H. Fang, C.-I. Weng, and J.-G. Chang, *Machining characterization of the nano-lithography process using atomic force microscopy*, *Nanotechnology* **11**, 181 (2000).
- [4] M. Ramiaczek-Krasowska, A. Szyszka, A. Stafiniak, R. Paszkiewicz, B. Paszkiewicz, and M. Tlaczala, *Application of AFM technique for creation of patterns in nanoscale*, *Opt. Appl.* **41**, 307 (2011).
- [5] M. Waiblinger, R. Jonckheere, T. Bret, D. Van den Heuvel, C. Baur, and G. Baralia, *The door opener for EUV mask repair*, **8441**, 84410F (2012).
- [6] C. Ehrlich, *Application data of the electron beam based photomask repair tool MeRiT MG*, *Proc. SPIE*, 145 (2005).
- [7] F. Aramaki, T. Kozakai, O. Matsuda, O. Takaoka, Y. Sugiyama, H. Oba, K. Aita, and A. Yasaka, *Photomask Repair Technology by using Gas Field Ion Source*, *Bacus* **29**, 1 (2013).
- [8] T. Robinson, R. White, R. Bozak, K. Roessler, B. Arruza, D. Hogle, M. Archuletta, and D. Lee, *New tools to enable photomask repair to the 32nm node*, **7488**, 74880F (2009).
- [9] M. Dellagiovanna, H. Yoshioka, H. Miyashita, S. Murai, T. Nakaue, O. Takaoka, a. Uemoto, S. Kikuchi, R. Hagiwara, and S. Benard, *A semi-automated AFM photomask repair process for manufacturing application using SPR6300*, *Photomask Technol.* 2007 **6730**, 673020 (2007).
- [10] B. LoBianco, R. White, and T. Nawrocki, *Use of nanomachining for 100 nanometer mask repair*, *Proc. SPIE* **4889**, 977818 (2002).

C

PERIODIC AVERAGE OF TIP-SAMPLE INTERACTION FORCE

To derive a relationship between the modulated TSI force and the state variables of the resonating cantilever, we use a generalized form of the well-known Derjaguin-Muller-Toporov (DMT) model which consist of the attractive van der Waals (vdW) force, repulsive Hertz, and a dissipative viscoelastic terms [1–3]. According to this model, the physical force f_{ts}^{ph} can be written as:

$$f_{ts}^{ph} = \frac{HR}{6(Z-x)_{D\sigma}^2} - \frac{4}{3}E_{Eff}R^{\frac{1}{2}}(x+\sigma-Z)_{D_0}^{\frac{3}{2}} - \eta R^{\frac{1}{2}}(x+\sigma-Z)_{D_0}^{\frac{1}{2}} \frac{dx}{dt}, \quad (C.1)$$

where H, R, Z , and σ are Hamaker constant, tip-radius, separation of the sample surface and the cantilever in its undeflected configuration, and the intermolecular distance, respectively. $E_{Eff} = (\frac{1-\nu_{tip}^2}{E_{tip}} + \frac{1-\nu_{sample}^2}{E_{sample}})^{-1}$ is the effective elasticity of the contact which is calculated from the elasticity (E) and Poisson ratio (ν) of the tip and the sample. η is the effective viscoelasticity of the contact area. The discontinuity function $(a)_{D_b}$ is defined to impose the discontinuity of the forces during the contact as: $(a)_{D_b} = \begin{cases} a & \text{if } a \geq b \\ b & \text{if } a < b \end{cases}$.

Normalizing the model in Eq(C.1) according to the same scales as in Eq(4.1), the non-dimensional form of the TSI force ($f_{ts} = \frac{f_{ts}^{ph}}{kA_0}$) can be written as:

$$f_{ts} = \frac{\alpha}{(h-x)_{D\sigma}^2} - \beta(x+\sigma-h)_{D_0}^{\frac{3}{2}} - \gamma(x+\sigma-h)_{D_0}^{\frac{1}{2}} \frac{dx}{dt}, \quad (C.2)$$

where, $h = \frac{Z}{A_0}$, $\alpha = \frac{HR}{6kA_0^3}$, $\beta = \frac{4E_{Eff}\sqrt{RA_0}}{3k}$, and $\gamma = \omega\eta\sqrt{RA_0^3}$, are the coefficients of the vdW, Hertz and viscoelastic forces, respectively. A_0 , and k represent the free air amplitude

and the spring constant of the cantilever. Applying the Fourier operation as explained in Section 4.2, we obtain:

$$F_{ts}^{(1)} = F_{vdW}^{(1)} - F_H^{(1)} - F_{vis}^{(1)}, \quad (C.3)$$

where the first harmonic of the van der Waals force ($F_{vdW}^{(1)}$), Hertzian contact force ($F_H^{(1)}$), and viscoelastic damping ($F_{vis}^{(1)}$) are defined as:

$$F_{vdW}^{(1)} = \alpha \int_0^{\frac{2\pi}{\omega}} \frac{e^{j\omega t} dt}{(h - \Re[X_2 e^{j\omega t}])_{D_\sigma}^2}, \quad (C.4a)$$

$$F_H^{(1)} = \beta \int_0^{\frac{2\pi}{\omega}} (\Re[X_2 e^{j\omega t}] + \sigma - h)_{D_0}^{\frac{3}{2}} e^{j\omega t} dt, \quad (C.4b)$$

$$F_{vis}^{(1)} = \gamma \int_0^{\frac{2\pi}{\omega}} (\Re[X_2 e^{j\omega t}] + \sigma - h)_{D_0}^{\frac{1}{2}} \Re[X_1 e^{j\omega t}] e^{j\omega t} dt. \quad (C.4c)$$

Considering the definition of $X_i = A_i e^{\varphi_i}$, $i = 1, 2$, and defining variables $\theta_i = \omega t + \varphi_i$, $i = 1, 2$, $\zeta_1 = \frac{h}{A_2}$, and $\zeta_2 = \frac{\sigma}{A_2}$, the integral in Eq(C.4a) can be simplified as:

$$\begin{aligned} \int_0^{\frac{2\pi}{\omega}} \frac{e^{j\omega t} dt}{(h - \Re[X_2 e^{j\omega t}])_{D_\sigma}^2} &= \int_{\varphi_2}^{2\pi + \varphi_2} \frac{e^{(\theta - \varphi_2)} d\theta}{(h - A_2 \Re[e^{j(\theta)}])_{D_\sigma}^2} \\ &= \frac{e^{-\varphi_2}}{A_2^2} \int_0^{2\pi} \frac{[\cos(\theta) + j \sin(\theta)] d\theta}{(\frac{h}{A_2} - \cos(\theta))_{D(\frac{\sigma}{A_2})}^2} = \frac{-X_2}{A_2^3} \int_0^{2\pi} \frac{\cos(\theta) d\theta}{(\zeta_1 - \cos(\theta))_{D(\zeta_2)}^2}. \end{aligned}$$

Note that:

$$\int_0^{2\pi} \frac{\sin(\theta) d\theta}{(\frac{h}{A_2} - \cos(\theta))_{D(\frac{\sigma}{A_2})}^2} = 0$$

because it is an odd periodic function of θ .

Repeating the same procedure for Eq(C.4b) and Eq(C.4c) we obtain:

$$\Re(F_{ts}^{(1)}) = (K_H - K_{vdW}) q_3 + C_{visco} q_1, \quad (C.5a)$$

$$\Im(F_{ts}^{(1)}) = (K_H - K_{vdW}) q_4 + C_{visco} q_2, \quad (C.5b)$$

where K_{vdW} , K_H , and C_{vis} are defined as:

$$K_{vdW} = \frac{\alpha}{A^3} I_1\left(\frac{h}{A}, \frac{\sigma}{A}\right), \quad (C.6a)$$

$$K_H = \beta A^{\frac{1}{2}} I_2\left(\frac{h}{A}, \frac{\sigma}{A}\right), \quad (C.6b)$$

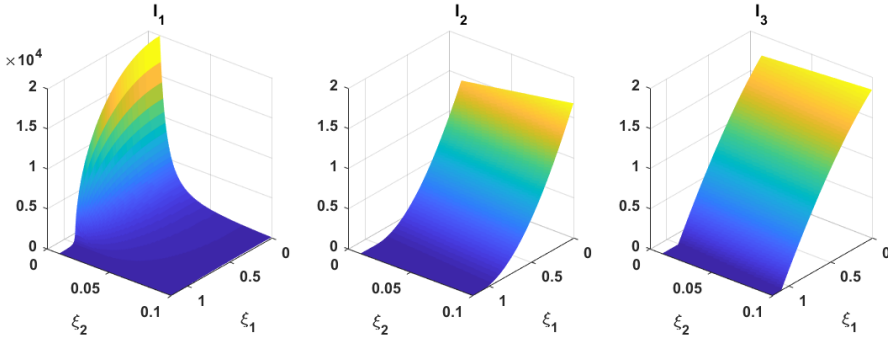


Figure C.1: Integral functions I_1 till I_3 as a function their arguments ξ_1 and ξ_2 .

$$C_{vis} = \gamma A^{-\frac{1}{2}} I_3\left(\frac{h}{A}, \frac{\sigma}{A}\right), \quad (\text{C.6c})$$

and can be considered as added negative stiffness due to the vdW force, added stiffness by the Hertz force, and the added damping of the viscoelastic force, respectively. The integral functions in Eq(C.6) are defined as:

$$I_1(\zeta_1, \zeta_2) = \int_0^{2\pi} \frac{\cos(\theta) d\theta}{(\zeta_1 - \cos(\theta))_{D\zeta_2}^2}, \quad (\text{C.7a})$$

$$I_2(\zeta_1, \zeta_2) = \int_0^{2\pi} (\cos(\theta) - \zeta_1 + \zeta_2)_{D_0}^{\frac{3}{2}} \cos(\theta) d\theta, \quad (\text{C.7b})$$

$$I_3(\zeta_1, \zeta_2) = \int_0^{2\pi} (\cos(\theta) - \zeta_1 + \zeta_2)_{D_0}^{\frac{1}{2}} \cos(\theta) d\theta, \quad (\text{C.7c})$$

and are illustrated in Fig. C.1. Note that, the conservative part of the force $((K_H - K_{vdW})X_2)$ is in the opposite direction of the modulated displacement (X_2), and the dissipative force $(C_{vis}X_1)$ is in the opposite direction of the modulated tip velocity (X_1). Therefore, $(K_H - K_{vdW})$, and C_{vis} can be considered as the added stiffness and the damping of the TSI force, respectively.

REFERENCES

- [1] H. V. Guzman, A. P. Perrino, and R. Garcia, *Peak forces in high-resolution imaging of soft matter in liquid*, *ACS nano* **7**, 3198 (2013).
- [2] S. Rützel, S. I. Lee, and A. Raman, *Nonlinear dynamics of atomic-force-microscope probes driven in lennard-jones potentials*, in *Proceedings of the Royal Society of London A: Mathematical, Physical and Engineering Sciences*, Vol. 459 (The Royal Society, 2003) pp. 1925–1948.

- [3] U. D. Schwarz, *A generalized analytical model for the elastic deformation of an adhesive contact between a sphere and a flat surface*, [Journal of Colloid and Interface Science](#) **261**, 99 (2003).

D

CALCULATION OF THE NONLINEAR FREQUENCY RESPONSE CURVE USING DEMODULATED FORMULATION

The steady-state frequency response of the cantilever can be calculated by substituting Eq(4.14) into Eq(4.10) and putting the $\dot{q}_i = 0$.

$$\underbrace{\left[\begin{array}{cc} 1 - \omega^2 & -\xi\omega \\ \xi\omega & 1 - \omega^2 \end{array} \right]}_{\Xi} + \underbrace{\left[\begin{array}{cc} K_H - K_{vdW} & -C_{vis}\omega \\ C_{vis}\omega & K_H - K_{vdW} \end{array} \right]}_{X_2} \underbrace{\begin{Bmatrix} q_3 \\ q_4 \end{Bmatrix}}_{Y} = \underbrace{\begin{Bmatrix} F_d \\ 0 \end{Bmatrix}}_{Y} \quad (D.1)$$

As it can be seen from Eq(C.6), the added nonlinear stiffness and damping values do not depend on the phase or frequency, instead they are only a function of amplitude. It is easy to check that this is the case for any time invariant non-linearity. Therefore, one can conclude that Eq(D.1) is always quadratic in terms of frequency square. To avoid solving the nonlinear Eq(D.1) for amplitude and phase, we suggest to scan the amplitude, and solve for frequency.

Therefore, we defined Π and Ξ in Eq(D.1). Considering Eq(4.10b), one can eliminate the phase by multiplying the Eq(D.1) by Ξ^{-1} , and left-multiply the transpose of the resultant by itself:

$$A^2 = Y^T \Xi^{-T} \Xi^{-1} Y \quad (D.2)$$

Independent of the type of the non-linearity (only if the nonlinearity is time-independent), $(\Xi \Xi^T)$ is always diagonal, with both of the elements equal to each other. Hence it leads to:

$$\frac{F_d^2}{A^2} = (1 + K_H - K_{vdW} - \omega^2)^2 + (\xi + C_{vis})^2 \omega^2 \quad (D.3)$$

which is a quadratic equation in terms of ω^2 and has an analytic solution for any value of the amplitude. The square root of the real and positive solutions of the Eq(D.3) show the frequency for each amplitude. After calculating the amplitude-frequency pair, the phase can be calculated simply by solving the Eq(D.1) for X_2 , which is linear.

LIST OF PUBLICATIONS

PATENTS

2. Hamed Sadeghian Marnani, **Aliasghar Keyvani Janbahan** *Method of performing surface measurements on a surface of a sample, and scanning probe microscopy system therefore*, [WO2017069622A1](#)-EP3365689A1. (from this thesis)
1. Hamed Sadeghian, Mehmet Selman Tamer, **Aliasghar Keyvani**, *Method of modifying a surface of a sample, and a scanning probe microscopy system*, [WO/2018/088901](#)-EP3321694A1. (from this thesis)

JOURNAL PAPERS

15. **Aliasghar Keyvani**, Mehmet Selman Tamer, Jan-Willem van Wingerden, Hans Goosen, Fred van Keulen, *A Comprehensive Model for Transient Behavior of Tapping Mode Atomic Force Microscope*, [Nonlinear Dynamics](#) 97: 1601 (2019). (from this thesis)
14. **Aliasghar Keyvani**, Mehmet Selman Tamer, Jan-Willem van Wingerden, Hans Goosen, Fred van Keulen, *Control of Tapping Mode Atomic Force Microscopy with Estimated Average Forces*, Submitted to *Mechatronics*. (from this thesis)
13. **Aliasghar Keyvani**, Hamed Sadeghian, Gijs van der Veen, Mehmet Selman Tamer, Hans Goosen, Fred van Keulen, *Real-Time Estimation of the Tip-Sample Interactions in Tapping Mode Atomic Force Microscopy with a Regularized Kalman Filter* Submitted to *IEEE Transaction on Nanotechnology*. (from this thesis)
12. **Aliasghar Keyvani**, Hamed Sadeghian, Hans Goosen, Fred van Keulen, *On the origin of amplitude reduction mechanism in tapping mode atomic force microscopy*, [Applied Physics Letters](#) 112, 163104 (2018). (from this thesis)
11. **Aliasghar Keyvani**, Farbod Alijani, Hamed Sadeghian, Klara Maturova, Hans Goosen, Fred van Keulen, *Chaos: The Speed Limiting Phenomenon in Dynamic Atomic Force Microscopy*, [Journal of Applied Physics](#) 122, 224306 (2017). (from this thesis)
10. **Aliasghar Keyvani**, Hamed Sadeghian, Mehmet Selman Tamer, Hans Goosen, Fred van Keulen, *Minimizing Tip-Sample Forces and Enhancing Sensitivity in Atomic Force Microscopy with Dynamically Compliant Cantilevers*, [Journal of Applied Physics](#) 121, 244505 (2017). (from this thesis)
9. Hamed Mobki, Morteza H Sadeghi, Ghader Rezazadeh, Mohammad Fathalilou, **Aliasghar Keyvani**, *Nonlinear behavior of a nano-scale beam considering length scale-parameter*, [Applied Mathematical Modelling](#) 38, 1881 (2014).
8. Ghader Rezazadeh, **Aliasghar Keyvani**, Morteza H Sadeghi, Manouchehr Bahrami, *Effects of ohmic resistance on dynamic characteristics and impedance of micro/nano cantilever beam resonators*, [Sensing and Imaging](#) 14, 1-12 (2013).

7. **Aliasghar Keyvani**, Morteza H Sadeghi, Ghader Rezazadeh, Manouchehr Bahrami, *Effects of squeeze film damping on a clamped-clamped beam MEMS filter*, [Journal of Micro-Bio Robotics](#) 8, 83-90 (2013).
6. Ghader Rezazadeh, **Aliasghar Keyvani**, Samad Jafarmadar, *On a MEMS based dynamic remote temperature sensor using transverse vibration of a bi-layer micro-cantilever*, [Measurement](#) 45, 580-589 (2012).
5. **Aliasghar Keyvani**, Morteza H Sadeghi, Mina Ghanbari, Ghader Rezazadeh, *Some design parameters and corrective factors of nano-electromechanical devices*, [Journal of Micro-Nano Mechatronics](#) 6, 59-63 (2011).
4. Hadi Madinei, **Aliasghar Keyvani**, Mehdi Atashparva, Rasool Shabani, Ghader Rezazadeh, *Modeling of a Bio Sensor Based on Detection of Antigens Concentration Using an Electrically Actuated Micro Cantilever*, [Sensors and Transducers](#) 125, 238 (2011).
3. Ghader Rezazadeh, Mina Ghanbari, Iraj Mirzaee, **Aliasghar Keyvani**, *On the modeling of a piezoelectrically actuated microsensor for simultaneous measurement of fluids viscosity and density*, [Measurement](#) 43, 1516-1524 (2010).
2. **Aliasghar Keyvani**, Ahmad Ghanbari, Jafar Keyghobadi, *Investigation of squeeze film effect on dynamic characteristics of electrically actuated fully clamped micro-beam*, [Sensors and Transducers](#) 123, 41 (2010).
1. Farid Vakili-Tahami, Hamed Mobki, **Aliasghar Keyvani**, Ghader Rezazadeh, *Pull-in Phenomena and Dynamic Response of a Capacitive Nano-beam Switch*, [Vol. Sensors and Transducers](#) 110, 26-37 (2009).

CONFERENCE PAPERS

16. Maarten E v Reijzen, Mehmet S Tamer, Maarten H v Es, Martijn v Riel, **Aliasghar Keyvani**, Hamed Sadeghian, Marco vd Lans *Improved sub-surface AFM using photothermal actuation* [Proc. SPIE Advanced Lithography 10959, 109590L, 2019, San Joze, United States](#)
15. **Aliasghar Keyvani**, Farbod Alijani, Hamed Sadeghian, Hans Goosen, Fred van Keulen, *A new Route for chaos in Tapping Mode Atomic Force Microscopy* [Chaos 2017, Barcelona, Spain.](#) (from this thesis)
14. **A. Keyvani**, H. Sadeghian, H. Goosen, F van Keulen, *Quantifying Amplitude Reduction Mechanism in Tapping Mode Atomic Force Microscopy* [Workshop on Nanomechanical Sensing 2016, Delft, the Netherlands.](#) (from this thesis)
13. M. S. Tamer, H. Sadeghian, **A. Keyvani**, H. Goosen, F van Keulen, *Quantitative measurement of tip-sample interaction forces in tapping mode atomic force microscopy*, [Workshop on Nanomechanical Sensing 2016, Delft, the Netherlands.](#)
12. **A. Keyvani**, M. S. Tamer, M. van Es, H. Sadeghian, *Simultaneous AFM Nano-Machining and Imaging for Photomask Repair*, [Proc. SPIE Advanced Lithography 9778-42, 2016, San Jose, United States.](#) (from this thesis)
11. **A. Keyvani**, H. Sadeghian, H. Goosen, F van Keulen, *Dynamically Compliant Probes for Atomic Force Microscopy*, [Workshop on Nanomechanical Sensing 2015, Auckland, New Zealand.](#) (from this thesis)

10. **A. Keyvani**, H. Sadeghian, H. Goosen, F. van Keulen, *Tip-Sample Interactions in Dynamically Compliant AFM Probes*, Workshop on Nanomechanical Sensing 2015 Auckland, New Zealand. (from this thesis)
9. **A. Keyvani**, H. Sadeghian, H. Goosen, F. van Keulen, *Transient Tip-Sample Interactions in High-Speed AFM Imaging of 3D Nanostructures*, [Proc. SPIE Advanced Lithography 9424-100, 2015, San Jose, United States](#). (from this thesis)
8. **A. Keyvani**, H. Sadeghian, H. Goosen, F. van Keulen, *Low Force Tapping Mode Imaging of Biological Samples with Tapered Cantilevers*, 17th Annual winter workshop on Advances in Single Molecule research for biology and NanoScience 2015, Linz, Austria. (from this thesis)
7. **A. Keyvani**, H. Sadeghian, H. Goosen, F. van Keulen, *Effect of Excitation Frequency on Tip Wear in Tapping Mode Atomic Force Microscopy*, International Scanning Probe Microscopy 2014, Seoul, Korea. (from this thesis)
6. **A. Keyvani**, H. Sadeghian, H. Goosen, F. van Keulen, *High Speed Atomic Force Microscopy for Wafer Inspection*, Workshop on Nanomechanical Sensing 2014, Madrid, Spain. (from this thesis)
5. **A. Keyvani**, F. Samadi, G. Rezazadeh, M. Sadeghi, *Computation of Electromagnetic Field Distribution on a MEMS Proximeter Using Meshless Galerkin Method*, 1st National conference on MEMS 16-17 nov. 2011 Khoy, Iran. Selected as distinguished work.
4. **A. Keyvani**, R. Shabani, *Quasi-Static Investigation of Squeeze Film Effect on a Fully Clamped Micro Beam*, 18th Annual International Conference on Mechanical Engineering-ISME 2010, Tehran, Iran
3. R. Shabani, **A. keyvani**, v. Asgarikhah, *Investigation of Bending and Stretching Effects in Static and Dynamic Behavior of a Circular Micro Plate*, 17th Annual International Conference on Mechanical Engineering-ISME 2009, Tehran, Iran
2. M. Atashparva, G. Rezazadeh, **A. Keyvani**, *Effects of Applied Voltage and Antigens on Eigen Frequency Shifting of a MEMS Biosensor*, 17th Annual International Conference on Mechanical Engineering ISME 2009, Tehran, Iran
1. M. Atashparva, G. Rezazadeh, **A. Keyvani**, *On the Sensitivity Increasing of a Capacitive Bio-Detector*, 2nd International Congress on Nanoscience and Nanotechnology, ICNN 2008, Tabriz, Iran

INVITED TALK

1. Dynamic Tuning of AFM Micro-cantilevers, Engineering Mechanics Symposium 29 October 2015, Hotel Papendal, Arnhem, The Netherlands. (from this thesis)

ACKNOWLEDGEMENTS

During this project, I very much enjoyed and prospered from the presence of many people which I would like to express my gratitude for. Getting to know these people is certainly the biggest achievement of my life; way above and beyond any academic or professional achievement.

First of All, I acknowledge my promoter Prof. dr. ir. Fred van Keulen and my daily supervisor Dr. ir. Hans Goosen for giving me the opportunity of working with them, the nice and insightful discussions, supporting and also challenging my ideas, and carefully reviewing all the output of my project. Their input for this project as well as my personal and professional growth is highly appreciated, and I would gladly keep working and discussing with them all my life. In short, it was an absolutely fantastic experience to work with them.

In this project, I closely collaborated with my fellow Ph.D. colleague Mehmet Selman Tamer. Mehmet has not only been essentially helpful in the experimental parts of the project, but also a very good and reliable friend. Working with such a noble, hardworking, and positive person was a pleasure and honor for me.

I have also benefited from collaborations and pleasant discussions with Dr. Murali Ghatkesar, Dr. ir. Jan-Willem van Wingerden, Dr. Farbod Alijani, Dr. ir. Gijs van der Veen, Dr. Hassan HosseinNia, Ir. Amir Firooznia, and Dr. Mustafa-Ali Arat. A total sum of all the input, ideas, and comments that I received from you would add up to a document probably larger than the present thesis. Also, I would like to thank Ir. Hozanna Miro, Dr. Gaurav Nada, Dr. Alard Katan, and Dr. Hugo Perez Graza who helped me and thought me a lot of useful techniques in micro-nano fabrication and testing techniques.

I spent a part of my Ph.D. work hours in TNO Optomechatronics, where I have met a group of highly skilled and experienced researchers and engineers which learned a lot from them. So I would like to thank all of them especially the members of the Control Group and NOMI team. I also would like to thank all the members of PME Department and SOM group, especially Banafshe, Rob, Max, Sanne, Roy, Emiel, Qi, Long, Matthijs, Can, and Alejandro for being such a good and friendly colleagues.

Finally, I would like to thank my mother Nadjibeh, my brother Aliakbar, my sister in law Negar, their lovely boy Ata, and my friends for their support and encouragement during this four years and before. They successfully put the smile on my face during busy and stressful Ph.D. time. My dearest friends Amir, Johan, Jessica, Umut, Willemijn, Melanie, Farid, Marjolein, Yashar, Marina, Naser, Cindy, Mehdi, and Mustafa are among the people who made the life fun for me during the last years.